Behaviour of GFRP-Reinforced Concrete Circular Columns Under Simulated Seismic Loading

by

Amr Elsayed Mohammed Abdallah

A Thesis submitted to the Faculty of Graduate Studies of

The University of Manitoba

in partial fulfilment of the requirements of the degree of

DOCTOR OF PHILOSOPHY

Department of Civil Engineering

University of Manitoba

Winnipeg, MB, Canada

ABSTRACT

Columns in earthquake-resistant reinforced concrete (RC) structures need adequate confinement to exhibit stable seismic response with satisfactory level of deformability. Circular RC columns can be confined using spirals or discrete hoops. While the use of non-corroding fibre-reinforced polymer (FRP) reinforcement has been established as a viable substitute for conventional steel, the available code provisions for seismic design of FRP confinement reinforcement are overly conservative. This is due to the scarcity of the available research data, particularly those related to high-strength concrete (HSC) columns and those with different aspect ratios. That is, the linear-elastic behavior of FRP material could be of concern when combined with the brittle nature of HSC or implemented in short columns, which could be significantly influenced by shear stresses.

A trailblazer research program was conducted to explore the seismic behaviour of glass FRP (GFRP)-RC circular columns, including experimental and numerical phases. The experimental work incorporated the construction and testing of fifteen full-scale GFRP-RC column-footing connections under concurrent axial loading and cyclic lateral drift reversals. The investigated parameters were the longitudinal reinforcement type, transverse reinforcement configuration, concrete compressive strength, axial load level and column aspect ratio.

The numerical phase included the construction and validation of a three-dimensional nonlinear finite-element model (FEM) against results from the experimental phase. The validated FEM was, then, used to conduct a comprehensive parametric study investigating the effect of the practical range of concrete compressive strength, spiral pitch, axial load level and column aspect ratio on the behaviour of such columns.

The results indicated the conservativeness of design provisions related to spiral pitch whereas the provisions of the Canadian Highway Bridge Design Code for lap splice length of discrete FRP hoops were found to be unsafe. Additionally, GFRP-reinforced HSC circular columns can exhibit stable seismic response with sufficient deformability when properly-confined. Unlike steel-RC columns, changing the aspect ratio insignificantly influenced the hysteretic response of GFRP-RC columns. Based on the results of this study, two new design models to predict the amount of FRP confinement reinforcement with remarkable accuracy were proposed.

ACKNOWLEDGEMENTS

All praise is due to almighty Allah, who endowed me with strength, guidance and blessings to complete this work. I wish to express my sincere gratitude and appreciation to my supervisor, Dr. Ehab El-Salakawy, PEng, FCSCE, FACI, FIIFC, Professor of Structural Engineering in the Department of Civil Engineering at the University of Manitoba, and Canada Research Chair in Durability and Modernization of Civil Infrastructure (2006-2016), for his wisdom, enthusiasm, inspiration, and encouragement through every step of the way. His continuous help, advice and support significantly contributed to the researcher and instructor I am.

Deepest gratitude is expressed to my PhD committee members, Dr. Emile Shehata, PEng, Senior Vice President at Tetra Tech Canada Inc., and Dr. Nan Wu, PEng, Associate Professor in the Department of Mechanical Engineering at the University of Manitoba, for their time and support. Additionally, I am deeply indebted to all my colleagues for their assistance throughout my program. Special thanks to Dr. Yasser Elgharafy, who passed away in August 2021, for his sincere assistance during the numerical phase of this study. The financial support provided by the Natural Sciences and Engineering Research Council of Canada (NSERC), the University of Manitoba Graduate Fellowship (UMGF), and the Manitoba Graduate Scholarship (MGS) is acknowledged. The GFRP reinforcement, generously provided by Pultrall Inc. (Thetford Mines, QC), is appreciated. The assistance received from the technical staff of the W. R. McQuade Heavy Structures Laboratory at the University of Manitoba is acknowledged.

There is no possible way I could express how thankful and grateful I am to my beloved parents, Elsayed and Reda. Their dedication, help, sacrifices, and prayers are always helping me being a better person and professional. I would also like to thank my siblings for their love, wishes, support and prayers. My love goes to my wife, Alaa, for her love, kindness, devotion, and understanding. Thank you for everything! Lastly, I would like to send my love to my precious son, Adam. You have been, and always will be, our source of happiness through all challenging times we have been through.

Amr Elsayed Abdallah, September 2021

To my beloved aunt, Haleema,

May Allah bless your soul.

To my beloved siblings, Ghada, Mohammed and Ahmed,

You are forever in my heart.

To Mom and Dad, Reda and Elsayed,

I hope this accomplishment brings me "another" step closer to making you proud of me.

You will always be my past, present, and future.

To my wife, Alaa, and my son, Adam,

You are my heart, soul, today, tomorrow, forever and my everything.

TABLE OF CONTENTS

LIST OF TABLES

LIST OF FIGURES

LIST OF NOTATIONS

A_c = cross-sectional area of column core;

A_F = area of the main FRP longitudinal reinforcing bars;

A_{Fv} = area of FRP shear reinforcement perpendicular to the axis of a member within the distance s;

A_g = gross cross-sectional area of the column;

A_{sh} = area of transverse reinforcement perpendicular to the axis of the member;

b_v = effective width of the web as per CSA S6-19;

b_w = minimum effective web width of the member as per CSA S806-12;

c = concrete core width or diameter;

c_{ts} = tension stiffening factor;

D = column diameter;

d = the least column dimension or effective depth of the member;

dA_c = area of unconfined concrete within the layer under consideration;

dA_{cc} = area of confined concrete within the layer under consideration;

d_b = nominal diameter of a reinforcing bar;

d_c = depth of centroid of layer under consideration from the extreme compression fiber;

d_h = hoop cross-sectional diameter;

d_{long} = effective shear depth as per CSA S6-19;

d_n = depth of compression zone;

d_s = nominal cross-sectional diameter of the hoop;

d_v = effective shear depth as per CSA S806-12;

E_c = elastic modulus of concrete in compression;

E_{EXP} = experimental total energy dissipation;

E_f = elastic modulus of FRP reinforcement in tension;

E_{FEM} = total energy dissipation estimated by FEM;

e = eccentricity of applied load from the centroid of the section;

f_c' = specified concrete compressive strength;

f_{cr} = cracking strength of concrete;

f_{Fh} = design stress level in FRP transverse confinement reinforcement;

f_{Fhcc} = Maximum design stress of transverse confinement reinforcement at the maximum confined concrete strength;

f_{Fu} = ultimate strength of the FRP reinforcement;

f_{Fv} = stress level in the FRP shear reinforcement;

$f_{le,FRP}$ = effective confinement pressure provided by FRP reinforcement;

f_t' = tensile strength of concrete;

$f_{t\text{-}cr}$ = tensile stress at the crack location;

G_F = specific fracture energy of concrete;

h_c = cross-sectional dimension of column core;

$I_{c,FRP}$ = modified version of the confinement index recommended by ACI-ASCE Committee 441 (ACI 2002) for FRP-RC columns;

$J_{Feng\text{-}M}$ = integrated performance index considering the generalized force as the bending moment;

$J_{Feng\text{-}V}$ = integrated performance index considering the generalized force as the lateral load;

$J_{0.0035}$ = integrated performance factor considering 3,500 με concrete compressive strain;

K_e = confinement effectiveness coefficient;

K_e = confinement effectiveness coefficient;

K_{EXP} = experimental initial stiffness;

K_{FEM} = initial stiffness estimated by FEM;

K_n = normal shear crack stiffness of cracked concrete;

K_t = tangential shear crack stiffness of cracked concrete;

k = ratio of depth of neutral axis to the reinforcement depth;

k_a = arch action coefficient;

k_c = confinement efficiency coefficient;

k_m = coefficient taking the effect of moment at section on shear strength into account;

k_r = reinforcement rigidity coefficient;

k_s = member size coefficient;

L = column shear span;

L_i = average length of column hinging region;

ℓ = initial gauge length of the diagonal LVDT;

N_f = factored axial load normal to the cross-section;

P = axial load applied to the column;

P_o = nominal unconfined axial capacity of the column;

$P_{r,max}$ = the maximum factored axial load resistance for a compression member;

P_{ro} = the factored axial load resistance at zero eccentricity;

$R_{A/P}$ = design index proposed by Bayrak and Sheikh (1997);

r_{FRP} = modified coefficient of Saatcioglu and Razvi (2002) for FRP-RC columns;

r_c^{lim} = reduction factor of compressive strength;

S_F = shear factor coefficient of concrete;

s = spiral pitch;

s_l = spacing of tie legs in rectangular columns;

V_{cr} = lateral cracking load applied to the column;

V_{EXP} = experimental lateral load capacity in pushing direction;

V_{FEM} = lateral load capacity in pushing direction as estimated by FEM;

V_r = factored shear resistance of FRP-RC members;

V_c = factored shear resistance provided by concrete;

V_{sF} = factored shear resistance provided by FRP transverse reinforcement in FRP-RC members;

V_{FRP} = factored shear resistance provided by FRP transverse reinforcement in FRP-RC members;

V'_{EXP} = experimental lateral load capacity in pulling direction;

V'_{FEM} = lateral load capacity in pulling direction as estimated by FEM;

w_{cr} = crack width;

w_d = critical compressive displacement of concrete;

y_i = vertical height of the midpoint of the i^{th} LVDT gauge length from the top surface of the footing;

α = initial inclination of the diagonal LVDT to the horizontal;

α_1 = ratio of average stress in rectangular compression block to the specified concrete strength;

β = factor used to account for shear resistance of cracked concrete (Chapter 2);

β = multiplier for the specific flow direction in ATENA/GiD (Chapter 8);

β_1 = ratio of depth of rectangular compression block to depth of the neutral axis;

β_c = concrete strength multiplier suggested for GFRP-RC circular columns;

γ = shear distortion angle;

Δ = lateral displacement at the column tip;

Δ_f = flexure displacement component;

Δ_s = slip displacement component;

δ = lateral drift ratio;

$\delta_{1,2}$ = axial deformation of a diagonal LVDT;

δ_{CSA} = failure drift estimated as per CSA S806-12 (CSA 2017);

δ_{EXP} = experimental failure drift;

δ_{FEM} = failure drift estimated by FEM;

δ_I = failure drift estimated using Model I (Equation 8.6);

δ_{II} = failure drift estimated using Model II (Equations 8.9 or Equation 8.10, as appropriate);

δ_{Pro} = failure drift estimated using Equation 6.5;

ε_{bot} = strain at outermost GFRP bar in tension;

ε_c = strain at centroid of layer under consideration in layered sectional analysis;

ε_{cp} = plastic strain at compressive strength;

ε_{cu} = ultimate compressive strain of concrete as per CSA standards or maximum usable concrete strain as per ACI standards;

ε_{FRP} = tensile strain at the centroid of FRP longitudinal reinforcement;

ε_{Fu} = ultimate tensile strain of FRP reinforcement;

ε_{top} = strain at extreme compression fiber;

θ = the angle of the diagonal compressive stress;

θ_i = flexural rotation of the i^{th} gauge length;

θ_s = slip rotation;

λ = concrete density factor;

μ = displacement deformability factor (Pan and Moehle 1989 in Chapter 5);

μ = Poisson's ratio (Chapter 8);

μ_Δ = displacement ductility parameter;

ρ = specific material weight;

ρ_f = longitudinal reinforcement ratio for FRP-RC columns;

ρ_{fb} = balanced reinforcement ratio for FRP-RC members;

ρ_{Fs} = transverse reinforcement volumetric ratio in FRP-RC members;

ρ_{sh} = volumetric ratio of transverse reinforcement in FRP-RC members;

ρ_{st} = longitudinal reinforcement ratio for steel-RC columns;

σ_c = stress in unconfined concrete corresponding to strain ε_c;

σ_{cc} = stress in confined concrete corresponding to strain ε_c;

σ_v = design stress of FRP shear reinforcement;

ϕ_c = material resistance factor for concrete, taken equal to unity;

ϕ_F = material resistance factor for FRP reinforcement, taken equal to unity; and

ϕ_{FRP} = material resistance factor for FRP reinforcement, taken equal to unity.

CHAPTER 1: INTRODUCTION

1.1. Background

Since early 1900s, steel has been used to reinforce concrete to provide tensile strength, ductility, shrinkage and cracking control, and many more advantages. Steel was believed to be protected against corrosion by the alkali nature of the concrete matrix. Nevertheless, corrosion problems aroused in many reinforced concrete (RC) structures, especially those located in harsh environments; such as bridges, parking garages, and marine structures. These structures represent a considerable portion of the infrastructure in North America, and particularly in Canada. Typically, the alternating freezing-thawing and wetting-drying cycles due to harsh weather in addition to the use of de-icing salts cause cracking of concrete. The latter, when combined with the infiltration of corrosive agents can initiate the electrochemical corrosion process, leading to strength and serviceability deterioration and, eventually, the loss of structural integrity.

Corrosion of steel reinforcement is a significant durability concern that contributes to progressive decay of structural integrity of RC structures. This requires recurring maintenance cycles, which result in significantly higher repair cost to preserve the service life of such structures. Several solutions have been proposed and implemented to limit the disastrous effects of corrosion including enlarging the outer concrete cover, improving concrete properties or the use of epoxy-coated, galvanized, or stainless-steel bars. Yet, they hardly delayed such detrimental effects rather than preventing them. Moreover, such approaches increased substantially the initial cost of the construction projects.

On the other hand, fibre-reinforced polymer (FRPs) reinforcement has proven to be a viable substitute to conventional steel bars, due to its non-corroding nature, electrical and magnetic non-conductivity (depending on the type of fibres incorporated), in addition to having much higher strength and less weight compared to steel reinforcing bars. Nonetheless, FRP reinforcing bars behave differently from steel counterparts. For instance, FRP bars have a relatively low modulus of elasticity when compared to steel bars, in addition to the elastic behaviour of the former up to failure without any yielding plateau (Figure 1.1). The anisotropic nature of FRP bars results in different compressive and shear responses from those observed for steel reinforcing bars. Therefore, the currently available design provisions for steel-RC structures cannot be directly

applied to FRP-RC ones. Instead, independent design provisions are provided for FRP-RC members either as stand-alone guidelines/standards (ACI 2015; CSA 2017) or within the available codes (AASHTO 2018; CSA 2019d). The research effort on FRP for the past few decades was mainly focused on the response of FRP bars as well as FRP-RC individual structural elements such as simply-supported beams and one-way slabs and recently, columns under monotonic loads. However, the behaviour of integrated RC elements such as beam-column, slab-column or column-footing joints is still in the early stages, especially those under seismic-simulated loading.

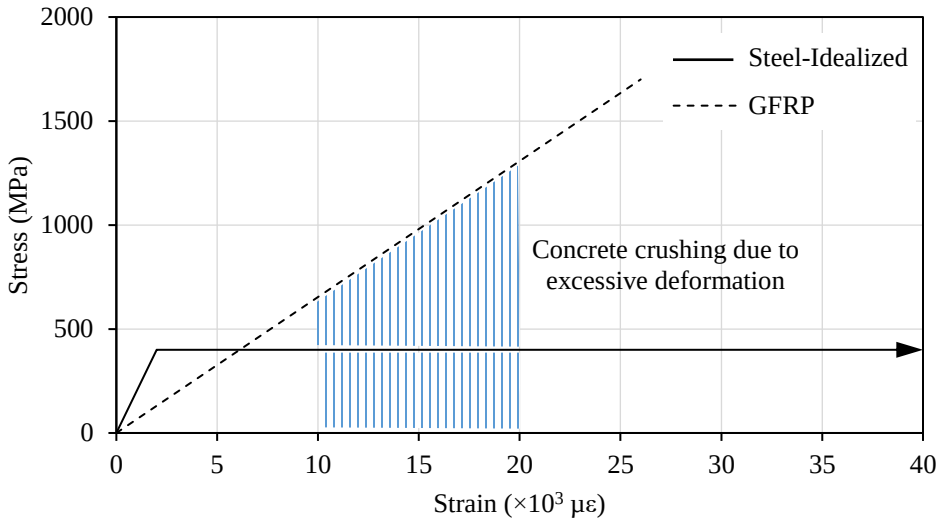

Figure 1.1: Stress-strain relationship for GFRP and steel reinforcement

The optimum response of RC structures located in earthquake-active areas should involve efficient dissipation of seismic energy through the desirable mechanisms while maintaining the structural integrity. This is stated by the different codes developed for steel-RC structures (ACI 2019a; CSA 2019b), which should be followed for FRP-RC structures as well. To date, the available experimental data on the seismic response of FRP-RC elements and connections is still limited.

1.2. Problem Definition

Columns are the main supporting elements in many RC structures, which can be constructed with a variety of shapes. The most common cross-sectional shapes of RC columns are circular and rectangular. Circular columns are often used because they have uniform stiffness and confinement action, whereas rectangular columns have non-uniform confinement due to stress concentration at their corners. Circular columns are usually more aesthetically-appealing and their smooth shapes

results in lower drag force in marine structures than rectangular ones. Additionally, circular columns facilitate maneuvering in structures such as bridges and parking garages. These structures are typically exposed to harsh environments, for which the non-corrodible FRP reinforcement is more suitable. However, the lower elastic modulus of FRP compared to steel in addition to the absence of yielding cast many doubts about the seismic performance of FRP-RC members.

The currently available codes in North America adopt the concept of strong column-weak beam for steel-RC moment-resisting frame (MRF) structures, in which yielding in the beams precedes yielding in columns (ACI 2019a; CSA 2019b). This is opposite to the weak column-strong beam system, which gives no warning before the building collapses under seismic excitations due to plastic hinging in the columns (Figure 1.2). However, to eventually prevent the formation of plastic hinges in columns at the first storey, it would require very large cross-sections for columns, which is cost ineffective. In addition, hinging at first storey columns may be helpful in order to achieve a complete inelastic deformation mechanism. Columns can even become the main source of energy dissipation in bridges where hinging in the superstructure is neither advisable nor feasible. An effective design for columns in MRFs should provide a sufficiently ductile behaviour with neither brittle flexural nor shear failure.

Recent research studies proved the feasibility of using GFRP reinforcement for concrete members and connections, including columns, under simulated seismic loading (Mady et al. 2011; Tavassoli et al. 2015; Ali and El-Salakawy 2016; Hasaballa and El-Salakawy 2016, 2018; Naqvi and El-Salakawy 2017; Ghomi and El-Salakawy 2018, 2019; El-Gendy and El-Salakawy 2019, 2020). The inelastic deformability of GFRP-RC members compensated for the ductility of the steel-RC ones, ensuring satisfactory levels of drift capacity and energy dissipation for the former. However, the development of design provisions for FRP-RC columns, especially under seismic loading, is still lagging. For instance, the use of FRP as main reinforcement in compression members is prohibited by the ACI 440.1R-15 (ACI 2015) guidelines, whereas less strict approach is adopted by AASHTO LRFD (AASHTO 2018) design guide and the Canadian standards CSA S806-12 (CSA 2017), which allow using FRP bars in columns without considering their contribution in load carrying capacity. On the contrary, the CSA S6-19 code (CSA 2019d) recognizes FRP bars in compression members with a contribution to load carrying capacity up to a compressive strain of 0.002.

The reason for such conservative measures associated with design of FRP-RC columns is the scarcity of research data. For example, the Canadian standards CSA S806-12 (CSA 2017) recognize discrete hoops as transverse reinforcement in circular columns with the same confinement efficiency as that of spirals. Despite this, the efficiency of circular hoops is not yet verified under seismic loading and no provisions are provided regarding the lap splice length of such hoops. A minimum lap splice length equal to 40 times the cross-sectional diameter of the hoop is set by CSA S6-19 (CSA 2019d), which was based on experimental results of FRP-RC columns tested under monotonic loading. Additionally, all available studies on FRP-RC columns used concrete compressive strengths of 55 MPa or less, which may raise concerns about the performance of high-strength concrete (HSC) columns, which are well-known for their brittle behaviour, when reinforced with elastic FRP bars.

Furthermore, the current seismic design provision for confinement reinforcement in FRP-RC columns (CSA 2017) was fundamentally derived from an empirical design model for steel-RC columns (Saatcioglu and Razvi 2002). The original design model assumed that the columns with smaller aspect ratio (i.e. length-to-diameter) would exhibit an inferior performance compared to longer counterparts, which was later refuted (Bae and Bayrak 2008). Considering the difference in behaviour of FRP and steel bars, the aforementioned assumption needs to be verified for FRP-RC columns.

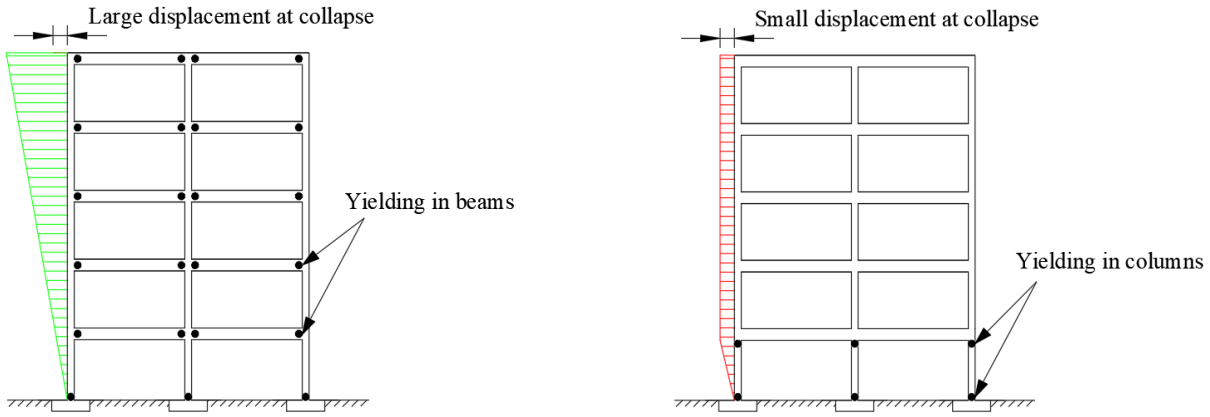

(a) Strong columns-weak beams (b) Weak columns–strong beams

Figure 1.2: Different performance mechanisms in moment-resisting frame structures

1.3. Scope of the Work

The scope of this study is to investigate the confinement behaviour of GFRP-RC circular columns under seismic loading through an extensive research program that included both experimental and numerical investigations. The experimental work encompassed the design, construction and testing of fifteen full-scale isolated column-footing specimens, while the numerical study used a non-linear finite element analysis (FEA) to evaluate the available design provisions for confinement reinforcement under seismic loading. Test specimens were assumed to be isolated from a prototype multi-storey frame building. Each specimen represented a first-storey column of the multistorey building, between the point of contra-flexure and the column–footing interface, with circular cross-section of 350-mm diameter, and varied length to achieve different aspect ratios. The specimens were tested under quasi-static, uni-directional lateral drift reversals along with constant axial loading. Effect of concrete strength under different axial load levels was also considered. Only one specimen was reinforced with steel bars and spiral as a reference specimen, whereas all other columns were reinforced longitudinally and laterally with GFRP reinforcement. The choice of GFRP in particular was mainly attributed to its large strain capacity, which could be beneficial under seismic loading conditions, and its relatively lower cost compared to other available types of FRP. The isolated test specimens were tested under concurrent axial loading and cyclic lateral drift reversals.

1.4. Research Objectives

The main objective of this research work was to study the confinement behaviour of GFRP-RC circular columns under simulated seismic loading. To fulfil this main objective, the following specific objectives were sought:

- Experimentally investigating the effect of key parameters on the seismic performance of GFRP-RC circular columns;
- Evaluating the currently available seismic design provisions for GFRP confinement reinforcement for RC columns and determining their adequacy;
- Constructing a reliable non-linear finite element model (FEM) for an in-depth study of the seismic performance of GFRP-RC circular columns; and

- Developing a design model for confinement reinforcement for GFRP-RC circular columns in seismic-resisting structures.

The following key parameters were experimentally studied:

- Reinforcement type (steel versus GFRP);
- Spiral pitch (50 and 85 mm);
- Transverse reinforcement configuration (hoops and spirals);
- Axial load level (0.1, 0.2 and 0.3 of the unconfined axial capacity of the column, P_o);
- Concrete compressive strength (35 and 80 MPa); and
- Column aspect ratio (3.0, 5.0 and 7.0).

1.5. Work Methodology

The research program comprised of two phases; experimental and numerical. The first phase involved the construction and experimental testing of fifteen full-scale column-footing RC specimens: one reinforced with steel and fourteen GFRP-RC specimens, under simultaneous axial loading and uniaxial lateral drift reversals up to failure. Each specimen resembled the lower segment of a first-storey column isolated from a prototype MRF structure having a varying storey height. Test specimens were constructed as circular columns with a diameter of 350 mm and varying lengths, and were cast with 1400 × 900 × 600 mm_footings. Two different concrete strengths (35 and 80 MPa) were used in addition to confinement using discrete hoops for two GFRP-RC columns. The details of design of the steel and GFRP-RC specimens can be found in Appendix A and B, respectively.

The numerical phase started with constructing a finite element model (FEM) to simulate the seismic response of the GFRP-RC columns, tested in the experimental phase, using the commercial software package ATENA/GiD (Červenka et al. 2020b). The accuracy and simulating efficiency of the FEM was validated against the results of the experimental study. Afterwards, the validated FEM was utilized to perform a comprehensive parametric study, where some key parameters affecting the seismic behaviour of GFRP-RC columns are investigated; such as concrete compressive strength, spiral pitch, axial load level and aspect ratio. Based on mathematical

analyses of the results of the parametric study, two new seismic design models for confinement reinforcement of GFRP-RC circular columns were proposed with significantly higher accuracy than the available design model by the Canadian standards (CSA 2017).

1.6. Thesis Organization

The thesis consists of nine chapters as outlined below:

- Chapter 1 provides a concise background about the research topic, defines the current problem and the scope of the research study, summarizes its main and specific objectives, and presents a brief description of the pursued methodology.
- Chapter 2 presents essential information with respect to the properties of FRP reinforcement along with an extensive review of the available experimental work on FRP-RC columns under monotonic and simulated-seismic loading. It also reviews the relevant research studies on steel-RC columns under cyclic lateral drifts, summarizes the currently available code provisions for design of FRP-RC columns and identifies the gap in the current research data on the seismic performance of FRP-RC columns.
- Chapter 3 discusses the research program in detail including the properties of used materials, the properties of the prototype structure and isolated test specimens, a description of the test setup and the details of loading procedure. Additionally, it explains the different aspects of the numerical study including the implemented constitutive models for materials, details of FEM, validation process and the selected variables for the parametric study.

The five chapters that follow are formatted as journal article style, where two articles were published and three are under review at the time of thesis submission.

- Chapter 4 (Article 1, published) compares the seismic behaviour of steel- versus GFRP-RC circular columns, evaluates the current limits for spiral pitch (CSA 2017) and assesses the feasibility of using GFRP discrete hoops as transverse reinforcement for GFRP-RC columns. It also provides recommendations for developing axial load-bending moment interaction diagrams for GFRP-RC circular columns with improved accuracy.

Abdallah, A. E. M., and El-Salakawy, E. 2021. "Confinement properties of GFRP-reinforced concrete circular columns under simulated seismic loading." *J. Compos. Constr.*, ASCE, 25 (2): 04020088, https://ascelibrary.org/doi/10.1061/%28ASCE%29CC.1943-5614.0001108.

- Chapter 5 (Article 2, published) investigates the seismic performance of GFRP-reinforced HSC columns having different spiral pitches and axial load levels. It also identifies analytically the most informative confinement and performance indexes for GFRP-RC circular columns.

  Abdallah, A. E., and El-Salakawy, E. F. 2021. "Seismic behavior of HSC circular columns reinforced with GFRP bars." *ACI Struct. J.*, 118 (5): 221-234, https://doi.org/10.14359/51732831.

- Chapter 6 (Article 3, in press) reveals the effect of aspect ratio on GFRP-RC circular columns under simulated seismic loading and different axial load levels. A modified version of the design equation by the Canadian standards (CSA 2017) is proposed to ease the over conservativeness of the original formula.

  Abdallah, A. E., and El-Salakawy, E. F. 2022. "Effect of aspect ratio on the seismic behavior of GFRP-RC columns." *ACI Struct. J.*, 119 (3), DOI: 10.14359/51734438, in press.

- Chapter 7 (Article 4, in press) investigates the combined effect of concrete compressive strength and aspect ratio on the seismic behaviour of GFRP-RC circular columns along with other factors such as axial load level and spiral pitch.

  Abdallah, A. E., and El-Salakawy, E. F. 2022. "Seismic performance of GFRP-RC circular columns with different aspect ratios and concrete strengths." *Eng. Struct.*, in press.

- Chapter 8 (Article 5, in press) explains the procedure of construction and validation of a numerical FEM to simulate the seismic response of GFRP-RC columns. The validated FEM is then used to carry out an extensive parametric study to investigate the impact of different key parameters, leading to new seismic design models for confinement reinforcement of GFRP-RC circular columns.

Abdallah, A. E., Selmy, Y., M., and El-Salakawy, E. 2022. "Confinement characteristics of GFRP-RC circular columns under simulated earthquake loading: a numerical study." *J. Compos. Constr.* ASCE, DOI: 10.1061/(ASCE)CC.1943-5614.0001195, in press

- Chapter 9 summarizes the main recommendations for the current standards based on the results of the experimental and numerical studies in addition to suggestions for future research work.

CHAPTER 2: LITERATURE REVIEW

2.1 Background

Columns are main supporting and load transferring elements in any RC structure. Therefore, all codes and guidelines handle the design of RC columns with great care to ensure a gradual failure. It is well-established that circular columns have the advantage of higher confinement efficiency over square and rectangular columns, due to having no corners and therefore, less arching action. The better confinement associated with circular columns, especially the spirally-reinforced ones, giving higher level of ductility compared to square and rectangular columns. Other advantages that can be recognized for circular columns include the ease of maneuvering around in parking garages or bridges and aesthetic properties. Steel reinforcement is usually used due to its favorable properties, especially its plasticity and yielding, which are the main source for ductility under any type of loading, and the main source for energy dissipation during seismic excitations.

During an earthquake, the failure mechanism for a steel-RC moment-resisting frame (MRF) structure would typically occur through the formation of plastic hinges in beams rather than columns. This mechanism, referred to as strong column-weak beam, can be achieved through proper design and detailing for beams and columns, allowing large lateral displacements for the structure prior to collapse. Nevertheless, hinging at first-story columns cannot be prevented; that is, it would need impractically increasing the cross-sections of these columns to avoid the formation of plastic hinges, which is not feasible. Furthermore, hinging at such location would be necessary to complete the plastic mechanism. Similarly, the formation of plastic hinges at the bottom of substructure of bridges would be inevitable under seismic excitations. Therefore, it is imperative to ensure sufficient levels of ductility, deformability and energy dissipation for the first-story columns of MRFs or substructures of bridges during earthquake events to cope with the other components of the plastic mechanism.

Columns constructed prior to the 1970s were designed for strength rather than ductility, resulting in largely spaced and poorly detailed confinement reinforcement (Galal et al. 2005). The severe and non-ductile modes of failure exhibited by such columns due to major earthquake events directed the researchers towards the design for ductility by imposing more strict requirements on the amount and spacing of confinement reinforcement in addition to special detailing for RC

members in earthquake-prone zones (Bayrak and Sheikh 1997). A significant amount of research was conducted to study the behavior of steel-RC columns under seismic loading (Park et al. 1982; Tanaka et al. 1985; Saatcioglu and Ozcebe 1989; Muguruma and Wanatabe 1990; Sheikh and Khoury 1993; Azizinamini et al. 1994; Sheikh et al. 1994; Bayrak and Sheikh 1997; Saatcioglu and Baingo 1999; Légeron and Paultre 2000; Paultre et al. 2001; Xiao and Yun 2002; Bae and Bayrak 2008; Paultre et al. 2009), allowing for more rationale design models and provisions (Saatcioglu and Razvi 2002; Elwood et al. 2009a, b).

Over the past few years, the behavior of FRP-RC columns under monotonic loading schemes was extensively studied, proving the feasibility of FRP as main reinforcement for compression members (Alsayed et al. 1999; De Luca et al. 2010; Pantelides et al. 2013; Jawaheri Zadeh and Nanni 2013; Afifi et al. 2014; Mohamed et al. 2014; Tobbi et al. 2014; Hadi et al. 2016; Hales et al. 2016; Hadhood et al. 2017; Elchalakani et al. 2018; Guérin et al. 2018; Xue et al. 2018; Liu et al. 2019; Mousa et al. 2019; Abdelazim et al. 2020; Barua and El-Salakawy 2020; Elchalakani et al. 2020; Barua et al. 2021). On the other hand, the available research studies on FRP-RC columns under simulated seismic loading are rather limited (Tavassoli et al. 2015; Ali and El-Salakawy 2016; Naqvi and El-Salakawy 2017; Naqvi et al. 2017; Elshamandy et al. 2018; Deng et al. 2018; Kharal and Sheikh 2018, 2020).

In this chapter, a general review is presented about the properties of FRP bars, aspects related to the behaviour of FRP-RC columns, especially under simulated seismic loading. In addition, some related research studies on the seismic performance of steel-RC columns will be briefly summarized.

2.2 Characteristics of FRP Composite Bars

As previously discussed, the physical and mechanical properties of FRP reinforcing bars are significantly different from those of conventional steel. According to ACI 440.1R-15 (ACI 2015), the main differences between FRP and steel reinforcement are:

- FRP is anisotropic while steel is an isotropic material;
- FRP bars cannot be shaped on-site, unlike steel bars;
- FRP bars, due to their anisotropy, have different coefficients of thermal expansion in the longitudinal direction from radial one;

- FRP is compromised when FRP-RC members are exposed to fire faster than steel would;
- In case of degradation, FRP bars would not jeopardize the integrity of the surrounding concrete, unlike steel which expands and spalls the concrete cover off (e.g. in case of corrosion);
- FRP bent bars have lower strength at the bend portion than the straight part;
- FRP bars have lower creep-rupture stress thresholds than steel;
- FRP bars behave linearly-elastic up to failure without any yielding plateau; and
- FRP has lower elastic modulus than steel, which makes serviceability limit states more likely to govern the design of FRP-RC members.

2.2.1 Physical properties

The physical properties of FRP are different from steel, especially the density and coefficients of thermal expansion (ACI 2015). The density of FRP bars ranges between one-sixth to one-fourth that of steel bars, which offers reduced transportation and labor costs in addition to ease of handling. On the other hand, the composite state of FRP bars makes their coefficients of thermal expansion different in the longitudinal and transverse directions; with the former dominated by the properties of the fibres and the latter dependent upon the resin. Generally, the transverse coefficient of thermal expansion of FRP would be much higher than that in the longitudinal direction and that of hardened concrete. Therefore, the thickness of the concrete cover should be carefully selected to avoid spalling when exposed to high temperatures.

2.2.2 Mechanical properties

2.2.2.1 Tensile behaviour

The tensile behaviour of FRP is characterized by its unidirectional nature since the fibres, which are the source of strength, are aligned in the longitudinal direction only. As shown in Figure 2.1, FRP reinforcement exhibits linear-elastic behaviour up to failure without undergoing any yielding plateau, unlike steel reinforcement. Therefore, FRP reinforcing bars are known for their brittle nature. It can also be observed that CFRP has similar axial stiffness to steel, whereas the axial stiffness of GFRP is much lower. Nevertheless, GFRP has higher strain capacity compared to CFRP, which is more beneficial especially under seismic loading. It can also be observed that FRP materials have much higher tensile strength than steel. Tensile properties of various FRP

reinforcing materials compared to steel are listed in Table 2.1. As mentioned earlier, the properties of FRP materials with the same constituents may vary according to the bar diameter, fibre-volume fraction and manufacturing process. Therefore, the properties of the final FRP product should be furnished by the producer for each batch. Furthermore, FRP bars cannot be bent after manufacturing since only thermosetting resins are permitted by current FRP design codes. Upon request, bent bars and ties can be shaped during manufacturing, but a strength reduction of around 40 to 50% is expected at the bend portion due to stress concentration (ACI 2015).

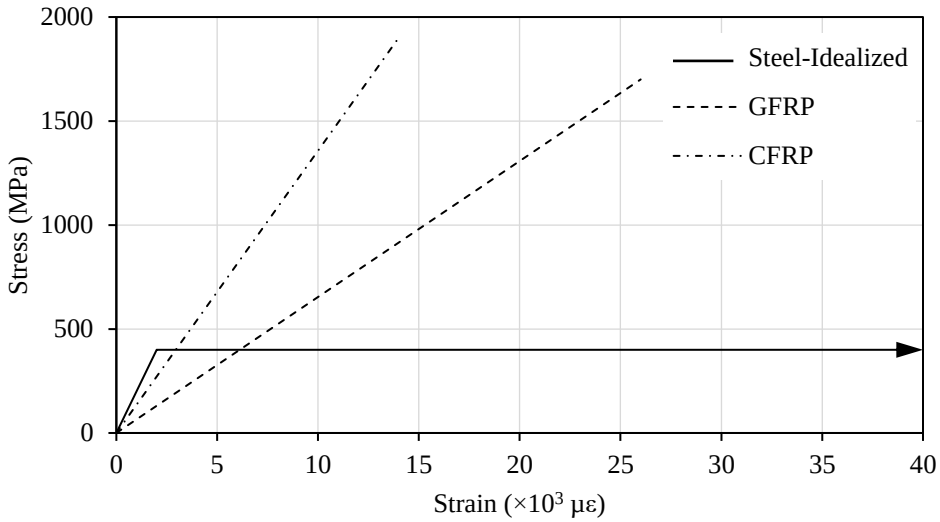

Figure 2.1: Schematic stress-strain relationship of FRP and steel reinforcement

2.2.2.2 Compressive behaviour

Generally, compressive strength of FRP is lower than its tensile strength as FRP materials are prone to buckling under compression, either as a whole entity or even micro buckling of individual fibres. Previous studies suggested reducing the value of compressive strength of FRP materials to 50% of its tensile strength, while the modulus of elasticity is the same under both cases of loading (Deitz et al. 2003; Tobbi et al. 2014; Tavassoli et al. 2015; Elchalakani et al. 2020). A recent study, however, concluded that the compressive strength of GFRP bars can reach up to 90% of their tensile strength (AlAjarmeh et al. 2019). To date, only the Canadian Highway Bridge Design Code, CSA S6-19 (CSA 2019d), considers the contribution of FRP bars in compression up to 2,000-με compressive strain. On the other hand, the other codes and guidelines in North America either do not recommend utilizing FRP as compressive reinforcement for compression and flexural members (AASHTO 2018; ACI 2015) or ignore its contribution if used (CSA 2017).

Table 2.1: Tensile properties of reinforcing bars (ACI 2015)

Property	Steel	GFRP	CFRP	AFRP
Tensile strength (MPa)	276-517[a]	483-16,00	600-3,690	1,720-2,540
Modulus of elasticity (GPa)	200	35-51	120-580	41-125
Ultimate tensile strain (με)	1,400-2,500 [a]	12,000-31,000	5,000-17,000	19,000-44,000

[a] At onset of yielding.

2.2.2.3 Shear behaviour

The FRP materials are well known for their anisotropic nature. Therefore, the interlaminar shear strength of FRP materials is known to be weak as it depends on the polymer resin, which is usually unreinforced in the transverse direction by fibres. The interlaminar shear strength of FRP bars is believed to be increased if some off-axis oriented fibres are introduced while manufacturing. In a similar manner to all other mechanical properties, the shear strength of FRP bars should be provided be the manufacturer (ACI 2015).

2.2.2.4 Bond behaviour

Surface and mechanical properties of the FRP bars, as well as the environmental conditions, are amongst the main factors impacting the bond strength of FRP bars with concrete. For FRP bars, surface can be prepared by chemicals to transfer bond stress by adhesion, sand-coating to transfer bond by friction, or ribbing to have bond transferred mechanically. Typically, when an FRP bar is embedded into concrete and subjected to tensile forces, stresses are transferred mainly through chemical bond until the initial slippage of the bar occurs. Afterwards, frictional or mechanical bond, or both, becomes the dominant stress transferring mechanism, depending upon the surface preparation technique (ACI 2015). However, surface condition is not the only factor affecting the bond strength of FRP bars. Concrete cover thickness, bar diameter, mechanical properties, and embedment length, and environmental conditions. A research study by Alves et al. (2011) concluded that for sand-coated GFRP bars, No. 16 (15.9-mm diameter) bars exhibited up to 35% higher bond strength than No. 19 (19.1-mm diameter) counterparts.

Few studies were conducted on the tensile lap splice length. Generally, the distribution of bond strength along the splice length was found to be non-linear, as the bond strength was found to be proportional to the square root of the development length (Mosley et al. 2008). A splice length of 30 times the bar diameter was recommended by Hasaballa et al. (2011) for beams in beam-column joints. Furthermore, for flexure-dominant GFRP-RC columns, a splice length of at least 60 times the bar diameter within the plastic hinge region was proposed by Naqvi and El-Salakawy (2017).

2.2.2.5 Durability of FRP Materials

The main phenomena affecting the durability of FRP bars, particularly tensile and bond strengths, are exposure to alkaline agents, variation of ambient humidity and temperature, and alternating freezing-thawing and wetting-drying cycles. As the resin encloses the fibres and protects them from the surrounding environment; the durability of FRPs bars would depend on the type of fibres, resin and fibre-volume fraction. For instance, the glass fibres can encounter high strength and stiffness degradation when exposed to alkaline solutions, aramid fibres will be influenced to a lower extent, whereas carbon fibres are the least susceptible to such issue. In addition, the combination of exposure to saline solution along with alternating freezing-thawing cycles can be detrimental to the tensile strength of GFRP and AFRP (ACI 2015).

2.3 Research on FRP-RC Columns under Monotonic Loading

To date, the ACI 440.1R-15 still does not recommend using FRP as main reinforcement for compression members nor as compression reinforcement for flexural member. Also, the Canadian standards for FRP-RC building structures, CSA S806-12 (CSA 2017), neglects the contribution of longitudinal FRP reinforcement in compression members and handles their design with great care. On the other hand, the Canadian standards for bridge structures, CSA S6-19 (CSA 2019d), allow using FRP as main reinforcement in columns and considers its contribution with a compressive strain limit of 2,000 με. In this section, some of the research work regarding FRP-RC columns under monotonic axial or eccentric loading is presented.

2.3.1 Behaviour of GFRP-RC columns under monotonic axial compression

The lower compressive strength of FRP materials compared to its tensile strength was a major concern regarding utilizing FRP bars in compression members. Reductions of ultimate axial capacity up to 13% were observed for replacement of the steel bars with GFRP during an early

attempt of testing FRP-RC columns (Alsayed et al. 1999; Pantelides et al. 2013). Later, slightly lower or comparable load capacities were observed for GFRP-RC columns when compared to their steel counterparts (De Luca et al. 2010; Lotfy 2010; Afifi et al. 2014; Tobbi et al. 2014). However, the contribution of the GFRP bars to the column capacity was found to be negligible. Besides, the surface condition of GFRP bars had a marginal effect on the performance of the columns (De Luca et al. 2010).

The longitudinal reinforcement ratio had an insignificant effect on the axial capacity of circular GFRP-RC columns, whereas a substantial influence was observed for such variable on the deformability (Afifi et al. 2014). In contrast, a considerable effect was reported for longitudinal reinforcement ratio in FRP-RC square columns (Tobbi et al. 2014).

The GFRP spirals reduced the cracking of the concrete cover for columns, and in turn, prevented corrosion (Pantelides et al. 2013). Adopting closer-spaced spirals with smaller diameter was found to be more effective than larger-spaced spirals with larger diameter (Afifi et al. 2014; Hadi et al. 2016a). Both FRP spirals and hoops according to the requirements of CSA S806-12 (CSA 2017) were found to efficiently confine the concrete core in the post-peak phase, with very similar strength and deformability (Mohamed et al. 2014). A splice length of 20 times the hoop cross-sectional diameter was found sufficient to provide comparable confinement to the FRP spirals. For square columns, closed ties provided more efficient lateral restraint than C-shaped ties (Tobbi et al. 2014).

2.3.2 Behaviour of GFRP-RC columns under monotonic eccentric loading

The feasibility of using FRP in eccentrically-loaded columns was proven and the FRP-RC columns could be analyzed using similar approach to that for steel-RC ones (Kawaguchi 1993; Choo et al. 2006). A minimum longitudinal reinforcement of 1.00% of the gross area of the column was suggested for FRP-RC columns in order to avoid the so-called brittle tension failure (Choo et al. 2006). Jawaheri Zadeh and Nanni (2013) suggested further to substitute the area of GFRP bars in compression with equivalent area of concrete; limit the tie spacing between 12 times the longitudinal bar diameter, 24 times the tie bar diameter, or the least dimension of the column cross-section; modify column stiffness based on the ratio of the moduli of elasticity of GFRP and steel longitudinal bars; modifying the slenderness limit to be 17; and limiting the maximum tensile strain for the GFRP longitudinal bars to 0.01 to avoid excessive lateral deflections.

Replacing steel with GFRP reinforcement resulted in reduction of the load capacity under all loading configurations (Hadi et al. 2016; Barua and El-Salakawy 2021). However, the GFRP-RC columns outperformed their steel-RC counterparts with respect to deformability.

The mode of failure varied as the eccentricity-to-diameter (*e/D*) ratio increased, from concrete crushing to flexure-tension failure, characterized by concrete crushing and spalling followed by gradual degradation of concrete compression block, with rupture of longitudinal GFRP bars in case of columns confined with discrete hoops (Hadhood et al. 2017a, d; Guérin et al. 2018; Barua and El-Salakawy 2021). Besides, the load capacity decreased as the *e/D* ratio increased.

The contribution of steel longitudinal bars in load capacity was about twice that of GFRP bars. However, ignoring this contribution for GFRP-RC columns led to overly conservative predictions for load capacity (Hadi et al. 2016). Additionally, increasing the longitudinal reinforcement ratio did not affect the axially-loaded column, while it significantly affected the peak load and post-peak behaviour of the eccentrically-loaded columns (Hadhood et al. 2017a, d; Guérin et al. 2018).

Decreasing the spiral pitch for GFRP-RC columns enhanced their load capacity and deformability (Hadi et al. 2016; Barua and El-Salakawy 2021). A lap splice length of 40 times the cross-sectional diameter of hoops was found adequate to confine the concrete core (Hadhood et al. 2017a). Decreasing the specified tie spacing of by the ratio of elastic moduli, of GFRP to steel bars, resulted in effective core confinement and buckling prevention for the longitudinal bars (Guérin et al. 2018).

A limited number of experimental studies is available on the performance of FRP-reinforced high-strength concrete (HSC) columns. Replacing steel reinforcement by GFRP resulted in a reduction of load capacity (by up to 12%) but increased the deformability (by up to 30%) for eccentrically-loaded columns, whereas no load reduction was observed for the axially-loaded HSC columns, yet with reduced deformability for GFRP-RC columns (Hadi et al. 2017; Hasan et al. 2017). Hadhood et al. (2017b, c) observed more sudden and explosive failure for CFRP-RC columns compared to their GFRP- or steel-RC counterparts when tested under low eccentricity. In addition, while the failure of GFRP-RC columns tested under high *e/D* ratios (>30%) was flexure-tension type, the CFRP-RC counterparts failed in a flexure-compression manner where CFRP bars failed in compression. Similar effect for longitudinal reinforcement ratio was observed for GFRP- and

CFRP-reinforced HSC columns. The efficiency of the GFRP spirals was reduced with the increase of load eccentricity, even with less spiral pitch (Hadi et al. 2017).

Few recent research studies investigated the slenderness effect on GFRP-RC columns. Hales et al. (2016) observed that columns teste under low *e/D* ratios (<10%) exhibited a material-type failure that was characterized by crushing of concrete core and spiral rupture. On the other hand, the slender HSC columns having *e/D* ratio of 33% failed in a stability-type buckling failure with double the lateral deflection exhibited by their counterparts with smaller *e/D* ratios. However, Abdelazim et al. (2020) reported a stability-type failure, where excessive tension cracks and lateral deformations triggered support rotation, only for slender columns tested under *e/D* ratio of 66%. Based on the experimental and analytical results, a modified slenderness limit of 18 was proposed for short columns bent in single curvature, in lieu of the limit set by CSA S806-12 (CSA 2017). Barua et al. (2021), on the other hand, observed similar effect for *e/D* ratio for the tested slenderness ratios (20 and 28). In addition, the slender GFRP-RC column exhibited 10 and 8% reduction of axial and lateral stiffness, respectively, compared to its steel-RC counterpart, which revealed the higher susceptibility of GFRP-RC columns to slenderness effects. For instance, increasing the slenderness ratio reduced the axial and lateral stiffness by up to 33 and 41%, respectively, compared with their shorter counterparts. Increasing the aspect ratio from 6.0 to 8.0 reduced the load capacity by 10% for square columns (Xue et al. 2018). Xue et al. (2018) also reported a marginal influence for the longitudinal reinforcement ratio on the load capacity.

Using GFRP spirals at a pitch equal to one-fourth the gross diameter of the column was found to effectively confine the concrete core for the tested columns (Barua et al. 2021).

2.4 Research on RC Columns under Seismic Loading

2.4.1 Seismic behaviour of steel-RC columns

2.4.1.1 Effect of axial load

It is well-established that the capability of the concrete core of sustaining compressive strains is proportional to the provided confinement pressure. In addition, increasing the axial load means increasing the compressive strain demand, and hence, higher axial load levels could decrease the lateral deformation capacity of the columns unless the confinement reinforcement is increased (Rabat et al. 1986; Saatcioglu and Ozcebe 1989; Sheikh and Khoury 1993; Elwood et al. 2009a).

Park et al. (1982) observed that the provided amount of confinement reinforcement according to the New Zealand code was somewhat excessive for the lower axial load levels ($P/f'_c .A_g = 0.2$), whereas it was unconservative for the higher axial load levels of 0.4 and 0.6 (i.e. P, f'_c and A_g are the applied axial load, concrete compressive strength and gross area of the column, respectively). Similar observations were reported by Watson and Park (1994). Tanaka et al. (1985) pointed out the significance of transverse reinforcement detailing under higher axial load levels for steel-RC square columns.

Increasing the axial load level was found to increase the flexural capacity and plastic hinge length, whereas the ductility was substantially decreased (Johal et al. 1987; Xiao and Yun 2002).

Muguruma and Wanatabe (1990) concluded that using high-strength steel ties with adequate detailing, the columns were able to achieve a displacement ductility factor more than 8.0, even under high axial load levels.

Sheikh and Khoury (1993) and Sheikh et al. (1994) concluded that the required amount of confinement reinforcement is proportional to concrete strength as long as the axial load level is measured in terms of P/P_o rather than $P/f'_c .A_g$, where P_o is the unconfined axial capacity of the column.

Watson et al. (1994) reported, based on theoretical analysis, that an increase of axial load level would result in greater amount of transverse reinforcement to achieve a certain curvature-ductility factor. This was proven experimentally by Bayrak and Sheikh (1997), where increasing the level of axial load was observed to reduce column ductility parameters and accelerate stiffness degradation. However, increasing the amount of transverse steel was found to be compensating for the effect of the higher axial load level. It was recommended for the ACI code provisions to include steel configuration, and level of axial load as design criteria for seismic-resistance columns.

Légeron and Paultre (2000) found that the experimental results related better to the requirement of the New Zealand code, which incorporated the axial load level as a design parameter for transverse reinforcement under seismic loading, rather than the ACI code. Similar conclusions were drawn by Palutre et al. (2001).

Bae and Bayrak (2008) concluded that the effect of axial load was complicated as it adversely affected the sectional behavior but increased the plastic hinge length. However, the higher axial loads had significant detrimental effect on the member behavior. This was justified as the adverse effects of high axial loads on sectional behavior exceeded the benefits gained from increased plastic hinge lengths under such high axial load level.

Paultre et al. (2009) observed comparable levels of ductility despite the different axial load levels applied, as the provided transverse reinforcement was designed considering the applied axial load level and yield strength of spirals, as proposed in a new design model.

2.4.1.2 Effect of aspect ratio

The effect of aspect ratio was extensively studied for steel-RC columns as the seismic response of such members changes with variation of column length-to-thickness ratio. For instance, slender columns such as those located in reception halls with large floor heights would need different design than columns in a typical residential building, to consider the additional design aspects associated with slenderness. A different behavior should also be expected for short or the so-called captive columns, as shown in Figure 2.2 (Saatcioglu 1991).

Davey and Park (1975) reported that the column displacement ductility capacity increased with the moment/shear ratio.

Iwasaki et al. (1985) concluded that lower aspect ratio resulted in lower displacement ductility capacity, which could be enhanced using larger transverse reinforcement ratio.

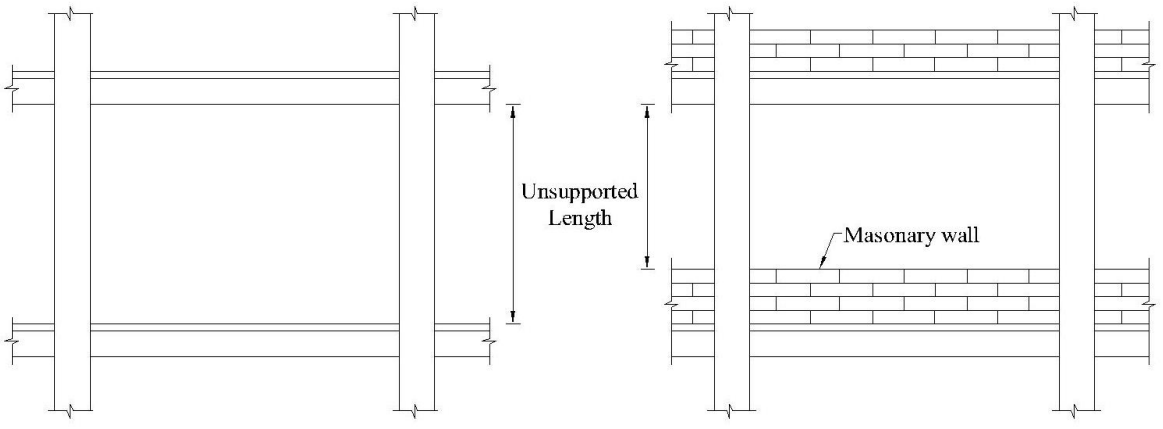

(a) Bare frame (b) Captive columns

Figure 2.2: The concept of captive columns (reproduced from Saatcioglu 1991)

Stone and Cheok (1989) tested two circular bridge columns with aspect ratios of 3.0 and 6.0, which both failed in a flexure-dominated mode and the measured displacement capacity and plastic hinge length were larger for the longer column. This agreed well with Sakai and Sheikh (1989).

Bayrak and Sheikh (1997) and Bayrak (1998) observed that increasing the aspect ratio resulted in reduced displacement ductility. On the other hand, the section ductility factors were marginally affected by variation of aspect ratio.

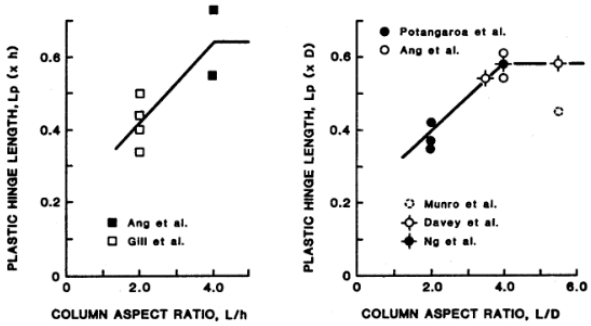

(a) Rectangular columns (b) Circular columns

Figure 2.3: Effect of column aspect ratio on plastic hinge length (Sakai and Sheikh 1989)

According to Lehman and Moehle (2000), the shortest column (aspect ratio of 4.0) exhibited the largest displacement ductility which was equal to 8.0, whereas the longer columns had the same displacement ductility capacity equal to 5.0.

Saatcioglu and Razvi (2002) proposed a displacement-based design approach for columns in seismic-active zones, where drift ratio was utilized as the performance criterion. The analytical results revealed that when the second-order moments attributed to *P*-Δ effect were considered in the analyses, the aspect ratio had an insignificant effect on drift capacity. On the other hand, when the *P*-Δ effect was omitted from the analyses, drift capacity exhibited a proportional increase with increasing the column aspect ratio. Therefore, a design model was proposed based on the results for the aspect ratio of 2.5.

Bae and Bayrak (2008) reported that the column with aspect ratio of 7.0 displayed a reduced lateral drift capacity, which was due to the strength decay associated with *P*-Δ effect. Prakash et al. (2010) reported flexural type of failure for columns with aspect ratios of 3.0 and 6.0. Though the column

was tested at a lower aspect ratio of L/D = 3.0, the failure was mainly dominated by flexure due to the relatively low longitudinal reinforcement ratio of the column and increased confinement.

2.4.1.3 Effect of longitudinal reinforcement ratio

The failure of a ductile flexure-dominant column would typically be due to strength decay of the cross section in compression or tension. Theoretically, if all other factors are constant for a column under seismic loading, variation of the longitudinal reinforcement ratio can change the distribution of compression and tension stresses which, in turn, may alter the overall response. In addition, the main factor controlling the effect of the longitudinal reinforcement ratio is the mode of failure. For instance, an increase in the longitudinal reinforcement ratio can reduce the ultimate curvature of a column failing in a compression-controlled manner. On the other hand, increasing the longitudinal reinforcement ratio may increase the displacement capacity for a column designed to exhibit a tension-controlled failure.

Lehman and Moehle (2000) concluded that the base rotation ductility increased proportionally with the longitudinal reinforcement ratio. The plastic hinge length also slightly increased as a larger longitudinal reinforcement ratio was used.

Saatcioglu and Razvi (2002) noticed insignificant changes in drift capacity with variation in longitudinal reinforcement ratio. Therefore, the longitudinal reinforcement ratio was not considered an influencing variable for confinement, and the proposed design model was developed using the results for an intermediate reinforcement ratio of 2%.

It was later clarified by Elwood et al. (2009b) that the amount of longitudinal reinforcement does not directly affect the confinement of square and rectangular column by itself. It is, however, the distribution of longitudinal reinforcement and the lateral restraint provided to it by ties and cross-ties that affect the confinement of such columns. On the other hand, variation of the longitudinal reinforcement ratio in circular column has a marginal influence on the confinement of concrete core.

2.4.1.4 Effect of transverse reinforcement ratio

Confinement is an essential parameter affecting the performance of columns in general, as the compressive behaviour of concrete was observed to be significantly improved by the presence of lateral support to the concrete core (Richart et al. 1928). Due to the non-uniform nature of the

confinement provided by rectilinear ties in square and rectangular columns, most of the research effort, especially after 1970s, addressed the significance of transverse reinforcement detailing in addition to the volumetric ratio to provide sufficient ductility to columns in earthquake-prone regions.

The importance of transverse reinforcement detailing was highlighted by Tanaka et al. (1985), who reported that 135° and 180° hooks would normally perform better than 90° ones, especially under high axial loads. Additionally, Johal et al. (1987) observed that only the columns having a combination of peripheral and inner closed ties achieved their theoretically predicted moment capacities. Similar observations were reported by Ozcebe and Saatcioglu (1987) and Saatcioglu and Ozcebe (1989). The results of Zahn et al. (1989) added that the tie spacing should be maintained within six times the longitudinal bar diameter to avoid premature buckling of longitudinal bars. The amount and configuration of transverse reinforcement affected the seismic response of HSC columns in a similar manner to NSC ones (Bayrak and Sheikh 1997)

Muguruma and Wanatabe (1990) concluded based on their test results that using high-strength steel ties with proper detailing can enable square HSC columns to achieve a displacement ductility factor more than 8.0, even under high axial load levels such as $0.63\, f'_c.A_g$.

Sheikh and Khoury (1993) and Sheikh et al. (1994) observed a proportional increase of column ductility with the amount of tie volumetric ratio. In addition, increasing the tie volumetric ratio increased the column strength. However, the moment capacities of the columns were marginally affected by the amount of transverse reinforcement.

Watson et al. (1994) concluded from their analytical study that an increase of axial load level, concrete strength, or relative cover-concrete thickness, or a decrease of longitudinal reinforcement ratio, would result in greater amount of transverse reinforcement to achieve a certain curvature-ductility factor.

Saatcioglu and Baingo (1999) concluded for circular HSC columns that an increase of the steel grade can compensate for low spiral volumetric ratio. Additionally, increasing the spiral pitch while maintaining the same spiral volumetric ratio resulted in significantly lower ultimate drift. due to the less effectively confined concrete core and insufficient lateral restraint provided for longitudinal bars.

Légeron and Paultre (2000) observed that the column with tie spacing-to-cross-sectional dimension of 0.2 achieved an ultimate drift ratio and displacement ductility about twice those of the column with the larger tie spacing. The significance of tie spacing on the achieved ultimate drift ratio was also corroborated by Xiao and Yun (2002). To avoid congestion of reinforcement due to the huge amount of transverse reinforcement required for HSC columns under high axial load levels, the use of high yield-strength steel for transverse reinforcement was proposed by Palutre et al. (2001).

Paultre et al. (2009) confirmed the conservativeness of the maximum spiral pitch (one-sixth the core diameter) set by the Canadian code (CSA A23.3-04) for HSC circular columns. On the other hand, the clear spacing requirements of the ACI code seemed to be more reasonable.

2.4.1.5 Effect of Concrete Strength

The hysteretic behaviour of HSC square columns was summarized by Xiao and Yun (2002) into three main stages: (1) initial stage where both unconfined concrete cover and confined concrete core are fully participating in the lateral load resistance; (2) stable behaviour, marked by concrete cover spalling, with plastic deformations of longitudinal steel yielding and confined core; and (3) deterioration and final failure. The lateral load capacity was typically reached at cover spalling.

The feasibility of HSC columns for use in ductile earthquake-resistant structures was demonstrated by Légeron and Paultre (2000) and Paultre et al. (2009), provided that a combination of adequate transverse reinforcement and efficient detailing, in case of square or rectangular columns, is provided.

Muguruma and Wanatabe (1990) concluded that large levels of ductility can be achieved for HSC columns using high-yield strength confining steel. It was also observed that the ductility provided by confinement reinforcement is reduced as the concrete strength increased. On the other hand, Azizinamini and Kuska (1994) recommended to limit the yield strength of transverse reinforcement to 414 MPa to limit tie spacing and, thus, avoid premature buckling of longitudinal bars.

Sheikh and Khoury (1993) and Sheikh et al. (1994) observed similar performance for the NSC and HSC columns tested under the same axial load level (P/P_o) and having the same fraction of transverse reinforcement compared to the amount required by the ACI code. It was also concluded

that the required amount of confinement reinforcement is proportional to concrete strength as long as the axial load level is measured in terms of P/P_o rather than $P/f'_c \cdot A_g$. It was found that for columns having the same axial load level measured as $P/f'_c \cdot A_g$, the NSC columns exhibited better ductility than HSC ones. On the other hand, when the axial load level was expressed as P/P_o, similar levels of energy absorption were observed, provided that an amount of transverse steel proportional to concrete strength is provided to the columns.

Bayrak and Sheikh (1997) proposed the concept of the factor $R_{A/P}$ which can be expressed as:

$$R_{A/P} = \frac{A_{sh}/A_{sh(ACI)}}{P/P_o} \qquad \text{Equation 2.1}$$

Where A_{sh} is the confinement reinforcement provided. It was reported that for two specimens with the same factor $R_{A/P}$, the confinement reinforcement was proportional to concrete compressive strength.

Saatcioglu and Baingo (1999) reported that increasing the concrete strength marginally affected the deformability of the columns as high levels of confinement were provided for all cases. On the other hand, the ultimate drift ratio was reduced when concrete strength increased (which agreed with Paultre et al. (2001)), yet all well-confined columns surpassed the drift ratio of 5.0% which indicated excellent performance. It was also reported, however, that when the lateral load degradation due to *P*-Δ effect is considered, all columns, including well-confined ones, exhibited significant degradation in lateral load resistance. This implied that the *P*-Δ effect is more significant for HSC columns, especially that the use of HSC would reduce the size of the concrete sections, leading to higher influence of *P*-Δ moments.

2.4.1.6 Effect of circular hoops versus spirals

Limited test data is available with regard to the performance of circular columns confined by discrete hoops versus spirally-confined ones, especially under seismic-simulated loading. Sheikh and Toklucu (1993) reported similar responses for axially-loaded RC circular columns with three different sizes reinforced laterally by spirals or discrete hoops. A superior confinement performance was observed for discrete hoops over spirals for one of the sizes included in that study. It was also noted that the independence of discrete hoops can be favorable as the rupture of a hoop will not affect the confinement action provided by other hoops, unlike spirals for which the

rupture of a turn will disrupt the continuity of the confinement pressure produced by the spiral over the length of the RC member.

Similarly, Saatcioglu and Baingo (1999) observed similar hysteretic responses under simultaneous axial loading and lateral drift reversals for HSC circular columns confined by spirals or discrete hoops. However, the visual inspection of the tested columns revealed that the hoops within the hinging region started to straighten out due to outward buckling of the longitudinal bars. Such observation was not recorded for spirally-confined columns due to the fact that they do not have hooks to be pushed outwards by the longitudinal bars. Therefore, it was concluded that spirals and hoops could exhibit comparable confinement under simulated seismic loading, although spirals seem to be more effective in terms of maintaining the integrity of concrete core and buckling prevention.

2.4.2 Seismic behaviour of FRP-RC columns

To date, the available research data regarding FRP-RC columns under seismic loading is scarce. The following subsections will include the research effort towards this issue and the effects of different parameters on the seismic performance of FRP-RC columns.

2.4.2.1 Effect of longitudinal reinforcement type and ratio

One of the earliest attempts to study the seismic response of FRP-RC columns was made by Sharbatdar (2003), who conducted tests on CFRP-RC columns having a 355 × 355-mm square cross-section, and 1,280-mm shear span and cast with large steel-RC footings. The axial load level (P/P_o) varied between 0.15 and 0.33 and the transverse reinforcement was provided by means of CFRP grids and with spacing of either 88 or 175 mm. It was concluded that all tested columns exhibited limited inelastic deformability with displacement ductility parameter ranging between 2.7 and 3.9 only. Increasing the longitudinal reinforcement ratio from 0.46 to 0.7% resulted in slight improvement to strength and deformability, although more lateral restraint to the longitudinal bars was provided to the specimen with larger longitudinal reinforcement ratio. In addition, using CFRP bars enabled the columns to display sufficient drift capacity which surpassed the 2.5% drift limit by the National Building Code of Canada, although some longitudinal CFRP bars failed in tension for the specimens tested under low axial load levels.

A single study can be found in literature on GFRP-RC circular columns, which was conducted by Tavassoli et al. (2015) on columns with a 356-mm diameter. In that study, two types of GFRP reinforcement were used; sand-coated and deformed. Stable responses were observed for the columns reinforced with GFRP bars and spirals, reaching rift ratios almost twice the design values, under different axial load levels. It was also reported that the type of GFRP material used did not have a significant effect on the behavior of the columns. A comparison with a steel-RC column tested in a previous study revealed lower energy and work indicators for the GFRP-RC column. However, the GFRP-RC column exhibited more stable response than its steel-RC counterpart, which can be attributed to the elastic behaviour of the GFRP, resulting in an increasing level of confinement by the GFRP spiral with increased deformation, which in turn, delays the crushing of the core concrete. On the other hand, the confinement becomes less effective once the steel transverse reinforcement starts yielding, resulting in more rapid strength and stiffness degradation. Similar observation was reported by Ali and El-Salakawy (2016).

Ali and El-Salakawy (2016) reported higher intensity of flexural cracks for the GFRP-RC square column specimens, having cross-sectional dimensions of 350 × 350 mm, comparing to the steel-RC counterpart. In addition, lower lateral load resistance was exhibited by the GFRP-RC specimen relatively to the steel-RC counterpart at the early stages, which was attributed to the low modulus of elasticity of the GFRP comparing to steel. Pinching of hysteretic loops was observed for steel-RC specimen and was attributed to the effect of yielding which results in plastic deformation for the column, while the hysteretic loops for GFRP-RC counterpart were found to be aiming at the origin of the load-drift ratio relationship due to the linear-elastic behaviour of GFRP. This was found in agreement with the results of cumulative energy dissipation, which was found for the GFRP-RC specimens to be approximately one-half that of the steel-RC counterpart at a drift ratio of 4.00%. However, the GFRP-RC columns were found to be capable of sustaining the gravity loads in presence of seismic activity, in a similar manner to the steel–RC columns, as the drift capacity of GFRP- RC specimens exceeded the 2.50 and the 4.00% limits by the National Building Code of Canada and CSA S806-12, respectively. Besides, the deformability of GFRP-RC columns compensated for the ductility of steel-RC columns. It was also observed that the first signs of failure for the steel-RC prototype were initiated at 6.5% drift ratio by buckling of the longitudinal bars. Then at 8.5% drift ratio crushing of the concrete core took place, followed by rupture of the longitudinal bars in the tension zone. On the other hand, all GFRP-RC specimens failed at a drift

ratio ranged between 8.5 to 12.5% by crushing of the concrete, followed by compression failure of the longitudinal bars. It was also observed from the hysteretic response that the steel-RC specimen reached a 58% strength degradation at failure, while for the GFRP-RC counterpart an insignificant strength degradation was recorded at failure at 12.5% drift ratio. the rotation of the plastic hinge governed the rotation for the steel-RC specimen, while for the GFRP-RC counterpart the cracking which extended up to mid height of the column due to the elasticity of the GFRP, had a greater role than in the steel-RC specimen. Moreover, observations from the strain profiles along the longitudinal steel extended through the footing showed that the length of GFRP longitudinal bars inside the footing was sufficient to develop bar capacity for all specimens, despite the different bond characteristics between steel and GFRP which required more development length.

Similar observations were reported by Elshamandy et al. (2018) for 400 × 400-mm square columns tested under axial load levels ($P/f'_c \, .A_g$) ranging between 0.2 and 0.4, where GFRP-RC columns exhibited stable hysteretic responses with almost no strength degradation, resulting in an enhanced deformability with high drift ratios at failure. Those attained drift ratio were more than 4%, proving the conservatism of the drift ratio limits provided by the North American codes. Moreover, the GFRP-RC columns dissipated almost 75% and 70% the energy dissipated by their steel-RC counterparts at 2.50% and 4.00% drift ratio, respectively.

The effect of longitudinal reinforcement ratio was studied by Ali and El-Salakawy (2016), who reported an increase of lateral capacity, accompanied with an adverse effect on the level of deformability, when the longitudinal reinforcement ratio increased. For instance, the specimens with 1.9 and 2.6% reinforcement ratios both exhibited approximately 50% decrease and 20% increase, on average, for the drift capacity and lateral load capacity, respectively, compared to the specimen having 1.3% reinforcement ratio. Elshamandy et al. (2018) observed no brittle tension failure for a longitudinal reinforcement ratio as low as 0.63%, under an axial load level of 20%.

Kharal and Sheikh (2020) concluded for their tests on GFRP- and hybrid (longitudinal steel bars + GFRP ties)-RC square columns that the specimens exhibited satisfactory performance under high axial load levels (P/P_o = 0.42 and 0.56). Replacing steel bars improved the flexural strength, deformability and the so-called member ductility level, whereas the lateral load capacity was decreased. It was also noted that the enhancement of flexural strength is more critical for GFRP-RC columns than those reinforced with steel to avoid underestimation of the shear demand.

2.4.2.2 Effect of axial load level

Sharbatdar (2003) observed about 25% increase in the lateral load capacity and 30% decrease in ultimate drift for the CFRP-RC square column subjected to higher axial load level compared to its counterpart tested under lower axial load. In addition, brittle tension failure was observed for the columns tested under axial load below the balanced load for the column cross-section.

Tavassoli et al. (2015) reported more damage and lower levels of deformability for the columns subjected to the higher axial load level (P/P_o = 0.42). It was also stated that the transverse reinforcement ratio is more critical for such high axially loaded columns. Experimental results of Ali and El-Salakawy (2016) indicated early strength gain for the specimens with higher axial loading. Nonetheless, the more axial load applied on the specimen, the more rapid the deterioration was. Additionally, lower levels of deformability were noticed at failure for the specimens loaded under higher axial load levels. An outcome of 15% and 50% decrease in strength and drift capacity at failure, respectively, was observed as a result of increasing the axial load level ($P/f'_c .A_g$) from 0.1 to 0.2. In addition, more stable rotation due to inelastic deformability hinge was reported for the column tested under the lowest axial load level and tie spacing compared to the other specimens subjected to higher axial loads, or having larger tie spacing. Similarly, Elshamandy et al. (2018) concluded that increasing the axial load level was found to decrease the deformability of GFRP-RC square columns, with no noticeable enhancement of strength. Similar results were reported by Kharal and Sheikh (2020).

2.4.2.3 Effect of transverse reinforcement ratio

It was noted by Sharbatdar (2003) that the spacing of the CFRP grids was an imperative parameter, which significantly affected lateral load capacity and deformability, especially for the longer columns. For example, decreasing the grid spacing from one-half to one-forth the side length of the cross section, for the columns having an aspect ratio of 6.23, resulted in an increase of 16% in lateral load capacity, whereas the drift capacity was increased by 160%. The enhancement was, however, less pronounced in the short columns having an aspect ratio of 3.65, where insignificant improvement was observed for lateral load capacity, while an increase of 30% was recorded for the drift capacity.

The GFRP-RC circular columns exhibited more stable response than the steel-RC counterparts (Tavassoli et al. 2015) reported a similar influence of spiral volumetric ratio and pitch for GFRP-

and steel-RC columns. In addition, the lateral load capacities for all specimens subjected to the same axial load level were similar as the lateral load capacities were typically developed during the first few cycles prior to concrete cover spalling, which would not be affected by spiral pitch or volumetric ratio. On the other hand, the moment capacity increased by 50% when the spiral pitch was reduced from 160 to 50 mm. The same reduction of spiral pitch increased the drift capacity approximately twofold, which denotes the effectiveness of decreasing spiral pitch in improving the confinement of concrete core and delaying buckling of the longitudinal bars. On the other hand, increasing the spiral size was not found as efficient as reducing the spiral pitch.

Ali and El-Salakawy (2016) stated that stable hysteresis behavior up to failure can be expected for GFRP-RC rectangular columns having well-distributed longitudinal reinforcement with proper laterally supported by closely-spaced stirrups. While the well-confined column failed at 12.5% by concrete core crushing, the columns with larger values of tie spacing exhibited a synchronous crushing of concrete along with buckling and compression failure of the longitudinal bars between ties took place at 8.5% drift ratio. In addition, the adequacy of the provisions of the Canadian standard CSA S806-12 (CSA 2017) for the amount of transverse reinforcement was proven through the experimental results. Increasing the GFRP tie spacing from *0.25d* to *0.33d* resulted in 50% less drift capacity and a strength degradation at failure of 25%, where *d* is the least column dimension. Moreover, the transverse reinforcement ratio was found to be critical for high axially-loaded columns.

In the study carried out by Elshamandy et al. (2018), the elasticity and linear behavior of GFRP rectilinear spirals and cross ties provided continuous confinement to the concrete core till the last stages of loading, on contrary to the steel ties which lose their confinement ability after yielding. Decreasing the spacing of the GFRP reinforcement from 150 to 80 mm enhanced the strength and stiffness by 23 and 60%, respectively. On the other hand, increasing the spacing from 80 to 100 mm resulted in only a 13% strength reduction without significantly altering the other behavioral aspects. This was the reason why the authors considered the requirement of CSA S806-12 (CSA 2017) for the tie spacing not to exceed 6 times the longitudinal bar diameter as overly conservative. It was recommended to consider the longitudinal reinforcement area while calculating the needed transverse reinforcement, which will result in larger amount of confinement reinforcement to

satisfy the strain limit. Furthermore, the secondary moments due to *P*-Δ effect were recommended to be considered for the high drift ratios.

2.4.2.4 Effect of aspect ratio

The available research data with respect to FRP-RC columns with different aspect ratios is very scarce and limited to either CFRP-RC columns (Sharbatdar 2003), GFRP-reinforced fibre-reinforced concrete columns (Deng et al. 2018), or hybrid (longitudinal steel bars + GFRP spirals)-RC columns (Kharal et al. 2021).

Sharbatdar (2003) observed for columns with aspect ratios of 6.23 and 3.65 that all columns failed in flexure. The main difference reported was the higher rate of strength degradation for the shorter columns due to higher shear stress reversals, which caused more diagonal cracking and higher deterioration of concrete core. The effects of other factors such as longitudinal reinforcement ratio and axial load level on short CFRP-RC columns were reported to be similar to their effects on long columns, except for the influence of transverse reinforcement ratio which was rather limited for the short columns.

Deng et al. (2018) tested GFRP-RC square columns under constant axial loading and cyclic lateral drift reversals. The concrete was mixed with macro-polypropylene fibres to increase deformability. It was reported that concrete spalling occurred earlier for columns with the lower aspect ratio of 2.68 than longer columns with aspect ratio of 3.71. In addition, the columns with aspect ratio of 3.71 failed in flexure and showed no failure-inducing diagonal cracks, whereas the columns with a lower aspect ratio of 2.68 suffered shear-bond failure with many diagonal cracks. Additionally, longer columns showed better ductility and energy dissipation compared to shorter ones. Furthermore, the influence of aspect ratio on GFRP-RC columns performance was notable. The specimens with axial load levels of 0.1 and aspect ratios of 3.71 and 2.68 showed lateral drift ratios of 5.06% and 4.87%, respectively. Additionally, the specimens with axial load level of 0.19 and aspect ratios 3.71 and 2.68 showed lateral drift ratios of 4.59% and 4.21%, respectively.

Kharal et al. (2021) compared their results of large circular hybrid (longitudinal steel bars + GFRP spirals)-RC columns having a 508-mm diameter with the results of similar but smaller columns, having a diameter of 356, tested by Tavasolli and Sheikh (2017). It was concluded that the effects associated with aspect ratio would be minimum as all compared columns failed in flexure.

However, comparable or better confinement and flexural strength were reported for the larger columns compared to their smaller counterparts.

2.4.2.5 Effect of lap splice

The behaviour of GFRP-RC spliced columns under seismic loading was only addressed by few research studies such as Naqvi and El-Salakawy (2017). Six full-scale square columns having 350-mm sides, 1650 mm shear span, with a 1400 × 1400 × 600-mm footing, were constructed and tested under simulated seismic loading with an axial load level ($P/f'_c . A_g$) of 0.1. It was concluded that the lap splice length of 60 d_b, where d_b is the diameter of the longitudinal bar, can be implemented as a lower bound for GFRP-RC square columns, since the shorter splice lengths exhibited strain lag and bond slippage. In addition, the adequacy of the CSA/S806-12 requirements for the amount of GFRP transverse reinforcement was proven for the spliced GFRP-RC square columns.

Naqvi et al. (2017) concluded that the columns with 60 d_b splice length showed comparable performance to non-spliced GFRP-RC columns, even under high axial loads (0.15 and 0.2 $f'_c . A_g$) despite the higher strength degradation displayed. Additionally, the incorporation of end-hooked steel fibres with a volume fraction of 1.0% into concrete enabled a GFRP-RC column with deficient splice length of 40 d_b to perform with satisfactory deformability, delaying the cover spalling and promoting the integrity of the concrete core.

2.5. Available Codes and Guidelines

To date, neither ACI 440.1R-15 (ACI 2015), CSA S806-12 (CSA 2017), nor CSA S6-19 (CSA 2019d) have complete guidelines for design of columns longitudinally reinforced with FRP bars in seismic areas. This can be attributed to the different mechanical properties of GFRP from those of steel, for both longitudinal and transverse reinforcements, as well as the lack of available research data.

2.5.1. Design for axial load and flexure

Although FRP-RC members are behaving in flexure in a similar way to steel-RC ones, the differences of mechanical properties such as linear elastic behaviour up to failure and low compressive strength of FRP bars should be considered. Therefore, some of the assumptions deemed for flexure design are modified to be as follows: (a) besides the concrete tensile strength,

the compressive strength of FRP bars is also neglected; and (b) the stress-strain behaviour of FRP reinforcement is linear-elastic up to failure.

For steel-RC flexural members, the tension-controlled failure is preferable as the inelastic deformation of steel beyond yielding is utilized, giving ductility to the section before failure, On the contrary, the FRP-RC members may exhibit a highly brittle tension failure under flexure if the failure is controlled by rupture of the FRP bars. Therefore, the available guidelines for design FRP-RC flexural members promote compression-controlled failure rather than a tension-controlled one. In such failure, the inelastic behaviour exhibited by concrete before crushing can provide some deformability for the FRP-RC section (ACI 2015; CSA 2017). In case of low FRP longitudinal reinforcement ratio, especially for GFRP-RC columns, the columns may exhibit the aforementioned brittle tension failure rather than developing a pure bending condition. Therefore, a minimum longitudinal reinforcement of 1.00% the gross area of the column section was suggested (Choo et al. 2006). A hypothetical balanced mode of failure is considered by the currently available guidelines for FRP-RC members (ACI 2015; CSA 2017), as the threshold between the desirable compression failure and the undesirable brittle tension failure. This hypothetical balanced failure assumes a simultaneous crushing of the concrete ($\varepsilon_c = \varepsilon_{cu}$) along with rupture of the outermost layer of the FRP reinforcement ($\varepsilon_{FRP} = \varepsilon_{Fu}$), when a balanced reinforcement ratio (ρ_{fb}) is provided. The provided longitudinal reinforcement ratio has to exceed the balanced reinforcement ratio in order to develop a compression-controlled mode of failure. Figures 2.4 and 2.5 show the strength (*P-M*) interaction diagram for steel-RC members and the theoretically developed diagram for GFRP-RC members, as suggested by Hadhood et al. (2017b), and based on the assumptions mentioned earlier. The interaction diagram for the GFRP-RC columns has the characteristic knee-shape found for steel RC columns. However, it is worth mentioning that the point of inflection of the diagram for circular GFRP-RC members cannot be regarded as balanced point. Figure 2.5 shows the strength (P-M) interaction diagram for a GFRP-RC column, where the moment increases with the reduction of axial load up to a certain point. Then the moment decreases with decreasing axial load, but the rate of decrease of moment capacity is relatively low.

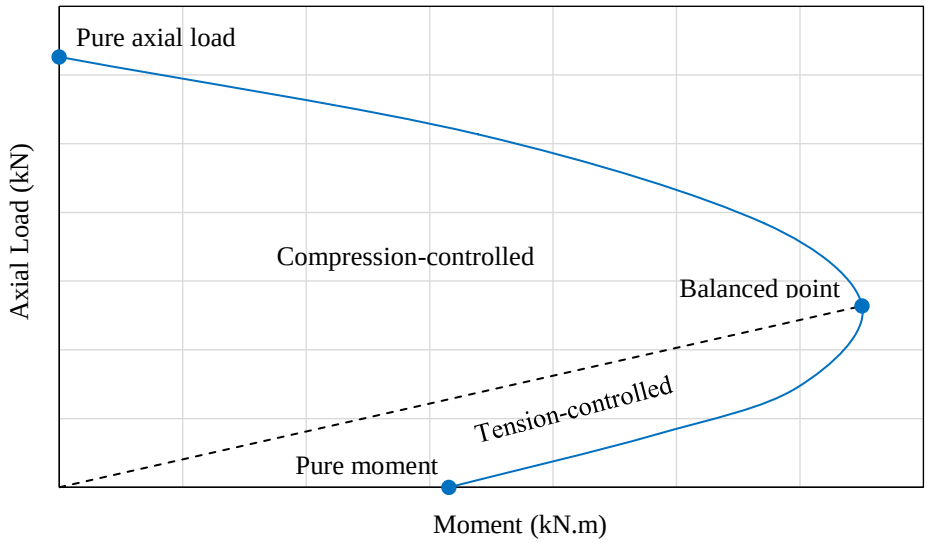

Figure 2.4: Typical strength (*P-M*) interaction diagram for a steel-RC column

2.5.1.1. The Canadian standard CSA S806-12

In the Canadian standard CSA S806-12 (CSA 2017), Clause 8.4.3.7 sets a minimum limit for the longitudinal reinforcement ratio of compression members equal to 1.00% of the column gross cross-sectional area. This limit was set based on the minimum reinforcement ratio of steel-RC columns, but later on, it was kept the same to avoid brittle tension failure under simultaneous axial load and bending, and to account for sustained load developed from concrete creep and shrinkage and transferred to the reinforcement. Furthermore, Clause 8.4.3.9 also sets 8.00% of the column cross-sectional gross area as a maximum longitudinal reinforcement ratio (including lap splices, if any) in order to avoid congestion of reinforcement.

In addition, Clause 8.4.1.4 requires the following condition to be satisfied in order to ensure compression-controlled failure for flexural members:

$$c/d \geq \frac{7}{7+2000\,\varepsilon_{Fu}} \qquad \text{Equation 2.2}$$

Where c is the distance from the extreme compression fibre to neutral axis; d is the distance between the extreme compression fibre and the centroid of longitudinal tension force; and ε_{Fu} is the ultimate tensile strain of longitudinal FRP reinforcement. It should be noted that the ultimate compressive strain of concrete, ε_{cu}, is taken as 0.0035.

The maximum factored axial load resistance for a compression member, a tied one in particular, is given by Clause 8.4.3.6 as:

$$P_{r,max} = 0.80\, P_{ro} \qquad \text{Equation 2.3}$$

where P_{ro} is the factored axial load resistance at zero eccentricity. The factor in Equation 2.3 is changed to 0.85 in case of spirally-reinforced column.

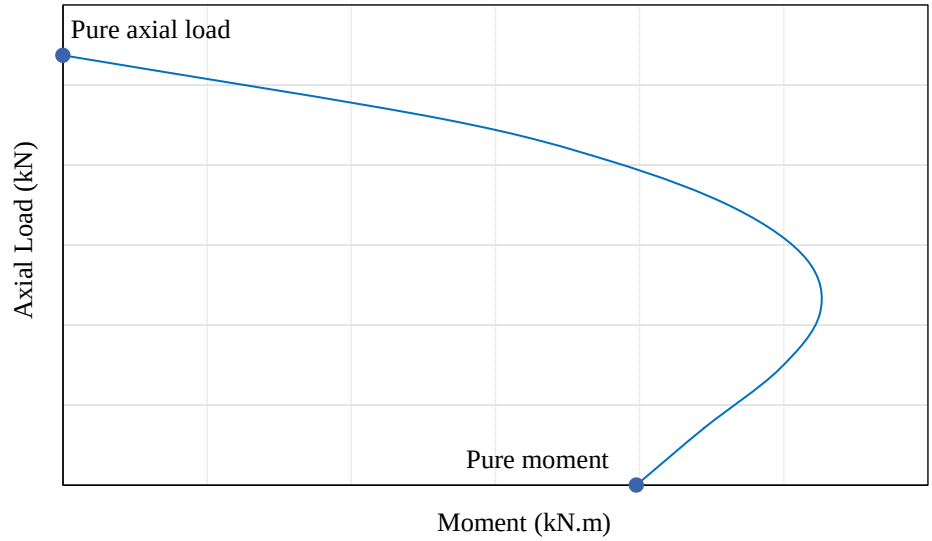

Figure 2.5: Theoretical strength (*P-M*) interaction diagram for a GFRP-RC column

2.5.1.2. The American guidelines ACI 440.1R-15

The balanced reinforcement ratio for flexural members, ρ_{fb}, is defined as per Clause 7.2.1 of ACI 440.1R-15 (ACI 2015), as a threshold between FRP rupture and concrete crushing limit states for a FRP-RC flexural member, which can be computed according to the following equation:

$$\rho_{fb} = 0.85\beta_1 \frac{f_c'}{f_{fu}} . \frac{E_f\, \varepsilon_{cu}}{E_f\, \varepsilon_{cu} + f_{fu}} \qquad \text{Equation 2.4}$$

Where ρ_{fb} is the balanced reinforcement ratio for FRP; β_1 is the ratio of depth of equivalent rectangular compressive stress block to depth of neutral axis; f_c' is the specified concrete compressive strength; f_{fu} is the design tensile strength of FRP; E_f is the modulus of elasticity of FRP reinforcement; and ε_{cu} is the maximum usable concrete strain which is taken as 0.003 by the

ACI standards. Yet, ACI 440.1R-15 still does not recommend using FRP as main reinforcement for columns or as compressive reinforcement in flexural members.

2.5.1.3.The Canadian code CSA S6-19

The Canadian code CSA S6-19 (CSA 2019d) has many similar provisions to those of the Canadian standard CSA S806-12 (CSA 2017), especially in terms of maximum and minimum longitudinal reinforcement ratios and the ultimate compressive strain of concrete. On the other hand, CSA S6-19 (CSA 2019d) is more conservative than CSA S806-12 (CSA 2017) with respect to the maximum factored axial load resistance for a compression member. For instance, the reduction factor is 0.75 and 0.8 in case of tied and spirally-reinforced columns, respectively. On the other hand, CSA S6-19 (CSA 2019d) is more lenient because it recognizes the contribution of FRP longitudinal bars in compression (Clause 16.8.9.1) to a stress limited to a corresponding compressive strain of 0.002.

2.5.2. Design for shear and confinement

2.5.2.1.The Canadian standards CSA S806-12

The factored shear resistance as given by CSA S806-12 (CSA 2017), Clause 8.4.4.4 can be calculated as:

$$V_r = V_c + V_{sF} \qquad \text{Equation 2.5}$$

Where V_r is the factored shear resistance of FRP-RC member; V_c is the factored shear resistance provided by concrete; and V_{sF} is the factored shear resistance provided by FRP shear reinforcement.

The factored shear resistance provided by concrete, V_c, for a flexural member subjected to axial compression, can be calculated as given by Clause 8.4.4.11:

$$V_c = \left\{0.05\lambda\phi_c k_m k_r (f'_c)^{\frac{1}{3}} b_w d_v\right\} k_s k_a \left(1 - \frac{N_f}{14A_g}\right)1 \qquad \text{Equation 2.6}$$

where λ is a factor to account for concrete density; ϕ_c is the concrete resistance factor; k_m is the coefficient taking the effect of moment at section on shear strength into account; k_r is the reinforcement rigidity coefficient; b_w is the minimum effective web width of the member; d_v is the effective shear depth; k_s is the member size coefficient; k_a is the arch action coefficient; N_f is

the factored axial load normal to the cross-section expresses with a negative sign as compression; and A_g is the gross area of the member cross-section. It is worth mentioning that the minimum limit for the value of V_c, when accompanied with axial compression is $0.11\sqrt{f_c'}b_w d_v$.

Also, the factored shear resistance provided by FRP shear reinforcement, V_{sF}, can be computed according to Clause 8.4.4.9 as follows:

$$V_{sF} = \frac{0.4\phi_F A_{Fv} f_{Fu} d_v}{s} \cot\theta \qquad \text{Equation 2.7}$$

Where ϕ_F is resistance factor for FRP reinforcement; A_{Fv} is the area of FRP shear reinforcement perpendicular to the axis of a member within the distance s; f_{Fu} is the ultimate strength of FRP shear reinforcement, limited by $0.005E_f$ as a maximum value; θ is the angle of the diagonal compressive stress; and s is the spacing of shear reinforcement.

Clause 8.4.5.2 specifies the minimum amount of shear reinforcement as:

$$A_{Fv,min} = 0.07\sqrt{f_c'}\frac{b_w s}{0.4 f_{Fu}} \qquad \text{Equation 2.8}$$

Where f_{Fu} is limited by the lesser of 1200 and $0.005E_f$, as an upper limit.

Also, Clause 8.4.3.13 defines the appropriate FRP spirals for compression members, in order to avoid longitudinal bars buckling and to provide reasonable confinement, as follows: the least of: (a) to have at least 6 mm diameter; (b) to have a pitch of at least 1/6 the core diameter; (c) to have a clear spacing between successive turns of a spiral between 25 and 75 mm; and (d) to have a volumetric ratio of at least as given by Equation 2.9:

$$\rho_{Fs} = \frac{f_c'}{f_{Fh}}\left(\frac{A_g}{A_c} - 1\right)\frac{P}{P_o} \qquad \text{Equation 2.9}$$

Where f_{Fh} is the design stress level in FRP transverse confinement reinforcement; A_c is the cross-sectional area of column core; P is the specified axial load on column section; P_o is the nominal unconfined axial load capacity of column calculated as $\alpha_1 f_c'\left(A_g - A_F\right)$ for columns with FRP longitudinal reinforcement.

Furthermore, CSA S806-12 (CSA 2017) has some special confinement provisions for seismic design. As described in Clause 12.7.3.3, the required area of the transverse FRP reinforcement for

moment resisting frame members under significant axial load, unless a greater amount is computed from Equations 2.7 through 2.9, must exceed the following value:

$$A_{sh} = 14sh_c \frac{f_c'}{f_{Fh}} \left(\frac{A_g}{A_c} - 1\right) \frac{P}{P_o} . \frac{\delta}{\sqrt{k_c}} \qquad \text{Equation 2.10}$$

where A_{sh} is the required area of transverse reinforcement; s is the transverse reinforcement spacing; h_c is the cross-sectional dimension of the column core; f_c' is the concrete compressive strength; f_{Fh} is the design stress level in FRP confinement reinforcement, taken as the least of 0.006 E_f or $\phi_f.f_{fu}$ where ϕ_f is the material resistance factor for FRP confinement reinforcement, taken as unity in this study, E_f and f_{fu} are the elastic modulus and ultimate tensile strength of FRP confinement reinforcement, respectively; A_g and A_c are the areas of the gross cross-section and column core, respectively; P/ P_o is the axial load level, taken $\geq$ 0.2; δ is the design drift, taken as 0.025 and 0.04 for moderately ductile and ductile MRFs, respectively; and k_c is the confinement efficiency coefficient, taken as unity for circular hoops or spirals and $0.15\sqrt{(h_c / s)(h_c / s_\ell)}$ for rectilinear transverse reinforcement, where s_ℓ is the spacing of tie legs in rectangular columns.

Moreover, the maximum FRP tie spacing for moment resisting frame members in seismic areas under significant axial loading is specified by Clause 12.7.3.4 as the least of: (a) one-fourth the minimum member dimension; (b) 6 times the diameter of the smallest longitudinal bar; and (c) 150 mm.

2.5.2.2.The Canadian code CSA S6-19

The Canadian code CSA S6-19 (CSA 2019d) estimate the shear strength of FRP-RC members in accordance with Clause 16.8.7.1, which can be summarized as follows. The factored shear resistance, V_r, can be calculated as:

$$V_r = V_c + V_{st} \qquad \text{Equation 2.11}$$

where V_c is the factored shear resistance provided by concrete; and V_{st} is the factored shear resistance provided by FRP shear reinforcement.

The factored shear resistance provided by concrete, V_c, can be calculated as given by Equation 2.12:

$$V_c = 2.5\beta\phi_c f_{cr} b_v d_{long} \quad \text{Equation 2.12}$$

where β is a factor taken as 0.18 for columns having minimum shear reinforcement; ϕ_c is the concrete resistance factor, taken as unity; f_{cr} is the cracking strength of concrete; b_v is the effective width of the web, taken as the gross diameter for circular sections; and d_{long} is the effective shear depth.

The factored shear resistance provided by FRP shear reinforcement, V_{st}, can be calculated as:

$$V_{st} = V_{FRP} = \frac{\phi_{FRP} A_v \sigma_v d_{long}}{s} \cot\theta \quad \text{Equation 2.13}$$

Where ϕ_{FRP} is resistance factor for FRP reinforcement; A_v is the area of FRP shear reinforcement perpendicular to the axis of a member within the distance s; σ_v is the design stress of FRP shear reinforcement; limited by $0.005E_{vFRP}$ for circular sections; θ is the angle of the diagonal compressive stress; and s is the spacing of shear reinforcement.

The minimum amount of shear reinforcement is specified as:

$$A_{v,min} = 0.06\sqrt{f_c'}\frac{b_w s}{\sigma_v} \quad \text{Equation 2.14}$$

Besides, CSA S6-19 (CSA 2019d) includes design provisions for column confinement. However, these provisions do not cover the seismic design of FRP-RC columns. The minimum diameter of FRP spirals or circular hoops is 6 mm, according to Clause 16.8.9.4.2. In addition, the clear spacing between hoops or successive turns of a spiral may not be less than 25 mm nor larger than 75 mm. The proper anchorage is specified for spirals as one and one-half extra turns at each end of the spiral unit embedded in the footing and the component supported above the footing. On the other hand, the proper anchorage length for discrete hoops is specified as a minimum lap splice length (L_d) equal to $40d_h$, where d_h is hoop diameter.

The volumetric ratio of spiral reinforcement, ρ_{Fs}, can be obtained from the following equation:

$$\rho_{Fs} = \frac{f_c'}{f_{Fh}}\left(\frac{A_g}{A_c} - 1\right)\frac{P}{P_o} \quad \text{Equation 2.15}$$

where $\frac{P}{P_o} \geq 0.2$; $\frac{A_g}{A_c} \geq 1.3$; f_{Fh} is defined as the least of $0.004E_f$ or $\phi_{FRP} f_{Fu}$, or the stress corresponding to the failure of corners, hooks, bends, or laps.

2.5.2.3.The American guidelines ACI 440.1R-15

Clause 8.2 of ACI440.1R-15 (ACI 2015) requires the nominal shear nominal shear resistance of a reinforced concrete cross section, V_n, which can be computed as follows, when multiplied by a strength reduction factor equals to 0.75, to exceed the factored shear force.

$$V_n = V_c + V_f \quad \text{Equation 2.16}$$

The shear resistance provided by concrete, V_c, is given as:

$$V_c = \frac{2}{5}\sqrt{f_c'}\, b_w (kd) \quad \text{Equation 2.17}$$

Where k is the ratio of depth of neutral axis to the reinforcement depth, which is dependent upon the FRP longitudinal reinforcement ratio,ρ_f, and the modular ratio,n_f.

Also, the shear resistance provided by FRP shear reinforcement, V_f, can be calculated as follows:

$$V_f = \frac{A_{fv} f_{fv} d}{s} \quad \text{Equation 2.18}$$

Where f_{fv} is the stress level in the FRP shear reinforcement, which is be limited to $0.004E_f$ to control shear crack widths, maintain shear integrity of the concrete, and to avoid failure at the bent portion of the FRP stirrup.

The amount of FRP shear reinforcement is required to exceed the lower limit given by:

$$A_{fv,min} = 0.35 \frac{b_w s}{f_{fv}} \quad \text{Equation 2.19}$$

The tie spacing is limited to the lesser of $d/2$ and 600 mm, as recommended by ACI 318-19 (ACI 2019a), to ensure that at least each shear crack is intercepted by one stirrup.

2.6. Gaps in the Available Data and Research Needs

The previous studies on the behaviour of GFRP-RC circular columns under simulated seismic loading studied the effects of axial load level, spiral pitch and diameter, type of surface treatment for GFRP reinforcement (sand-coated versus ribbed), and the hybrid combination of steel longitudinal bars with GFRP spirals (Tavassoli et al. 2015; Tavassoli and Sheikh 2017; Kharal et al. 2021). Some other available studies investigated the behaviour of square GFRP-RC columns

under different parameters (Ali and El-Salakawy 2016; Naqvi and El-Salakawy 2017; Naqvi et al. 2017; Elshamandy et al. 2018; Kharal and Sheikh 2020).

The research gap for circular GFRP-RC columns includes:

- **Aspect ratio**: there is no available recent data, keeping up with the development of polymers science and manufacturing technology, regarding the effect of aspect ratio on square or circular GFRP-RC columns under simulated seismic loading, despite the addressed effect of aspect ratio on plastic hinge length, *P*-Δ effect, deformability of columns (Sakai and Sheikh 1989; Lehman and Moehle 2000; Bae and Bayrak 2008). In addition, the adopted equation for confinement reinforcement of circular columns in CSA/S806-12 (CSA 2017), clause 12.7.3.3, is the same equation proposed by Saatcioglu and Razvi (2002). The only change in CSA S806-12 (CSA 2017) was the replacement of yield strength of transverse steel with the stress limit of FRP transverse reinforcement, defined as the least of $0.006E_F$ or $\phi_F f_{Fu}$. This equation considered an aspect ratio of 2.5 based on pushover analyses of steel-RC columns.

- **Concrete compressive strength**: No available test data exists for GFRP-RC columns constructed using high-strength concrete, despite the fact that CSA S806-12 (CSA 2017) includes concrete strength up to 80 MPa in the equation for confinement requirement, along with the previously reported effects of high-strength concrete on the behaviour and confinement requirements of steel-RC columns, especially under high axial loads and with large aspect ratios (Saatcioglu and Baingo 1999; Bayrak and Sheikh 1997; Paultre et al. 2001).

- **GFRP hoops:** The use of GFRP individual hoop reinforcement is addressed by the current CSA S806-12 (CSA 2017). However, there is no available research data regarding using individual circular hoops as transverse reinforcement for GFRP-RC columns under the effect of seismic excitations.

- **Lap splices:** There is no experimental data available on lap splices of longitudinal reinforcement in circular GFRP-RC columns under simultaneous axial loading and lateral reversals.

Based on the previous discussion, the following variables were considered in this study: aspect ratio (L/D); axial load level (P/P_o); concrete compressive strength (f_c'); circular hoops versus spiral reinforcement; and the splice length of the hoops.

CHAPTER 3: RESEARCH PROGRAM

3.1. General

The literature review highlighted the key parameters affecting the seismic response of GFRP-RC circular columns including transverse reinforcement type and ratio, concrete compressive strength, axial load level and aspect ratio. The research program presented herein comprised of two main phases, namely, experimental and numerical. The experimental phase included constructing and testing of fifteen full-scale column-footing specimens in the W. R. McQuade Heavy Structures Laboratory at the University of Manitoba to evaluate the influence of the key parameters mentioned earlier on the seismic performance of GFRP-RC columns. In light of the results of the experimental phase, a numerical study was conducted to expand the current knowledge about the behaviour of GFRP-RC circular columns. In that phase, an FEM was constructed and validated against the experimental results. The validated FEM was then utilized to perform a parametric study to further explore the effects of few main variables on the seismic response of GFRP-RC columns. Based upon the results of FEA, a new design model was proposed.

3.2. Experimental Study

3.2.1. Material properties

3.2.1.1. Concrete

Ready mixed, normal-weight concrete with two different target compressive strengths of 35 MPa (normal strength) and 80 MPa (high strength), respectively, were used. The concrete had a maximum nominal aggregate size of 19 mm, and a target slump of 120 mm. To determine the actual compressive strength for each column on test day, tests on 100 × 200 mm standard concrete cylinders were carried out as per CSA A23.1-19/A23.2-19 (CSA 2019a).

3.2.1.2. Reinforcement

Deformed G400 steel bars and spirals, according to CSA standards (CSA 2019b), were used to reinforce the steel-RC specimen and all footings. The longitudinal reinforcement of the steel-RC column and footings was provided as 15M steel bars, whereas 10M steel spirals were used as confinement reinforcement. The mechanical properties of steel reinforcement were obtained following CSA G30.18-09 (CSA 2019c), as listed in Table 3.1.

On the other hand, sand-coated GFRP bars, circular hoops and spirals were used for the GFRP-RC columns, as shown in Figure 3.1. The mechanical properties of the GFRP reinforcement are summarized in Table 3.1, as provided in the certificate of compliance issued by the manufacturer (Pultrall Inc. 2019). Lab tests were carried out on straight GFRP bars to confirm the properties provided by the manufacturer (CSA 2017).

Table 3.1: Mechanical properties of steel and GFRP reinforcement

Bar size	Diameter (mm)	Area (mm^2)	Modulus of elasticity (GPa)	Tensile strength (MPa)	Ultimate strain (%)
Steel bars and spirals					
15M	15.9	200	200	460 [a]	0.23 [a]
10M (Spirals)	11.3	100	200	420 [a]	0.21 [a]
GFRP bars, spirals and hoops					
No. 16	15.9	197.9 [b] [235] [c]	65.7 [d]	1,711 [d]	2.60 [d]
No. 10 (Spirals/Hoops)	9.5	71.0 [b] [83] [c]	58.4 [d]	1,376 [d]	2.36 [d]

[a] Yield/proof strength determined as per CSA G30.18-09 (CSA 2019c).

[b] Nominal area as per CSA S807-19 (CSA 2019e).

[c] Measured area by immersion test as per Annex A of CSA S806-12 (CSA 2017).

[d] Measured as per Annex C of CSA S806-12 (CSA 2017).

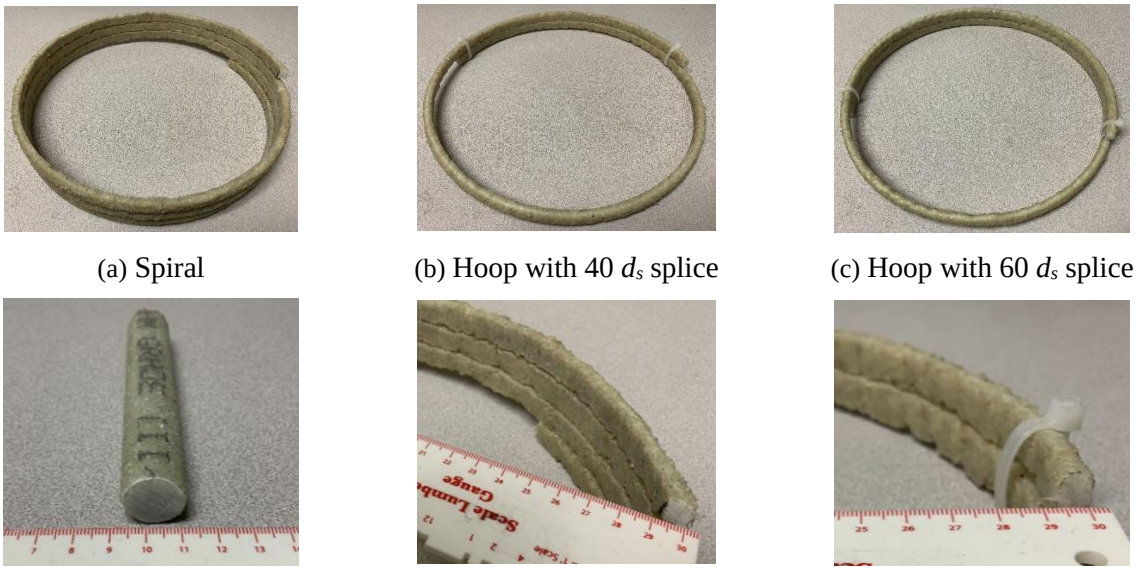

(a) Spiral (b) Hoop with 40 d_s splice (c) Hoop with 60 d_s splice

(d) GFRP longitudinal bar (e) Spiral-close-up view (f) Hoop-close-up view

Figure 3.1: Samples of GFRP transverse reinforcement (dimensions in mm)

3.2.2. Test specimens

The experimental program involved constructing and testing of fifteen full-scale isolated column-footing specimens. The investigated parameters considered in this study were as follows:

- Reinforcement type (steel and GFRP);
- Circular hoops and spiral reinforcement;
- Splice length of the circular GFRP hoops;
- Axial load level (P/P_o);
- Concrete compressive strength (f_c'); and
- Aspect ratio (L/D).

where P is the applied axial load; P_o is the nominal unconfined axial capacity of the column; and L and D are the shear span and diameter of the column, respectively. This section outlines the details of the test matrix including the design of a multi-storey frame office building, the isolation of the specimens and the construction process.

3.2.2.1. Prototype design and isolated test specimens

To acquire full-scale test specimens, a prototype structure should be designed under specified limit states depending on the purpose and location of the structure. Then the test specimen should be isolated from the prototype structure so that the specimen and its test setup should simulate the actual performance of the followed members/connections in the prototype. A steel-RC, six-storey frame office building located in the City of Vancouver, BC, Canada, was selected as the prototype structure for this experimental study with a typical floor height of 3.5 m. The building had 7 bays in the N-S direction, each of 6.0 m width and 3 bays in the E-W direction. Two of these bays were office bays of 9.0 m width, with a central corridor bay 6.0-m wide in between, as shown in Figure 3.2. The floor system is one-way slab system, spanning in the E-W direction and supported by girders and secondary beams in the N-S direction, with 110-mm slab thickness. The cross-sections of secondary beams were 300-mm wide × 350-mm thick, while for the girders the cross-sections were 400 × 600 mm, and 400 × 550 mm for the bottom and top three stories, respectively. All columns were preliminarily assumed to be circular with a diameter of 350 mm.

The building was designed as a ductile moment-resisting frame (MRF) in accordance with CSA A23.3-19 (CSA 2019b) to carry its own self-weight in addition to a partition allowance of 1.0

kN/m^2 on all floors, and specified live loads of 2.4 kN/m^2 and 4.8 kN/m^2 for the office spaces and corridor bay, respectively (NRCC 2020). The structure was analyzed under the dead, live and equivalent earthquake loads and the straining actions at the bases of the columns were computed. This resulted in the first-storey columns to be under significant axial loading (i.e., $P > 0.1 f'_c A_g$). Therefore, the design of an exterior steel-RC column was conducted as per Clause 21.4.1.1 of CSA A23.3-19 (CSA 2019b), resulting in a circular cross-section with 350-mm diameter and a longitudinal reinforcement ratio of 1.25%. More details on load estimation, analysis and design for the prototype building and the steel-RC columns can be found in Appendix A.

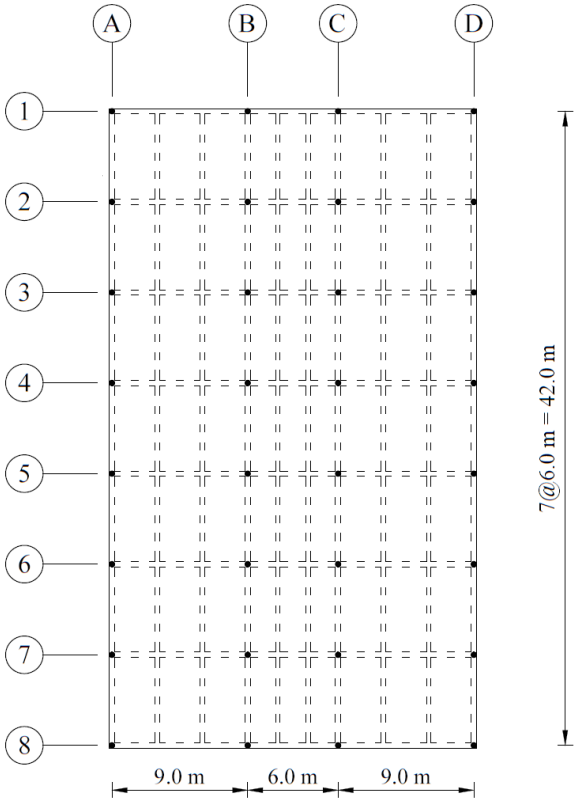

Figure 3.2: Plan view for the prototype structure

The isolated test specimen resembled the lower segment of a first-storey exterior column between the top surface of the footing and the point of contra-flexure, which was assumed at the mid-height of the column (Figure 3.3). Therefore, the specimen was modeled as a cantilever column fixed at the footing, as will be discussed in Section 3.2.4. The column had a diameter of 350 mm and a shear span (i.e. the height between the column–footing interface and the line of action of the lateral load) equal to 1,750 mm. Due to the limited data on modelling whole RC structures entirely

reinforced with GFRP, the GFRP-RC were following the dimensions of the isolated steel-RC specimen, whereas the GFRP-RC columns were checked for flexure, shear and confinement in accordance with CSA S806-12 (CSA 2017) and CSA S6-19 (CSA 2019d), as detailed in Appendix B. The specimens were assumed to be hypothetically loaded under gravity loads and uniaxial lateral drift reversals, simulating the seismic action in one direction only.

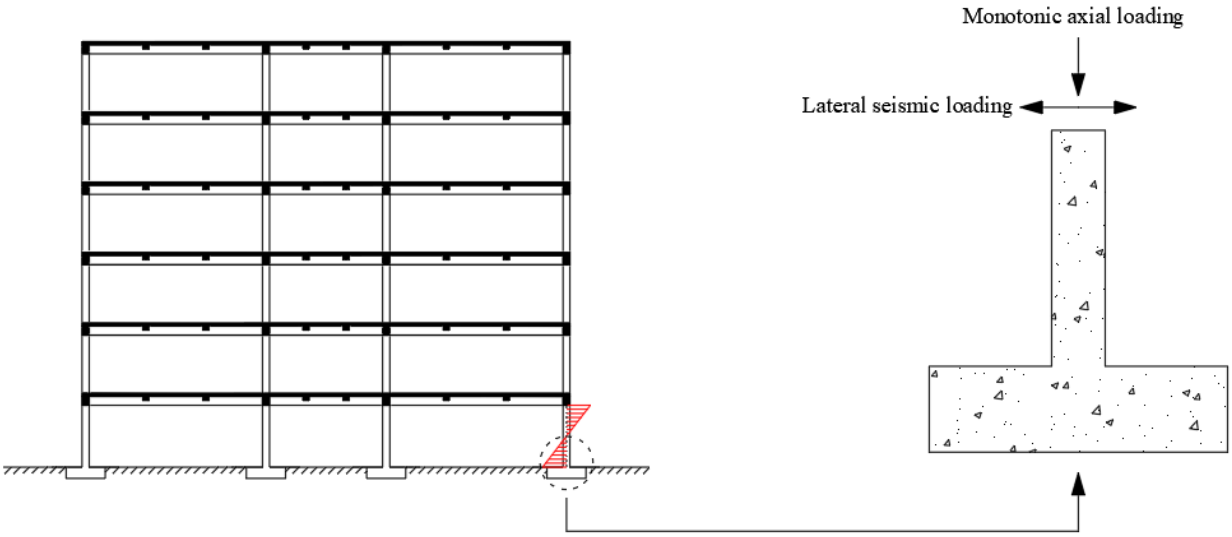

Figure 3.3: Sectional elevation of the prototype structure and the isolated specimen

3.2.2.2. Description of the test matrix

The columns had a diameter of 350 mm whereas the shear span was either 1,050, 1,750 or 2,450 mm, representing a column aspect ratio of 3.0, 5.0 and 7.0, respectively. The intermediate aspect ratio (i.e. 5.0) was selected as it represented a typical storey height in MRF structures. On the other hand, the aspect ratios of 3.0 and 7.0 were selected to investigate the performance of the so-called captive columns (Fig. 2.2) and the long columns that could be found at the entrances of buildings with large floor height, respectively. A rigid 1,400 × 900 × 600-mm steel-RC footing was adequately reinforced with 15M steel bars to ensure fixity to each column and withstand cyclic drift reversals without significant cracking. The dimensions of the footings were designed to resist the anticipated axial load and moment during testing with sufficient safety margin, since the isolated specimens were only subjected to a specific load case. Such approach was adopted by several researchers whose test results indicated clear confinement effect by the provided footings (Sheikh and Khoury 1993; Bayrak and Sheikh 1997; Xiao and Yun 2002; Paultre et al. 2009; Ali

and El-Salakawy 2016; Kharal and Sheikh 2020). Furthermore, to enable attaching the hydraulic actuator to the circular specimens in the laboratory, as will be discussed in Section 3.2.4, each column was cast monolithically with a prismatic head measuring 510 × 440 × 400 mm. The mid-height of each head coincided with the line of action of the lateral load, making the overall height of each column equal to its shear span plus additional 200 mm.

A total of fifteen full-scale column-footing specimens were constructed and tested under concurrent axial loading and cyclic lateral drift reversals. The investigated parameters were the reinforcement type (steel versus GFRP), use of circular hoops versus spiral reinforcement, splice length of the circular GFRP hoops, axial load level, concrete compressive strength, and aspect ratio. Ten columns were cast using NSC while the remaining five were constructed using HSC. A column was reinforced longitudinally with 15M steel bars and laterally with 10M steel spiral as a reference specimen. On the other hand, the other fourteen columns were reinforced with No. 16 (15.9-mm diameter) longitudinal GFRP bars and confined by either No. 10 (9.5-mm diameter) GFRP spirals for twelve columns or No. 10 GFRP discrete circular hoops for the remaining two columns. Two different lap splice lengths were used for the circular GFRP hoops; $40d_h$ as per Clause 16.8.9.4.2 (c) of CSA S6-19 (CSA 2019d), where d_h is the nominal cross-sectional diameter of the hoop; and $60d_h$.

All steel and GFRP spirals were anchored by one and a half extra turns at each end, in accordance with Clause 25.7.3.4 of ACI 318-19 (ACI 2019b). The confinement reinforcement of the steel-RC column was designed according to Clauses 9.7.6.4.3, 18.7.5.3, and 18.7.5.4 of ACI 318-19 (ACI 2019b) and Clauses 10.9.4, 21.2.8.1, 21.2.8.2, 21.3.2.6.3, and 21.4.4.3 of CSA A23.3-19 (CSA 2019b), resulting in a spiral pitch of 85 mm (center-to-center). On the other hand, the spiral pitch of the GFRP-RC columns varied between 85 and 50 mm, where the first value followed the requirements of Clauses 12.7.3.4 and 16.8.9.4.2 (a) of CSA S806-12 (CSA 2017) and CSA S6-19 (CSA 2019d), respectively, whereas the second value satisfied Clause 8.4.3.13 of CSA S806-12 (CSA 2017). All spirals and hoops were initially designed to have an outer diameter of 290 mm, so that the clear concrete cover would be 30 mm. However, only the steel spiral satisfied this requirement whereas the GFRP spirals and hoops, due to production specifications, had an outer diameter of 310 mm, resulting in a clear concrete cover of 30 mm to the longitudinal reinforcement bars.

The axial load level was applied as a fraction of the nominal unconfined axial load capacity, P_o, as will be discussed in detail in Section 3.2.4. Three axial load levels were considered in this study; 0.2, which was applied to eleven specimens, 0.3, which was applied to three specimens, and 0.1 that was applied to only one specimen. Tables 3.2 and 3.3 summarize the details of test specimens and their designations throughout the different chapters of this thesis, respectively. In addition, the concrete dimensions and details of reinforcement of the test specimens are included in Figures 3.4 through 3.8.

Table 3.2. Details of test matrix

Specimen ID	Aspect ratio (L/D)	Axial load (P/P_o)	Concrete strength f_c' [a] (MPa)	Longitudinal reinforcement			Transverse reinforcement		
				Type	Bars	ρ_f [ρ_{st}] [b] *(%)*	Type	Diameter (mm)	Pitch (mm)
S1	5.0	0.2	36.5 ± 0.9	Steel	6-15M	[1.25][b]	Steel spirals	11.3	85
G1	5.0	0.2	36.9 ± 0.4	GFRP	6-No.16	1.23	GFRP spirals	9.5	85
G2	5.0	0.2	36.0 ± 2.0				GFRP spirals		50
G3	5.0	0.2	41.8 ± 0.8				GFRP hoops-40d_h splice		85
G4	5.0	0.2	44.8 ± 0.8				GFRP hoops-60d_h splice		85
G5	5.0	0.3	41.4 ± 0.7				GFRP spirals		85
G6	5.0	0.2	86.4 ± 2.4				GFRP spirals		85
G7	5.0	0.2	89.4 ± 1.8				GFRP spirals		50
G8	5.0	0.1	87.3 ± 2.5				GFRP spirals		50
G9	3.0	0.2	44.2 ± 0.1				GFRP spirals		85
G10	3.0	0.3	45.9 ± 0.7				GFRP spirals		85
G11	7.0	0.2	43.3 ± 0.7				GFRP spirals		85
G12	7.0	0.3	43.2 ± 0.3				GFRP spirals		85
G13	7.0	0.2	75.5 ± 1.1				GFRP spirals		85
G14	7.0	0.2	81.4 ± 0.7				GFRP spirals		50

[a] Values represent the mean strength of three 100 × 200-mm test cylinders and its standard deviation

[b] Values between brackets represent reinforcement ratio in case of steel reinforcement

Table 3.3. Designations of test specimens

Specimen ID	Designation in thesis				
	Ch. 4	Ch. 5	Ch. 6	Ch. 7	Ch. 8
S1	S-0.2-85s-XX	–	–	–	–
G1	G-0.2-85s-XX	GN-0.2-85	G-5.0-0.2	GN-5.0-0.2-85	GN-5.0-0.2-85
G2	G-0.2-50s-XX	GN-0.2-50	–	GN-5.0-0.2-50	GN-5.0-0.2-50
G3	G-0.2-85h-40d_s	–	–	–	–
G4	G-0.2-85h-60d_s	–	–	–	–
G5	G-0.3-85s-XX	–	G-5.0-0.3	GN-5.0-0.3-85	GN-5.0-0.3-85
G6	–	GH-0.2-85	–	GH-5.0-0.2-85	GH-5.0-0.2-85
G7	–	GH-0.2-50	–	GH-5.0-0.2-50	GH-5.0-0.2-50
G8	–	GH-0.1-50	–	–	GH-5.0-0.1-50
G9	–	–	G-3.0-0.2	–	–
G10	–	–	G-3.0-0.3	–	–
G11	–	–	G-7.0-0.2	GN-7.0-0.2-85	–
G12	–	–	G-7.0-0.3	GN-7.0-0.3-85	–
G13	–	–	–	GH-7.0-0.2-85	–
G14	–	–	–	GH-7.0-0.2-50	–

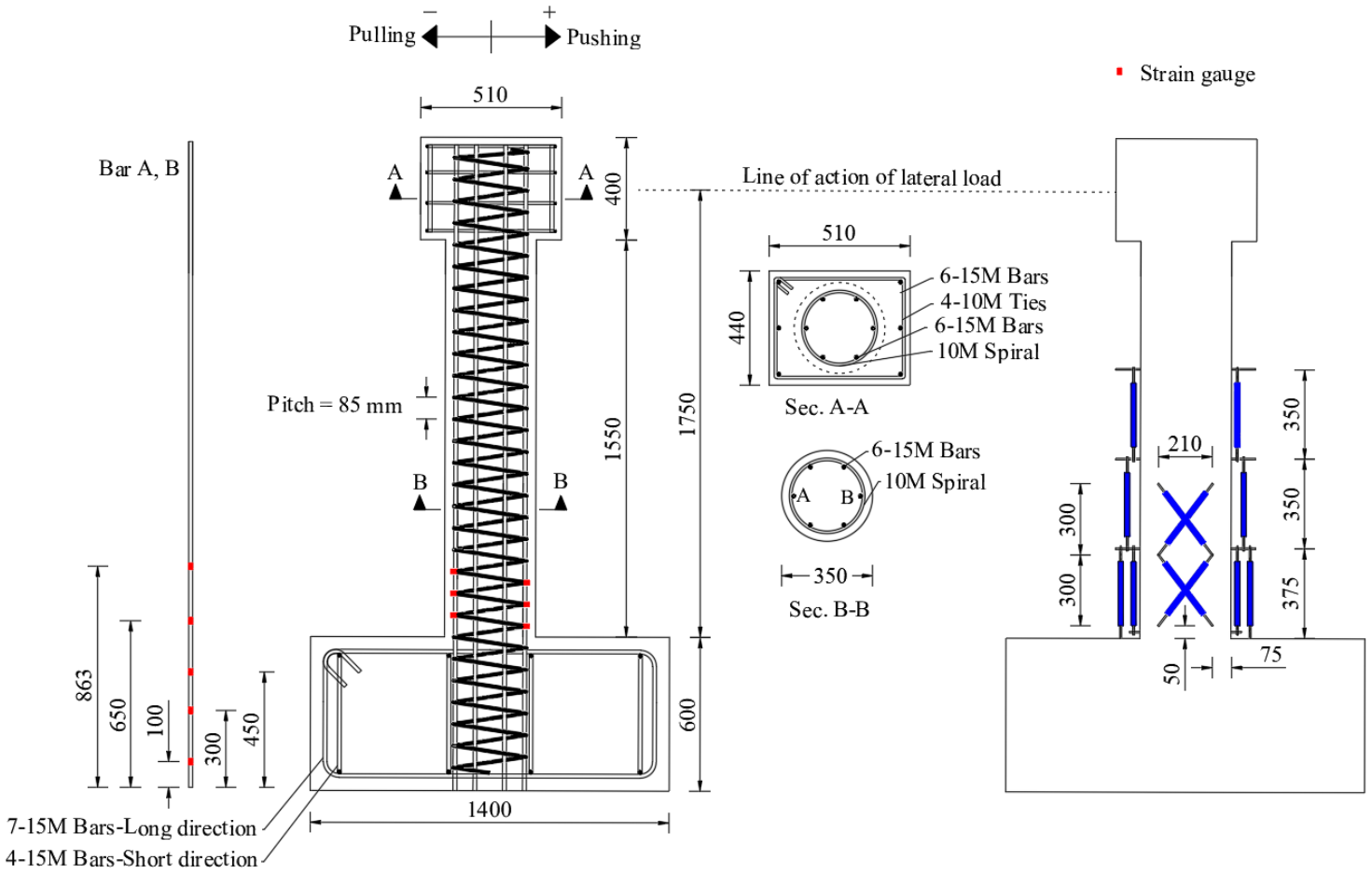

(a) Details of reinforcement and locations of strain gauges (b) Configuration of LVDTs

Figure 3.4: Details of specimens S1 and instrumentation (all dimensions in mm)

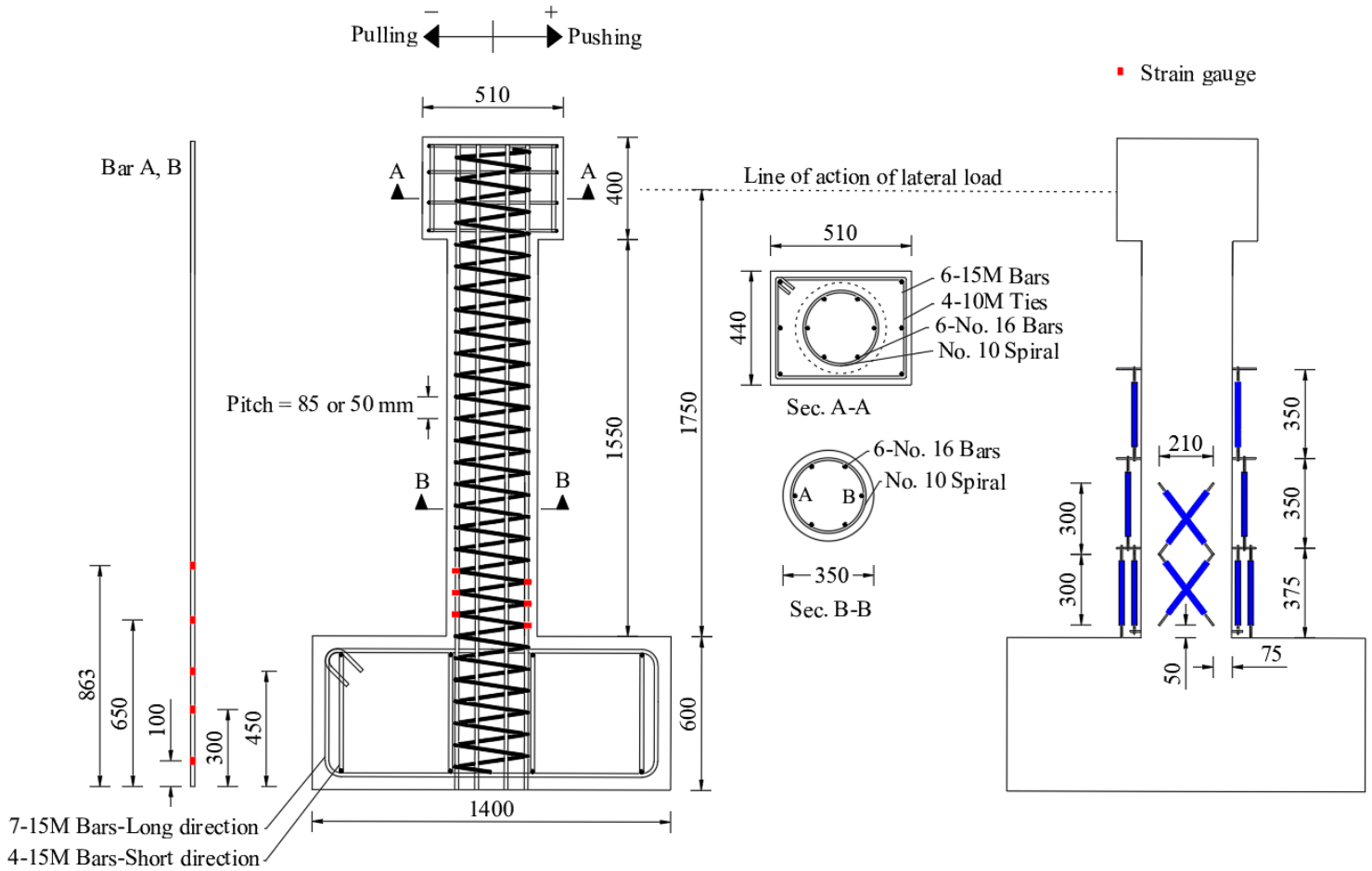

(a) Details of reinforcement and locations of strain gauges (b) Configuration of LVDTs

Figure 3.5: Details of specimens G1, G2, and G5-G8 and their instrumentation (all dimensions in mm)

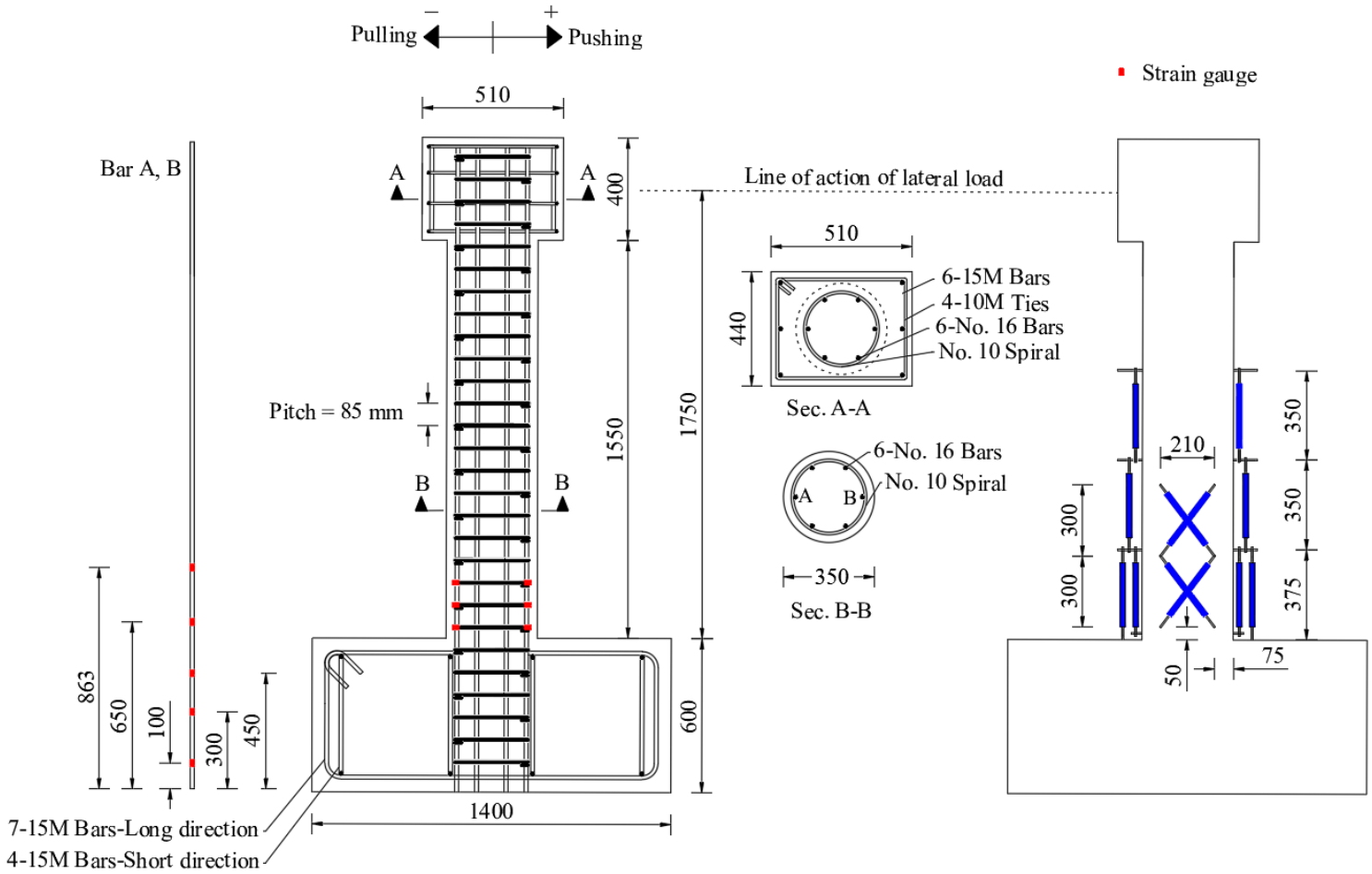

(a) Details of reinforcement and locations of strain gauges (b) Configuration of LVDTs

Figure 3.6: Details of specimens G3, and G4 and their instrumentation (all dimensions in mm)

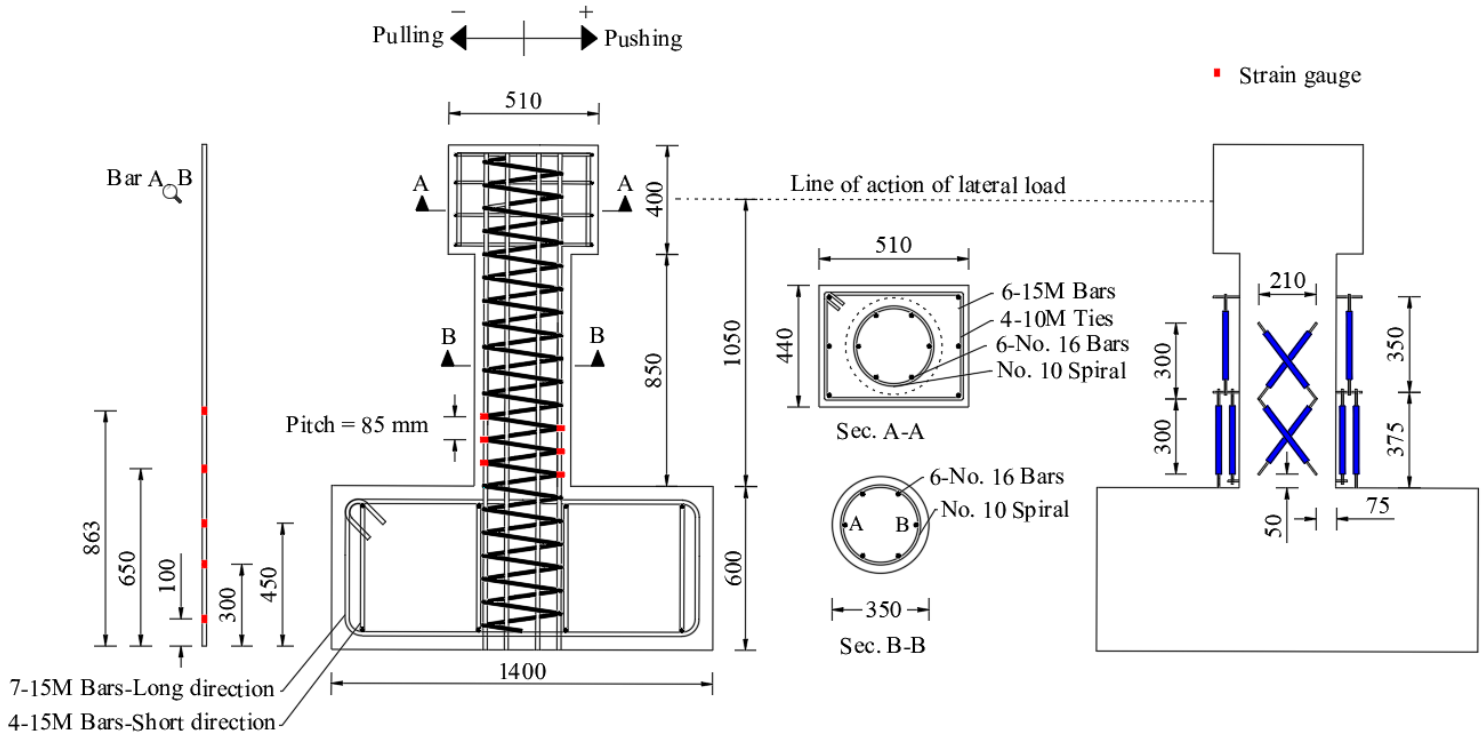

(a) Details of reinforcement and locations of strain gauges (b) Configuration of LVDTs

Figure 3.7: Details of specimens G9, and G10 and their instrumentation (all dimensions in mm)

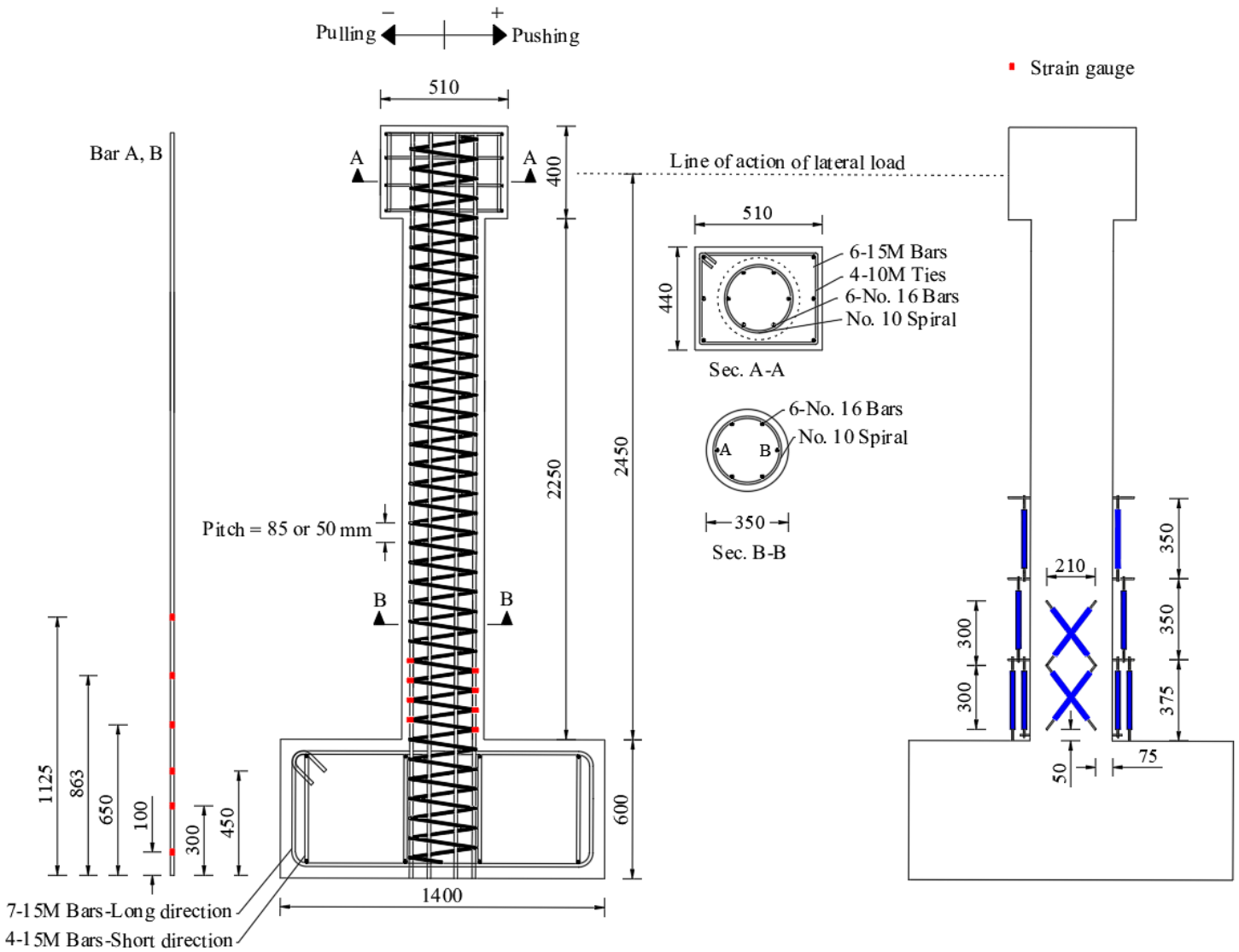

(a) Details of reinforcement and locations of strain gauges (b) Configuration of LVDTs

Figure 3.8: Details of specimens G11-G14 and their instrumentation (all dimensions in mm)

3.2.2.3. Construction of the specimens

The reinforcement cages and formwork were assembled on a flat 4,800 × 3,700-mm wooden platform, as shown in Figure 3.9. To simulate the common construction practice, the footings were cast first followed by assembling the formwork of the columns and casting them (Figure 3.10). To ensure safety while casting the long columns (G11-G14), only the footings were cast on the wooden platform. Then the hardened footings were moved beside another high wooden platform to secure casting of the columns (Figure 3.11). The footings were wet-cured for 7 days in a water-tight curing tent, whereas the columns were left to cure inside their forms for 7 days before stripping them out.

(a) Fabricating the GFRP-RC reinforcement cages

Figure 3.9: Preparation of specimens on the wooden platform

(b) Steel-RC cages and formwork of the footings in place

Figure 3.9: Preparation of specimens on the wooden platform – continued

(a) Casting footings of the GFRP-RC columns G6 and G7

Figure 3.10: The sequence of casting for test specimens (examples G6 and G7)

(b) Columns of the GFRP-RC specimens G6 and G7 ready for casting

Figure 3.10: The sequence of casting for test specimens (examples G6 and G7) – continued

(a) Moving hardened footing

(b) Casting long column

Figure 3.11: Preparation and casting for the long columns having an aspect ratio of 7.0 (examples G11 and G12)

3.2.3. Instrumentation

A load cell was attached to the hydraulic jack applying the axial loading, as discussed later in Section 3.2.4, to monitor the applied load during the test. For specimens S1, and G1-G10, sixteen 6-mm long electrical-resistance strain gauges (ESGs) were attached to several locations along the outermost longitudinal bars and spirals/hoops above the column–footing interface, as depicted by Figures 3.4 to 3.8. Due to the longer hinging regions anticipated for specimens G11-G14, twenty ESGs were attached to the outermost longitudinal bars and spirals as shown in Figure 3.8.

To monitor the different components of the lateral displacement; flexural, slip and shear displacements (Sezen and Moehle 2006), six pairs of linear variable displacement transducers (LVDTs) were fixed along 1,075 mm above the column–footing interface, with the configurations shown in Figures 3.4 to 3.6 and Figure 3.8. Only five pairs of LVDTs were used for specimens G9 and G10 (aspect ratio of 3.0) due to the column height limitation, as observed in Figure 3.7. Generally, the readings of vertical LVDTs were used to compute rotations associated with column flexural deformations. The rotations were typically calculated based on the linear relationships including the elongation and contraction of the LVDTS along with the horizontal distance apart, in accordance with the assumption that plane sections remain plane after bending (drifting). The only exception was the outermost lower pair of LVDTs, for which the lower ends were fixed at the top surface of the footing, which resulted in incorporating the rotation component due to longitudinal bar elongation and slippage within the readings of the LVDTs. Furthermore, to measure the deformations associated with shear distortion, two pairs of diagonal LVDTs were fixed across the column as described in Figures 3.4 through 3.8. All instrumentation was connected to a computerized data acquisition (DAQ) system to display and record real-time readings during the tests.

3.2.4. Test setup

The test setup, showed in Figures 3.12 to 3.14, comprised of three main components; the dynamic hydraulic actuator, the axial loading frame and the RC alignment blocks. The horizontal loads/drift reversals were applied using a horizontal hydraulic actuator, with $\pm$ 1,000-kN and $\pm$ 250-mm load and stroke capacities, respectively, which was post-tensioned to a rigid RC reaction wall through premade holes. The positive and negative signs for the applied loads or drifts denoted pushing and pulling the columns, respectively. The axial load was applied through a 2,000-kN load capacity

hydraulic jack, for which the reaction was transferred to the laboratory floor through a hinged steel loading frame, which consisted of two 100 × 100 × 12-mm hollow steel section (HSS) links pinned to clevis pin assemblies that was bolted to a stiffened steel spreader I-beam. The lower ends of the HSS link members were pinned to clevis pin assemblies anchored to two RC supporting blocks. The hinged steel frame was assembled to ensure free in-plane rotation while maintaining a constant axial loading on the column. An RC leveling slab was cast prior to placing the specimen to enable the alignment of the longitudinal axis of the actuator with the mid-height of the column head. The footing, RC leveling slab and blocks were anchored to the laboratory strong floor using post-tensioned high-strength threaded bars. For each aspect ratio, a different set of HSS link members, RC slab and RC supporting blocks were used to accommodate the differences in column height, as shown in Figures 3.12 to 3.14.

Figure 3.12: Test setup for specimens G9 and G10 (aspect ratio = 3.0)

Figure 3.13: Test setup for specimens S1, and G1-G8 (aspect ratio = 5.0)

3.2.5. Test procedure

Applying the specified axial load marked the commencement of the test, where such axial load was calculated as a ratio of the nominal unconfined axial capacity of the column, P_o; according to the Canadian standards CSA S806-12 (CSA 2017):

$$P_o = \alpha_1 \phi_c f_c^{'} (A_g - A_F) \qquad \text{Equation 3.1}$$

where α_1 is the average stress in the rectangular compression block with respect to the specified concrete strength, f_c'; ϕ_c is the resistance factor for concrete, taken as unity; A_g is the gross cross-sectional area of the column; and A_F is the total area of the column longitudinal FRP reinforcement.

Applying the specified axial load typically resulted in a lateral reaction on the actuator without lateral displacement. This lateral action was counteracted through the computerized controller of the hydraulic actuator. Once a zero lateral load was reached, two load-controlled cycles were applied to obtain the

Figure 3.14: Test setup for specimens G11-G14 (aspect ratio = 7.0)

horizontal cracking load and simulate the column at service stage (Figure 3.15a). The load-controlled phase included a cracking cycle followed by a service cycle, with peak lateral loads corresponding to concrete first cracking and 60% of the yield strain in the outermost steel bar in tension (CSA 2019b), respectively. For a GFRP-RC column such as G1, the peak lateral load at service developed similar concrete compressive strain to that of its steel-RC counterpart (i.e. S1) under its lateral service load. It should be noted that for a GFRP-RC column that had no steel-RC counterpart (e.g. G3-G14), a hypothetical steel-RC counterpart with the same aspect ratio, transverse reinforcement configuration and spacing, concrete compressive strength and axial load level was considered to estimate its service load (CSA 2019b). Then the service load of the GFRP-RC column was calculated using the aforementioned criteria. At the end of each loading cycle, the

actuator reached zero lateral load whereas the lateral drift was not zero as a result of stiffness degradation.

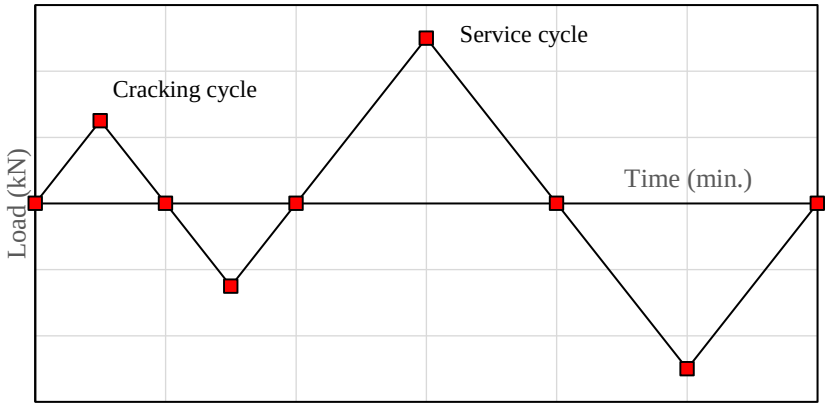

(a) Load-controlled phase

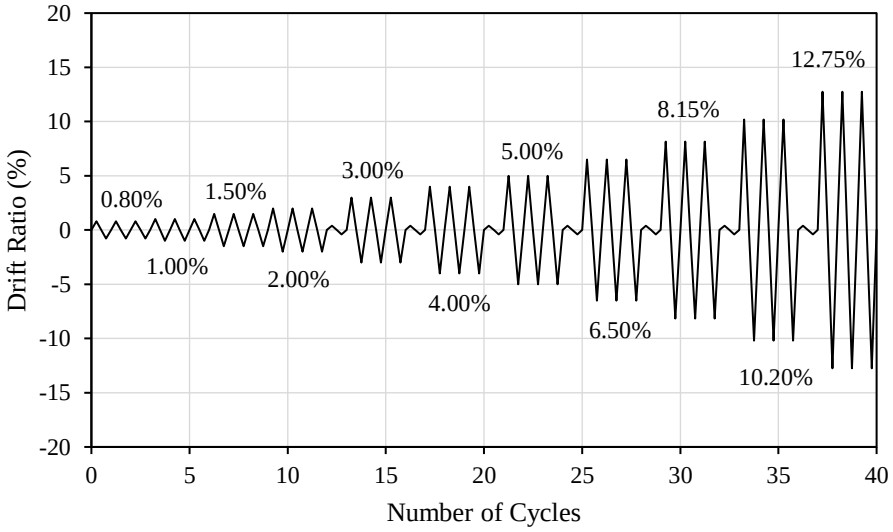

(b) Displacement-controlled phase

Figure 3.15: Lateral loading/drifting procedure

The column was subjected to the uniaxial drift reversals thereafter, following a typical displacement history in accordance with ACI 374.1-05 (ACI 2019b), as depicted by Figure 3.15b. successive quasi-static lateral drift reversals were applied in several steps at a frequency of 0.01 Hz. Three cycles having the same drift ratio (i.e. the percentage of the applied lateral displacement at mid-height of the column head divided by the column shear span) were applied for each drift

step, to ensure a stable crack propagation. To assess the stiffness degradation, if any, a load-controlled service cycle was applied after the drift ratio of 2.00% and every drift step that follows (Ali and El-Salakawy 2016; Hasaballa and El-Salakawy 2016, 2018; Naqvi and El-Salakawy 2017; Ghomi and El-Salakawy 2018, 2019). Typically, the actuator reached zero lateral drift at the end of each drift step, while the lateral load increased above zero with increasing the drift ratio applied, which was attributed to the progressively deteriorating stiffness of the column, The axial load was continuously monitored and promptly adjusted, as required, to ensure a constant axial load equal to the specified value throughout the test. Finally, tests were terminated when the lateral load capacity of the columns dropped by 25% or more.

3.3. Numerical Study

3.3.1. General

Despite the amount of research investigating the seismic behaviour of FRP-RC columns (Sharbatdar 2003; Tavassoli et al. 2015; Ali and El-Salakawy 2016; Naqvi and El-Salakawy 2017; Naqvi et al. 2017; Elshamandy et al. 2018; Kharal and Sheikh 2020), the performance of FRP-RC columns under earthquake excitations is far from being fully understood. The nonlinear finite-element analysis (FEA) can serve as an efficient tool providing reliable and extensive intuitive understanding of such performance. Most of the available numerical studies on FRP-RC columns studied their behaviour under monotonic loading schemes (Elchalakani et al. 2018; Alnajmi and Abed 2020; Raza et al. 2020; Tahir et al. 2021). This numerical study was based on a three-dimensional (3D) nonlinear finite-element model (FEM) constructed using ATENA/GID software package (Červenka et al. 2020a). This software has been considerably utilized in many recent research studies to model various types of FRP-RC members (Mahmoud and El-Salakawy 2016; Ghomi and El-Salakawy 2018; Attia et al. 2020; El-Gendy and El-Salakawy 2021). The FEM was then validated against the results of the previously discussed experimental study on GFRP-RC circular columns. Afterwards, the validated FEM was used to conduct an extensive parametric study addressing the influence of some key parameters on the seismic response of GFRP-RC columns. Design models with substantially enhanced accuracy were developed based on the numerical results. The following sections include some details of the constructed FEM.

3.3.2. Components of FEM and boundary conditions

The FEMs were modeled after GFRP-RC circular columns confined with spirals, where the dimensions followed those of specimens G1, G2, and G5-G8. The main elements comprising the FEM were: (1) column, (2) footing, (3) column head, (4) longitudinal bars and spirals, and (5) loading and supporting steel plates, as depicted by Figure 3.16. To ensure strain compatibility between each two adjacent segments, fully-rigid contact surfaces were defined in between.

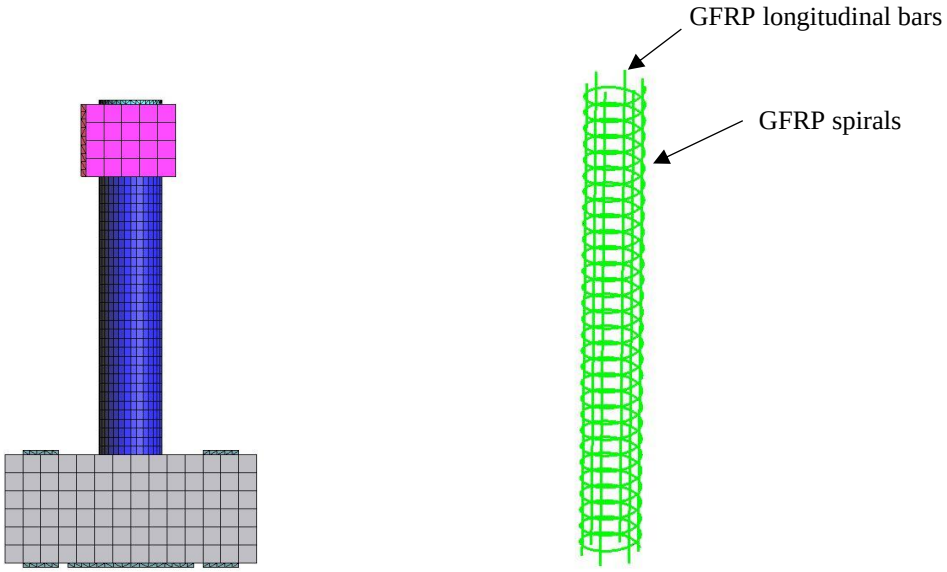

(a) Mesh discretization (b) Discrete reinforcement

Figure 3.16: Typical details of FEM

To simulate the post-tensioning applied to the footing, eight steel plates, measuring 200 × 200 × 25 mm, were created and restrained in all global directions; four above and four below the footing. Additionally, to eliminate any downward deflection for the footing under the axial load, a 600 × 500 × 25-mm steel supporting plate was placed below the footing and restricted in global Z direction. To transfer the applied loads to the FEM without any stress concentration, two steel loading plates having a thickness of 25 mm were utilized; a circular one with a diameter equal to 350mm diameter on top of the column head and a rectangular one measured 440 × 400 mm on the east side of the column head (considering global X axis as the west).

A comprehensive preliminary study was performed to determine the most effective material type and mesh type and size for each component. It was decided to model the concrete elements using

the eight-node "CCIsoBrick" hexahedral elements, the four-node tetrahedral elements were utilized to model the steel plates, whereas the GFRP reinforcement was modeled as 1D reinforcement "CCIsoTruss" elements (Figure 3.17). Mesh size of 50 mm was used for the columns and steel plates whereas the column head and footing were modeled with 100-mm sized mesh since increasing the mesh size had an insignificant effect on the performance of the columns.

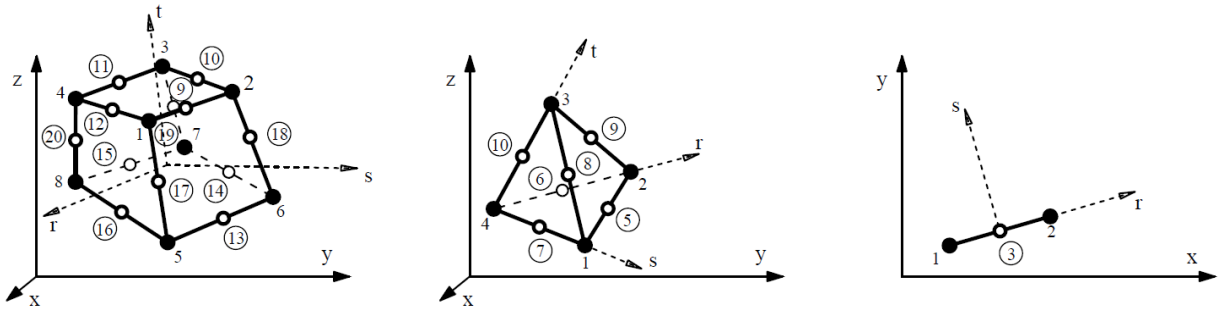

(a) Hexahedral element (b) Tetrahedral element (c) Truss element

Figure 3.17: Solid 3D elements used to model the FEMs (Červenka et al. 2020b)

3.3.3. Concrete material

The fracture-plastic constitutive model (CC3D Non-Linear Cementitious 2) available in ATENA/GID software package (Červenka et al. 2020b) was used to model the concrete material. This model combines the plasticity model for compressive behaviour and concrete crushing while the cracking is typically modeled using the Rankine fracture model (Figure 3.18). the constitutive laws of Van Mier (1986) were incorporated to model the concrete behaviour in compression and crushing.

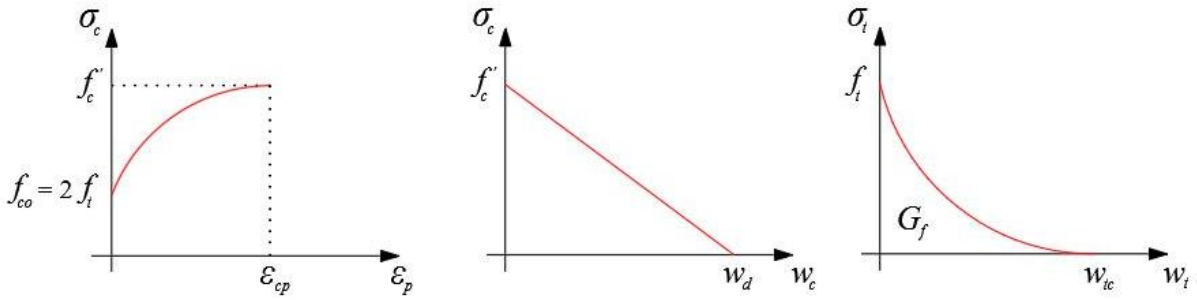

(a) Compressive hardening (b) Compressive softening (c) Tensile softening

Figure 3.18: Constitutive laws of concrete (Adapted from Červenka et al. 2020b)

As recommended by previous research studies (Sasmal et al. 2013; Hosseini et al. 2019), the critical compressive displacement, w_d, indicated in Figure 3.18b, was taken as 5 mm in this study. Besides, the reduction in concrete compressive strength after cracking (Vecchio and Collins 1986) was recognized by the reduction factor, r_c^{lim}, which was set as 0.8, indicating that the residual compressive strength in the direction parallel to cracking would be at least 80% of the uncracked concrete compressive strength. The model also accounts for the contribution of intact concrete between cracks to the tensile stiffness of the RC member (i.e. tension stiffening) by implementing a tension stiffening factor, c_{ts}, that describes the relative limiting value of tensile strength (Figure 3.19). The tension stiffening factor was defined as 0.4, as recommended by the CEB-FIP Model Code 1990 (CEB 1993). The properties of concrete were estimated as indicated in the following equations [Equation 3.2 to 3.4] (Červenka et al. 2020b), whereas the fundamental parameters defined for concrete in the FEMs were summarized in Table 3.4.

$$f_t^{'} = 0.27 f_c^{'2/3} \qquad \text{Equation 3.2}$$

$$G_F = 0.000025 f_t^{'} \quad [MN/m] \qquad \text{Equation 3.3}$$

$$E_c = \left(6{,}500 - 19.8 f_c^{'}\right)\sqrt{f_c^{'}} \qquad \text{Equation 3.4}$$

The model implements either a fixed or rotating cracking orientation and enables the reduction of shear stiffness after cracking. For this study, the fixed crack model was used as it was found to best resemble the behavior of experimentally tested specimens. The normal and tangential shear crack stiffnesses, referred to as K_n and K_t, respectively, are related through the shear factor coefficient, S_F, where Equation 3.5 describes the shear stiffness normal to the crack.

$$K_n = \frac{f_{t-cr}}{w_{cr}} \qquad \text{Equation 3.5}$$

$$K_t = S_F K_n \qquad \text{Equation 3.6}$$

where $f_{t\text{-}cr}$ is the tensile stress at the crack location and w_{cr} is the crack width.

To simulate crack closure associated with unloading, an unloading factor of zero was used for FEMs as recommended in the literature (Ghomi and El-Salakawy 2018; Hosseini et al. 2019; Setiawan et al. 2019; El-Gendy and El-Salakawy 2021).

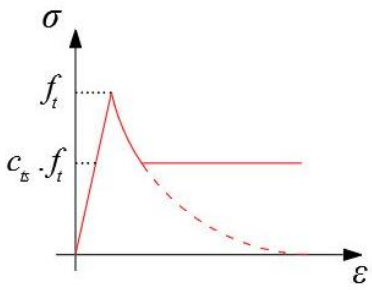

Figure 3.19: Tension stiffening of concrete (Adapted from Červenka et al. 2020b)

Table 3.4: Input parameters for the concrete constitutive model used in the FEMs

Material Property	NSC Columns	HSC Columns
Elastic modulus, E_c (MPa)	35,082	44,700
Poisson's ratio, μ	0.2	0.2
Compressive strength, f_c' (MPa)	37.0	90.0
Tensile strength, f_t (MPa)	3.0	4.9
Specific fracture energy, G_F ($\times 10^{-5}$ MN/m)	8.2	12.3
Fixed crack model coefficient	1.0	1.0
Tension stiffening factor, c_{ts}	0.4	0.4
Maximum aggregate size (mm)	19.0	19.0
Shear factor	20.0	20.0
Unloading factor	0.0	0.0
Critical compressive displacement, w_d (mm)	-5.0	-5.0
Plastic strain at compressive strength, ε_{cp} ($\times 10^{-3}$)	1.05	2.01
Reduction of strength due to cracks, $r_{c,lim}$	0.80	0.80
Failure surface eccentricity	0.52	0.52
Multiplier for the specific flow direction, β	0.50	0.50
Specific material weight, ρ (MN/m^3)	0.023	0.023

3.3.4. Reinforcement material

The properties of the GFRP reinforcement were assumed as provided in the previously discussed experimental study in Table 3.1. To model the stress-strain response of the GFRP reinforcement, a user-defined multi-linear constitutive law was used (Nagy-György et al. 2012). In this model, as

shown in Figure 3.20a, a linear relationship can be observed from zero to the ultimate strength of the GFRP material, f_{Fu}, followed by a linear descending branch until reaching a minimum value of 0.1 f_{Fu}, which would enable stress redistribution after localized failure of GFRP, if any.

While perfect bond can be assumed between reinforcement and concrete, this may result in unrealistic outcomes as the excessive cracking and damage of concrete, especially under cyclic load/drift reversals, would affect the bond. Instead, a predefined bond-slip model can be defined such as the CEB-FIP Model Code 1990 (CEB 1993) or the model of Bigaj (1999), which are typically used to model the bond-slip response of the conventional steel reinforcement. For FRP reinforcement, the user-defined bond-slip model is usually utilized (Mahmoud and El-Salakawy 2016; Ghomi and El-Salakawy 2018; Attia et al. 2020; El-Gendy and El-Salakawy 2021). The latter option was implemented in this numerical study for the GFRP longitudinal bars based on the experimental results of Alves et al. (2011), as shown in Figure 3.20b. On the other hand, perfect bond was defined for the GFRP spirals as the experimental results indicated no signs of slippage for the GFRP spirals, as discussed in the following chapters.

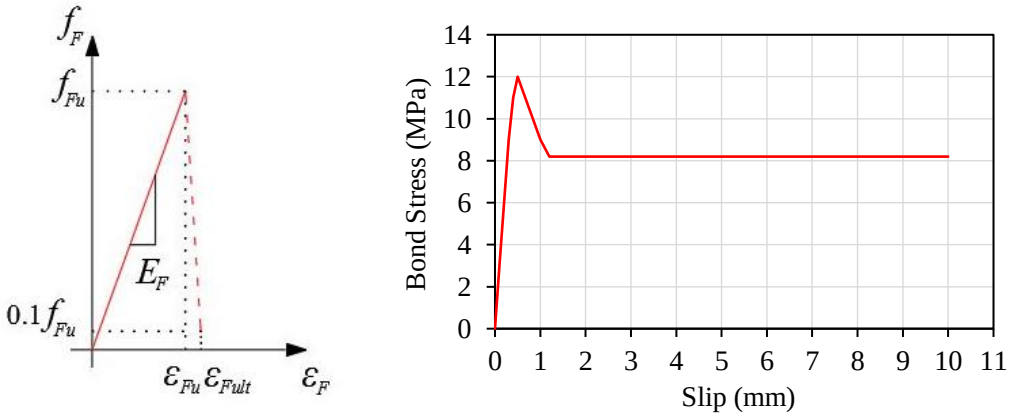

(a) Multi-linear stress-strain law (b) Bond-slip relationship

Figure 3.20: Constitutive laws for GFRP discrete reinforcement (Adapted from Alves et al. 2011)

The smeared reinforcement model was used in the three global directions (*x*, *y* and *z*) for the column head and footing, with a reinforcement ratio of 1.0 and 3.0%, respectively (Hosseini et al. 2019). This option was utilized since it exhibited a comparable performance to that of a similar FEM with discrete steel reinforcement during a preliminary step of this study, yet with much minimized calculation time and complexity for the former. It should be noted that the smeared

reinforcement model would typically assume a perfect bond between the reinforcement and the concrete (Červenka et al. 2020b).

3.3.5. Model validation and parametric study

The numerical results of the constructed FEM were validated against the experimental results of six GFRP-RC specimens, namely, G1, G2 and G5-G8. The results of specimens such as S1, G3 and G4 were not included within the scope of the validation process. The validation was performed with respect to cracking pattern, hysteretic response, initial stiffness and energy dissipation.

The validated FEM was then used to conduct an extensive parametric study to study the influence of some key parameters on the seismic performance of GFRP-RC columns. Figure 3.21 shows a flow chart including the details of FEMs incorporated in this parametric study. The FEMs were designated using a five-character alphanumeric code, where the first character, G, denoted the GFRP reinforcement used to reinforce all models. The second number referred to the concrete compressive strength (e.g., 30 for f_c' = 30 MPa). The third number represented the column aspect ratio, the fourth fraction indicated the axial load level, defined as the ratio of applied axial load, P, to the unconfined axial capacity of the column, P_o, whereas the fifth number identified the spiral pitch.

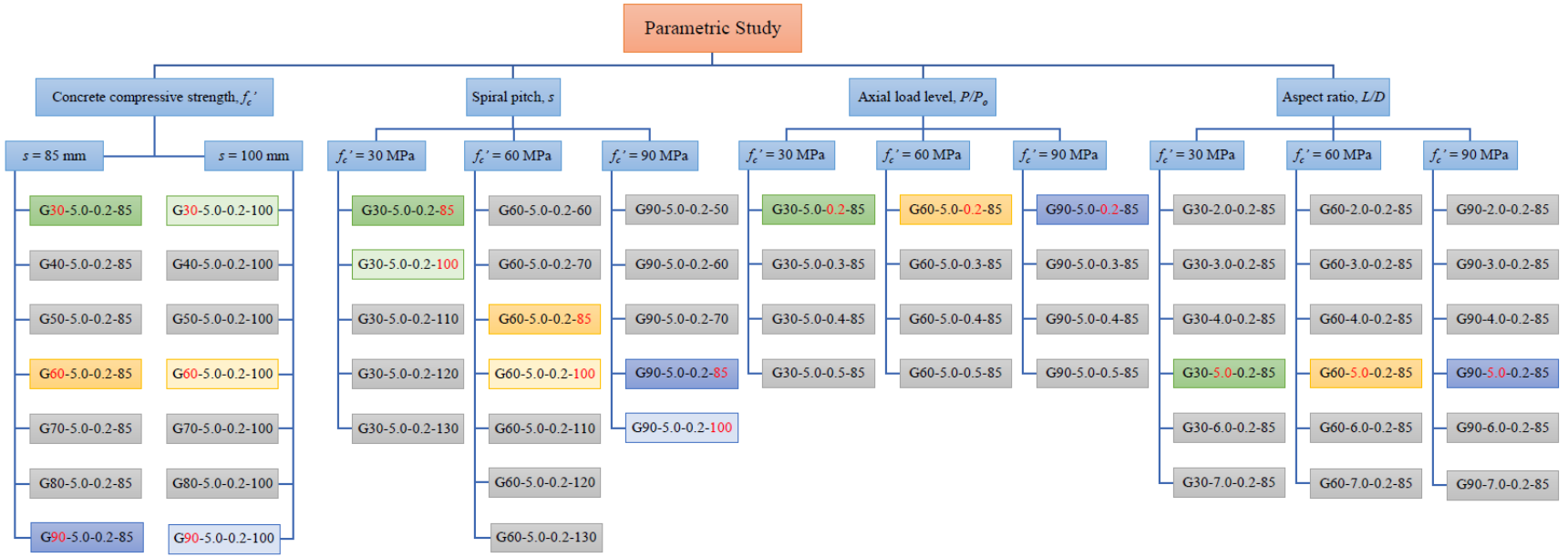

Figure 3.21: Test matrix for the numerical parametric study

CHAPTER 4: CONFINEMENT PROPERTIES OF GFRP-REINFORCED CONCRETE CIRCULAR COLUMNS UNDER SIMULATED SEISMIC LOADING

Authors' Affiliations and Roles:

- **Amr E. Abdallah**, PhD Candidate, Department of Civil Engineering, University of Manitoba.
  Role: Methodology, Investigation, Formal analysis, Validation, Visualization and Writing-Original Draft.

- **Ehab F. El-Salakawy**, Professor of Civil Engineering, Department of Civil Engineering, University of Manitoba.
  Role: Conceptualization, Methodology, Writing-Review & Editing, Supervision, Project administration, Resources and Funding acquisition.

Journal and Status:

Journal of Composites for Construction, ASCE, published online on December 18, 2020.

Reference:

Abdallah, A. E. M., and El-Salakawy, E. F. 2021. "Confinement properties of GFRP-reinforced concrete circular columns under simulated seismic loading." *J. Compos. Constr.* ASCE, 25 (2): 04020088, https://ascelibrary.org/doi/10.1061/%28ASCE%29CC.1943-5614.0001108.

Note:

The manuscript had been slightly altered from the original paper by renumbering the tables and figures to include the chapter number. In addition, the reference list and list of notations have been moved to the appropriate sections in the thesis as indicated in the table of contents.

Abstract

Columns in earthquake-resistant reinforced concrete (RC) structures need to be adequately confined to provide satisfactory levels of stability and deformability. In circular RC columns, confinement can be provided by spirals or hoops. This paper presents an investigation of the glass fiber-reinforced polymer (GFRP) confinement reinforcement requirements in columns of moment-resisting frames. Six full-scale circular RC columns were tested under simultaneous axial loading and unidirectional cyclic lateral drift reversals. The studied parameters were longitudinal reinforcement type, transverse reinforcement shape and pitch, and axial load level. Test results indicated that the maximum spiral pitch of one-fourth the gross diameter of the column as per the Canadian code for FRP-RC structures was reasonable and sufficiently conservative. In addition, GFRP circular hoops require larger lap splice length than that specified by the Canadian Highway Bridge Design Code to provide comparable confinement to GFRP spirals. The experimental results were estimated by a simplified method based on available confinement models, codes and guidelines for FRP-RC structures. It is recommended to consider the compressive strength of GFRP longitudinal bars with a compressive strain limit of 0.002 in circular GFRP-RC columns.

Keywords: Glass fiber-reinforced polymer (GFRP); circular column; spiral pitch; circular hoops; seismic loading; axial load level; interaction diagram.

4.1. Introduction

Reinforced concrete (RC) circular columns are often used due to their uniform stiffness and confinement behavior, aesthetic appearance, ease of maneuver in structures such as bridges and parking garages, and low drag force in offshore structures. However, many of these structures are exposed to aggressive environments, where corrosion of reinforcing steel is a major issue. The noncorrodible fiber-reinforced polymers (FRPs) reinforcement has been recently established as an alternative to steel to overcome such issues. Moreover, glass FRP (GFRP) is increasingly widespread in RC structures due to its lower cost and satisfactory strain capacity with respect to other types of FRP. However, GFRP reinforcement has linear-elastic behavior with relatively low elastic modulus and no yielding plateau. This property, in particular, made the seismic energy dissipating capability of GFRP-RC members questionable, as seismic energy in earthquake-resistant structures is mainly dissipated through inelastic deformations of their structural members. Conversely, recent research studies demonstrated the feasibility of using GFRP reinforcement in beam-column joints, flat plates, and columns under seismic-simulated loading with satisfactory levels of energy absorption (Mady et al. 2011; Tavassoli et al. 2015; Ali and El-Salakawy 2016; Hasaballa and El-Salakawy 2016, 2018; Naqvi and El-Salakawy 2017; Ghomi and El-Salakawy 2018, 2019; El-Gendy and El-Salakawy 2019, 2020).

Previous research on GFRP-RC columns under monotonic loading conditions proved the feasibility of using GFRP in columns (Alsayed et al. 1999; De Luca et al. 2010; Zadeh and Nanni 2013; Afifi et al. 2014; Mohamed et al. 2014; Tobbi et al. 2014; Hadhood et al. 2017; Elchalakani et al. 2018; Barua and El-Salakawy 2020; Elchalakani et al. 2020). In addition, stable seismic response was reported for well-confined GFRP-RC columns with minimal effect of GFRP type or transverse reinforcement's cross-sectional diameter (Tavassoli et al. 2015; Ali and El-Salakawy 2016). Moreover, GFRP spirals provided continuous confinement to the concrete core up to failure of the column, unlike steel spirals, which provided reduced confinement after yielding, resulting in a rapidly deteriorating concrete core (Tavassoli et al. 2015). Furthermore, the deformability of GFRP-RC columns compensated for the ductility of steel-RC ones with satisfactory levels of energy dissipation under a wide range of axial load levels (Ali and El-Salakawy 2016; Naqvi and El-Salakawy 2017; Elshamandy et al. 2018). Replacing steel bars with GFRP ones enhanced the

deformability and member ductility level, but dramatically decreased moment and shear capacities of the column (Kharal and Sheikh 2018, 2020).

Nonetheless, the lack of experimental data on behavior of FRP-RC columns could be the reason that the currently available codes and guidelines for design of FRP-RC structures impose many restrictions on column design. For instance, the ACI 440.1R-15 (ACI 2015) design guidelines do not recognize FRP as the main reinforcement in compression members. On the other hand, the Canadian codes CSA S806-12 (CSA 2017) and CSA S6-19 (CSA 2019d) allow using FRP as main reinforcement in columns. While the former neglects FRP's contribution to load capacity, the latter considers it with a compressive strain limit of 2,000 με. Moreover, CSA S806-12 (CSA 2017) imposes a very strict upper bound for spiral/circular hoop pitch of one-sixth the column's core diameter, unlike CSA S6-19 (CSA 2019d), which limits the clear spacing between 25 and 75 mm. Furthermore, while FRP circular hoops are recognized by both Canadian codes (CSA 2017, 2019d) as a form of transverse reinforcement for columns, only CSA S6-19 (CSA 2019d) specifies $40d_s$ as minimum lap splice length, where d_s is the hoop's nominal cross-sectional diameter. This was based on tests by Mohamed et al. (2014) and Hadhood et al. (2017) on GFRP-RC columns under axial and eccentric compression, respectively. Yet, neither the feasibility of GFRP hoops nor their minimum lap splice length has been investigated under seismic-simulated loading. For steel-RC columns, the discrete hoops are normally anchored through end hooks around longitudinal bars, which are not available for GFRP hoops. Saatcioglu and Baingo (1999) observed comparable performance for steel-RC columns reinforced by spirals and discrete hoops that were hooked into the concrete core. In addition, the authors reported that the behavior of steel-RC columns during seismic events indicated that a localized fracture of a steel spiral resulted in its complete unwinding. This, in turn, would make the anticipated benefits provided by the continuity of spiral reinforcement questionable. Therefore, it was of interest to explore the behavior of GFRP-RC columns confined with GFRP hoops.

The current study is a part of an ongoing research project to study the confinement behavior of GFRP-RC circular columns under simulated seismic loading. The purpose of this paper is to check the adequacy and lap splice length of circular GFRP hoops for columns under seismic loading. In addition, performing a direct comparison between GFRP and steel-RC columns and checking the current limits for spiral pitch in the Canadian codes (CSA 2017, 2019d) under different axial load levels are amongst the objectives of this study. Moreover, the experimental results were used to

develop an axial load-bending moment interaction diagram. Then they were compared with theoretical predictions using layered sectional analysis and modified code provisions to evaluate the currently available code predictions and stress-strain models.

4.2. Experimental Program

4.2.1. Materials

Test specimens were cast using ready-mixed, normal-strength concrete with a target 28-day compressive strength of 35 MPa. To obtain the actual concrete compressive strength on the day of testing for each specimen, tests on 100 × 200 mm standard concrete cylinders were conducted according to CSA A23.1-19 (CSA 2019a), as listed in Table 4.1. Deformed G400 steel bars and spirals were used to reinforce the steel-RC reference specimen, while sand-coated GFRP bars, spirals, and hoops were used to reinforce the other five GFRP-RC specimens, as shown in Figure 4.1 (Pultrall Inc. 2019). The mechanical properties of the used reinforcing bars, spirals and hoops are listed in Table 4.2, as provided in the manufacturer's certificate of compliance or as obtained from lab testing, as appropriate. The yield strength and associated strain of the steel bars and spirals were obtained as per CSA G30.18-09 (CSA 2019c). On the other hand, the ultimate tensile strength and strain for GFRP bars, spirals and hoops using their nominal areas in accordance with CSA S807-19 (CSA 2019e), and the average tensile force in accordance with Annex C of CSA S806-12 (CSA 2017). It should be also noted that the tensile properties for GFRP spirals and hoops were obtained through tests on straight bars with the same diameter and properties.

4.2.2. Specimen details and construction process

Six full-scale column–footing connections were constructed and tested under constant axial load and unidirectional cyclic lateral drift reversals. The test specimen represented a column segment between column–footing interface and point of contra-flexure, assumed at the mid-height of the column. This simulated the lower segment of first-story columns in a multistory structure or a cantilever bridge column acting in single curvature between the column's base and the center of mass of the superstructure. Columns had a diameter of 350 mm and a shear span (i.e., the distance between the column–footing interface and the point of lateral load application) equals to 1,750 mm to promote flexural-controlled failure. Rigid footings, measuring 1,400 × 900 × 600 mm, were adequately reinforced with 15M steel bars to ensure fixity to the column and resistance to drift

reversals without cracking in the footings during testing. No GFRP reinforcement was used to reinforce the footings.

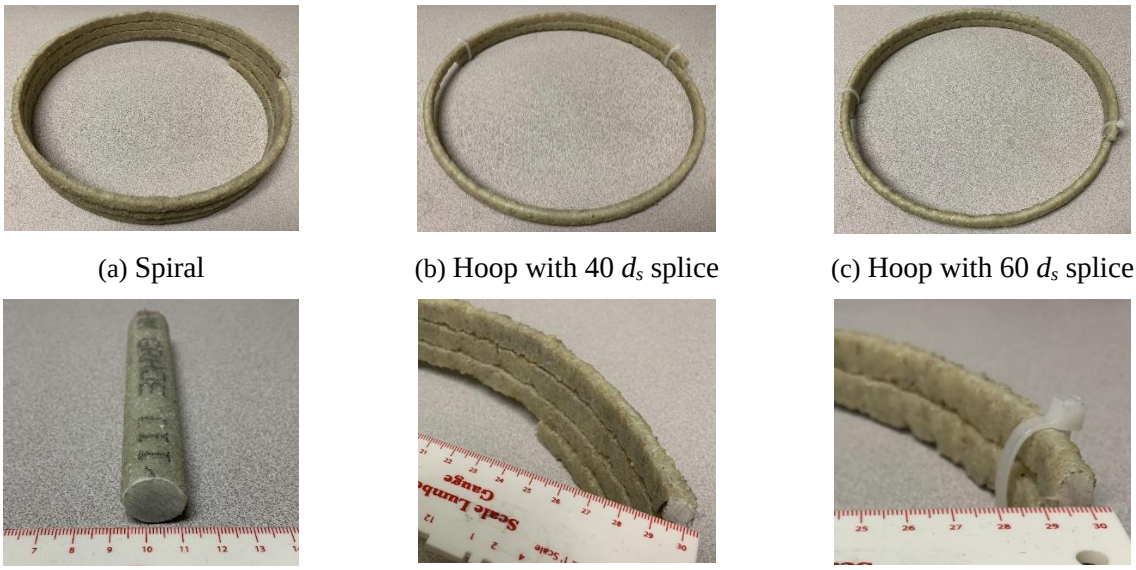

(a) Spiral (b) Hoop with 40 d_s splice (c) Hoop with 60 d_s splice

(d) GFRP longitudinal bar (e) Spiral close-up view (f) Hoop close-up view

Figure 4.1: Samples of GFRP transverse reinforcement (dimensions in mm)

One column was reinforced with 15M steel longitudinal bars and 10M steel spiral as a reference specimen. The other five specimens were reinforced longitudinally with No. 16 (15.9-mm diameter) GFRP bars, whereas the transverse reinforcement varied between No. 10 (9.5-mm diameter) GFRP spirals for three specimens and No. 10 GFRP circular hoops for the remaining two specimens (Figure 4.2). Lap splice length of circular hoops equals to $40d_s$ was used for one specimen in accordance with Clause 16.8.9.4.2 (c) of CSA S6-19 (CSA 2019d), where d_s is the hoop's nominal cross-sectional diameter. On the other hand, the other specimen confined by circular hoops had a lap splice length of $60d_s$. The flexural design for the steel-RC column was performed according to Section 10.1 and Clause 10.10.4 of the Canadian standards CSA A23.3-19 (CSA 2019b). In addition, the confinement reinforcement for that specimen was checked against Clauses 9.7.6.4.3, 18.7.5.3, and 18.7.5.4 of the ACI 318-19 (ACI 2019b) and Clauses 10.9.4, 21.2.8.1, 21.2.8.2, 21.3.2.6.3, and 21.4.4.3 of the CSA A23.3-19 (CSA 2019b). By contrast, the confinement reinforcement for GFRP-RC columns was designed as per Clauses 8.4.3.13 and 12.7.3.4 of CSA S806-12 (CSA 2017), Clause 16.8.9.4.2 of CSA S6-19 (CSA 2019d) and the research findings of the previously mentioned studies, as applicable. For instance, the development length of longitudinal GFRP bars into footings was selected following the findings of Ali and El-

Salakawy (2016). To simulate the common construction practice, footings were cast first followed by casting columns.

The designation of the test specimens was a five-character code, where the first character, S or G, identifies the reinforcement type, whether steel or GFRP, respectively; the second represents the axial load level as a ratio of the applied axial load, P, to the nominal unconfined axial capacity of the GFRP-RC column, P_o; the third character denotes the transverse reinforcement spacing or pitch; the fourth character, s or h, defines the transverse reinforcement type, as spiral or hoops, respectively; the fifth defines the lap splice length for specimens incorporating GFRP circular hoops, while it was denoted as XX for the spiral-reinforced ones. For example, specimen G-0.2-85s-XX was reinforced by GFRP bars and a GFRP spiral at a pitch of 85 mm, and subjected to an axial load equals to 0.2 of its nominal unconfined axial capacity. The test matrix is shown in Table 4.1.

4.2.3. Test setup and instrumentation

The lateral load reversals were applied to specimens by means of a horizontal hydraulic actuator, with $\pm$1,000-kN load and $\pm$250-mm stroke capacities, mounted on a rigid RC reaction wall and pinned to the column head. The positive and negative signs for load and drift indicate pushing and pulling directions, respectively. The specimen was placed on top of a 400-mm thick concrete leveling pad to align the longitudinal axis of the hydraulic actuator with the mid-height of the column head. The constant axial load was applied on the column using a 2,000-kN capacity hydraulic jack. This hydraulic jack was attached to a hinged steel loading frame, pinned to two large supporting concrete blocks, to transfer that axial load safely to the laboratory strong floor while allowing lateral displacement for the column head. The footing, leveling pad, and concrete blocks were post-tensioned to the laboratory strong floor using threaded high-strength steel bars. Details of the test setup are shown in Figure 4.3.

Sixteen electrical-resistance strain gauges were attached per specimen to the longitudinal bars and spirals at critical locations; within the expected hinging region and along the embedded length into the footing (Figure 4.2). Moreover, the total rotation of the column and the rotation component due to the plastic hinge (inelastic deformability hinge for GFRP-RC specimens) were measured using two pairs of linear variable displacement transducers (LVDTs) within the hinging region. Each pair of LVDTs was placed vertically against the column at equal horizontal spaces from the

column's extreme fibers (Figure 4.3b). The rotation for each pair was obtained as the summation of the LVDTs' readings divided by their horizontal spacing. The difference between the two rotations represented the rotation component due to the main crack at the column–footing interface, including rigid body rotation.

4.2.4. Test procedure

The test started by applying the specified axial load, which was a ratio of the nominal unconfined axial capacity, P_o; computed as per the Canadian code CSA S806-12 (CSA 2017) as follows:

$$P_o = \alpha_1 \phi_c f_c' \left(A_g - A_F \right) \quad \text{Equation 4.1}$$

where α_1 = the ratio of average stress in the rectangular compression block to the specified concrete strength; ϕ_c = the material resistance factor for concrete, taken as unity; f_c' = specified concrete compressive strength; A_g = the gross sectional area of the column; and A_F = the area of FRP main reinforcement. To determine the cracking load and represent the column at service, a load-controlled phase was undergone first, followed by the displacement-controlled phase that simulated earthquake excitations.

The load-controlled phase involved a cracking cycle followed by a service cycle, with peak lateral loads corresponding to concrete first cracking and 60% of the yield strain in the outermost steel bar in tension (CSA 2019b), respectively. For a GFRP-RC specimen, the peak lateral service load developed similar concrete compressive strain to that of its steel-RC counterpart under its lateral service load. The displacement-controlled phase included applying consecutive quasi-static lateral drift cyclic reversals in several steps at a frequency of 0.01 Hz. Each drift step comprised three identical cycles, in terms of drift ratio, to ensure stable crack propagation. The drift ratio was determined as the applied lateral drift at the column head divided by the column's shear span. Each drift applied was a multiplier of the preceding drift step as per ACI 374.1-05 (ACI 2019a). After a drift ratio of 2.0%, a load-controlled service load cycle was applied after each drift step to assess the stiffness degradation, if any (Ali and El-Salakawy 2016; Hasaballa and El-Salakawy 2016, 2018; Naqvi and El-Salakawy 2017; Ghomi and El-Salakawy 2018, 2019). The test was terminated when the peak lateral load under a specific drift was less than 75% the maximum lateral load capacity recorded for the specimen.

Table 4.1: Details of test matrix

Specimen ID	Axial load (P/P_o)	Cracking load applied (kN)	Concrete strength f_c' [a] (MPa)	Longitudinal reinforcement			Transverse reinforcement		
				Type	Bars	ρ_f [ρ_{st}] [b] *(%)*	Type	Diameter (mm)	Pitch (mm)
S-0.2-85s-XX	0.2	25	36.5 ± 0.9	Steel	6-15M	[1.25][b]	Steel spirals	11.3	85
G-0.2-85s-XX	0.2	25	36.9 ± 0.4	GFRP	6-No.16	1.23	GFRP spirals	9.5	85
G-0.2-50s-XX	0.2	25	36.0 ± 2.0	GFRP	6-No.16	1.23	GFRP spirals	9.5	50
G-0.2-85h-40d_s	0.2	25	41.8 ± 0.8	GFRP	6-No.16	1.23	GFRP hoops-40d_s splice	9.5	85
G-0.2-85h-60d_s	0.2	25	44.8 ± 1.7	GFRP	6-No.16	1.23	GFRP hoops-60d_s splice	9.5	85
G-0.3-85s-XX	0.3	35	41.4 ± 0.7	GFRP	6-No.16	1.23	GFRP spirals	9.5	85

[a] Values represent the mean strength of three 100 × 200-mm test cylinders and its standard deviation.

[b] Values between brackets represent reinforcement ratio in case of steel reinforcement.

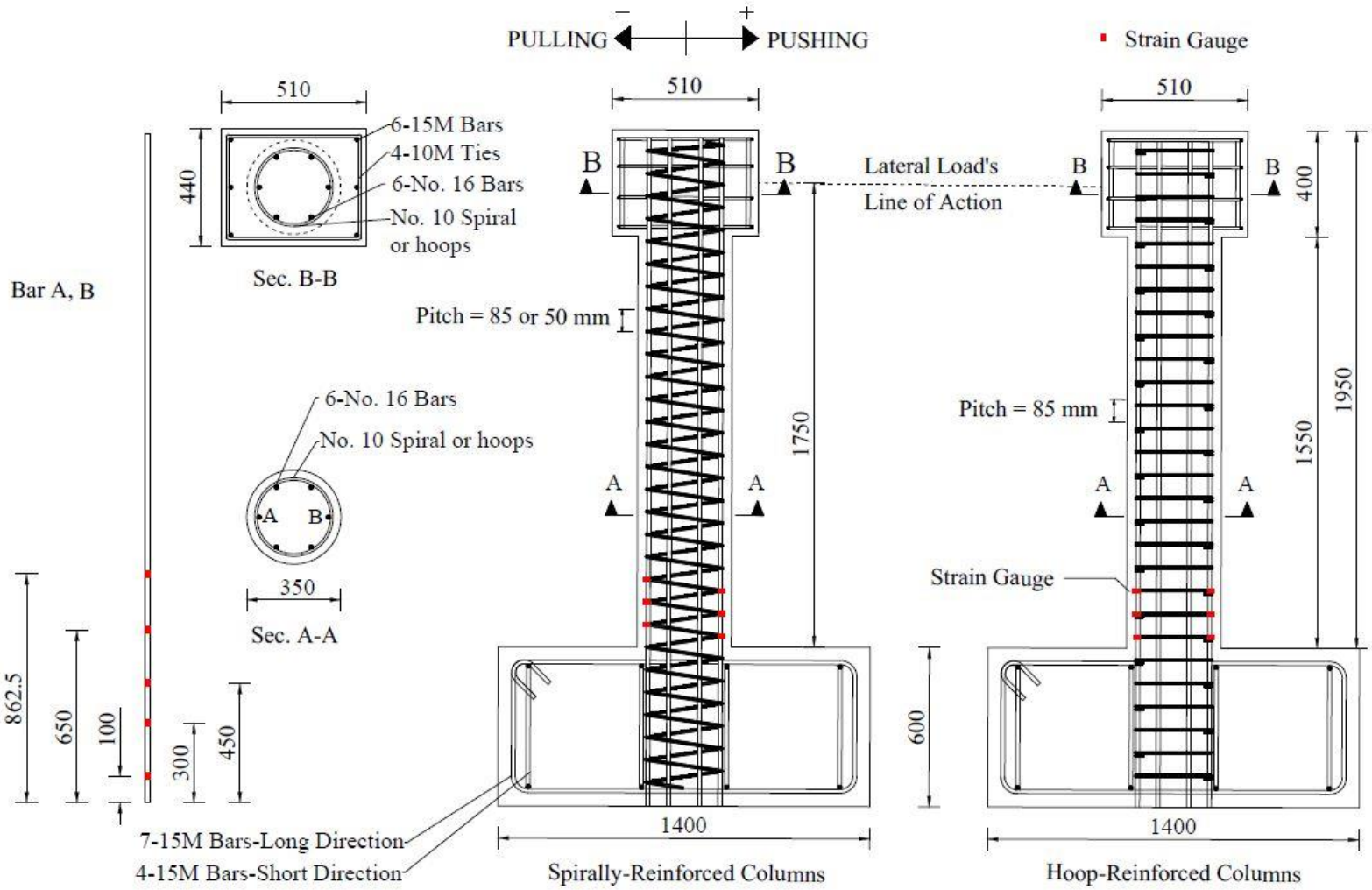

Figure 4.2: Details of test specimens, reinforcement and strain gauges' locations for spirally- and hoop-reinforced specimens (all dimensions in mm)

Table 4.2: Mechanical properties of steel and GFRP reinforcement

Bar type	Nominal diameter (mm)	Area (mm^2)	Modulus of elasticity (GPa)	Tensile strength (MPa) [a]	Ultimate strain (%) [a]
Steel bars and spirals					
15M	15.9	200	200	460	0.23
10M (Spirals)	11.3	100	200	420	0.21
GFRP bars, spirals and hoops					
No. 16	15.9	197.9 [b] [235] [c]	65.7 [d]	1,711 [d]	2.60 [d]
No. 10 (Spirals/Hoops)	9.5	71.0 [b] [83] [c]	58.4 [d]	1,376 [d]	2.36 [d]

[a] Determined as per CSA G30.18-09 (CSA 2019c).
[b] Nominal area as per CSA S807-19 (CSA 2019e).
[c] Measured area by immersion test as per Annex A of CSA S806-12 (CSA 2017).
[d] Measured as per Annex C of CSA S806-12 (CSA 2017).

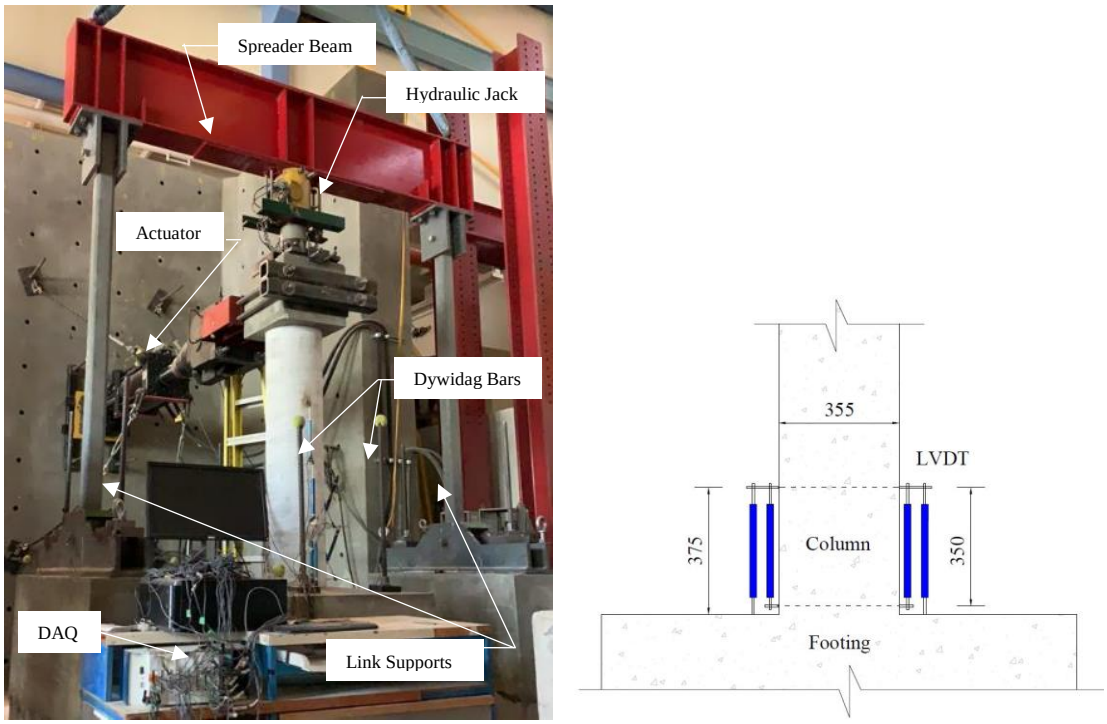

(a) Test Setup (b) LVDTs configuration

Figure 4.3: Details of test setup (all dimensions in mm)

4.3. Experimental Results and Discussion

4.3.1. General observations and mode of failure

All specimens exhibited flexure failure as shown in Figure 4.4. For the steel-RC reference specimen S-0.2-85s-XX, horizontal flexural cracks initiated at a lateral cracking load of approximately 25 kN. During the displacement-controlled phase, more flexural cracks were observed near extreme fibers. Spalling of concrete cover was initiated at 3.00% drift ratio followed by buckling of the longitudinal bars at 5.00% drift ratio. Subsequently, crushing of the concrete core occurred at 6.50% drift ratio followed by rupture of the outermost longitudinal bars. Spalling of concrete cover extended approximately 350 mm above the column–footing interface at failure.

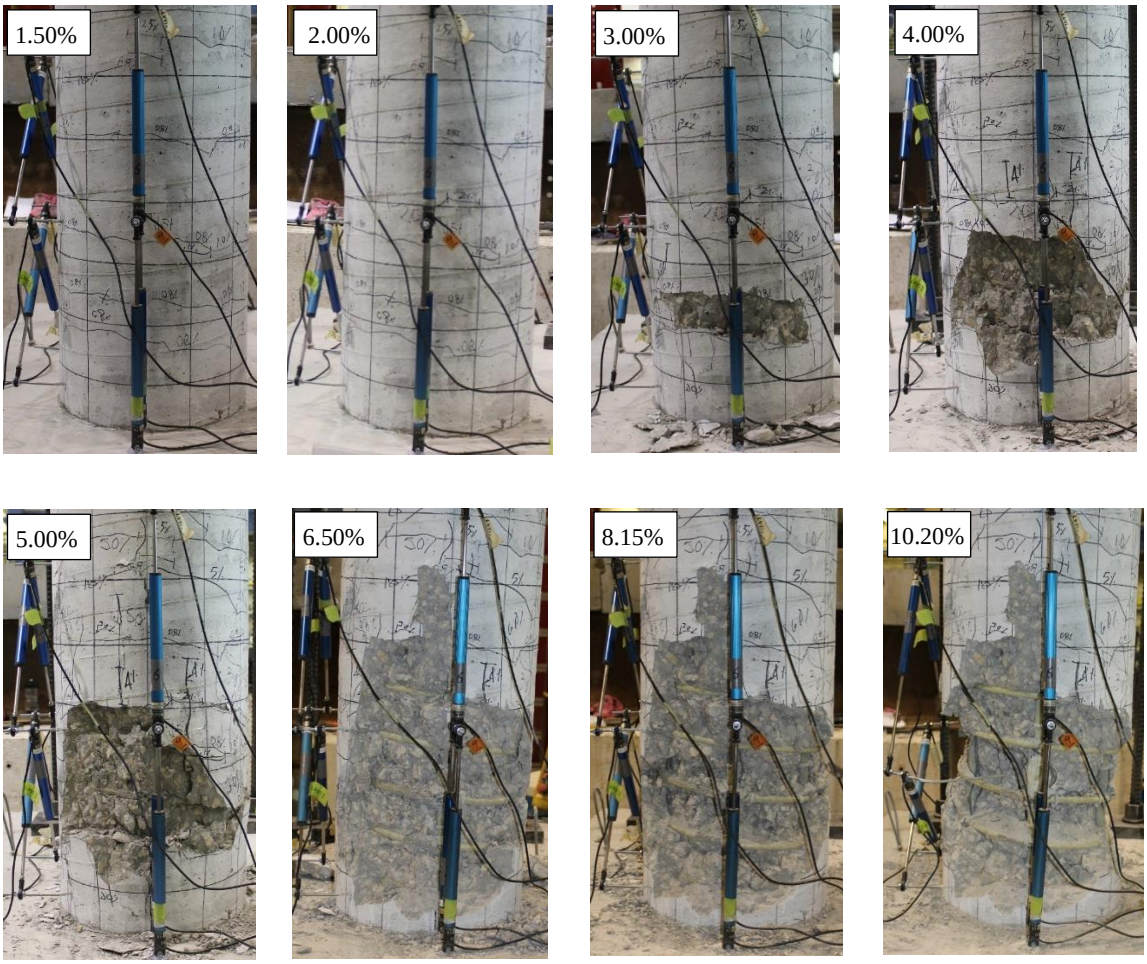

Figure 4.4: Typical sequence of failure for test specimens - Specimen G-0.2-85s-XX

For all GFRP-RC specimens, flexural cracks were developed in a similar manner to S-0.2-85s-XX but with higher intensity (Figure 4.4). The lateral cracking load for G-0.3-85s-XX was

approximately 35 kN due to the higher axial load applied that required a larger lateral load to initiate cracking. Lateral cracking loads applied to each specimen are listed in Table 4.1. Concrete cover spalling started at 2.00% drift ratio for G-0.2-50s-XX and G-0.3-85s-XX and at 3.00% drift ratio for G-0.2-85s-XX, G-0.2-85h-40d_s, and G-0.2-85h-60d_s. Failure in all spirally reinforced GFRP-RC specimens was characterized by simultaneous crushing of the concrete core and compression failure of the extreme longitudinal bar. Specimens G-0.2-85s-XX, G-0.2-50s-XX, and G-0.3-85s-XX failed at 10.20, 12.75, and 6.50% drift ratios, respectively, with the cover spalling region extending approximately 525, 500, and 475 mm above the column–footing interface, respectively. Figure 4.5 shows the test specimens at failure.

Table 4.3: Theoretical and experimental lateral load and drift capacities

Specimen ID	Theoretical capacity		Experimental lateral capacity		
	Lateral load (kN)	Drift (%)	Maximum (kN)	At failure (kN)	Strength Degradation (%)
S-0.2-85s-XX	63	–	+93.8 at 3.00% drift -85.0 at 2.00% drift	+62.0 at 6.50% drift	34
G-0.2-85s-XX	54	5.2[a]	+94.1 at 4.00% drift -96.0 at 10.20% drift	+58.8 at 10.20% drift	38
G-0.2-50s-XX	54	9.1[a]	+103.3 at 8.15% drift -115.6 at 10.20% drift	+61.8 at 12.30% drift	41
G-0.2-85h-40d_s	54	4.6[a]	+97.7 at 5.00% drift -82.8 at 6.50% drift	+71.0[b] at 6.50% drift	27
G-0.2-85h-60d_s	54	4.6[a]	+96.4 at 6.50% drift -103.1 at 6.50% drift	+49.3 at 10.20% drift	49
G-0.3-85s-XX	58	3.11[a]	+101.2 at 2.00% drift -77.5 at 2.00% drift	+73.0 at 6.50% drift	28

[a] Calculated as per Clause 12.7.3.3 of CSA S806-12 (CSA 2017).
[b] Specimen failed during service cycle.

On the other hand, G-0.2-85h-40d_s exhibited 27% strength degradation at 6.50% drift ratio. Nevertheless, the specimen underwent a service cycle afterwards, in which the concrete core was devastated with longitudinal bars buckled and delaminated, and the GFRP hoops at critical section opened up. Increasing the lap splice length of the GFRP hoops to 60d_s resulted in a comparable drift capacity (i.e., maximum drift ratio survived by the specimen for three complete cycles) for

G-0.2-85h-60d_s to that of G-0.2-85s-XX, failing at 10.20% drift ratio with the outermost bar failing in compression.

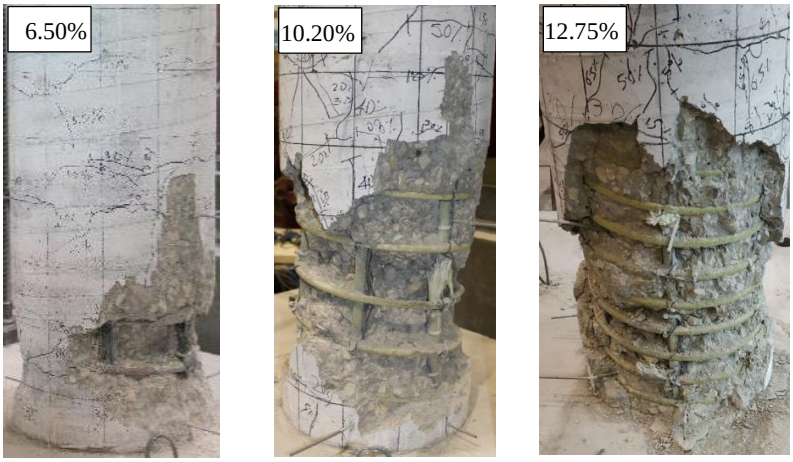

(a) S-0.2-85s-XX (b) G-0.2-85s-XX (c) G-0.2-50s-XX

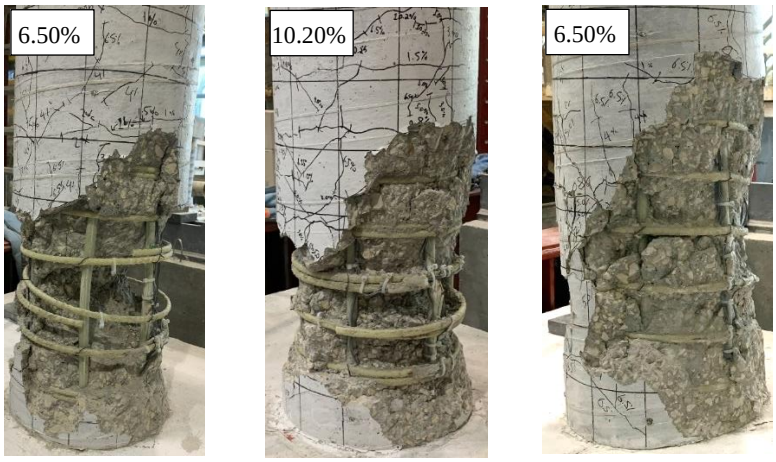

(d) G-0.2-85h-40d_s (e) G-0.2-85h-60d_s (f) G-0.3-85s-XX

Figure 4.5: Test specimens at failure

4.3.2. Effect of reinforcement type

Figure 4.6 shows the lateral load-drift envelopes for the test specimens. For all specimens, the lateral resistance in the pushing direction exceeded that in pulling direction. Such behavior is typical under cyclic lateral drift reversals as they typically start by pushing (Hasaballa and El-Salakawy 2016, 2018). Nonetheless, G-0.2-85s-XX, G-0.2-50s-XX, and G-0.2-85h-60d_s experienced greater lateral load resistance on the pulling side at or beyond 5.00% drift ratio. Similar behavior was reported by Lehman and Moehle (2000), Ali and El-Salakawy (2016), and Ghomi and El-Salakawy (2020). The steel-RC column, S-0.2-85s-XX, reached its maximum

lateral load capacity (93.8 kN) at a drift ratio of 3.00%. Then, the lateral resistance declined continuously until failure occurred at 6.50% drift ratio with 34% strength degradation. The experimental maximum lateral loads and drifts along with the theoretically predicted ones are listed in Table 4.3. The theoretical values were estimated in accordance with CSA A23.3-19 (CSA 2019b) and CSA S806-12 (CSA 2017), as appropriate.

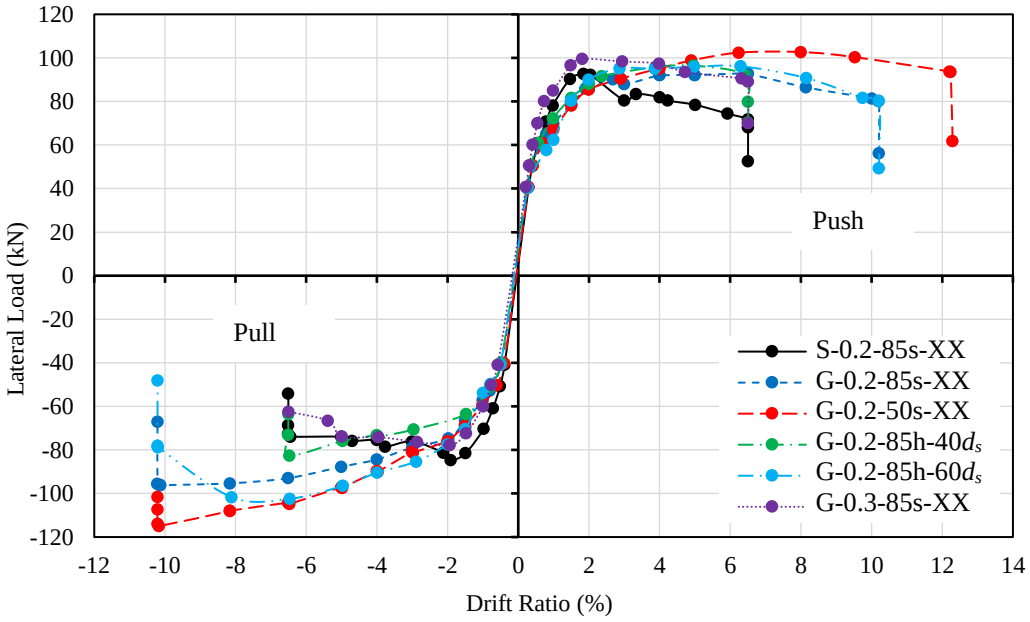

Figure 4.6: Envelopes of hysteresis diagrams for test specimens

As shown in Figure 4.6, G-0.2-85s-XX exhibited softer hysteretic response compared with S-0.2-85s-XX during the early stages of loading due to the relatively low elastic modulus of GFRP. The maximum lateral load capacity of G-0.2-85s-XX (94.1 kN) was reached at 4.00% drift ratio and continued with an insignificant change up to 6.50% drift ratio. Then the lateral resistance dropped gradually until failure occurred at a drift ratio of 10.20%. This improvement in the behavior of the GFRP-RC column could be due to the relatively high tensile strength of GFRP at large drifts and the continuous confinement provided by GFRP spirals up to failure. As expected, Figure 4.7shows that the hysteresis diagrams of the GFRP-RC specimens exhibited much narrower loops with considerably less pinching compared with those of S-0.2-85s-XX. This occurred because of the linear-elastic behavior of the GFRP reinforcement and absence of yielding. Furthermore, the moment–drift ratio relationships are depicted in Figure 4.8. It is worth mentioning that those hysteresis loops represented the total moment at the critical section, including that developed due to *P*-Δ effects. The reduction in lateral load resistance due to the *P*-Δ effect was around 20% of

the total moment capacity at 4.00% drift ratio for steel- and GFRP-RC specimens. The secondary moments for test specimens at each drift ratio are listed in Table 4.4.

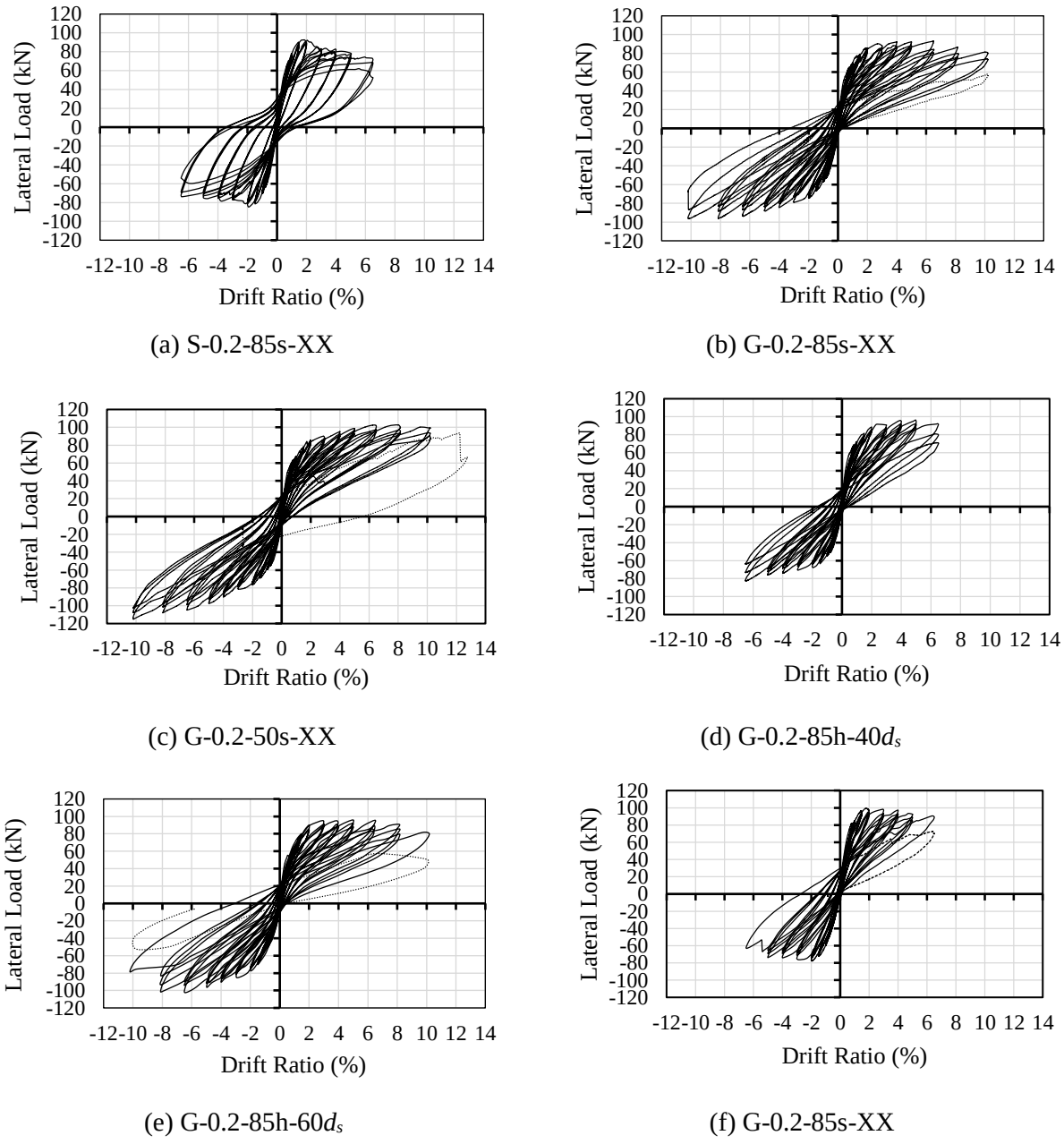

(a) S-0.2-85s-XX

(b) G-0.2-85s-XX

(c) G-0.2-50s-XX

(d) G-0.2-85h-40d_s

(e) G-0.2-85h-60d_s

(f) G-0.2-85s-XX

Figure 4.7: Hysteresis diagrams for test specimens

This difference between the hysteresis diagrams of the specimens was reflected on the cumulative energy dissipated-drift ratio relationships. As shown in Figure 4.9, S-0.2-85s-XX dissipated 105% higher energy than that dissipated by specimen G-0.2-85s-XX at 4.00% drift ratio. As suggested

by previous studies (Hasaballa and El-Salakawy 2016; Ghomi and El-Salakawy 2019), such an issue can be overcome by providing an integrated earthquake-resisting system comprising GFRP-RC moment-resisting frames (MRFs) and shear walls. Thus, not only the energy dissipation issue would be solved, but also the advantage of high elasticity of GFRP reinforcement could be also exploited, leading to reduced post-earthquake maintenance cost compared with steel-RC structures.

Table 4.4: Secondary moment effects on test specimens

	Secondary Moment/ Total Moment (%)									
Drift Ratio (%) / Specimen ID	0.80	1.00	1.50	2.00	3.00	4.00	5.00	6.50	8.15	10.20
S-0.2-85s-XX	6.03	6.75	8.62	10.72	12.65	21.23	25.49	31.83	_	_
G-0.2-85s-XX	6.85	7.97	10.11	12.20	15.66	19.92	23.05	27.86	33.61	39.28
G-0.2-50s-XX	6.75	7.88	10.10	11.98	15.55	19.32	22.05	25.35	30.43	34.96
G-0.2-85h-40d_s	6.92	7.94	10.17	12.33	16.76	20.44	24.22	28.43	_	_
G-0.2-85h-60d_s	6.21	7.10	9.96	11.99	15.43	19.16	22.59	27.18	32.13	41.06
G-0.3-85s-XX	9.45	10.22	12.83	15.00	21.62	27.48	32.41	38.59	_	_

The maximum strain in the extreme longitudinal reinforcement bars along the hinging region is plotted against the drift ratio in Figure 4.10. The relationships were comparable for all specimens up to 1.50% drift ratio, beyond which the strains developed in steel longitudinal bars were significantly larger than those induced in GFRP ones. This was also expected due to the yielding of steel and its larger elastic modulus compared with GFRP. Moreover, higher strains were observed in GFRP spirals than those developed in the steel one (Figure 4.11). At 4.00% drift ratio, which represents the drift ratio limit by CSA S806-12 (CSA 2017) for ductile MRF systems, the recorded spiral strain for S-0.2-85s-XX and G-0.2-85s-XX was 2,220 and 6,830 με, respectively. This drift limit was set by CSA S806-12 (CSA 2017) for ductile moment-resisting frames, as beyond this drift ratio, the integrity of a building and safety of occupants would be greatly jeopardized. The spiral strain for the steel-RC specimen was below the strain limit of 2,500 με set by CSA A23.3-19 (CSA 2019b), whereas the spiral strain of G-0.2-85s-XX exceeded the limit 6,000 με set by CSA S806-12 of (CSA 2017). The strain limit of 6,000 με was set by CSA S806-12 (CSA 2017) as a limiting value to ensure reaching the design drift ratio without rupturing of

the transverse reinforcement due to shear effects. Unlike the steel spiral, the GFRP spiral provided a continuously increasing confinement to G-0.2-85s-XX, reaching 84% of its ultimate strain prior to gauge damage.

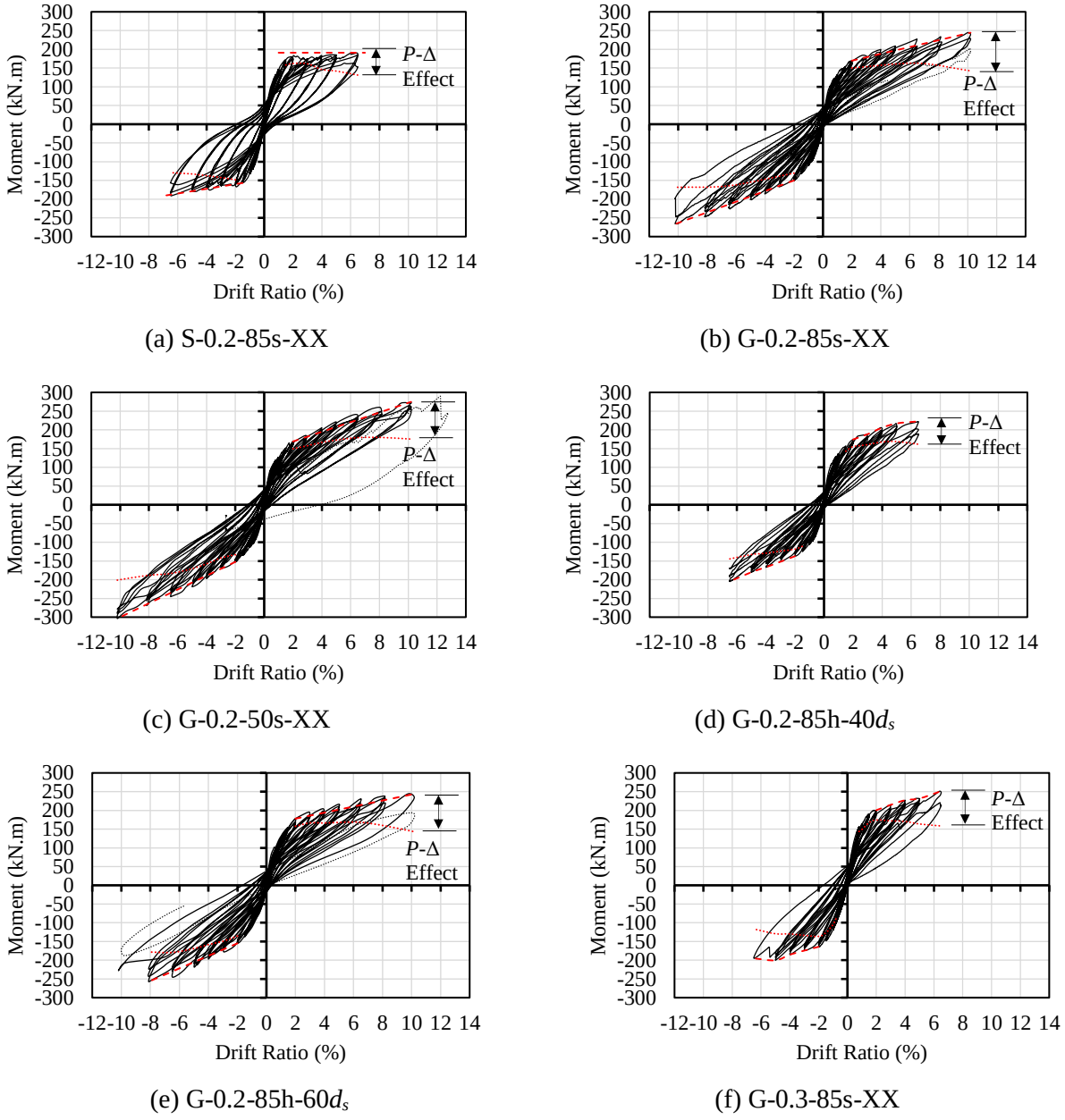

(a) S-0.2-85s-XX

(b) G-0.2-85s-XX

(c) G-0.2-50s-XX

(d) G-0.2-85h-40d_s

(e) G-0.2-85h-60d_s

(f) G-0.3-85s-XX

Figure 4.8: Hysteresis moment-drift ratio relationship for test specimens

Strains at five locations along each extreme longitudinal bar (Figure 4.2) were measured to plot the strain profiles as depicted in Figure 4.12. The adequacy of the development length of GFRP longitudinal bars into the footing was verified as the strain distribution terminated within the

embedment length. However, the location of zero strain varied for steel and GFRP-RC specimens, which can be attributed mainly to the different bond behavior of steel and GFRP, and the lower modulus of elasticity of GFRP (Ali and El-Salakawy 2016; Naqvi and El-Salakawy 2017). Furthermore, uniform longitudinal strains were recorded within the hinging region for G-0.2-85s-XX, while higher strains were intensified right above the interface for S-0.2-85s-XX. This agrees well with the observations concerning concrete cover spalling regions, which extended for G-0.2-85s-XX to approximately 1.5 times that of S-0.2-85s-XX.

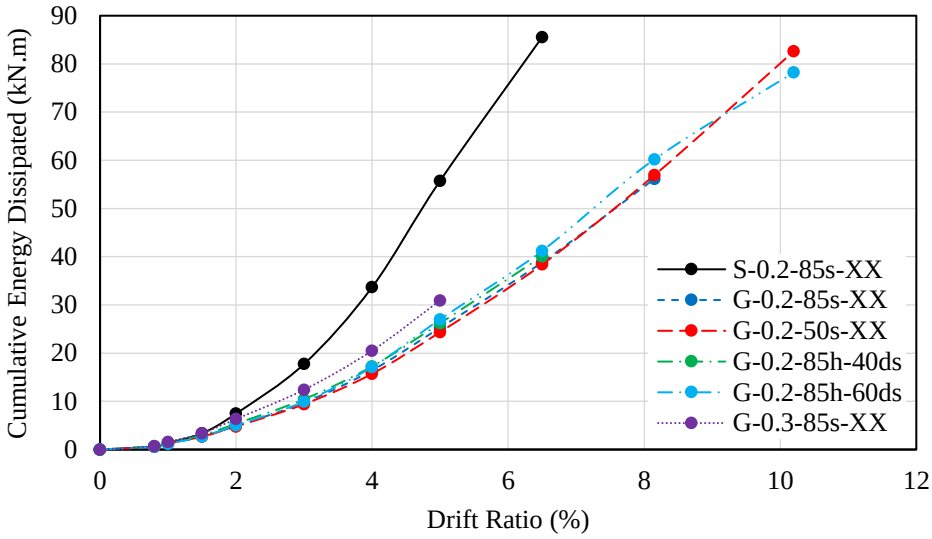

Figure 4.9: Cumulative energy dissipated by test specimens

The column total rotation at the interface can be divided into three main categories (Figure 4.13); (1) rotation of plastic hinge (inelastic deformability hinge in case of GFRP-RC specimens), measured by the inner pair of LVDTs (Figure 4.3b); (2) rotation due to main crack at the column–footing interface, computed as the difference between the rotations measured by each pair of LVDTs (Figure 4.3b); and (3) rotation due to other components, computed as the difference between column drift angle and the rotation measured by the outermost pair of LVDTs (Ali and El-Salakawy 2016; Naqvi and El-Salakawy 2017; Hasaballa and El-Salakawy 2018). Examples of other components include column curvature and cracking outside the hinging region, and rotation due to shear. The contribution of each component was computed with respect to the column total drift angle. For all specimens, the contribution ratios of the three components experienced insignificant changes until 2.00% drift ratio. Then a significant increase to the plastic (inelastic

deformability) hinge component occurred with a different rate for each specimen. Moreover, as the spalled off region for G-0.2-85s-XX extended beyond the gauge length of the LVDT pairs, larger rotation due to cracking outside instrumented segment can be expected compared with that of S-0.2-85s-XX. Overall, the aforementioned observations agreed well with the findings of previous studies on GFRP and steel-RC square columns (Ali and El-Salakawy 2016; Naqvi and El-Salakawy 2017).

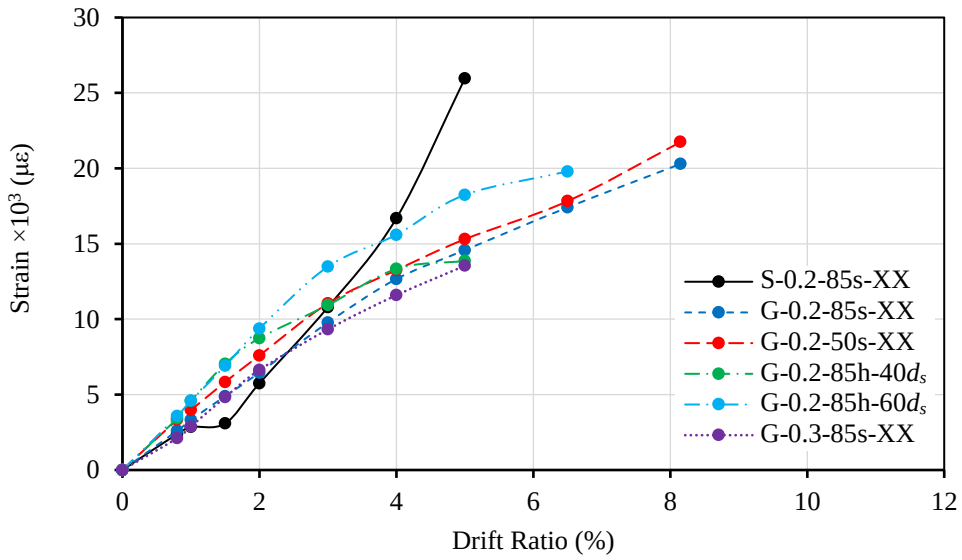

Figure 4.10: Maximum strain in extreme longitudinal bar of column at hinging region versus drift ratio

4.3.3. Effect of transverse reinforcement shape and spacing

Decreasing transverse reinforcement spacing for GFRP-RC columns under seismic loading was reported to significantly enhance strength and deformability (Tavassoli et al. 2015; Ali and El-Salakawy 2016; Naqvi and El-Salakawy 2017). Decreasing spiral pitch in this study from 85 to 50 mm enhanced both lateral load and drift capacities by 10 and 25%, respectively, as shown in Figure 4.6. Decreasing the spiral pitch did not alter the strength decay due to the *P*-Δ effect, as shown in Figure 4.8. In addition, the cumulative energy dissipated by both G-0.2-85s-XX and G-0.2-50s-XX was similar through all stages of loading (Figure 4.9). The overall cumulative energy dissipated by G-0.2-50s-XX, however, was higher than that dissipated by G-0.2-85s-XX. Furthermore, the resemblance between the maximum longitudinal reinforcement and spiral strains beyond the concrete cover spalling, and longitudinal strain profiles of G-0.2-85s-XX and G-0.2-

50s-XX (Figures 4.10 through 4.12) emphasized the effectiveness of the spiral pitch of one-fourth the column's gross diameter. Even at 4.00% drift ratio, the measured spiral strain for G-0.2-50s-XX was 7,310 με, which also exceeded the strain limit of 6,000 με set by CSA S806-12 (CSA 2017). Despite there was a relatively significant decrease of spiral strains for the 50 mm pitch beyond 4.00% drift ratio, this did not necessarily mean increased confinement effectiveness. In fact, such decrease of pitch means, in turn, a larger amount of spiral reinforcement per unit volume of concrete core and, hence, less stress in each turn of the spiral. Moreover, an insignificant change of contributions of each rotation component was noticed beyond 4.00% drift ratio (Figure 4.13).

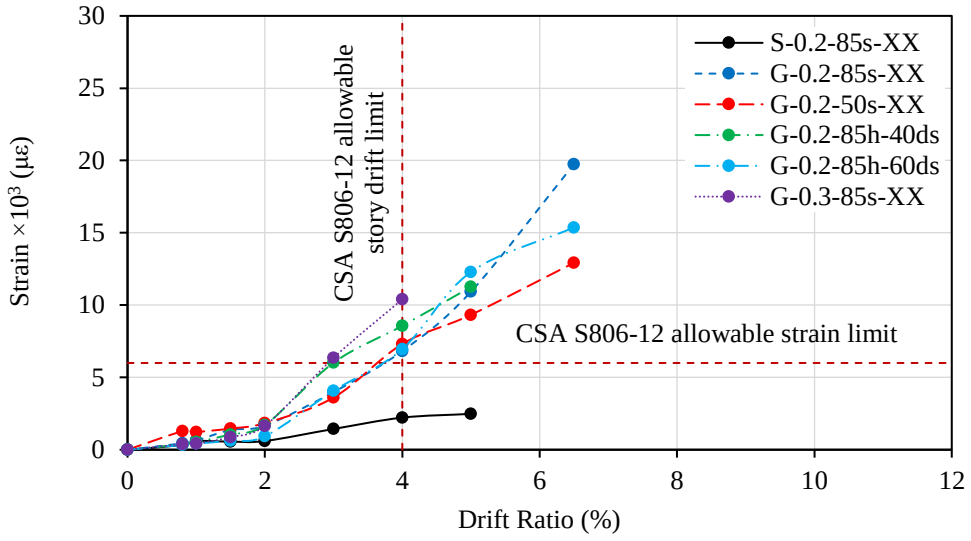

Figure 4.11: Maximum spiral/hoop strain versus drift ratio

The GFRP hoops with a splice length equal to 40 d_s were capable of providing comparable confinement to spirals up to 5.00% drift ratio, at which the maximum lateral load capacity for G-0.2-85h-40d_s (97.7 kN) was reached (Figure 4.6). Nonetheless, the hysteretic response deteriorated rapidly afterwards with a 27% strength degradation at 6.50% drift ratio, right before sudden failure under the lateral service load. It is true that G-0.2-85h-40d_s survived 5.00% drift ratio, which is larger than the drift limit for ductile MRFs as per CSA S806-12 (CSA 2017). However, the effect of the lap splice could be noticeable in case of higher axial load levels. For example, spirally reinforced specimen G-0.3-85s-XX had a drift capacity of 5.00%, which could presumably have been lower if the same GFRP hoops were utilized instead. On the other hand, G-0.2-85h-60d_s exhibited comparable hysteretic response to that of G-0.2-85s-XX through all stages of loading, achieving similar lateral load and drift capacities.

Figures 4.8, 4.9, 4.10 and 4.12 indicate that using circular hoops did not alter the strength reduction due to the *P*-Δ effect, energy dissipating capability, or the maximum longitudinal reinforcement strains of the column. Only a slight increase in maximum longitudinal reinforcement strains for G-0.2-85h-60d_s over those of G-0.2-85s-XX was observed.

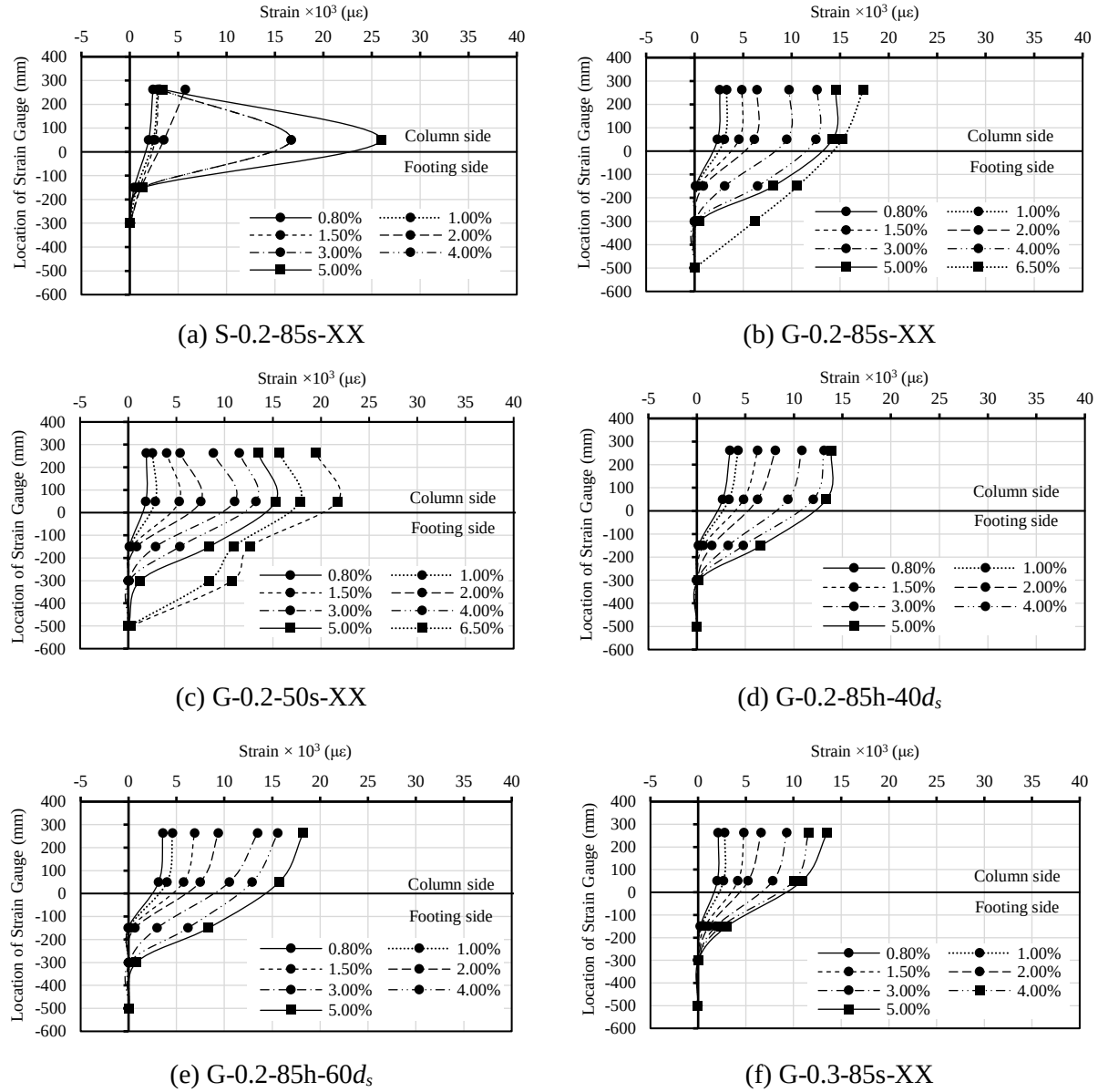

(a) S-0.2-85s-XX

(b) G-0.2-85s-XX

(c) G-0.2-50s-XX

(d) G-0.2-85h-40d_s

(e) G-0.2-85h-60d_s

(f) G-0.3-85s-XX

Figure 4.12: Strain profile of column's extreme longitudinal bar for test specimens

Conversely, Figure 4.11 shows larger transverse reinforcement strains for G-0.2-85h-40d_s over those of G-0.2-85s-XX, exceeding the strain limit of 6,000 με at 3.00% drift ratio (CSA 2017). The rate of increase for G-0.2-85h-40d_s declined afterwards, reaching 11,260 με at 5.00% drift

ratio, which was close to the spiral strain of G-0.2-85s-XX at the same drift ratio (10,930 με). On the other hand, similar transverse reinforcement strains were noticed for G-0.2-85s-XX and G-0.2-85h-60d_s. This also emphasizes the inadequacy of the lap splice length of 40 d_s as it could not transfer the hoop stress, which was well below the ultimate tensile strength, whereas comparable confinement behavior to GFRP spirals was provided by GFRP hoops with 60 d_s lap splice length**.** Furthermore, an increase of the contribution of rigid body rotation for G-0.2-85h-40d_s compared to the spiral-reinforced specimen was noticed (Figure 4.13). However, the strain profile in Figure 4.12 did not indicate such behavior. Specimen G-0.2-85h-60d_s, however, exhibited similar contribution percentages to those of the spiral-reinforced counterpart column. Although CSA S6-19 (CSA 2019d) specifies a minimum lap splice length for GFRP circular hoops equals to 40 d_s, the current study suggests increasing the aforementioned requirement to 60 d_s for columns in active seismic zones.

4.3.4. Effect of axial load level

As shown in Figure 4.6, early strength gain was exhibited by G-0.3-85s-XX, reaching its maximum lateral load capacity (101.2 kN) at 2.00% drift ratio. At the same drift ratio, the lateral resistance of G-0.2-85s-XX was 86.8 kN. Subsequently, the specimen with a higher axial load level exhibited continuous strength degradation until failure occurred at a drift ratio of 6.50% with strength degradation of 28%. On the other hand, G-0.2-85s-XX exhibited a more stable hysteretic response with 163% higher drift capacity than G-0.3-85s-XX. In addition, the magnitude of the *P*-Δ moment increased from 20 to 27% at 4.00% drift ratio when the axial load level increased from 20 to 30%. The early deterioration noticed for the hysteretic response of G-0.3-85s-XX might be the reason for the relatively higher amount of energy dissipated shown in Figure 4.9. The maximum longitudinal reinforcement strains along the hinging region were not significantly affected by increasing the applied axial load (Figures 4.10 and 4.12*).* Contrarily, spiral strains of G-0.3-85s-XX were remarkably larger than those of G-0.2-85s-XX, especially after 2.00% drift ratio. This was consistent with the visual observation as cover spalling initiated for G-0.3-85s-XX at the aforementioned drift ratio. Moreover, the maximum spiral strain recorded for G-0.3-85s-XX was 10,400 με at 4.00% drift ratio, which was approximately 1.5 times the corresponding strain in G-0.2-85s-XX. This was also expected as increasing the axial load level was reported to increase the outward lateral stress on the concrete core and, hence, higher confinement stresses should be induced (Tavassoli et al. 2015; Ali and El-Salakawy 2016; Naqvi and El-Salakawy 2017).

Furthermore, at 4.00% drift ratio the rotation was mainly dominated by inelastic deformability hinge and rigid body rotation for G-0.3-85s-XX (Figure 4.13). This can be attributed to the intensified damage occurred within the hinging region for the specimen with a higher axial load level.

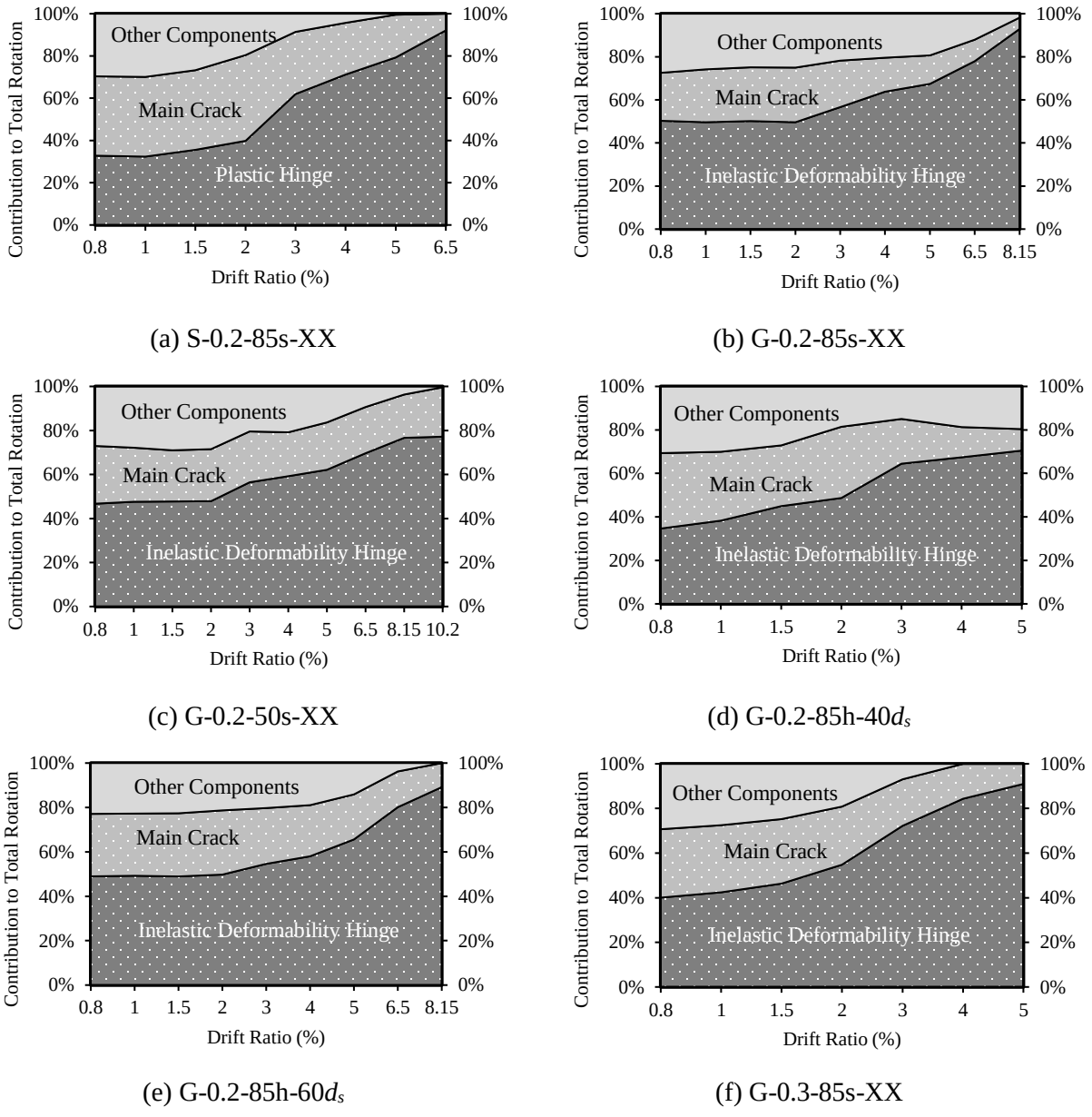

(a) S-0.2-85s-XX

(b) G-0.2-85s-XX

(c) G-0.2-50s-XX

(d) G-0.2-85h-40d_s

(e) G-0.2-85h-60d_s

(f) G-0.3-85s-XX

Figure 4.13: Percentage of contributions to column's total drift angle for test specimens

These results were in good agreement with experimental findings of previous studies as specimens with lower axial load levels exhibited more stable hysteretic response with higher drift capacity

and deformability (Tavassoli et al. 2015; Ali and El-Salakawy 2016; Naqvi and El-Salakawy 2017).

4.4. Interaction Diagrams

Three different methods were used to develop theoretical interaction diagrams of GFRP-columns: layered section analysis; CSA S6-19 (CSA 2019d) and modified CSA S806-12 (CSA 2017) provisions; and modified ACI 440.1R-15 guidelines (ACI 2015). The experimental data of another study with similar specimen dimensions, reinforcement properties and spiral pitches tested under axial and eccentric loading was also used to construct the experimental interaction diagram (Barua and El-Salakawy 2020).

The layered section analysis was performed in a similar manner to Tavassoli (2013) and Elchalakani et al. (2020). In this method, the column cross-section was divided into a finite number of segments with a depth of 5 mm each (Figure 4.14). The axial load and moment capacities, just before cover spalling, were obtained along the diagram by setting the strain at the extreme compression fiber, ε_{top}, to be –3,500 με as per CSA S806-12 (CSA 2017) and changing the strain in the outermost GFRP in tension, ε_{bot}, between –3,500 με and the rupture strain of 26,000 με. The positive and negative signs indicated tensile and compressive strains, respectively. After a preliminary analysis, it was found that the model proposed by Desayi and Krishnan (1964) underestimated the unconfined concrete stresses (Figure 4.15a). Therefore, it was decided to use the modified Desayi and Krishnan model introduced by Elchalakani et al. (2020) to establish the stress-strain relationship for unconfined concrete. On the other hand, the stress-strain relationship for confined concrete was developed using Sankholkar et al. (2018) model. This model was selected as it yielded moderately conservative results at all loading stages (Figure 4.15b) compared with the confinement models of Kappos and Konstantinidis (1999), recommended by Elchalakani et al. (2018) and Elchalakani et al. (2020), and Hales et al. (2017). Concrete tensile strength was neglected, whereas the compressive strength of GFRP bars was considered with a maximum strain of 0.002 as recommended by CSA S6-19 (CSA 2019d) or as half its tensile strength (Tobbi et al. 2014; Tavassoli et al. 2015; Hadhood et al. 2017; Elchalakani et al. 2020). A linear-elastic behavior was considered for GFRP in tension and compression with the same modulus of elasticity. The strains were calculated at the centroid of each segment from strain compatibility. The stresses in concrete were computed at each strain value according to the stress-strain model assigned to each

type of concrete (i.e., confined and unconfined). The effectively confined core was identified as per the confinement model used. The axial load and moment capacities were obtained by summing up the forces of each element and moments of these forces about the centroid of the column cross-section, respectively. The aforementioned analysis is summarized in Figure 4.14.

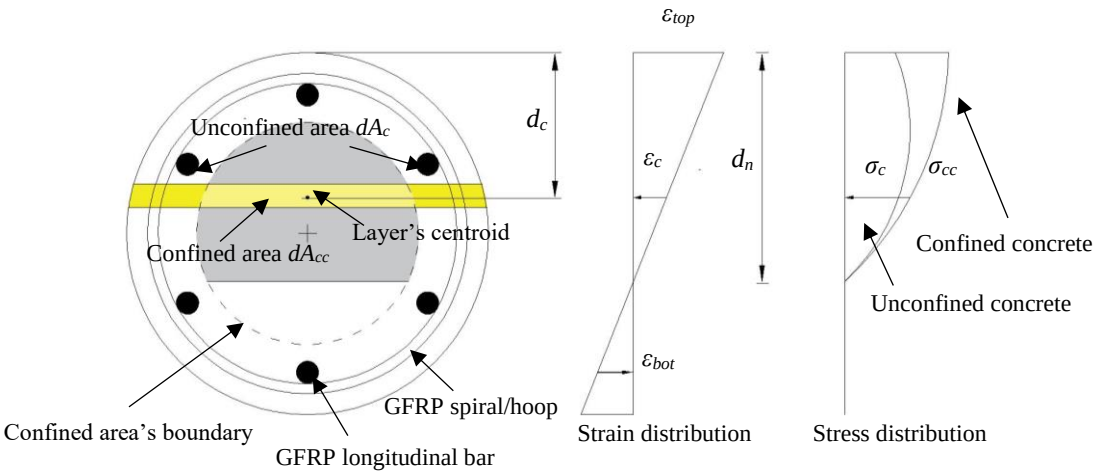

Figure 4.14: Layered sectional analysis to develop theoretical interaction diagram

Moreover, interaction diagrams were constructed by modifying the provisions of CSA S806-12 (CSA 2017) and ACI 440.1R-15 (ACI 2015). Two types of modifications were incorporated: the compressive strength of GFRP with a maximum strain of 0.002 (CSA 2019d) or as half its tensile strength; and the compressive strength of GFRP along with a modification factor, β_c, to concrete compressive strength. This factor, β_c, was introduced by Elchalakani et al. (2020) to be used as an extra multiplier for concrete strength for the tension-controlled region of the interaction diagram. This was conducted based on the assumption that the current rectangular stress block (RSB) factors considered in CSA S806-12 (CSA 2017), CSA S6-19 (CSA 2019d), and ACI 440.1R-15 (ACI 2015), namely, α_1 and β_1**,** were developed for rectangular and square cross-sections and not conservative enough for circular ones. The strain ε_{top} was taken as –3,500 με whereas ε_{bot} was changed between –3,500 με and 26,000 με for modified CSA S806-12 (CSA 2017) and CSA S6-19 provisions (CSA 2019d). On the other hand, the value –3,500 με was replaced by –3,000 με for modified ACI 440.1R-15 provisions (ACI 2015). It should be noted that in Figure 4.16, S6 refers to CSA S6-19 (CSA 2019d), S806 refers to CSA S806-12 (CSA 2017), and ACI refers to ACI 440.1-15 (ACI 2015).

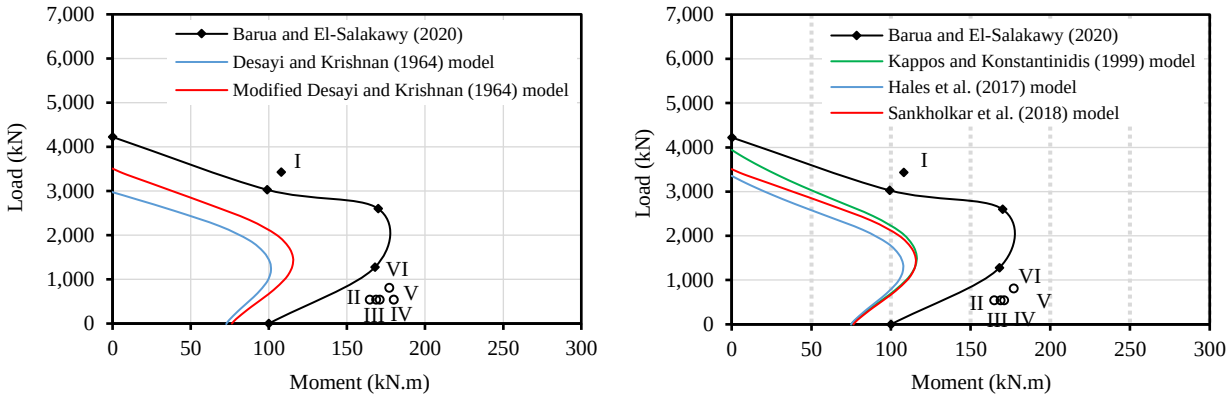

(a) Unconfined concrete (b) Confined concrete

I: Barua and El-Salakawy (2020) (s=50 mm, e=30 mm) II: G-0.2-85s-XX III: G-0.2-85h-60d_s

IV: G-0.2-85h-40d_s V: G-0.2-50s-XX VI: G-0.3-85s-XX

Figure 4.15: Preliminary analysis to evaluate stress-strain models

It was noticed that the value of β_c, calculated according to Elchalakani et al. (2020), ranged between 0.77 and 0.89 and from 0.87 to 0.99 for the modified CSA S806-12 (CSA 2017) and ACI 440-1R-15 (ACI 2015) calculations, respectively, when ε_{bot} ranged between 0 and 26,000 με. Conservative values of β_c equal to 0.77 and 0.87 were selected to construct the interaction diagrams using the modified CSA S806-12 (CSA 2017) and ACI 440.1R-15 (ACI 2015) provisions, respectively. The interaction diagrams developed using layered sectional analyses were reasonably conservative with respect to the experimental one at all loading conditions (Figure 4.16a). In addition, taking compressive strength of GFRP bars into account provided a better estimation of the column response. However, the results were very similar when the compressive strength of GFRP was considered as half its tensile strength and with a maximum compressive strain of 0.002, which indicated the effectiveness of such strain limit. Moreover, setting a compressive strain limit of 0.003 resulted in similar results to those when compressive strength equals to half the tensile strength for GFRP bars was set, depending on the method used for analysis. For instance, the predicted interaction diagram using a compressive strain limit of 0.003 and using half the tensile strength were close for layered analysis, CSA S806-12 (CSA 2017) and CSA S6-19 (CSA 2019d) provisions. On the other hand, such predictions were identical when the provisions of ACI 440-1R-15 (ACI 2015) were used.

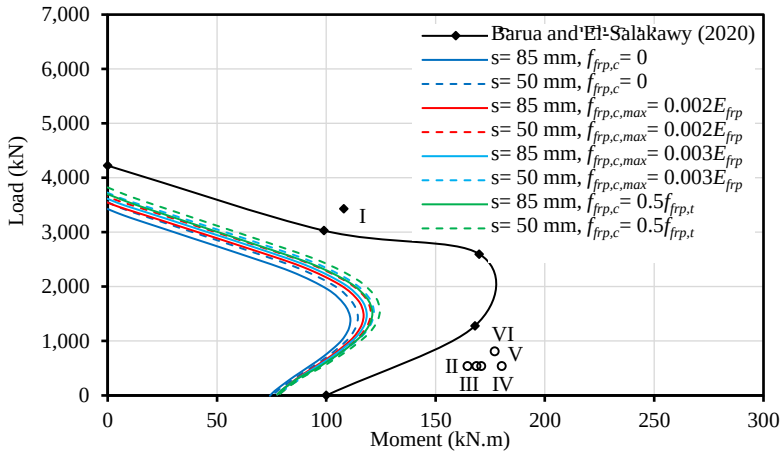

(a) layered sectional analysis

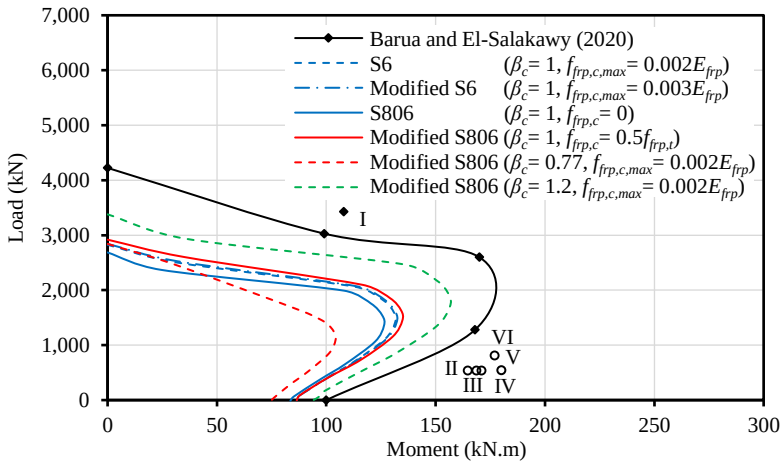

(b) CSA S806-12 and CSA S6-19 (CSA 2017; CSA 2019d)

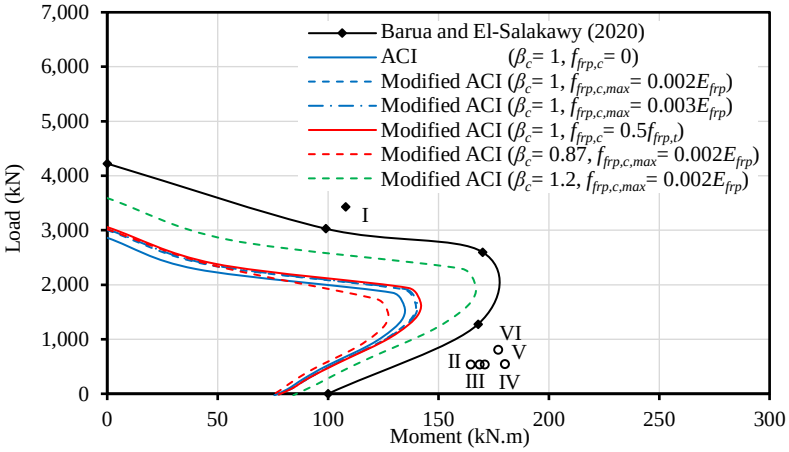

(c) ACI 440.1R-15 (ACI 2015)

I: Barua and El-Salakawy (2020)

(*s*=50 mm, *e*=30 mm)

II: G-0.2-85s-XX

III: G-0.2-85h-60d_s

IV: G-0.2-85h-40d_s

V: G-0.2-50s-XX

VI: G-0.3-85s-XX

Figure 4.16: Experimental versus theoretical interaction diagrams

This could be attributed to the higher maximum usable strain of concrete (3,500 με) considered for the Canadian codes' provisions (CSA 2017, 2019d). The used confinement model was able to reflect the effect of spiral pitch at low eccentricities, which could not be attained using the Kappos and Konstantinidis (1999) model, and its minimal effect at higher eccentricities. Yet, these predictions were very conservative compared with the experimental results, especially around the inflection point of the diagram. This may be attributed to the fact that the applied stress-strain models were meant for axially loaded columns and not eccentricity-based.

As shown in Figures 4.16 *(*b and c), the interaction diagrams developed using the unmodified CSA S806-12 (CSA 2017) and ACI 440.1R-15 (ACI 2015) predictions were very conservative with respect to the experimental results. Therefore, the modified CSA S806-12 (CSA 2017) and ACI 440.1R-15 (ACI 2015) predictions including factor β_c were too conservative. Better results were obtained by setting β_c as 1.0 and considering the compressive strength of GFRP bars. Again, similar predictions were obtained by setting a compressive strain limit of 0.002 (CSA 2019d) or 0.003, and considering the compressive strength of GFRP as half its tensile strength. Furthermore, applying a value of β_c equals to 1.2 for all loading conditions improved the accuracy of the developed interaction diagrams. This contradicts the findings of Elchalakani et al. (2020), which may be due to the difference in size of specimens, number of longitudinal GFRP bars, and mechanical properties of GFRP bars and spirals. In general, the predictions by modified code provisions were more accurate compared with layered sectional analysis results.

4.5. Conclusions

Based on the experimental observations and analytical results, the following conclusions can be drawn:

1. The circular GFRP-RC column exhibited similar lateral load capacity to its steel-RC counterpart. However, the GFRP-RC column showed a more stable hysteretic response with higher drift capacity. Despite the GFRP-RC column dissipated approximately half the energy dissipated by its steel-RC counterpart, this was deemed satisfactory.
2. The requirement of the Canadian code CSA S806-12 (CSA 2017) for maximum spiral pitch to be one-sixth the effective core diameter was found to be very conservative. On the other hand, the limit for maximum spiral pitch as one-fourth the column's gross diameter was more reasonable. In this study, decreasing the spiral pitch from one-fourth the gross diameter of

the column to one-sixth the effective core diameter increased the lateral load capacity and drift capacity by 10% and 25% only, respectively. Moreover, the effect of spiral pitch on other behavioral aspects was insignificant.

3. The Canadian highway bridge design code CSA S6-19 (CSA 2019d) specifies a minimum lap splice length for GFRP circular hoops equal to 40 times its nominal cross-sectional diameter. However, the above mentioned lap splice length was insufficient to provide similar confinement to that of GFRP spirals for the GFRP-RC column through all stages of simulated seismic loading. Instead, the results of this study recommend increasing this minimum lap splice length to be 60 times the nominal cross-sectional diameter of GFRP hoops. The hoops with such splice length were capable of providing similar strength and deformability to those provided by GFRP spirals.

4. Increasing the axial load level provided early strength gain with slight increase of lateral load capacity. Nevertheless, this came at the expense of rapidly deteriorating concrete core and less deformability and drift capacity. For example, increasing the axial load level from 20% to 30% the nominal axial capacity resulted in increasing the lateral load capacity by only 7% but the drift capacity was decreased by 39%. Furthermore, the reduction in lateral load resistance due to P-Δ effect increased by approximately 35%.

5. The currently available codes and guidelines for FRP-RC structures may require another modification factor, β_c, for concrete strength in the rectangular stress block. However, this factor needs to be more than or equal to unity. Previous research that suggested values β_c less than 1.0, which can be attributed to incorporating GFRP bars with less strength and strain capacities than those used in this study.

6. Considering the compressive strength of GFRP longitudinal bars in columns with a compressive strain limit of 0.002 according to CSA S6-19 (CSA 2019d) improved the accuracy of theoretically developed axial load-bending moment interaction diagrams. In addition, the predicted diagrams were sufficiently conservative against experimental results.

7. Layered sectional analysis resulted in a reasonably conservative pure axial load and moment capacities, whereas it yielded very conservative predictions for eccentric loading conditions in between. This may be attributed to the fact that all available confinement models to date for FRP-RC columns are not eccentricity-based.

CHAPTER 5: SEISMIC BEHAVIOR OF HIGH-STRENGTH CONCRETE CIRCULAR COLUMNS REINFORCED WITH GLASS FIBER-REINFORCED POLYMER BARS

Authors' Affiliations and Roles:

- **Amr E. Abdallah**, PhD Candidate, Department of Civil Engineering, University of Manitoba.
  Role: Methodology, Investigation, Formal analysis, Validation, Visualization and Writing-Original Draft.

- **Ehab F. El-Salakawy**, Professor of Civil Engineering, Department of Civil Engineering, University of Manitoba.
  Role: Conceptualization, Methodology, Writing-Review & Editing, Supervision, Project administration, Resources and Funding acquisition.

Journal and Status:

American Concrete Institute (ACI) Structural Journal, published in September/October 2021 issue.

Reference:

Abdallah, A. E., and El-Salakawy, E. F. 2021. "Seismic behavior of high-strength concrete circular columns reinforced with glass fiber-reinforced polymer bars." *ACI Struct. J.*, 118 (5): 221-234, https://doi.org/10.14359/51732831.

Note:

The manuscript had been slightly altered from the original paper by renumbering the tables and figures to include the chapter number. In addition, the reference list has been moved to the appropriate sections in the thesis as indicated in the table of contents.

Abstract

The linear elastic behavior of fiber-reinforced polymer (FRP) reinforcement makes it controversial to implement in seismic-resistant reinforced concrete (RC) structures. More concerns could be raised when such reinforcement is associated with high-strength concrete (HSC). Columns in multi-story buildings or bridges are common examples of structural members constructed using HSC. To date, all available research data on glass FRP (GFRP)-RC columns have shown that they have a maximum limit of concrete compressive strength equal to approximately 55 MPa. The results of five full-scale column-footing specimens are presented to study the seismic response of GFRP-RC columns, highlighting the effect of concrete compressive strength alongside other factors such as spiral pitch and axial load. It is concluded that when properly confined, GFRP-reinforced HSC circular columns can exhibit a stable seismic response with sufficient deformability. Moreover, several confinement and performance indexes were adjusted and evaluated to introduce an informative relationship for the design of GFRP-RC columns.

Keywords: Axial load level; circular columns; confinement index; glass fiber-reinforced polymer (GFRP); high-strength concrete (HSC); performance index; seismic loading; spiral pitch

5.1. Introduction

For several decades, high-strength concrete (HSC) has been increasingly widespread, especially in compression members of reinforced concrete (RC) high-rise buildings and long-span bridges, due to its favorable properties. These attractive aspects include, but are not limited to, superior compressive strength, stiffness, and durability (ACI 2002; ACI 2010). While the latter, in particular, has promoted the use of HSC for RC structures in harsh environments, the exposure to such aggressive agents stimulates corrosion of typically used steel reinforcement, impairing the durability of the whole structure. Fortunately, fiber-reinforced polymer (FRP) reinforcement has been established as a viable alternative to steel, eliminating the corrosion-related issues. Moreover, glass FRP (GFRP) has the advantages of relatively low cost and acceptable strain capacity compared with other FRP types. GFRP behaves in a linear-elastic manner up to failure, with a relatively low elastic modulus and without any yielding plateau. Such behavior has cast many concerns regarding the adequacy of GFRP reinforcement for earthquake-resistant structures—that is, the main source of seismic energy dissipation for an RC structure would be the inelastic deformations experienced by its structural components. Recent studies, however, have verified the suitability of GFRP reinforcement for columns, beam-column joints, and flat plates in seismic-active zones (Tavassoli et al. 2015; Ali and El-Salakawy 2016; Naqvi and El-Salakawy 2017; Elshamandy et al. 2018; Hasaballa and El-Salakawy 2018; Ghomi and El-Salakawy 2019; El-Gendy and El-Salakawy 2020). Well-confined GFRP-RC columns exhibited stable hysteretic responses and were marginally affected by GFRP surface texture or the size of transverse reinforcement reinforcement (Tavassoli et al. 2015; Ali and El-Salakawy 2016). Despite the lack of ductility in such columns, their different design philosophy introduced deformability as compensatory for ductility in steel-RC columns under various axial load levels (Ali and El-Salakawy 2016; Naqvi and El-Salakawy 2017; Elshamandy et al. 2018). Moreover, an innovative dual-hybrid earthquake-resisting structural system was proposed by Hasaballa and El-Salakawy (2018) and Ghomi and El-Salakawy (2019), incorporating GFRP-RC moment-resisting frames (MRFs) alongside shear walls. Consequently, the energy absorption capability of the structure would be boosted because of the presence of shear walls. Furthermore, the noncorrodible nature of GFRP would minimize the maintenance costs that are typically required to alleviate corrosion-induced damages. The high elasticity of GFRP would result in more sustainable structures that would require less post-earthquake maintenance expenses, unlike steel-RC structures, which need

high repair budgets or total replacement following a seismic event due to steel yielding. Additionally, GFRP reinforcement was more beneficial than steel in regard to member deformability, measured in terms of the drift ratio and displacement ductility parameter, for RC columns in earthquake-prone zones (Kharal and Sheikh 2020). However, GFRP reinforcement had a negative impact on the moment and shear capacities of such columns.

All the aforementioned studies used concrete compressive strengths of 55 MPa or less, leaving the seismic response and energy-dissipating efficiency of GFRP questionable when incorporated with the well-known brittle behavior of HSC. Few studies concerning axially and eccentrically loaded GFRP-reinforced HSC are available (Hadhood et al. 2017; Hadi et al. 2017; Hasan et al. 2017; Hasan et al. 2019). Generally, eccentrically loaded GFRP-reinforced HSC columns were more affected by increasing the longitudinal reinforcement ratio, but less influenced by the transverse reinforcement ratio, while the opposite was true for axially loaded ones (Hadhood et al. 2017; Hadi et al. 2017). In addition, the higher the concrete strength, the higher the load and moment capacities would be (Hadhood et al. 2017; Hadi et al. 2017; Hasan et al. 2017), although this augmentation would occur to the detriment of deformability. Furthermore, normal-strength concrete (NSC) columns benefited from decreasing the spiral pitch more than their HSC counterparts (Hasan et al. 2019).

Some available codes and guidelines indirectly dissuade the use of FRP as main reinforcement for compression members (ACI 2015) or neglect its allowance of load capacity (CSA 2017). However, the Canadian Highway Bridge Design Code CSA S6-19 (CSA 2019d) recognizes FRP as main reinforcement and its contribution to load capacity in compression members with a compressive strain upper bound of 2,000 με. The scarcity of experimental data on GFRP-RC columns, especially with HSC and those under seismic loading, could be the reason for such stringent provisions. The Canadian standard CSA S806-12 (CSA 2017), for instance, restricts the spiral pitch to a maximum of one-sixth the core diameter of the column, and it curbs the concrete compressive strength for confinement reinforcement design to 80 MPa. Alternatively, the CSA S6-19 (CSA 2019d) limits the clear spacing of FRP spirals between 25 and 75 mm.

This paper is affiliated with a broader ongoing research program dedicated to the seismic behavior of circular GFRP-RC columns. Investigating the behavior of GFRP-reinforced HSC columns under different axial load levels, and the synergistic effect of concrete strength and spiral pitch are among the main goals of the current study. The current provisions of the available codes were also

evaluated based upon the outcomes of the experimental work. Previously introduced confinement and performance indexes were adjusted and evaluated for GFRP-RC columns to establish reliable relationships for design purposes.

5.2. Research Significance

The current provision for the design of confinement reinforcement in GFRP-RC columns (CSA 2017) is based on an empirical approach developed for steel reinforcement (Saatcioglu and Razvi 2002). The coefficients of the aforementioned approach were based upon data of steel-RC columns under seismic loading, mostly constructed using NSC. The design approach was then extended to steel-reinforced HSC columns through a parametric study. Thus, experimental data on GFRP-reinforced HSC columns is necessary to evaluate the available code provisions. The pioneer experimental program presented herein gives fundamental insights into the seismic behavior of GFRP-reinforced HSC columns, focusing on their confinement behavior and corresponding deformability.

5.3. Description of Specimens and Test Program

5.3.1. Test specimens

Five full-scale column specimens were constructed and tested to investigate the effect of concrete strength on GFRP-RC circular columns under simultaneous axial and reversible cyclic lateral loading. A rigid 1,400 × 900 × 600 mm steel-RC footing was designed for each column to provide it with sufficient fixity. The footings were adequately reinforced with 15M (16 mm diameter) steel bars to withstand cyclic load reversals without significant cracking. Each specimen resembled the bottom-most portion of a column between the foundation level and the assumed point of contra-flexure. That was equivalent to the lower portion of a bridge pier column bent in double-curvature, or a first-story column in a multi-story MRF structure, with a 350-mm column diameter and a clear column height of 3500 mm. Hence, the shear span of the extracted column (that is, the distance between the top surface of the footing and the line of action of the lateral load) was 1750 mm, which stimulated a flexural type of failure. The GFRP-RC columns were designed in accordance with CSA S806-12 (CSA 2017), CSA S6-19 (CSA 2019d) and the recommendations of the related recent research studies, as appropriate. All columns were reinforced longitudinally and transversely, with No. 16 (15.9 mm diameter) and No. 10 (9.5 mm diameter) GFRP bars and

spirals, respectively. The spirals had an outer diameter of 310 mm, resulting in a clear concrete cover of 20 mm (0.79 in.). The spiral pitch varied between 85 and 50 mm, as per Clauses 12.7.3.4 and 8.4.3.13 of CSA S806-12 (CSA 2017), respectively. Two columns were constructed using NSC, whereas HSC was used to construct the other three specimens. The longitudinal bars of the columns were embedded into footings for the entire height of the latter. Footings were cast, and then the columns in a subsequent phase, in a similar sequence to common construction practice.

The specimens were labeled using two letters and two numbers. The first letter, G, refers to the GFRP reinforcement used in all the specimens; the second, N or H, indicates whether the specimen was constructed using NSC or HSC, respectively. The third is a number that identifies the axial load level as a ratio of the applied axial load, P, to the nominal unconfined axial capacity of the GFRP-RC column, P_o, while the last number represents the spiral pitch. For example, GH-0.2-85 was constructed using HSC, reinforced with a GFRP spiral at an 85 mm (3.35 in.) pitch, and tested under a constant axial load of $0.2P_o$. The concrete dimensions and reinforcement details of the test specimens are depicted in Figure 5.1a, while the properties of the specimens are listed in Table 5.1.

Table 5.1: Properties of test specimens

Specimen ID	Axial load level, P/P_o	Cracking load applied (kN)	Concrete strength, f_c' (MPa)	Spiral pitch (mm)
GN-0.2-85	0.2	25	36.9 $\pm$ 0.4	85
GN-0.2-50	0.2	25	36.0 $\pm$ 2.0	50
GH-0.2-85	0.2	62	86.4 $\pm$ 2.4	85
GH-0.2-50	0.2	62	89.4 $\pm$ 1.8	50
GH-0.1-50	0.1	29	87.3 $\pm$ 2.5	50

5.3.2. Materials

Ready mixed, normal-weight concrete was used with two different strengths: normal and high strength with a target 28-day compressive strength of 35 and 80 MPa, respectively. Tests on 100 × 200 mm standard concrete cylinders were carried out in accordance with CSA A23.1-19/A23.2-19 (CSA 2019a) to determine the actual concrete compressive strength for each column on testing day (Table 5.1). In addition, sand-coated GFRP size No. 16 bars (15.9 mm diameter) and size No. 10 spirals (9.5 mm diameter) were used to reinforce all the specimens longitudinally and

transversely, respectively. The physical and mechanical properties of the reinforcing bars and spirals are summarized in Table 5.2, based on laboratory testing (CSA 2017), or as listed in the compliance certificate provided by the manufacturer (Pultrall Inc. 2019), as appropriate.

5.3.3. Instrumentation

Figure 5.1a shows the locations of the strain gauges, which were 16 in total per specimen, along the outermost longitudinal bars and on the spiral within the expected hinging region. In addition, two pairs of linear variable displacement transducers (LVDTs) per specimen were mounted at the column hinging region against the extreme fibers (Figure 5.1b and c), each at an equal distance from the column face, to monitor the different aspects of column rotation (Ali and El-Salakawy 2016; Naqvi and El-Salakawy 2017). These included flexural rotations, rotations due to the main crack at the column-footing interface, and rotations due to other components, such as cracking outside the hinging region and shear deformation. A pair of LVDTs was mounted at approximately 25 mm above the column-footing interface to measure the rotation component due to flexure. Another pair was fixed at the interface to monitor the rotation component due to flexure and rigid-body rotation (i.e., bar slip). The difference between the total drift ratio of the column and the aforementioned rotation component was equal to the rotation attributed to the other components, as mentioned earlier.

Table 5.2: Mechanical properties of GFRP reinforcement

Bar type	Nominal diameter (mm)	Area (mm^2)	Modulus of elasticity (GPa)	Tensile strength (MPa)	Ultimate strain (%)
No. 16	15.9	197.9[a] (235)[b]	65.7[c]	1,711[d]	2.60[e]
No. 10 (Spirals)	9.5	71[a] (83)[b]	58.4[e]	1,376[d, e]	2.36[g]

[a] Nominal area as per CSA S807-19 (CSA 2019e).
[b] Measured area as per Annex A of CSA S806-12 (CSA 2017).
[c] Measured as per Annex C of CSA S806-12 (CSA 2017).
[d] Calculated using nominal area and average force as per Annex C of CSA S806-12 (CSA 2017).
[e] Based upon tests on straight bars of the same diameter and properties as per Annex C of CSA S806-12 (CSA 2017).

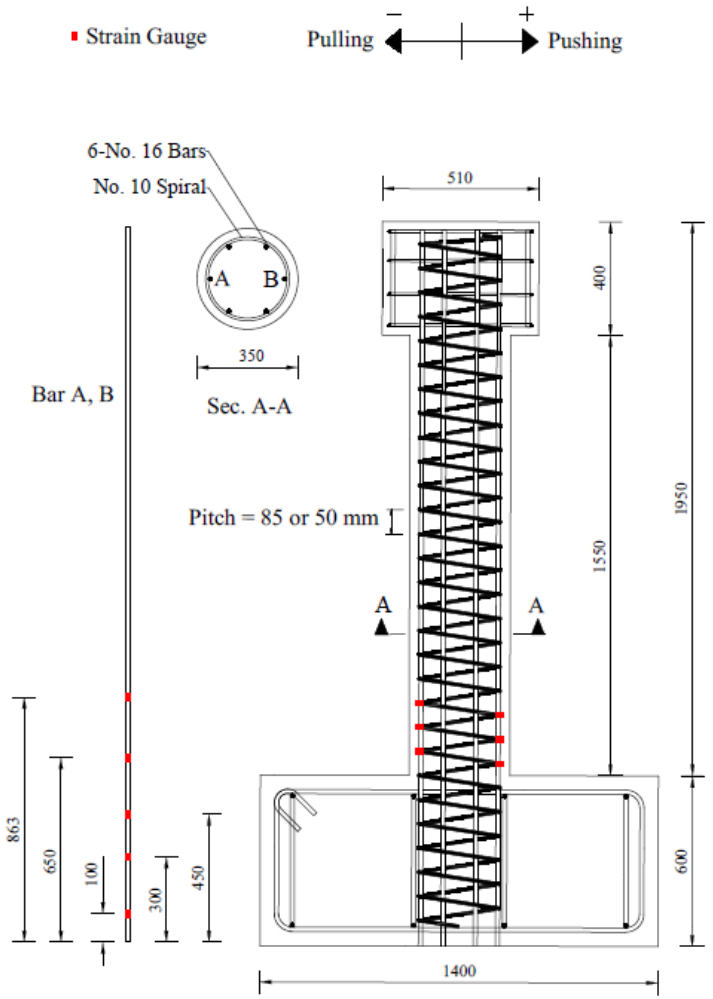

(a) Details of test specimens and strain gauges

(b) Test set-up

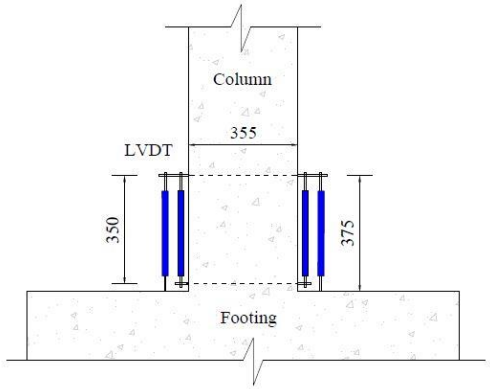

(c) Locations of LVDTs

Figure 5.1: Details of test specimens and test setup (all dimensions in mm)

5.3.4. Test setup and procedure

A horizontal, fully dynamic hydraulic actuator with ± 1,000 kN and ± 250 mm load and stroke capacities, respectively, was used to apply the reversed-cyclic lateral loading (Figure 5.1b). The lateral load and drift had a positive sign while pushing the column, and a negative sign when pulling it. A steel hinged-frame supported by two RC blocks was used to apply the constant axial load on the column through a 2,000 kN load capacity-hydraulic jack. The axial load was computed as a ratio of the nominal unconfined axial capacity, P_o, as per CSA S806-12 (CSA 2017):

$$P_o = \alpha_1 \phi_c f_c' \left(A_g - A_F \right) \quad \text{Equation 5.1}$$

where α_1 is the ratio of average stress in the rectangular compression block to the specified concrete strength, f_c'; ϕ_c is the material resistance factor for concrete (taken as unity); A_g is the gross cross-sectional area of the column; and A_F is the area of FRP main reinforcement.

The loading frame was pinned at both ends (i.e., the steel I-beam and the RC blocks) to allow movement with the horizontal drift of the column head while maintaining constant axial loading. Threaded, high-strength steel bars were inserted into the footing and RC blocks through premade holes to anchor the specimen and the steel frame to the laboratory strong floor.

The loading procedure began with applying the specified axial load. Then, lateral loading commenced by applying a load-controlled phase. This phase comprised of a cracking cycle prior to a service cycle, to identify the cracking load and simulate the column at service, respectively. The peak lateral load for the cracking cycle coincided with the first cracking of the concrete, whereas that of the service cycle developed a similar concrete compressive strain to that of its hypothetical steel-RC counterpart under its lateral service load, as per CSA A23.3-19 (CSA 2019b). Afterwards, a displacement-controlled phase was applied to simulate earthquake excitations in accordance with ACI 374.1-05 (ACI 2019b). Successive quasi-static lateral drift reversals were applied in several steps: three cycles each, at a 0.01 Hz frequency, to ensure stable crack propagation. Moreover, a load-controlled service cycle, with the same peak lateral load as the first service cycle, was undergone after each drift step beyond a 2% drift ratio to evaluate the stiffness degradation, if it existed (Ali and El-Salakawy 2016; Naqvi and El-Salakawy 2017; Hasaballa and El-Salakawy 2018; Ghomi and El-Salakawy 2019). The drift ratio is defined as the ratio between the lateral displacement of column head to the shear span of the column. The axial load was continuously monitored and promptly adjusted, as needed, to ensure a constant axial load

equal to the specified value. Tests were terminated after the lateral load capacity dropped by at least 25%.

5.4. Experimental Results and Discussion

5.4.1. General behavior and mode of failure

Figure 5.2 shows an example for the sequence of damage throughout the test. All test specimens experienced flexure failure, as shown in Figure 5.3. Concrete first cracking was observed for NSC specimens under a 25 kN lateral load, as listed in Table 5.3. In addition, concrete cover spalling was initiated for both GN-0.2-50 and GN-0.2-85 at a drift ratio of 3.0%. Furthermore, GN-0.2-50 and GN-0.2-85 failed at 12.75% and 10.20% drift ratios, with cover spalling regions extending approximately 500 and 525 mm above the column–footing interface, respectively. The failure of both specimens was characterized by a simultaneous crushing of the concrete core and compression failure of the outermost longitudinal bar. As expected, the first crack was noticed for HSC specimens GH-0.2-85 and GH-0.2-50 at a lateral load of 62 kN, while GH-0.1-50 experienced its first crack at a lateral load equal to 29 kN. The drift ratio of 2.00% marked the initiation of cover spalling for GH-0.2-85, whereas spalling started later at a drift ratio of 3.00% for GH-0.2-50 and GH-0.1-50. Specimen GH-0.2-85 failed at a 4.00% drift ratio in an explosive manner due to the crushing of the concrete core alongside spiral rupture. Nonetheless, no longitudinal bar failure was observed. Contrarily, GH-0.2-50 failed at a drift ratio of 10.20% by way of compression failure of four longitudinal bars, including the outermost ones, spiral rupture and devastation of the concrete core. Furthermore, spalling of the concrete cover stretched over a length of 650 and 420 mm for GH-0.2-85 and GH-0.2-50, respectively. The failure of GH-0.1-50 was comparable to that of GN-0.2-50, taking place at a 12.75% drift ratio with concurrent concrete core crushing and the outermost longitudinal bar failing in compression. However, the cover spalling region extended approximately 400 mm above the column-footing interface, which was significantly less than the inelastic deformability hinge length of GN-0.2-50. Notably, the lengths of the cover spalling regions of GH-0.1-50 and GH-0.2-50 were similar despite their different axial load levels, which contradicted Paultre et al. (2009) but concurred with Sheikh et al. (1994).

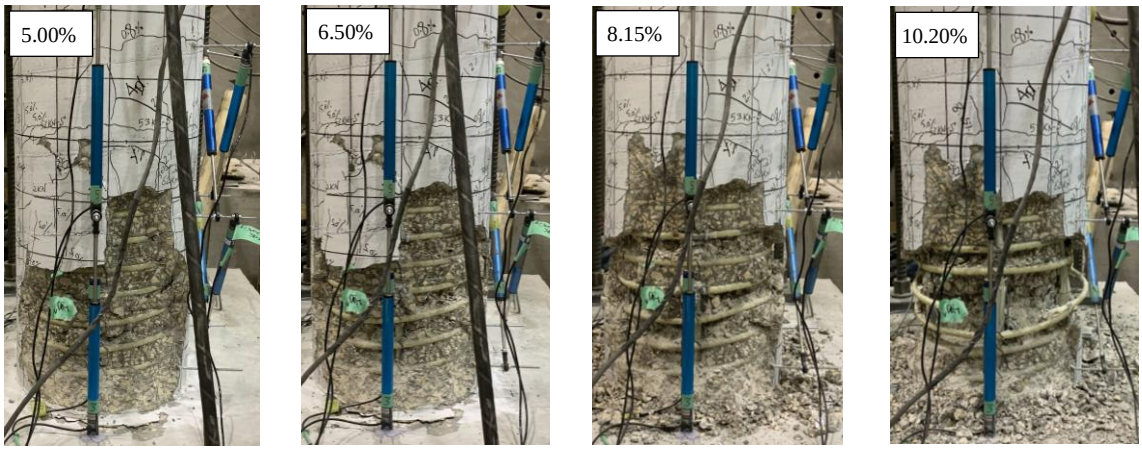

(a) Damaging sequence for specimen GH-0.2-50

(b) Close-up view for bar and spiral failure – specimen GH-0.2-50.

Figure 5.2: Typical damaging sequence for test specimens

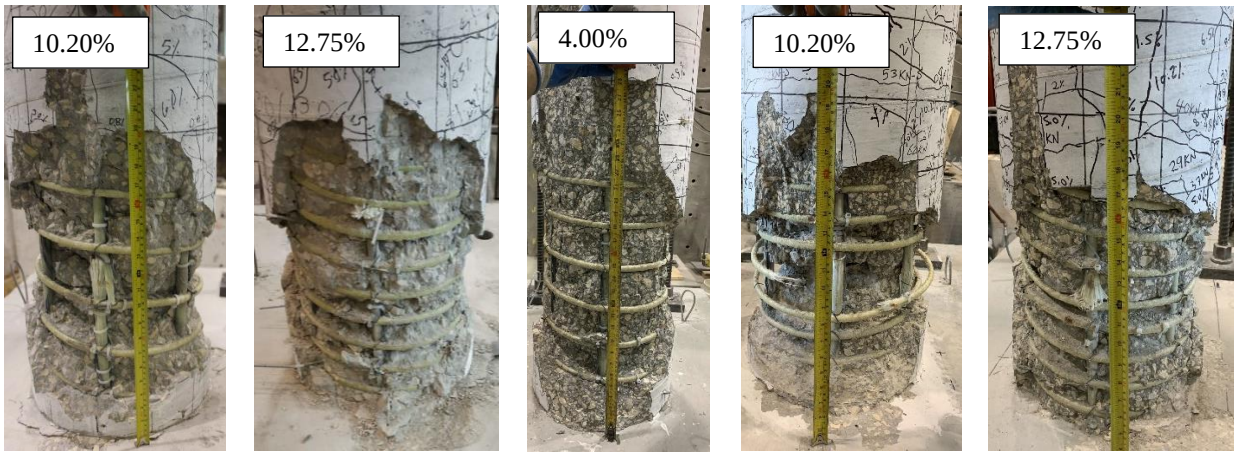

(a) GN-0.2-85 (b) GN-0.2-50 (c) GH-0.2-85 (d) GH-0.2-50 (e) GH-0.1-50

Figure 5.3: Test specimens at failure

5.4.2. Effect of spiral pitch

Figure 5.4 shows the envelopes of lateral load versus drift ratio relationships for all tested specimens. It was reported that decreased transverse reinforcement spacing in GFRP-RC columns considerably improved their strength and deformability (Tavassoli et al. 2015; Ali and El-Salakawy 2016; Naqvi and El-Salakawy 2017; Elshamandy et al. 2018). It was observed in this study, however, that decreasing the spiral pitch of NSC specimens from 85 to 50 mm resulted in only 10% and 25% increases in maximum lateral load and drift capacities, respectively. Table 5.3 includes the experimental peak and failure lateral loads and drifts alongside theoretically predicted capacities (CSA 2017). It should be noted that the applied axial load was considered for lateral load capacity predictions, yet there were large discrepancies between the calculated and the experimental values. This could be attributed to the fact that the theoretical lateral load capacities were estimated neglecting the contribution of longitudinal GFRP bars in the compression zone and the effect of the confined concrete core. All specimens exhibited narrow hysteresis loops with their unloading branch aiming towards the origin (Figure 5.5), which is typical for GFRP-RC specimens (Tavassoli et al. 2015; Ali and El-Salakawy 2016; Naqvi and El-Salakawy 2017; Elshamandy et al. 2018).

Table 5.3: Theoretical and experimental lateral load and drift capacities

Specimen ID	Theoretical capacity		Experimental lateral capacity		
	Lateral load (kN)	Drift [a] (%)	Maximum (kN)	At failure (kN)	Strength Degradation (%)
GN-0.2-85	54.0	5.20	94.1 at 4.00% drift -96.0 at -10.20% drift	58.8 at 10.20% drift	38.0
GN-0.2-50	54.0	9.10	103.3 at 8.15% drift -115.6 at -10.20% drift	94.0 at 12.50% drift	9.0
GH-0.2-85	98.0	2.20	145.3 at 2.00% drift -117 at -2.00% drift	115.0 at 4.00% drift	21.0
GH-0.2-50	98.0	3.70	146.5 at 4.00% drift -121.5 at -8.15% drift	108.0 at 8.75% drift	27.0
GH-0.1-50	80.0	7.50	111.1 at 6.50% drift -119.2 at -10.00% drift	97.0 at 12.35% drift	13.0

[a] Calculated as per Clause 12.7.3.3 of CSA S806-12 (CSA 2017).

Additionally, similar levels of cumulative energy dissipation are observed in Figure 5.6 for GN-0.2-85 and GN-0.2-50 throughout all loading steps. This could be attributed to the high elasticity of the GFRP longitudinal bars. The maximum longitudinal and spiral strains over the hinging region were plotted versus the drift ratio in Figures 5.7 and 5.8, respectively. Such relationships were also similar for GN-0.2-85 and GN-0.2-50. Even the spiral strain of GN-0.2-50 at a 4.00% drift ratio exceeded the 6,000 με limit of CSA S806-12 (CSA 2017), reaching a spiral strain of 6,820 με. This may indicate the conservativeness of such a strain limit, as these specimens exceeded it; yet, they survived the drift ratio limit for ductile MRFs (i.e., 4.00%).

The strain distribution along the embedded length of each outermost longitudinal bar was plotted using the maximum readings of five strain gauges, as demonstrated in Figure 5.9. The strain distributions indicated sufficient development length for all specimens. Moreover, similar strain profiles are observed for both GN-0.2-85 and GN-0.2-50 throughout the tests. As discussed earlier, two pairs of LVDTs were used to monitor the contribution of the different rotation components (i.e., flexural component, rotation due to main crack at interface, and other components) to the total drift ratio of the columns. Figure 5.10 shows the variation of the different rotation aspects with increasing drift ratio, where negligible changes were observed in the contributions of each rotation component beyond a 4.00% drift ratio for GN-0.2-85 and GN-0.2-50.

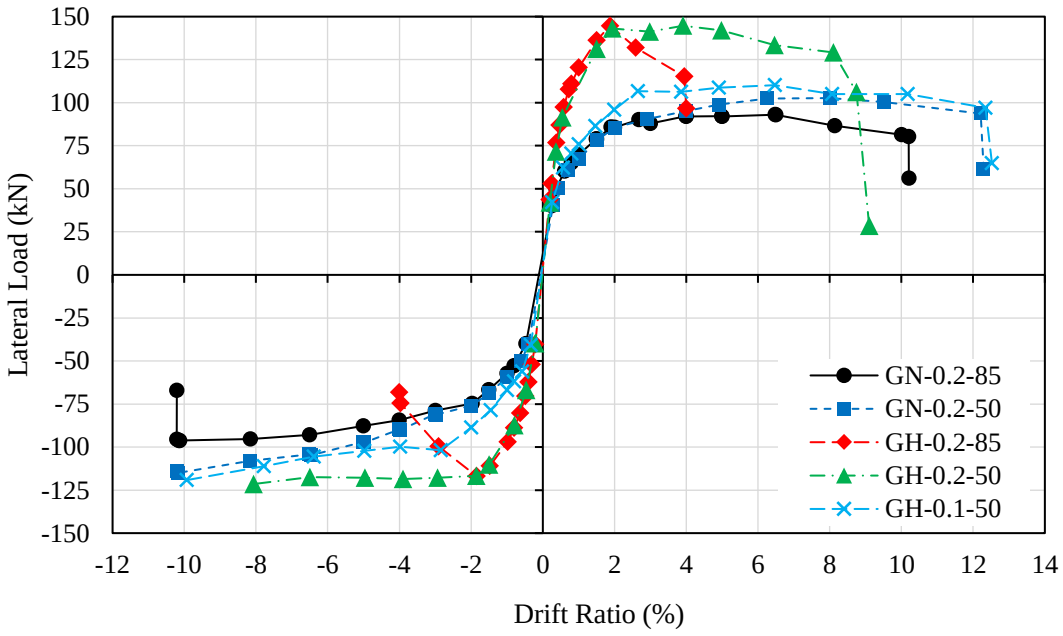

Figure 5.4: Envelopes of hysteresis diagrams for test specimens

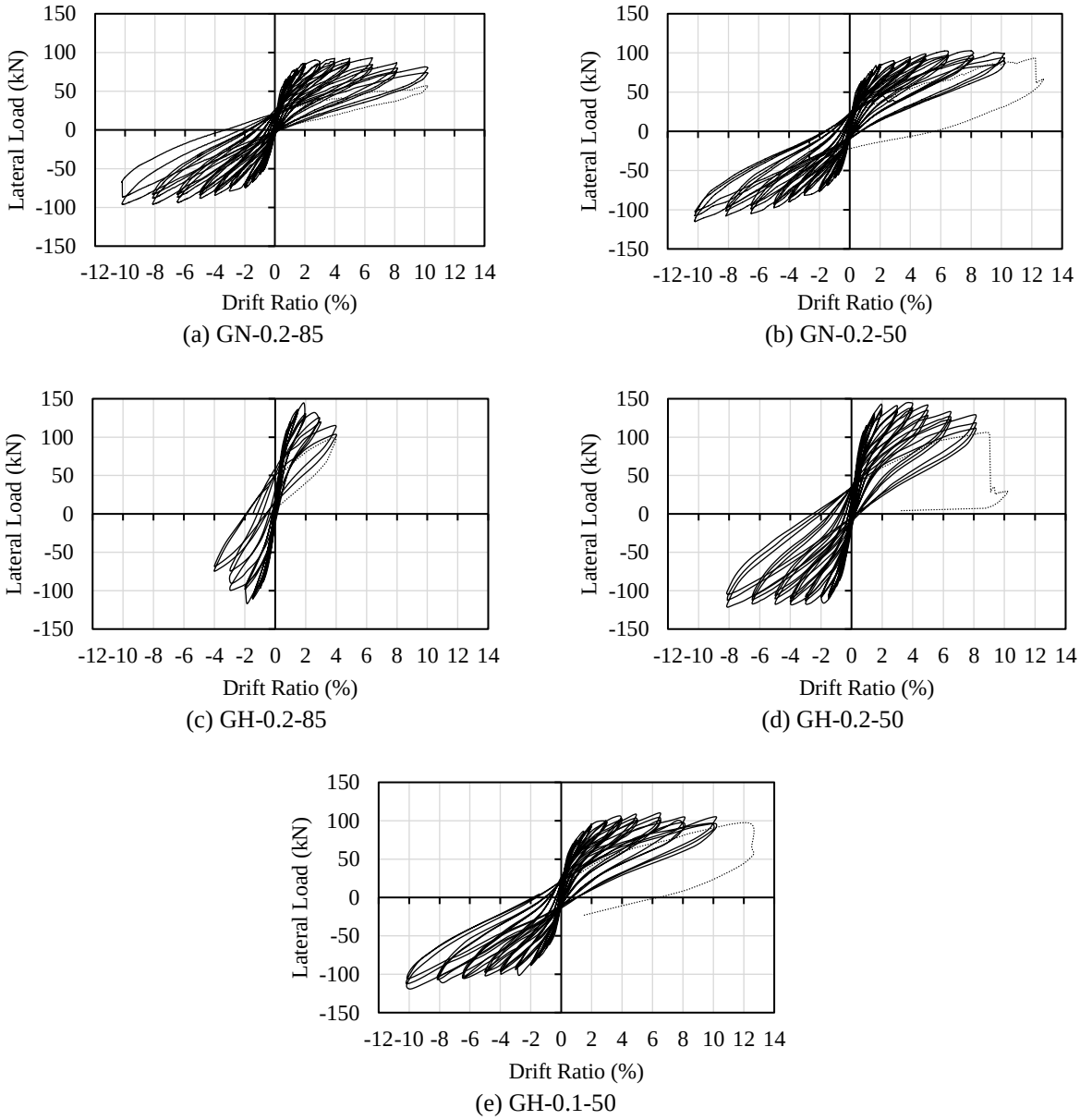

(a) GN-0.2-85 (b) GN-0.2-50

(c) GH-0.2-85 (d) GH-0.2-50

(e) GH-0.1-50

Figure 5.5: Hysteresis diagrams for test specimens

Decreasing the spiral pitch from 85 to 50 mm in the HSC specimens hardly affected the lateral load capacity but significantly increased the drift capacity by 172%, as shown in Figure 5.4. Notably, the cumulative energy dissipated by both GH-0.2-85 and GH-0.2-50 was similar through all stages of loading, until the failure of the former, as depicted in Figure 5.6. Similarly, both specimens exhibited similar maximum longitudinal strains up to a 3.00% drift ratio, and then the strain of GH-0.2-50 exceeded that of GH-0.2-85 (Figure 5.7). Furthermore, the contributions of

each rotation component were comparable for both specimens until the failure of GH-0.2-85 (Figure 5.10). On the other hand, GH-0.2-85 showed a remarkable increase in maximum spiral strains compared with GH-0.2-50 beyond a 1.50% drift ratio, reaching approximately 120% over that of GH-0.2-50 at a 4.00% drift ratio, as shown in Figure 5.8. Although GH-0.2-85 exhibited spiral rupture during a 4.00% drift ratio, the maximum recorded spiral strain was only approximately 54% of the spiral ultimate strain. This can be attributed to the fact that spiral rupture occurred above the instrumented region due to the unexpectedly large cover spalling region. Despite being too conservative for the NSC columns, the aforementioned results corroborated the necessity of a spiral pitch limit of one-sixth the core diameter of the column, as per Clause 8.4.3.13 of CSA S806-12 (CSA 2017) for GFRP-reinforced HSC columns in ductile MRFs, to guarantee a satisfactory level of deformability.

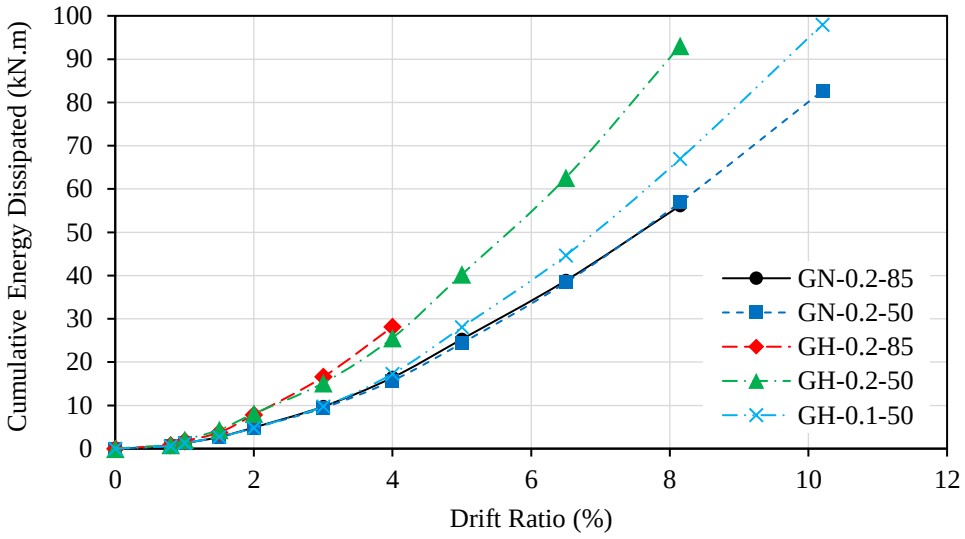

Figure 5.6: Cumulative energy dissipated by test specimens

5.4.3. Effect of concrete strength under the same axial load level

Previous studies on steel-RC columns reported earlier concrete cover spalling for HSC columns compared with their NSC counterparts (ACI 2002). The premature spalling of HSC was also observed by Hadi et al. (2017) in GFRP-reinforced HSC specimens. This was true for specimens with an 85 mm spiral pitch. On the other hand, the cover spalling started at the same drift ratio for both specimens with a spiral pitch of 50 mm. It was also observed that both GH-0.2-50 and GH-0.2-85 reached a maximum lateral load of approximately 146.5 and 145.3 kN, representing

approximately a 42% and 55% increase over those of GN-0.2-50 (103.3 kN) and GN-0.2-85 (94.1 kN), respectively (Figure 5.4). However, this came at the expense of drift capacity, which was decreased for GH-0.2-50 and GH-0.2-85 by 20% and 63%, respectively, compared with GN-0.2-50 and GN-0.2-85. In addition, the maximum lateral load was reached at 2.00% and 4.00% drifts for GH-0.2-85 and GH-0.2-50, respectively. The initial hysteretic responses of the HSC specimens were stiffer than their NSC equivalents. Generally, the lateral load resistance was greater in the pushing direction than in the pulling direction, which is typical under reversed-cyclic lateral loading, as loading usually starts by pushing (Hasaballa and El-Salakawy 2018). At the completion of each drift step, GH-0.2-50 and GH-0.2-85 had dissipated more energy than their NSC counterparts had, contrary to what was reported for steel-RC columns (Sheikh et al. 1994; Bayrak and Sheikh 1997; Paultre et al. 2009), as shown in Figure 5.6. This was expected, because at the same drift ratio, the HSC columns withstood much higher lateral load than the NSC counterparts did. At the 4.00% drift limit of CSA S806-12 (CSA 2017), GH-0.2-50 and GH-0.2-85 dissipated approximately 63% and 70% more energy than the respective NSC counterparts, respectively.

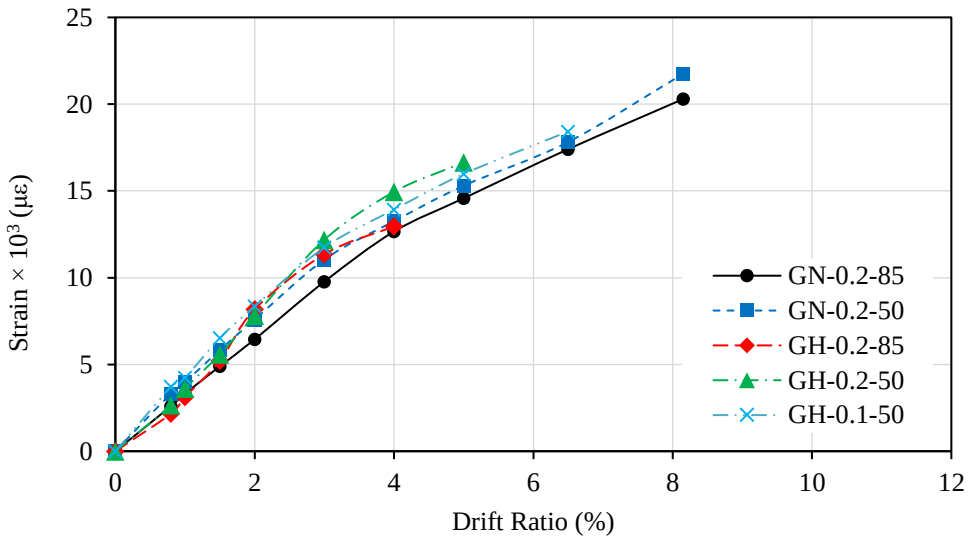

Figure 5.7: Maximum strain in outermost longitudinal bar at column hinging region versus drift ratio

As shown in Figure 5.7, each HSC specimen exhibited similar maximum longitudinal strains to its NSC equivalent. Specimen GH-0.2-50 showed similar spiral strains to GN-0.2-50 until a drift ratio of 4.00%, beyond which higher spiral strains were recorded for the HSC specimen (Figure 5.8). Moreover, the maximum spiral strain for GH-0.2-50 was 5,720 με at a 4.00% drift ratio, as opposed

to that of GN-0.2-50, which exceeded the CSA S806-12 (CSA 2017) limit of 6,000 με. Specimen GH-0.2-85 experienced similar spiral strains to GN-0.2-85 until a 1.50% drift ratio, followed by a spike for the HSC column.

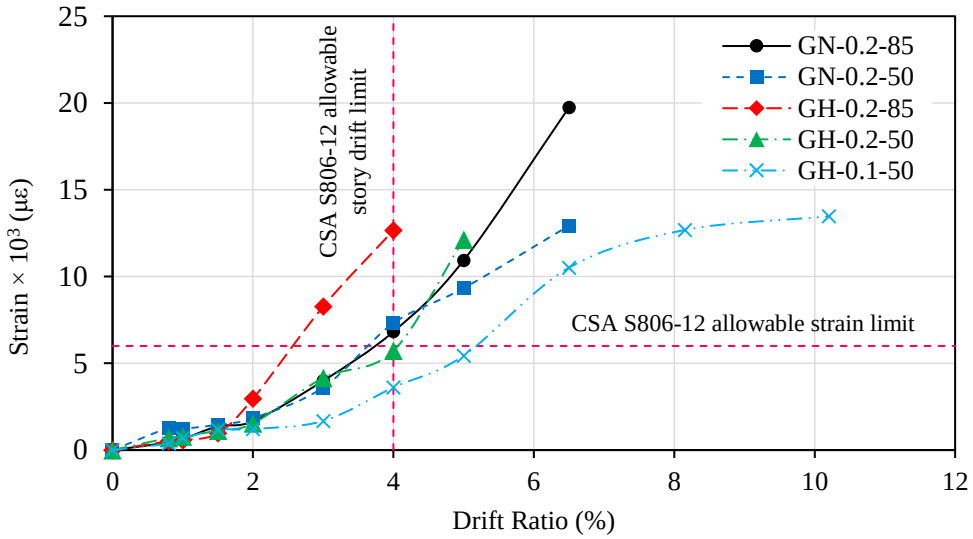

Figure 5.8: Maximum spiral strain versus drift ratio

The percentages of the rotation component associated with the inelastic deformability hinge were similar for both GH-0.2-50 and GN-0.2-50 up to a 2.00% drift ratio. After that, the aforementioned contribution for GH-0.2-50 rapidly surpassed that of GN-0.2-50, as depicted in Figure 5.10. On the other hand, GH-0.2-85 exhibited a larger contribution due to other components than GN-0.2-85, which may justify the larger length of the cover spalling region of the former. Moreover, the inelastic deformability hinge contribution of GH-0.2-85 increased over that of GN-0.2-85 beyond a 1.50% drift ratio. These results indicated a more stable response for the NSC columns compared with their HSC counterparts, which suggests that additional caution may be required when designing GFRP confining reinforcement for HSC columns.

5.4.4. Effect of concrete strength under similar axial loads

Specimens GN-0.2-50 and GH-0.1-50 were subjected to axial loads of 540 and 590 kN, respectively. Contrary to the steel-RC columns, the cover spalling commenced at the same drift ratio (3.00%) for NSC and HSC specimens. As expected, the initial stiffness of GH-0.1-50 was higher than that of GN-0.2-50 (Figure 5.4), and, GH-0.1-50 resisted higher lateral loads during the early stages of loading than GN-0.2-50 did, reaching a lateral load of 108.2 kN at a 3.00% drift

ratio, which was 20% higher than that reached by GN-0.2-50. Notably, GH-0.1-50 reached a maximum lateral load of 111.1 kN at a 6.50% drift ratio, which represented an increase of only 8% over that of GN-0.2-50 (103.3 kN). It was also observed that concrete cover spalling did not alter the lateral load resistance for either of the specimens. Additionally, both specimens had a drift capacity of 10.20%, which suggests that the use of HSC in GFRP-RC columns had an insignificant effect on their deformability and lateral load capacity, considering similar axial loads were applied. This, in turn, may prevent any further restrictions on the design of confinement reinforcement accounting for any unexpected increase of concrete compressive strength in practice.

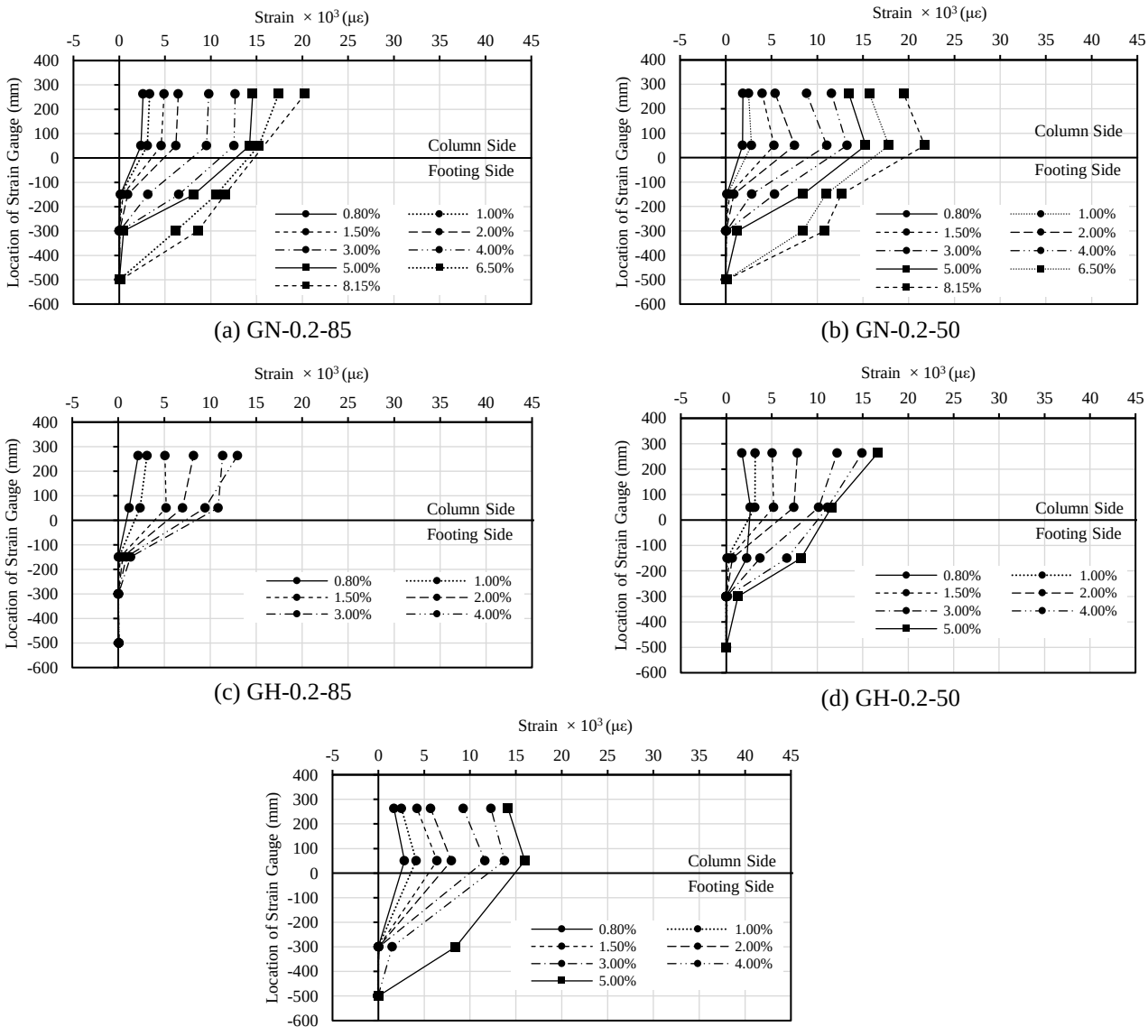

(a) GN-0.2-85

(b) GN-0.2-50

(c) GH-0.2-85

(d) GH-0.2-50

(e) GH-0.1-50

Figure 5.9: Strain profile in the outermost longitudinal bar

Both specimens exhibited a larger lateral load resistance on the pulling side beyond a 5.00% drift ratio. Similarities also existed for dissipated energy, maximum longitudinal strains, and rotation components of both specimens (Figure 5.6, 5.7 and 5.10). As shown in Figure 5.8, GN-0.2-50 exhibited higher spiral strains than those of GH-0.1-50 at all loading steps beyond a 2.00% drift ratio, showing a 102% increase at a 4.00% drift ratio. This was anticipated for HSC specimens, as increasing concrete strength is expected to produce less concrete core dilation under similar axial loads owing to its enhanced stiffness (ACI 2002; Hadi et al. 2017; Hasan et al. 2019).

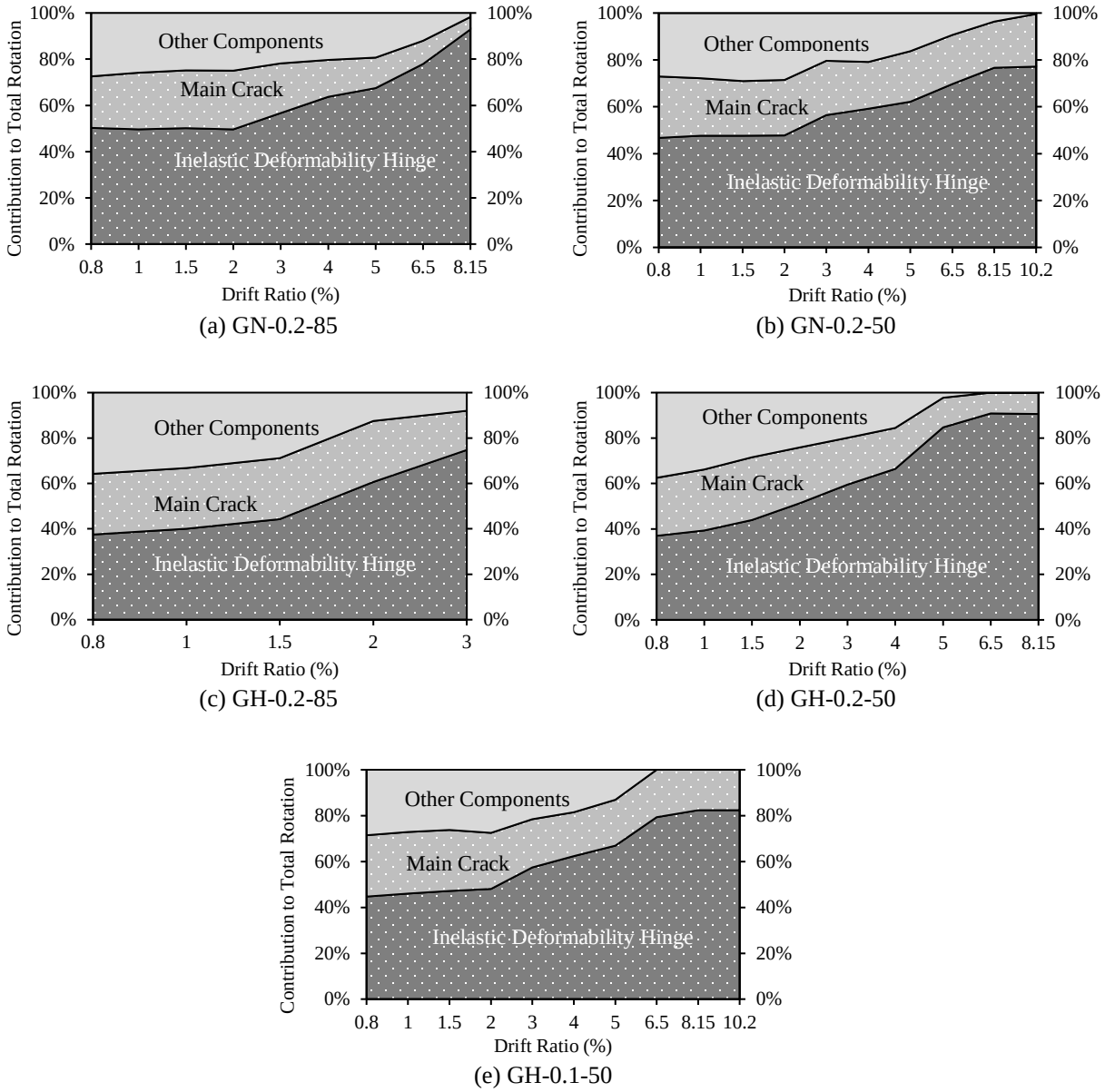

Figure 5.10: Percentages of contributions to the total drift angle of the column

5.4.5. Effect of axial load level

Specimens GH-0.1-50 and GH-0.2-50 reached their maximum lateral load capacities of 111.1 and 146.5 kN at 6.50% and 4.00% drift ratios, respectively, as shown in Figure 5.4. Additionally, GH-0.2-50 underwent significant strength degradation, starting at a drift ratio of 6.50%. In contrast, GH-0.1-50 exhibited a more stable hysteretic response with little or no strength degradation until a 10.20% drift ratio. Furthermore, increasing the axial load level from 0.1 to 0.2 resulted in an increase of 32% of the lateral load capacity, but decreased drift capacity by approximately 20%. Moreover, GH-0.2-50 consistently dissipated more energy throughout all cycles until failure when compared with GH-0.1-50 (Figure 5.6). This contradicted the comparable energy dissipation reported for steel- and GFRP-reinforced HSC and NSC columns, respectively, under different axial load levels (Sheikh et al. 1994; Bayrak and Sheikh 1997; Paultre et al. 2009; Tavassoli et al. 2015; Ali and El-Salakawy 2016). At the drift ratio limit of 4.00% (CSA 2017), GH-0.2-50 dissipated 48% more energy than GH-0.1-50.

The maximum longitudinal strains and the strain profiles of the outermost longitudinal bars of both specimens were almost identical during all loading steps, as shown in Figures 5.7 and 5.9, respectively. Furthermore, the maximum spiral strains of GH-0.2-50 were consistently approximately double those of GH-0.1-50 until a 3.00% drift ratio (Figure 5.8), which marked the onset of cover spalling. Then, as expected, the spiral strains in GH-0.2-50 rapidly increased, reaching a strain of 12,130 με at a 5.00% drift ratio, representing a 123% increase over the corresponding strain in GH-0.1-50, before strain gauge malfunctioned. Notably, the rotation component of the inelastic deformability hinge increased more rapidly for GH-0.2-50 than GH-0.1-50, as depicted by Figure 5.10, which indicated a more stable response for the HSC column under a lower axial load level.

5.5. Confinement versus Performance Indexes

An extensive analysis of test results was performed in order to establish a general relationship that relates the confinement provided to the specimen to its performance under seismic loading. In this study, some previously introduced confinement coefficients and indexes for steel-RC columns were refined to suit GFRP reinforcement. For instance, the coefficient *r* of Saatcioglu and Razvi (2002) was modified to be:

$$r_{FRP} = \frac{\rho_{sh} \cdot f_{Fh}}{f_c' [\frac{A_g}{A_c} - 1]}$$ Equation 5.2

where ρ_{sh} is the volumetric ratio of transverse reinforcement; f_{Fh} is the design stress level in FRP transverse confinement reinforcement (the least of 0.006 E_F or $\phi_F.f_{Fu}$, where E_F, ϕ_F, and f_{Fu} are the elastic modulus, material resistance factor, and ultimate strength for the FRP material, respectively), calculated in accordance with CSA S806-12 (CSA 2017), instead of the yield strength of steel transverse reinforcement, f_{yh}, used in the original equation (Saatcioglu and Razvi 2002); f_c' is the concrete compressive strength; and A_g and A_c are the gross and concrete core areas, respectively.

Similarly, the confinement index, I_c, recommended by Joint ACI-ASCE Committee 441 (ACI 2002) was modified as follows

$$I_{c,FRP} = \frac{\rho_{sh} \cdot f_{Fh}}{f_c'}$$ Equation 5.3

In addition, the variable $R_{A/P}$, introduced by Bayrak and Sheikh (1997) was refined to comply with the available design provisions for FRP-RC structures. As such, $A_{sh\ (ACI)}$ in the original formula was replaced by $A_{sh\ (CSA\ S806\text{-}12)}$, where the former and latter represented the amounts of confinement reinforcement required by ACI 318-89 (1989) and as per Clause 12.7.3.3 of CSA S806-12 (CSA 2017) for steel- and FRP-RC columns in active seismic zones, respectively.

$$R_{A/P,FRP} = \frac{A_{sh} / A_{sh\,(CSA\,S\,806-12)}}{P / P_o}$$ Equation 5.4

where A_{sh} is the total cross-sectional area of the actual confinement reinforcement provided.

Furthermore, due to the differences between the behavior of concrete confined with steel or GFRP, the effective confinement index, I_e, proposed by Cusson and Paultre (1995), was adjusted as follows:

$$I_{e,FRP} = \frac{f_{\ell e,FRP}}{f_c'}$$ Equation 5.5

where $f_{\ell e,FRP}$ is the effective confinement pressure, calculated as per Equation 5.6:

$$f_{\ell e,FRP} = \frac{K_e f_{Fhcc} A_{sh}}{sc} \quad \text{Equation 5.6}$$

where K_e is the confinement effectiveness coefficient; f_{Fhcc} was considered the maximum design stress of GFRP transverse reinforcement at the drift level of 4.00% (i.e., the same as f_{Fh} (CSA 2017)), in lieu of stress in the steel transverse reinforcement at the maximum confined concrete strength, f_{hcc}, associated with the unmodified expression; s is the transverse reinforcement center-to-center spacing; and c is the concrete core width or diameter.

The confinement indexes were computed for the specimens of this study along with GFRP-reinforced NSC circular columns from another study (Tavassoli et al. 2015). It should be noted that the axial load levels of the latter study were recalculated as per Equation 5.1 to be consistent with those tested in this study. The aforementioned indexes were compared with several performance parameters. The first performance indicator was the drift ratio, which is well-recognized by the displacement-based design philosophy of CSA S806-12 (CSA 2017). The so-called displacement ductility parameter, μ_Δ, defined as the ratio of ultimate to member-yield drifts, as depicted in Figure 5.11a (Tavassoli et al. 2015), was also calculated, as a clearer correlation was observed between the effective confinement index, I_e, and the displacement ductility parameter of steel-RC columns (Paultre et al. 2001). Another factor, μ, known as the displacement deformability factor, was introduced by Pan and Moehle (1989) for slab-column connections and later refined by El-Gendy and El-Salakawy (2020) for GFRP-RC flat-plate systems. This factor, defined as the ratio of ultimate to member-yield drift ratios (Figure 5.11b), was also computed for each specimen in the experimental database.

A number of integrated performance factors that depend on both forces and displacements were proposed, with one of the earliest attempts conducted by Jaeger et al. (1995). Due to the high uncertainty with the recorded values of curvature, especially near failure of specimens, the displacement ductility factor was used rather than the curvature-related one. Moreover, the moment and displacement corresponding to a 3,500 με concrete compressive strain at extreme fiber were used instead of at service for calculations of the deformability factor, $J_{0.0035}$, as recommended by Elshamandy et al. (2018). Deng et al. (2018) concluded that the integrated performance index, referred to herein as J_{Feng}, introduced by Mufti et al. (1996) and refined by Feng et al. (2005), could be used to evaluate the seismic performance of GFRP-RC columns under

simulated seismic loading. In this study, the integrated performance index was calculated once by considering the generalized force as the bending moment ($J_{Feng\text{-}M}$), and another time using lateral load ($J_{Feng\text{-}V}$). For both cases, the generalized deformation was taken as the lateral displacement. Due to limited information about concrete strains for the specimens of Tavassoli et al. (2015), the lateral loads, bending moments, and lateral displacements corresponding to concrete compressive strains of 1,000 and 3,500 με were taken as the values corresponding to the displacement Δ_e and concrete cover spalling, respectively. Figures 5.12 through 5.17 show the relationship between each confinement index and performance indexes for all specimens.

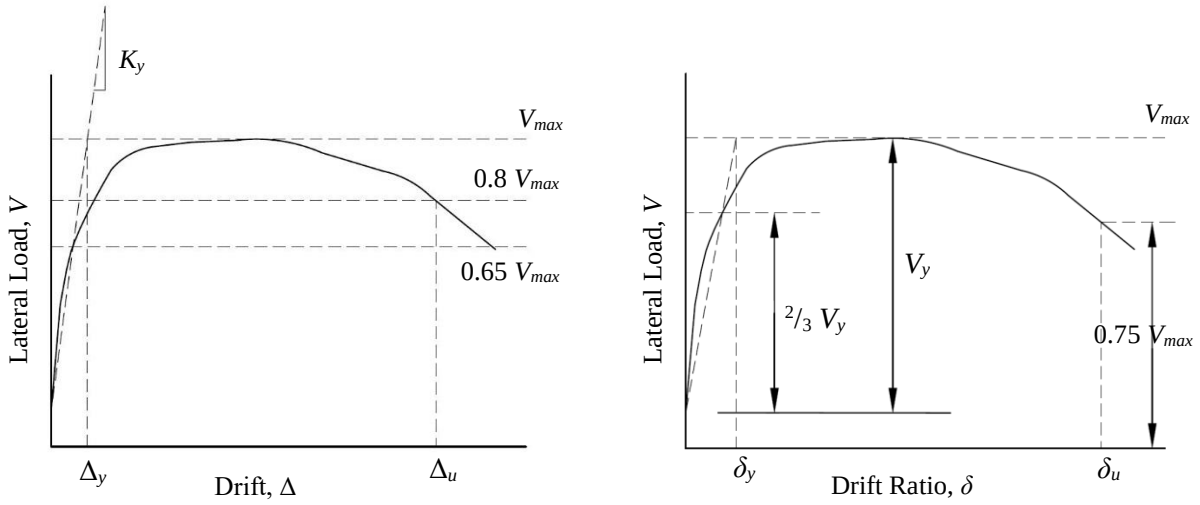

(a) Displacement ductility parameter (b) Deformability factor

Figure 5.11: Determination of displacement ductility parameter and deformability factor

The trend lines in Figures 5.12 through 5.17 show a correlation to some extent between the confinement indexes and the different performance indexes. In addition, the three confinement indexes, r_{FRP}, $I_{c,FRP}$, and $I_{e,FRP}$, showed similar scatter and captured well the effect of an increased axial load level, which decreased the effectiveness of increased confinement. The modified factor $R_{A/P,FRP}$ correlated well with the performance indexes of the specimens; that is, regardless of the concrete strength, an increase of $R_{A/P,FRP}$ corresponded to an increase in the performance factor. Better assessment for those relationships could be performed with tested specimens covering more values of $R_{A/P,FRP}$. Furthermore, it was observed that the relationships against the drift ratio showed less scatter compared with those against displacement ductility or deformability parameters, and substantially less scatter was generally observed for the relationships with the performance factors $J_{0.0035}$, $J_{Feng\text{-}M}$, and $J_{Feng\text{-}V}$. For the adjusted variable $R_{A/P,FRP}$, less scatter was noticed for the

relationships with the integrated performance factors $J_{Feng\text{-}M}$, and $J_{Feng\text{-}V}$. This may indicate the suitability of such performance factors to assess the seismic response of GFRP-RC columns. Further research is required to establish the acceptance criteria based on such indicators.

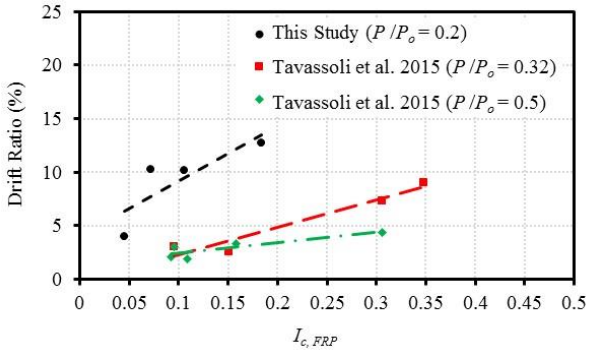

(a) Confinement index

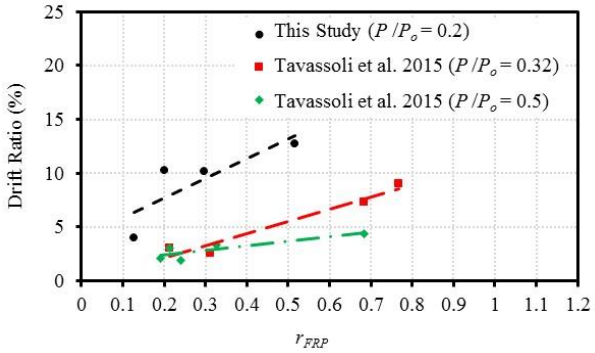

(b) r_{FRP} parameter

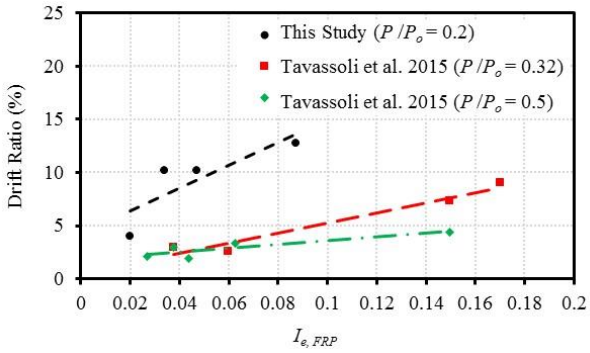

(c) Effective confinement index

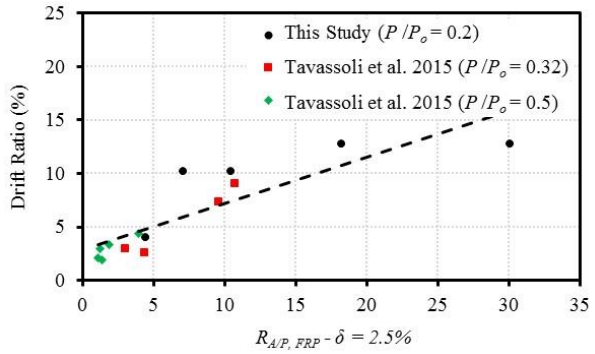

(d) $R_{A/P, FRP}$ at 2.5% drift

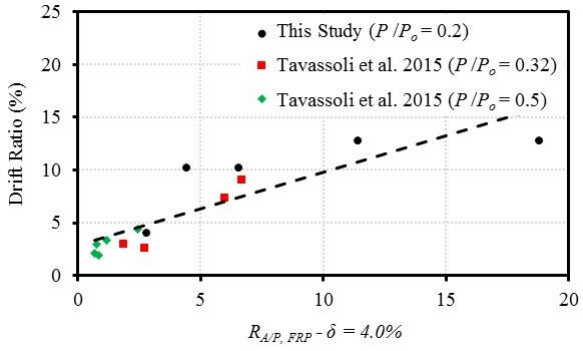

(e) $R_{A/P, FRP}$ at 4.0% drift

Figure 5.12: Relationships of different confinement indexes versus drift ratio

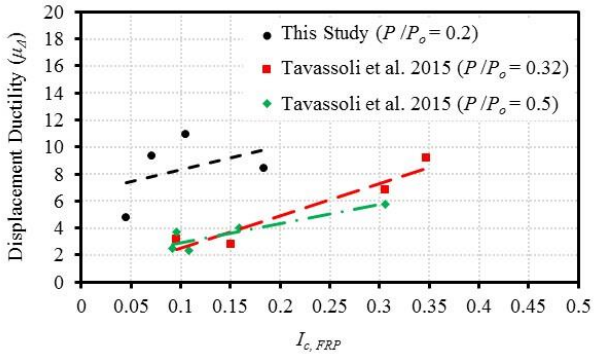

(a) Confinement index

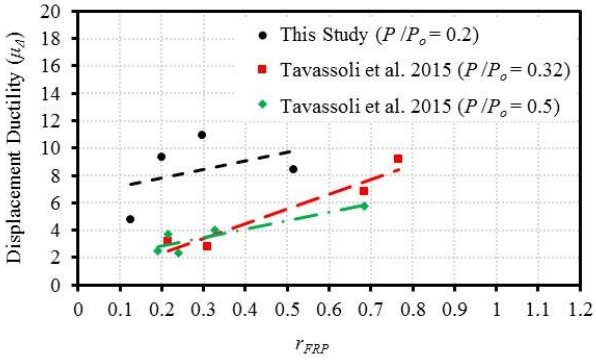

(b) r_{FRP} parameter

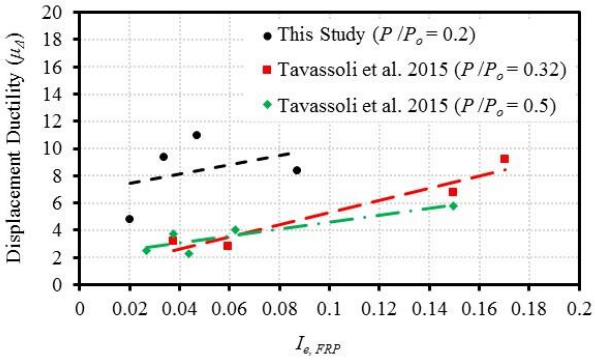

(c) Effective confinement index

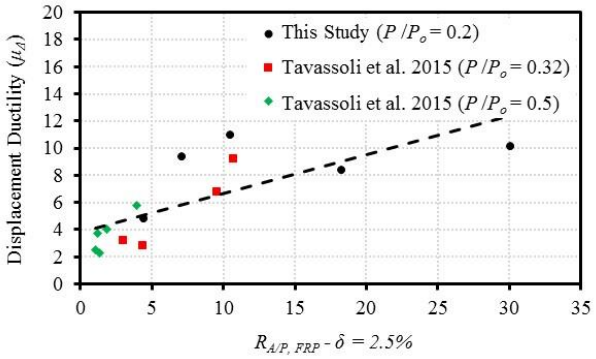

(d) $R_{A/P, FRP}$ at 2.5% drift

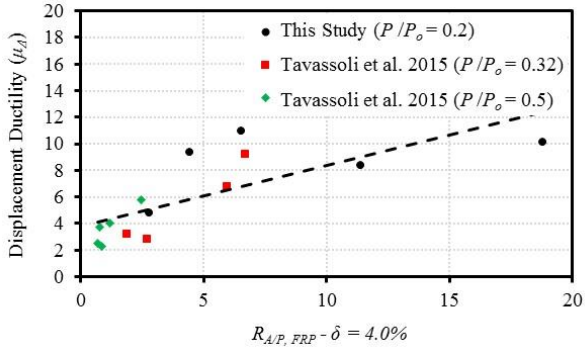

(e) $R_{A/P, FRP}$ at 4.0% drift

Figure 5.13: Relationships of different confinement indexes versus displacement ductility

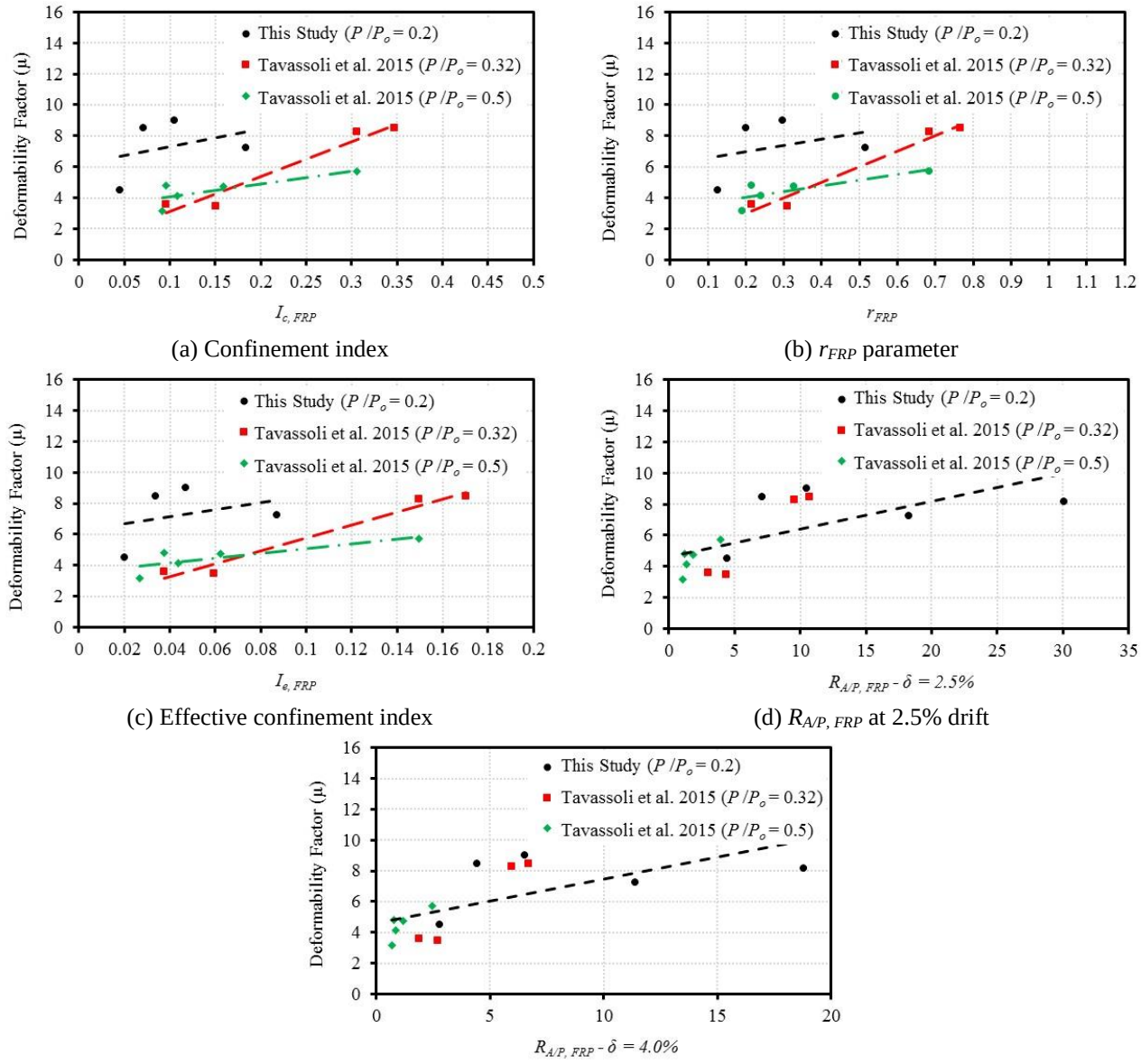

(a) Confinement index

(b) r_{FRP} parameter

(c) Effective confinement index

(d) $R_{A/P, FRP}$ at 2.5% drift

(e) $R_{A/P, FRP}$ at 4.0% drift

Figure 5.14: Relationships of different confinement indexes versus deformability factor (μ)

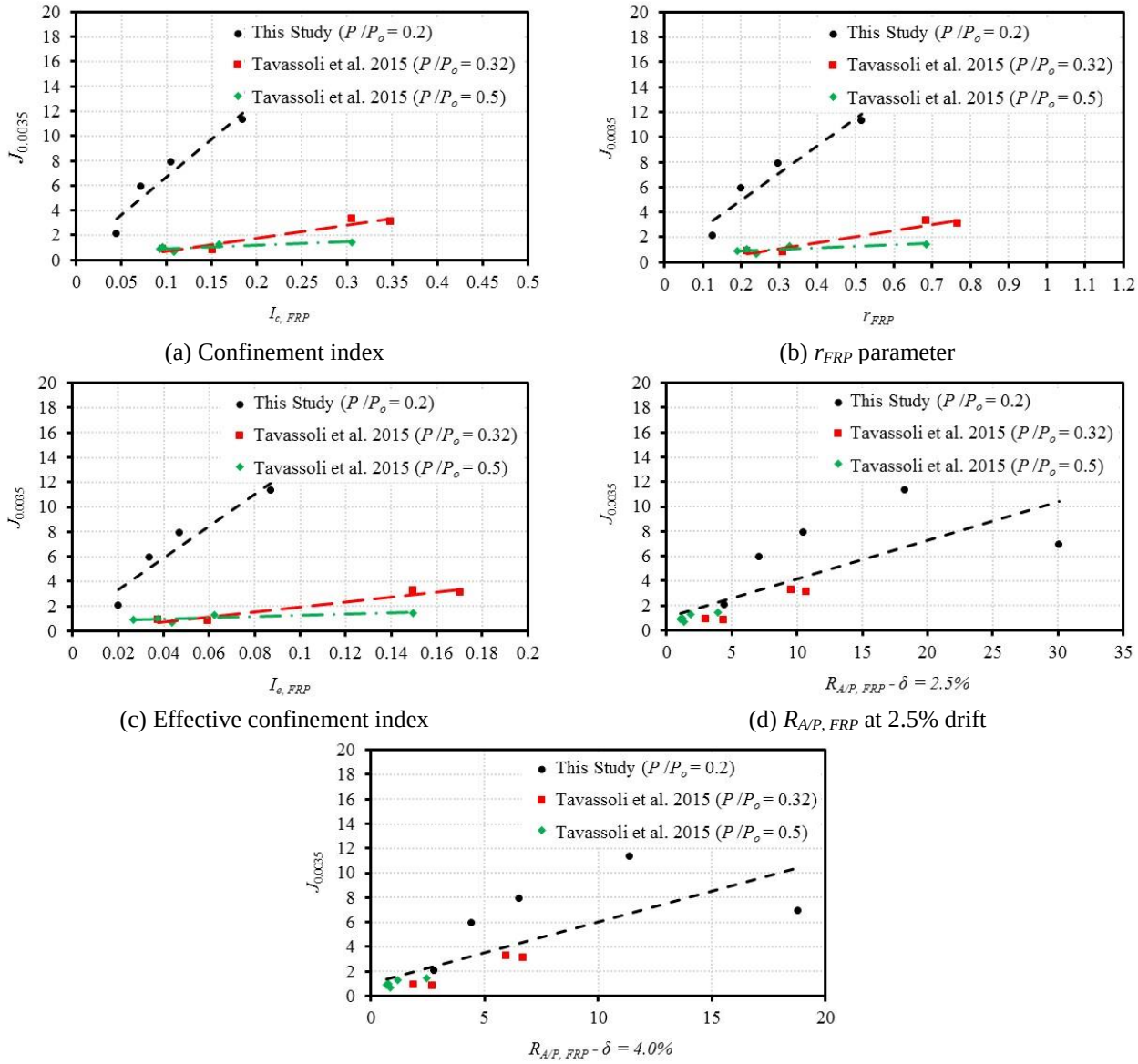

(a) Confinement index

(b) r_{FRP} parameter

(c) Effective confinement index

(d) $R_{A/P, FRP}$ at 2.5% drift

(e) $R_{A/P, FRP}$ at 4.0% drift

Figure 5.15: Relationships of different confinement indexes versus deformability factor ($J_{0.0035}$)

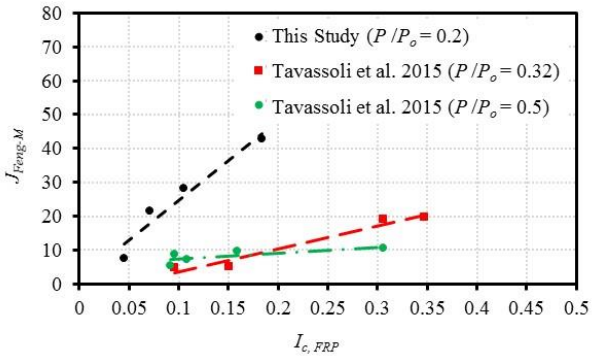

(a) Confinement index

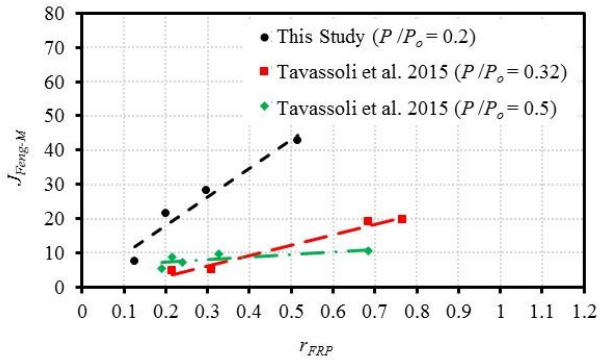

(b) r_{FRP} parameter

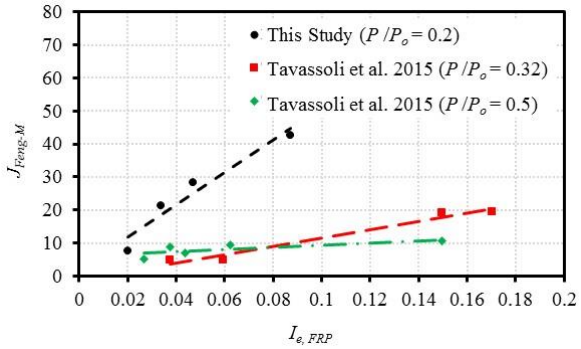

(c) Effective confinement index

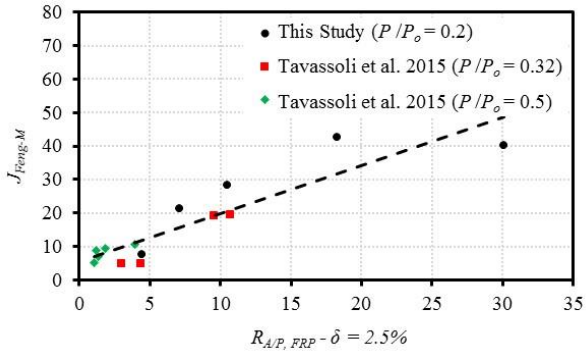

(d) $R_{A/P, FRP}$ at 2.5% drift

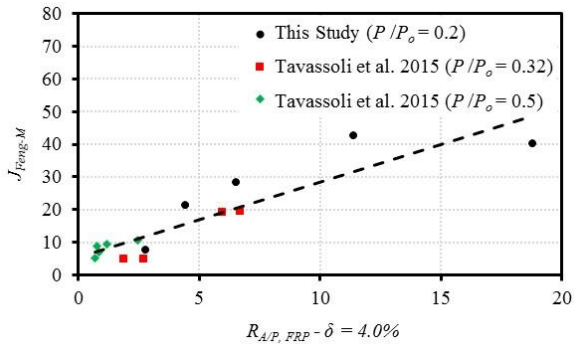

(e) $R_{A/P, FRP}$ at 4.0% drift

Figure 5.16: Relationships of different confinement indexes versus performance factor (J_{Feng-M})

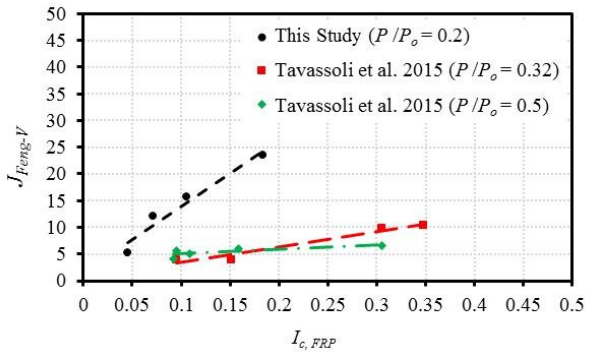

(a) Confinement index

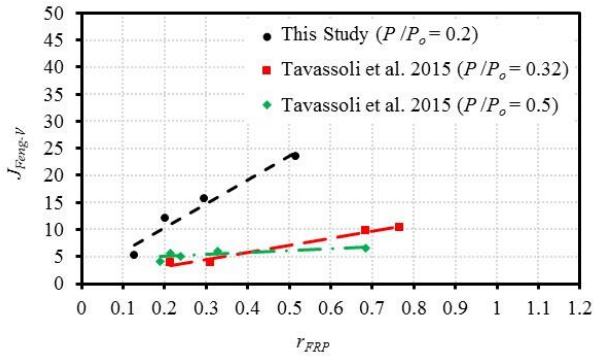

(b) r_{FRP} parameter

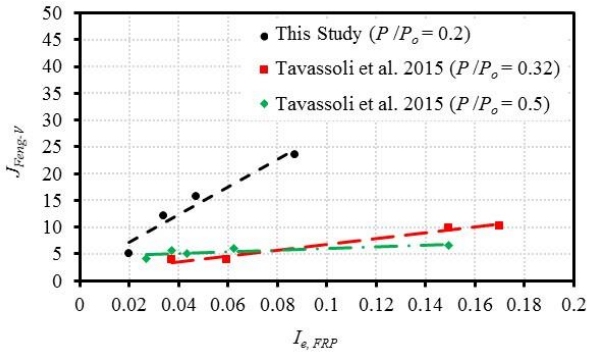

(c) Effective confinement index

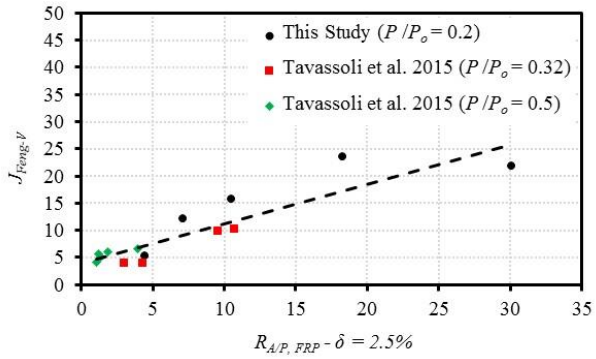

(d) $R_{A/P, FRP}$ at 2.5% drift

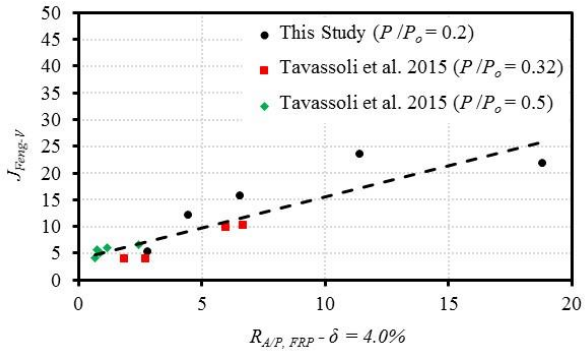

(e) $R_{A/P, FRP}$ at 4.0% drift

Figure 5.17: Relationships of different confinement indexes versus performance factor (J_{Feng-V})

5.6. Conclusions

Based on the experimental observations and analytical results found in this study, the following conclusions can be ascertained:

1. The requirement for the maximum spiral pitch to be one-sixth the effective core diameter was overly conservative for glass fiber-reinforced polymer (GFRP)-reinforced normal-strength concrete (NSC) columns when compared with the limit of one-fourth the gross

diameter of the column. On the other hand, the former limit was necessary for GFRP-reinforced high- strength concrete (HSC) columns in ductile moment-resisting frames (MRFs). While decreasing the spiral pitch from 85 to 50 mm hardly affected the lateral load capacity or energy dissipation of the GFRP-reinforced HSC columns, it significantly increased the drift capacity (by 172%).

2. The requirement for the maximum spiral pitch to be one-sixth the effective core diameter was overly conservative for glass fiber-reinforced polymer (GFRP)-reinforced normal-strength concrete (NSC) columns when compared with the limit of one-fourth the gross diameter of the column. On the other hand, the former limit was necessary for GFRP-reinforced high- strength concrete (HSC) columns in ductile moment-resisting frames (MRFs). While decreasing the spiral pitch from 85 to 50 mm hardly affected the lateral load capacity or energy dissipation of the GFRP-reinforced HSC columns, it significantly increased the drift capacity (by 172%).
3. The well-confined HSC columns surpassed the drift ratio limits of 2.50% and 4.00% required by the National Building Code of Canada (NBC) (2020) and CSA S806-12 (CSA 2017) for ductile MRFs, respectively. Although the specimen confined at 85 mm spiral pitch did not satisfy the 4.00% drift limit of CSA S806-12 (CSA 2017), it did satisfy both its design drift capacity and the drift limit for moderately ductile MRFs (CSA 2017).
4. Increasing concrete strength from 35 to 85 MPa with constant axial load level resulted in an enhanced initial lateral stiffness and increased lateral load capacity by 55% and 42% and energy dissipation by 70% and 63% for specimens with spiral pitches of 85 and 50 mm, respectively. Nonetheless, these augmentations were obtained at the cost of a reduced drift capacity, by 63% and 20% for moderately and well-confined columns, respectively. This indicates that extra caution is required when designing confinement reinforcement in GFRP-reinforced HSC columns.
5. The drift capacity, lateral load capacity, deformability, and energy dissipation of NSC and HSC columns were very similar when subjected to comparable axial loads. However, higher lateral load resistance at early stages of loading and higher energy dissipation beyond a 4.00% drift ratio were observed for the HSC column with respect to its NSC counterpart.

6. Increasing the axial load level for HSC specimens significantly improved the lateral load capacity and energy absorption, but adversely affected the deformability and drift capacity. This contradicts observations for GFRP-reinforced NSC and steel-reinforced HSC columns, which exhibited similar and decreased energy dissipation with higher axial load levels, respectively.
7. Of the performance indexes used, the integrated performance index, referred to as J_{Feng} (Feng et al. 2005), showed the best correlation with confinement indexes, with less scatter than all other performance indexes. The modified variable $R_{A/P,FRP}$ correlated well with the aforementioned performance index regardless of concrete compressive strength.

CHAPTER 6: EFFECT OF ASPECT RATIO ON THE SEISMIC BEHAVIOR OF GLASS FIBER-REINFORCED POLYMER-REINFORCED CONCRETE COLUMNS

Authors' Affiliations and Roles:

- **Amr E. Abdallah**, PhD Candidate, Department of Civil Engineering, University of Manitoba.
  Role: Methodology, Investigation, Formal analysis, Validation, Visualization and Writing-Original Draft.

- **Ehab F. El-Salakawy**, Professor of Civil Engineering, Department of Civil Engineering, University of Manitoba.
  Role: Conceptualization, Methodology, Writing-Review & Editing, Supervision, Project administration, Resources and Funding acquisition.

Journal and Status:

American Concrete Institute (ACI) Structural Journal, in press.

Reference:

Abdallah, A. E., and El-Salakawy, E. F. 2022. "Effect of aspect ratio on the seismic behavior of glass fiber-reinforced polymer-reinforced concrete columns." *ACI Struct. J.*, 119 (3), DOI: 10.14359/51734438, in press.

Note:

The manuscript had been slightly altered from the original paper by renumbering the tables and figures to include the chapter number. In addition, the reference list has been moved to the appropriate sections in the thesis as indicated in the table of contents.

Abstract

The available provisions for seismic design of fiber-reinforced polymer- reinforced concrete (FRP-RC) columns were fundamentally derived from design models created for steel-RC ones due to the limited research data on the former. This, in turn, may justify the conservativeness of such provisions, particularly those concerning the design of confinement reinforcement for columns with different aspect ratios. This study investigates the effect of aspect ratio and axial load level on the seismic response of columns reinforced with glass FRP (GFRP) by testing six full-scale GFRP-RC circular columns under earthquake-simulated loading. The experimental results revealed that unlike steel-RC columns, changing the aspect ratio insignificantly influenced the hysteretic response of GFRP-RC columns, indicating that the available code provisions for confinement reinforcement design are overly strict. Furthermore, recommendations are proposed for the seismic design of confinement reinforcement in GFRP-RC columns.

Keywords: Glass fiber-reinforced polymer (GFRP); seismic loading; circular columns; aspect ratio; axial load level; proposed equation.

6.1. Introduction

The ever-increasing widespread acceptance of the non-corrodible fiber-reinforced polymer (FRP) reinforcement to be used in various reinforced concrete (RC) structures, in lieu of conventional steel reinforcement, demands design provisions that are tailored to the characteristics of such reinforcement. That is, the design approaches of steel-RC structures cannot be directly applied to FRP-RC ones due to major differences in their mechanical performance. The aforementioned differences include, but are not limited to, the linear elastic behavior of FRP up to failure with relatively low elastic modulus and lacking yielding plateau, and limited strain capacity. Such properties raised concerns regarding the efficiency of FRP-RC structures in seismic-active zones, which were refuted later by recent research (Tavassoli et al. 2015; Ali and El-Salakawy 2016; Hasaballa and El-Salakawy 2016, 2018; Naqvi and El-Salakawy 2017; Elshamandy et al. 2018; Ghomi and El-Salakawy 2018, 2019; El-Gendy and El-Salakawy 2019, 2020; Abdallah and El-Salakawy 2021a, b). Yet, although the presently available codes and guidelines such as the CSA S806-12 (CSA 2017), CSA S6-19 (CSA 2019b) and ACI 440.1R-15 (ACI 2015) include detailed design provisions for a variety of structural elements such as beams, slabs and flat plates, the provisions related to design of columns are still lagging behind due to the scarcity of experimental data, which may explain the conservativeness of those provisions. For instance, the ACI 440.1R-15 (ACI 2015) design guidelines do not allow the use of FRP as main reinforcement in compression members, while the Canadian standards CSA S806-12 (CSA 2017) do not recognize the contribution of such reinforcement in compression. On the other hand, the Canadian highway bridge design code, CSA S6-19 (CSA 2019b) accounts for the contribution of FRP in compression with a maximum compressive strain of 2,000 με.

Throughout the last decade, several studies were dedicated to study the behavior of FRP-RC columns under monotonic loading schemes (De Luca et al. 2010; Pantelides et al. 2013; Afifi et al. 2014; Mohamed et al. 2014; Tobbi et al. 2014; Hadhood et al. 2017; Hadi et al. 2016; Hadhood et al. 2017; Hales et al. 2016; Guérin et al. 2018; Xue et al. 2018; Liu et al. 2019; Mousa et al. 2019; Abdelazim et al. 2020; Barua and El-Salakawy 2020; Elchalakani et al. 2020; Barua et al. 2021a). It is worth mentioning that most of the aforementioned studies used glass FRP (GFRP) in particular due to its attractive attributes such as its reasonable cost and satisfactory strain capacity. Nonetheless, the available research data on FRP columns under simulated seismic loading was rather limited (Tavassoli et al. 2015; Ali and El-Salakawy 2016; Naqvi and El-Salakawy 2017;

Elshamandy et al. 2018; Kharal and Sheikh 2018, 2020; Abdallah and El-Salakawy 2021a, b). These studies reported satisfactory hysteretic response for adequately-confined GFRP-RC columns with acceptable levels of energy dissipation under various axial load levels. Additionally, insignificant influence was noticed for the surface texture of GFRP or cross-sectional diameter of transverse reinforcement (Tavassoli et al. 2015). Furthermore, the deformability-based design approach of GFRP-RC columns substituted for the typical ductility requirement for steel-RC members. It was also found that while replacing steel with GFRP may adversely affect the shear and moment capacities of columns, it could enhance their deformability and member behavior (Kharal and Sheikh 2018, 2020). Moreover, some studies demonstrated that the current provisions for confinement reinforcement spacing are too strict (Ali and El-Salakawy 2016; Abdallah and El-Salakawy 2021a). This could be attributed to the fact that the currently available design equation of the Canadian standards CSA S806-12 (CSA 2017) was directly adopted from the design model developed by Saatcioglu and Razvi (2002) for steel-RC columns. In this model, the effect of column aspect ratio, defined as the ratio of column length to either cross-sectional dimension for rectangular columns or to diameter for circular ones, was found to be proportional to its drift capacity under seismic loading. This was based on previous research work on a wide range of aspect ratios (Sakai and Sheik 1989; Saatcioglu 1991; Li 1994; Razvi and Saatcioglu 1996; Lehman and Moehle 1999). However, such perspective was later refuted for steel-RC columns by Bae and Bayrak (2008), who concluded that increasing the column aspect ratio may adversely affect the drift capacity depending on the axial load level. Yet, the proportional relationship between drift capacity and column aspect ratio was neither supported nor rebutted for GFRP-RC columns, apart from few studies that used fiber-reinforced concrete, other FRP types or hybrid reinforcement (steel + GFRP) configuration (Sharbatdar 2003; Deng et al. 2018; Kharal et al. 2021a). Therefore, this paper, which extends a proceeding research project on the seismic behavior of GFRP-RC columns (Abdallah and El-Salakawy 2021a, b), investigates the effect of column aspect ratio along with axial load level on the seismic response and deformability of such columns. In addition, making recommendations for the design of confinement reinforcement in columns located in seismic active zones was amongst the aims of this study.

6.2. Research Significance

The current research program addresses the scarcity of experimental data on the confinement properties of FRP-RC columns under seismic loading. The effect of column aspect ratio under

various axial load levels was investigated, proving the conservative nature of the current code provisions, which were based upon an assumption that shorter columns are less deformable. Furthermore, based on the results of this pioneer experimental research, recommendations for the seismic design of confinement reinforcement of FRP-RC columns are introduced.

6.3. Experimental Program

6.3.1. Materials

The longitudinal and confining reinforcement was sand-coated GFRP size No. 16 bars (15.9-mm diameter) and size No. 10 spirals (9.5-mm diameter), respectively. Table 6.1 includes a summary of the physical and mechanical properties of the used GFRP bars and spirals as reported in the product certificate provided by the manufacturer (Pultrall Inc. 2019) or as determined by laboratory testing, as appropriate (CSA 2017). All test specimens were cast using ready-mixed, normal-weight concrete having a specified 28-day compressive strength of 35 MPa. Standard 100 × 200-mm concrete cylinders were prepared out of each batch and tested as per CSA A23.1-19/A23.2-19 (CSA 2019a) on testing day of each column, as provided in Table 6.2.

Table 6.1: Mechanical properties of GFRP reinforcement

Bar type	Nominal diameter mm	Area mm^2	Modulus of elasticity GPa	Tensile strength MPa	Ultimate strain (%)
No. 16	15.9	197.9[a] (235)[b]	65.7[c]	1,711[d]	2.60[d]
No. 10 (Spirals)	9.5	71[a] (83)[b]	58.4[c]	1,376[d, e]	2.36 [d, e]

[a] Nominal area according to CSA S807-19 (CSA 2019c).
[b] Actual area measured as per Annex A of CSA S806-12 (CSA 2017).
[c] Calculated in accordance with Annex C of CSA S806-12 (CSA 2017).
[d] Calculated using nominal area and average force as per Annex C of CSA S806-12 (CSA 2017).
[e] Obtained from tests on straight bars from the same batch following Annex C of CSA S806-12 (CSA 2017).

6.3.2. Test specimens

The test program incorporated casting and testing of six full-scale column-footing connections under simultaneous axial loading and reversible cyclic lateral drifts. Each column was stemming out of a rigid 1,400 × 900 × 600-mm footing, adequately reinforced with 15M (16-mm diameter),

to ensure rotational fixity for the column without significant cracking during testing. Each specimen replicated the lowermost segment of a column between the top surface of the footing and the theoretically-assumed point of contra-flexure, which may represent the lower portion of a first-story column in a multi-story moment-resisting frame (MRF) or a cantilever bridge pier. All columns had a diameter of 350 mm, whereas the shear span (i.e. the distance between top surface of the footing and lateral load's line of action) was either 1,050 or 2,450 mm, resulting in a length-to-diameter ratio (i.e. aspect ratio) of 3.0 or 7.0, respectively. The lower aspect ratio resembled some cases of short bridge piers or the so-called captive columns in multi-story moment resisting frames (MRFs), as depicted by Figure 6.1, while the larger aspect ratio represented longer columns that could be found at the entrances of buildings with large floor height. Design of specimens was performed following CSA S806-12 (CSA 2017), CSA S6-19 (CSA 2019b) in addition to the recommendations of recent research work (Ali and El-Salakawy 2016, Deng et al. 2018, Abdallah and El-Salakawy 2021a), as applicable. In addition, all columns were confined at an 85-mm spiral pitch as per Clause 12.7.3.4 of CSA S806-12 (CSA 2017) and as deemed adequate in the literature (Abdallah and El-Salakawy 2021a). It was deemed of interest to investigate the seismic behavior of specimens with an aspect ratio of 3.0 as they were found to fail in shear when analyzed using the actual lateral load capacity of other columns tested earlier in this study (Abdallah and El-Salakawy 2021a) along with the available code provisions for shear design (CSA 2017).

Table 6.2: Properties of test specimens

Specimen ID	Aspect ratio, *L/D*	Axial load level, P/P_o	Cracking load applied kN	Concrete strength, f_c' MPa	Average length of hinging region, L_i mm
G-3.0-0.2	3.0	0.2	47	44.2 $\pm$ 0.1	407
G-3.0-0.3	3.0	0.3	85	45.9 $\pm$ 0.7	460
G-5.0-0.2	5.0	0.2	24	36.9 $\pm$ 0.4	525
G-5.0-0.3	5.0	0.3	30	41.4 $\pm$ 0.7	525
G-7.0-0.2	7.0	0.2	28	43.3 $\pm$ 0.7	680
G-7.0-0.3	7.0	0.3	37	43.2 $\pm$ 0.3	660

The specimens were cast in two successive pours, following the conventional construction practice, starting with the footings while the columns were cast afterwards. For each aspect ratio, a specimen was tested under an axial load level of 0.2, whereas an axial load level equals to 0.3 was applied to the other one.

Furthermore, two specimens were used from the previous work conducted by the authors to be compared against the specimens of this study (Abdallah and El-Salakawy 2021a). The two specimens had the same properties as those tested in this study except for the shear span, which was 1,750 mm, resulting in an aspect ratio of 5.0.

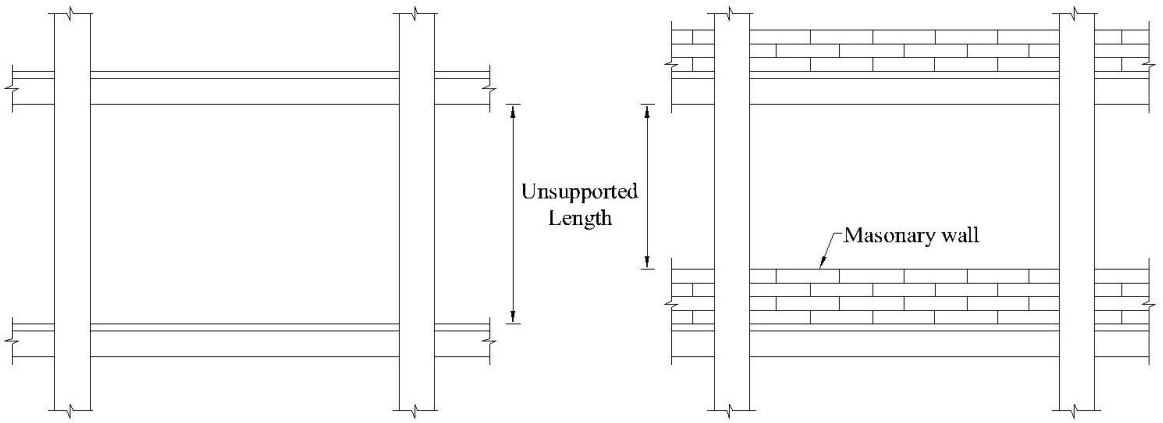

(a) Bare frame (b) Captive columns

Figure 6.1: The concept of captive columns (Saatcioglu 1991)

The specimens were designated using a three-character label, in which the first character, G, denotes the GFRP used to reinforce all columns. The second one is a number that refers to the column aspect ratio, while the last character denotes the axial load level, represented by the applied axial load, P, as a fraction of the nominal unconfined axial capacity of the GFRP-RC column, P_o. For instance, G-3.0-0.2 is a GFRP-RC column with a length-to-diameter ratio of 3.0 and axial load level of 0.2. It is worthwhile to note that the labels of the specimens used from the previous work were adjusted to the format used in this study for the ease of referencing. The test matrix is listed in Table 6.2, while Figure 6.2a demonstrates the design dimensions and details of reinforcement for test specimens.

6.3.3. Instrumentation

Sixteen electrical-resistance strain gauges per column was attached to the extreme bars and the spiral along the anticipated hinging region, as depicted by Figure 6.2a. Besides, the different elements of the horizontal displacement at mid-height of the column head were monitored using multiple pairs of linear variable displacement transducers (LVDTs), fixed along the anticipated hinging region and beyond, as shown in Figure 6.2b. For the aspect ratios of 5.0 and 7.0, six pairs of LVDTs were used, whereas the top pair of vertical LVDTs was excluded for the specimens

having an aspect ratio of 3.0. Generally, two pairs were fixed vertically along the bottom segment of the column; one of which was mounted 25 mm above the column–footing interface to obtain the individual displacement component due to flexure, whereas the other pair had its lower ends attached to the top surface of the footing (i.e., at the interface) to measure the combined displacement due to flexure and rigid body rotation. In addition, two pairs of LVDTs were mounted diagonally across the southern face of the column to record the horizontal displacement associated with shear distortion of column panels. The remaining vertical LVDTs were measuring the flexural displacement along the rest of the column, up to a maximum height above the interface equal to 1,075 mm for aspect ratios of 5.0 and 7.0, or 725 mm for the specimens with the aspect ratio of 3.0, respectively.

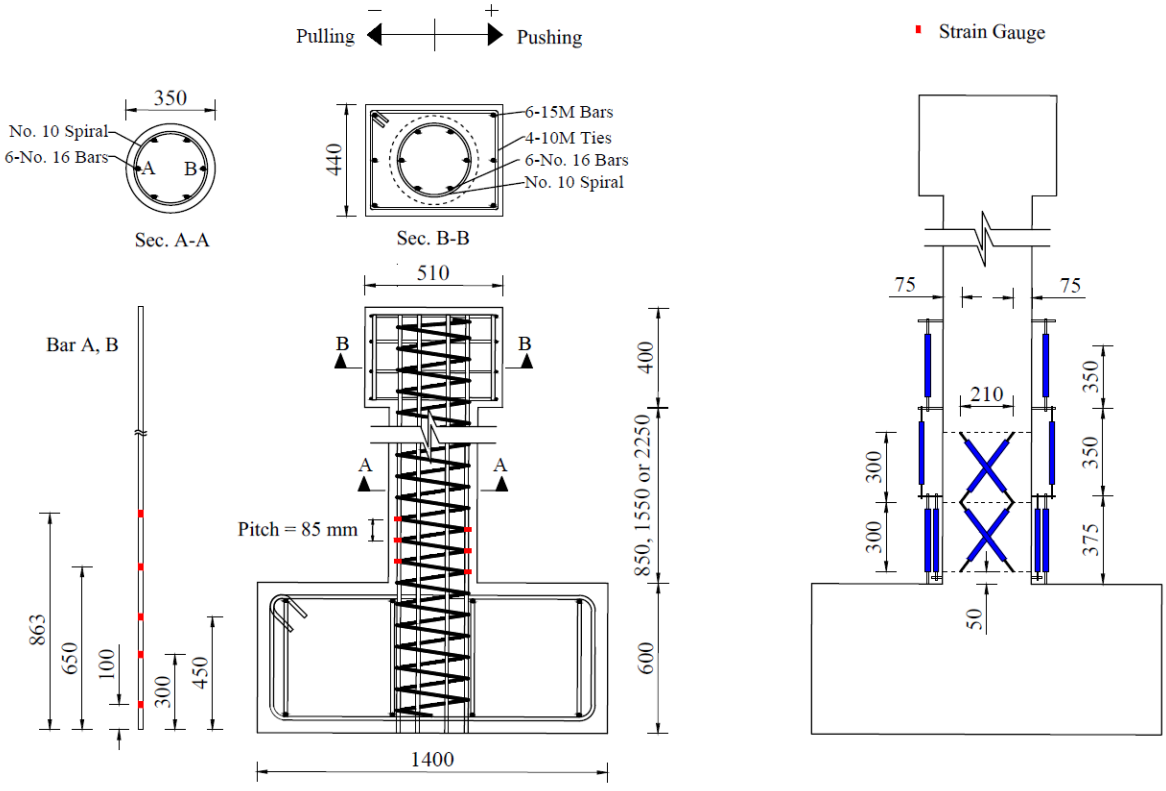

(a) Specimen details and locations of strain gauges (b) Arrangement of LVDTs

Figure 6.2: Details of tested specimens and instrumentation (all dimensions in mm)

6.3.4. Test setup and procedure

The test setup comprised of three main elements; the dynamic hydraulic actuator, the axial loading frame and the RC alignment blocks. The horizontally aligned hydraulic actuator, which had ± 1,000-kN and ±

250-mm load and displacement capacities, respectively, was post-tensioned to an RC reaction wall through premade holes and utilized to apply the horizontal load or drift reversals. The positive sign indicated pushing the specimen as a result of the applied load or drift and the opposite was true when the load or drift resulted in pulling the column.

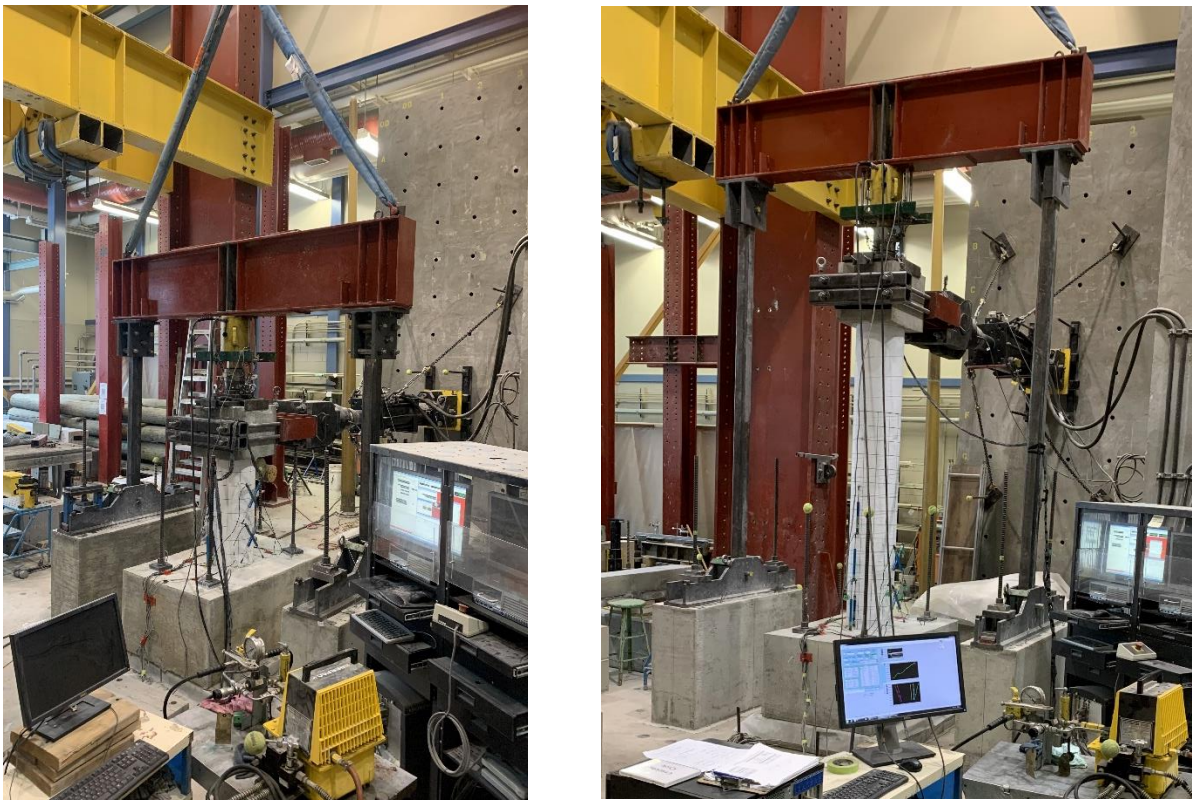

(a) Aspect ratio = 3.0 (b) Aspect ratio = 7.0

Figure 6.3: Details of test setup

The axial load was applied using a 2,000-kN load capacity hydraulic jack, transferring its reactions to the laboratory floor through a hinged steel loading frame, which consisted of two hollow steel section (HSS) links pinned to a steel spreader I-beam. An RC slab was placed below the specimen to align the actuator with the mid-height of the column head. In addition, the bottom ends of the steel axial loading frame were pinned to two RC blocks. This hinged steel frame maintained the applied axial load in the direction of the longitudinal axis of the column, while moving along with the lateral drift of the column head. The footing, RC leveling slab and blocks were anchored to the laboratory strong floor using post-tensioned high-strength threaded bars. For each aspect ratio, a different set of HSS links, RC slab and RC blocks were used to align the specimen with the hydraulic actuator and axial loading frame, which is evident from Figure 6.3. It is worth

mentioning that the test setups shown in Figures 6.3a and b were for columns with aspect ratios of 3.0 and 7.0, respectively, while the details of test setup for aspect ratio of 5.0 could be found elsewhere (Abdallah and El-Salakawy 2021b).

Applying the specified axial load marked the beginning of the test, where that axial load was calculated as a fraction of the nominal unconfined axial capacity of the column, P_o; in accordance with the Canadian standards CSA S806-12 (CSA 2017):

$$P_o = \alpha_1 \phi_c f_c^{'} (A_g - A_F) \qquad \text{Equation 6.1}$$

where α_1 is the average stress in the rectangular compression block with respect to the specified concrete strength, f_c'; ϕ_c is the resistance factor for concrete, which was taken as unity; A_g is the gross cross-sectional area of the column; and A_F is the total area of the main FRP reinforcement. Once the specified axial load was reached, it was maintained constant throughout the test. Afterwards, two load-controlled cycles were applied to obtain the horizontal cracking load and simulate the column at service stage. The column was subjected to the uniaxial drift reversals thereafter, following a typical displacement history as per ACI 374.1-05 (ACI 2019). Quasi-static lateral drift reversals were applied successively at a frequency of 0.01 Hz with three cycles having the same drift ratio (defined as the lateral displacement of at mid-height of the column head as a percentage of the column shear span) for each drift step, ensuring that the cracks would propagate in a stable manner. To assess the stiffness degradation, if any, a load-controlled service cycle was applied after each drift step beyond 2.00% drift ratio (Ali and El-Salakawy 2016; Hasaballa and El-Salakawy 2016, 2018; Naqvi and El-Salakawy 2017; Ghomi and El-Salakawy 2018, 2019; Abdallah and El-Salakawy 2021a, b). Finally, tests were halted when the specimens exhibited a degradation of the lateral load resistance by 25% or more.

6.4. Test Results and Discussion

6.4.1. General behavior and modes of failure

Generally, the lateral load at first cracking increased as the axial load level increased or as the aspect ratio decreased, which is evident from the listed lateral cracking loads in Table 6.2. The only exception was when the aspect ratio increased from 5.0 to 7.0, which can be attributed to the larger concrete compressive strength of the longer columns. In addition, the unpredictable nature of crack initiation, where the first cracking may start inside the column rather than on the outer surface, could delay the visual observation of cracking until a higher lateral load is reached. The

commencement of cover spalling occurred during a drift ratio of 2.00% for G-3.0-0.3 and G-5.0-0.3; 3.00% for G-3.0-0.2, G-5.0-0.2 and G-7.0-0.3; and 4.00% for G-7.0-0.2. In addition, the failure drift was 10.20% for all specimens under 0.2 axial load level, 6.50% for G-3.0-0.3 and G-5.0-0.3, while G-7.0-0.3 failed at 8.15% drift ratio. This concurred with the observations of Deng. et al. (2018) for GFRP-RC columns constructed with fiber-reinforced concrete. On the other hand, this contradicted with the findings of Sharbatdar (2003), where shorter CFRP-RC specimens failed at lower drift ratios. Moreover, the average length of cover spalling region for the specimens, as tabulated in Table 6.2, indicates a direct proportionality with aspect ratio while the influence of axial load level on the average length of cover spalling region was marginal. Such a nearly-linear relationship between column aspect ratio and length of hinging region for GFRP-RC was found to be completely different than that of steel-RC columns as reported by Sakai and Sheikh (1989), as shown in Figure 6.4. In the latter relationship, the hinge length-to-column diameter ratios were much less than those of the former one, with an upper bound for aspect ratio at approximately 4.0 for steel-RC columns, beyond which, insignificant change of hinge length-to-column diameter ratio could be observed.

All columns failed in flexure, even though higher-intensity shear cracking was observed for the specimens with the aspect ratio of 3.0, which agreed with the findings of Sharbatdar (2003) for CFRP-RC columns. Nonetheless, no faster rate of strength degradation was observed for G-3.0-0.2 or G-3.0-0.3 compared to their longer counterparts, as it would be discussed later. The flexure-controlled type of failure for G-3.0-0.2 and G-3.0-0.3 suggests that the available code provisions for shear in CSA S806-12 (CSA 2017) could be too conservative to be applied for GFRP-RC columns in seismic-active zones because the aforementioned specimens were anticipated to fail in shear based on such provisions. Furthermore, the results of this study along with those of Sharbatdar (2003) and Deng et al. (2018) may suggest that the aspect ratio of 3.0 is the lower bound of the flexure-controlled mode of failure for FRP-RC columns.

Failure was identified for specimens G-3.0-0.2, G-5.0-0.2, G-5.0-0.3 and G-7.0-0.2 by concurrent crushing of concrete core along with compression failure of the extreme longitudinal bar (Abdallah and El-Salakawy 2021a), followed by failure of another two bars on the compression side for G-3.0-0.2 and spiral rupture for G-7.0-0.2. On the other hand, G-3.0-0.3 exhibited concrete core crushing, three-bar delamination and spiral rupture at failure, whereas G-7.0-0.3 failed by way of simultaneous concrete core crushing, compression failure of three bars and spiral rupture. It should

be noted that as a safety precaution, the hydraulic actuator was set back to zero position after failure of the specimen, during which more bars were damaged for some specimens. This included failure of a delaminated bar for G-3.0-0.3, and compression failure of all longitudinal bars for G-7.0-0.2 and G-7.0-0.3. The modes of failure for all test specimens are shown in Figure 6.5.

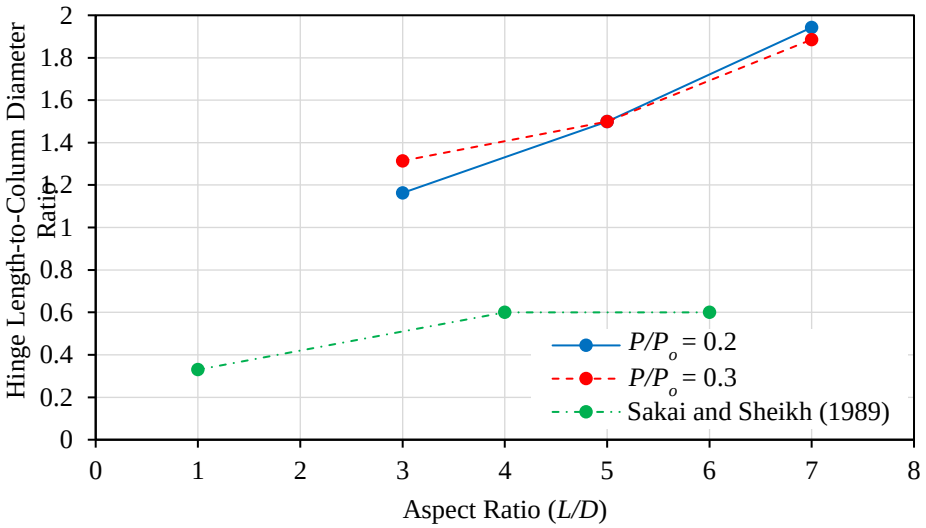

Figure 6.4: Effect of column aspect ratio on hinge length

Table 6.3: Theoretical and experimental lateral load and drift capacities

Specimen ID	Theoretical capacity		Experimental lateral capacity		
	Lateral load (kN)	Drift [a] (%)	Maximum (kN)	At failure (kN)	Strength Degradation (%)
G-3.0-0.2	90.0	5.20	+158.0 at 4.00% drift -181.5 at -8.15% drift	-111.9 at -10.00% drift	38.3
G-3.0-0.3	96.7	3.11	+189.1 at 4.00% drift -195.5 at -5.00% drift	+98.7 at 6.17% drift	47.8
G-5.0-0.2	54.0	5.20	+94.1 at 4.00% drift -96.0 at -10.20% drift	+58.8 at 10.20% drift	37.5
G-5.0-0.3	58.0	3.11	+101.2 at 2.00% drift –77.5 at -2.00% drift	+73.0 at 6.50% drift	27.9
G-7.0-0.2	38.6	5.20	+68.8 at 4.00% drift -67.7 at -10.20% drift	+56.8 at 10.20% drift	17.4
G-7.0-0.3	41.4	3.11	+70.4 at 3.00% drift -69.1 at -4.00% drift	+64.0 at 8.15% drift	9.1

[a] Calculated according to Clause 12.7.3.3 of CSA S806-12 (CSA 2017).

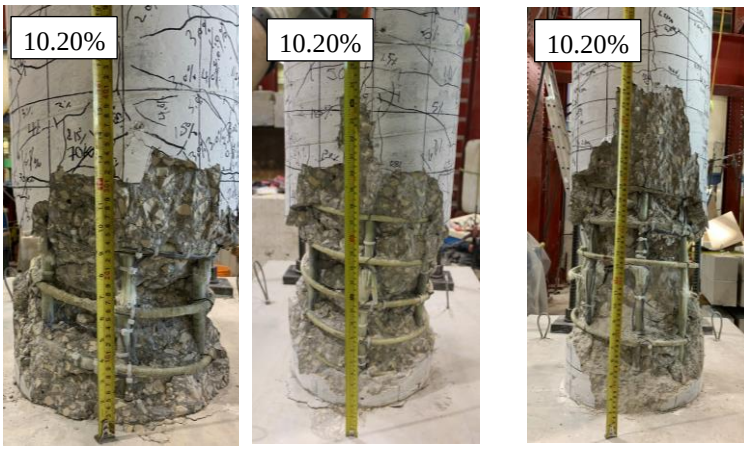

(a) G-3.0-0.2 (b) G-5.0-0.2 (c) G-7.0-0.2

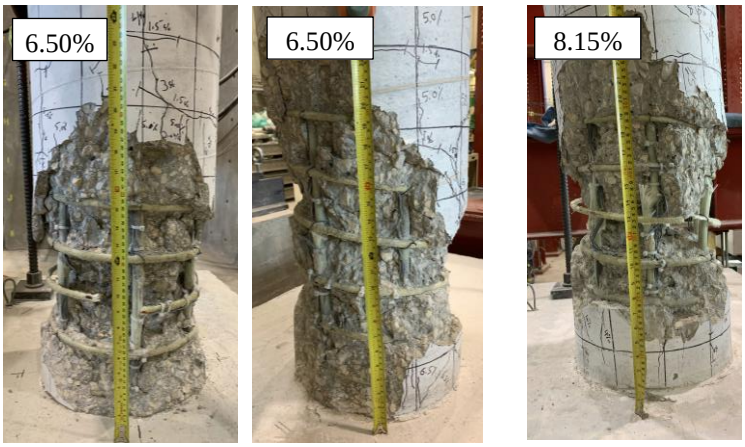

(d) G-3.0-0.3 (e) G-5.0-0.3 (f) G-7.0-0.3

Figure 6.5: Test specimens at failure (all dimensions in mm)

6.4.2. Hysteretic response

The envelopes of the lateral load-drift ratio relationship for tested specimens are shown in Figure 6.6. The initial stiffness for all specimens were similar due to having comparable concrete strength. Obviously, the lateral load resistance decreased significantly as the column aspect ratio increased, due to the change of shear span while the moment capacity of the cross-section would presumably remain constant. In addition, an increase of axial load level resulted in larger lateral load capacity but more rapid strength decay and less deformable behavior, which was less pronounced as the aspect ratio increased. The lateral load capacity increased by 14, 8 and 3% when the axial load level increased from 0.2 to 0.3 P_o for aspect ratios of 3.0, 5.0 and 7.0, respectively. Furthermore, the effect of increasing axial load level was comparable for aspect ratios of 3.0 and 5.0, with a 36% decrease in failure drift, while it was less impactful for the aspect ratio of 7.0, where the

reduction of failure drift was only 20%. Generally, all specimens surpassed the drift ratio limit for ductile MRFs, which is equal to 4.00%, as set by CSA S806-12 (CSA 2017). Due to the various aspect ratios considered in this study, it was deemed informative to compare the hysteretic responses of the specimens in terms of bending moment at the critical section, rather than lateral load, versus drift ratio, as depicted in Figures 6.7 and 6.8. The moment at the critical section was calculated as the product of the lateral load and the lever arm, where the lever arm was equal to the shear span measured from the center of the hinging region in lieu of the column–footing interface (Tavassoli et al. 2015).

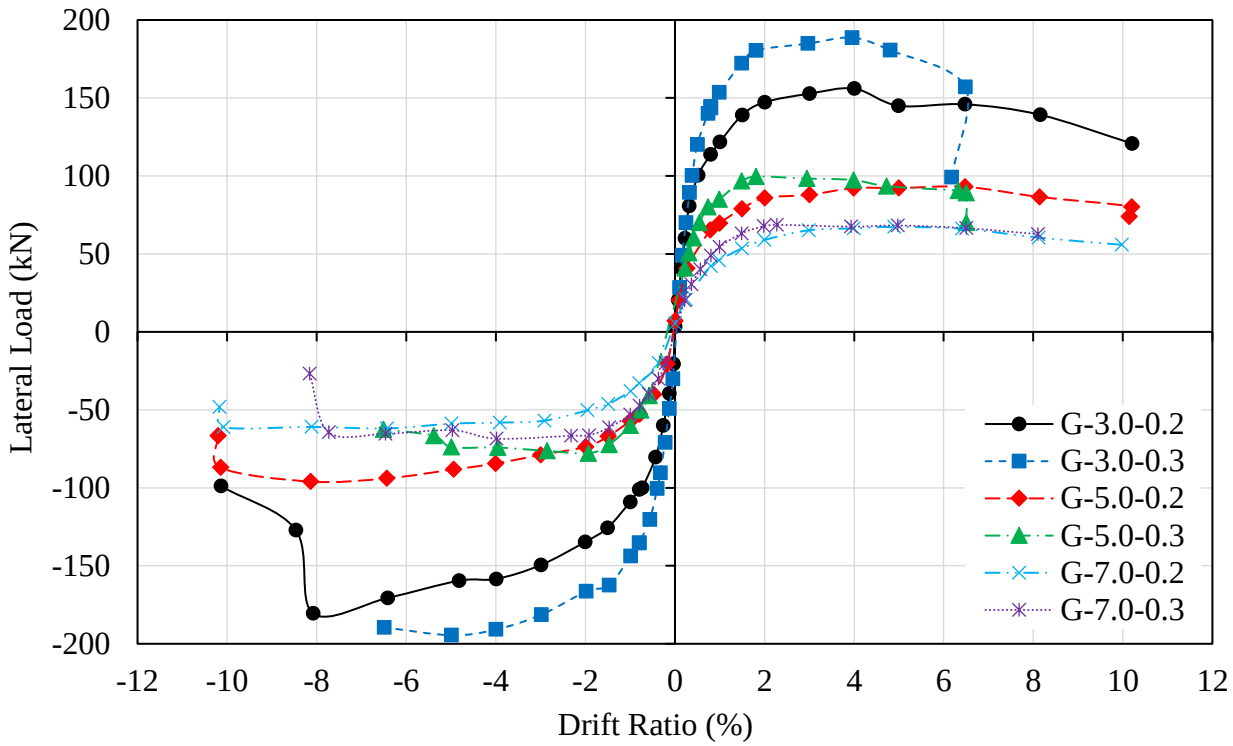

Figure 6.6: Envelopes of hysteresis diagrams for test specimens

Increasing the axial load level slightly improved the moment capacity of the columns by 11, 7 and 7% for aspect ratios of 3.0, 5.0, and 7.0, respectively, at the expense of drift capacity (i.e., maximum drift ratio endured by the specimen for three full cycles). However, increasing the aspect ratio had an insignificant effect on either the moment or drift capacity, apart from a few exceptions such as the relatively softer response for the aspect ratio of 3.0 under the axial load level of 20% on the pushing side, and the larger drift capacity by 30% under an axial load level of 30% for the aspect ratio of 7.0. This, in turn, may indicate that the available code provisions for seismic design

of transverse reinforcement in columns are overly strict as they were based on the assumption that decreasing aspect ratio would result in a considerably less deformability. Table 6.3 lists the experimental and theoretically-calculated lateral load and moment capacities and failure drifts alongside the strength degradation at failure.

6.4.3. Energy dissipation

In earthquake-prone zones, the RC members are expected to dissipate the seismic energy through many ways that include, but not limited to, concrete cracking, inelastic deformations of concrete and reinforcement at hinging zones. Hinging at the bottom segments of first story columns of MRFs or bridge piers is inevitable to complete the inelastic mechanism in earthquake-resistant structures. An effective means to investigate the damping efficiency of an RC member is to check its dissipated seismic energy. The cumulative energy dissipation, represented by cumulative area of lateral load-drift hysteresis loops, was plotted against drift ratio for the tested specimens in Figure 6.9. It was noticed that increasing the axial load level resulted in a marginal increase for the cumulative energy dissipated, regardless of the aspect ratio. On the other hand, a decrease in the overall energy dissipated occurred due to increasing the column aspect ratio from 3.0 to 5.0, reaching 22 and 13% reduction when subjected to an axial load level of 20 and 30%, respectively. The change in energy dissipation was, however, insignificant when the aspect ratio increased further to 7.0.

6.4.4. Longitudinal reinforcement strains

The maximum strains in the longitudinal GFRP bars were plotted against column drift ratio as depicted by Figure 6.10. The previous research on steel-RC columns either did not discuss the effect of column aspect ratio on the strains in the longitudinal reinforcement (Razvi and Saatcioglu 1996; Bae and Bayrak 2008) or indicated that the strain in longitudinal bars was directly proportional to column length-to-diameter ratio (Lehman and Moehle 2000). Nonetheless, the strain-drift relationships for the different aspect ratios tested in this study were basically similar, apart from the increase for the strains of G-3.0-0.3 and G-5.0-0.2 over their counterparts with different aspect ratio. Such inconsistent variations with the aspect ratio could be attributed to the localized nature of strain gauge measurements, which may give a false magnification in some cases. Furthermore, increasing the axial load level from 0.2 to 0.3 P_o resulted in larger longitudinal

reinforcement strains for the aspect ratio of 3.0, reaching a 14% increase at 4.00% drift ratio. On the other hand, the change of strains was minimal for specimens with 5.0 and 7.0 aspect ratios.

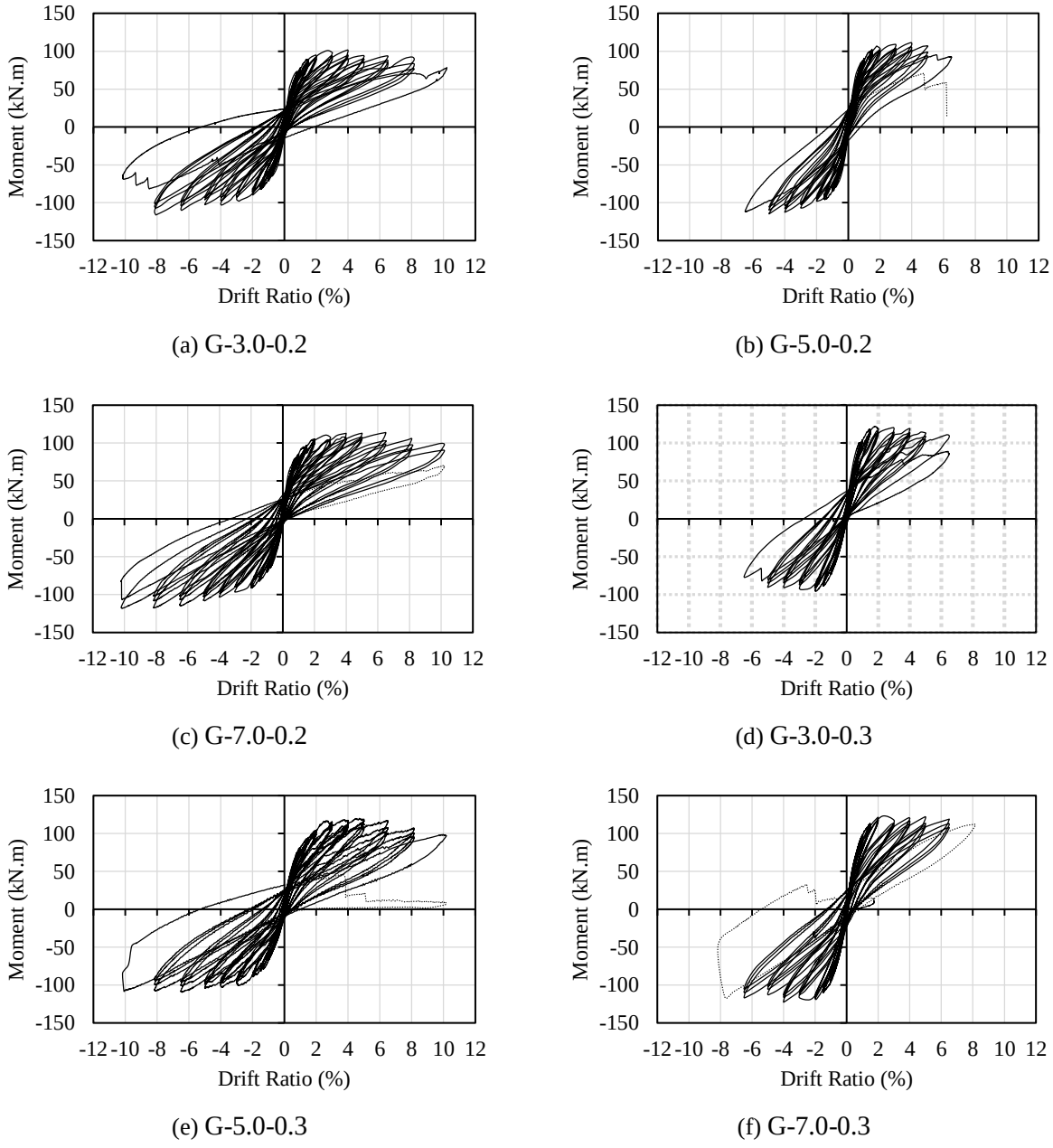

(a) G-3.0-0.2 (b) G-5.0-0.2

(c) G-7.0-0.2 (d) G-3.0-0.3

(e) G-5.0-0.3 (f) G-7.0-0.3

Figure 6.7: Hysteresis diagrams for test specimens

Moreover, the strain profiles of the outermost bars for each specimen, as acquired from the readings of electrical strain gauges attached to the bars along the hinging region and the embedded length into the footings, are shown in Figure 6.11. Generally, for all specimens, the strains in the longitudinal bars of the column diminished within the embedded length into the footings,

indicating sufficient anchorage length for such bars. However, the specimens with the aspect ratio of 3.0 experienced higher longitudinal bars strains along the embedded portion, which contradicted the observations of Sharbatdar (2003). Such higher strains along the embedded segments of the longitudinal bars could be attributed to the increased rigid-body rotations for such specimens, as would be discussed later. In addition, each two specimens with the same aspect ratio exhibited similar strain distributions up to a drift ratio of 2.00%, beyond which, the strain profiles showed slight variations.

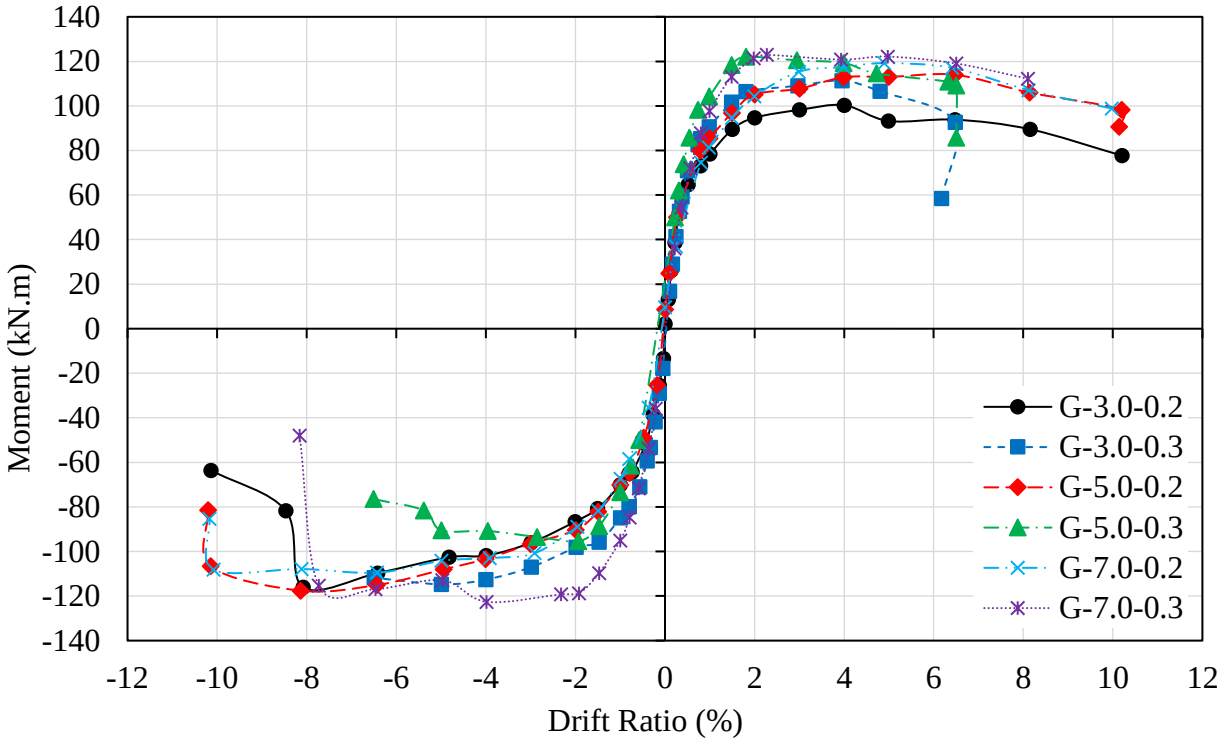

Figure 6.8: Envelopes of moment-drift ratio hysteresis diagrams for test specimens

6.4.5. Spiral strains

Figure 6.12 shows the variation of the maximum spiral strain of each test specimen against the drift ratio. For the lower axial load level, an obvious increase of spiral strains was observed for the specimen with the aspect ratio of 3.0 over its counterparts with larger aspect ratios, which exhibited similar spiral strains. The maximum spiral strain of G-3.0-0.2 was 40% higher than those of G-5.0-0.2 and G-7.0-0.2 at 4.00% drift ratio, surpassing the 6,000-με limit set by CSA S806-12 (CSA 2017). This could be attributed to the increased shear deformation for G-3.0-0.2 comparing to its longer counterparts. Afterwards, spiral strains varied inconsistently for the three specimens. The

specimens with the higher axial load level, on the other hand, experienced similar spiral strains and exceeded the spiral strain limit of the Canadian code for FRP-RC structures (CSA 2017). Moreover, changing the axial load level did not considerably influence the spiral strains for aspect ratios 3.0 and 7.0, while resulting in an increase for specimens with the aspect ratio of 5.0. Overall, the reported observations for GFRP-RC columns herein contradict those reported by Lehman and Moehle (2000) for steel-RC columns, where an increase of aspect ratio was consistently accompanied by higher spiral strains. Furthermore, most of the tested specimens exceeded the 6,000-με spiral strain limit (CSA 2017), yet they all achieved satisfactory hysteresis responses and drift capacities, which could indicate the conservativeness of such limit.

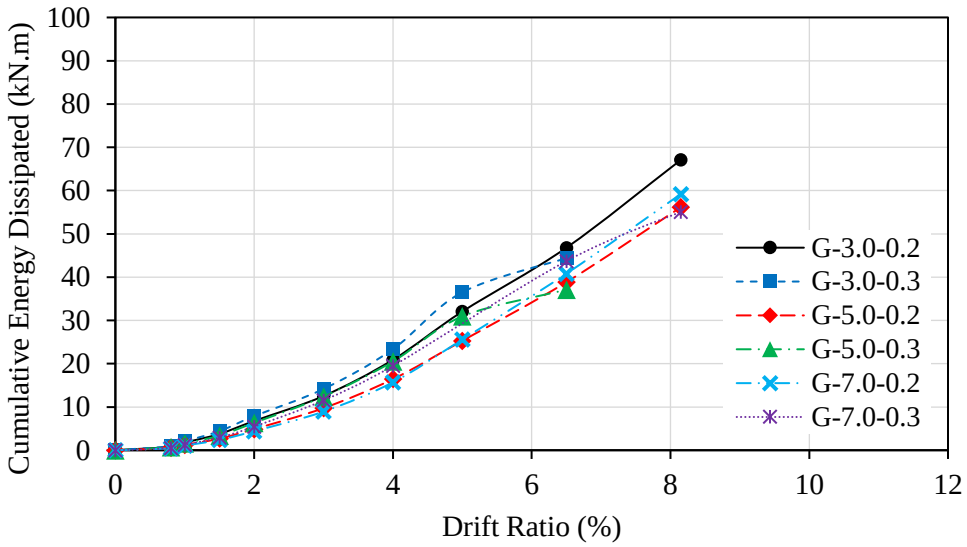

Figure 6.9: Cumulative energy dissipated by test specimens

6.4.6. Displacement components

The lateral drift at the tip of each column can be estimated as the summation of three main components; the flexure displacement, Δ_f, the displacement due to bar slip, Δ_s, and the shear displacement, Δ_{sh} (Li 1994, Lehman and Moehle 1999, Sezen and Moehle 2006). The flexure displacement component was obtained by integrating the curvature along the column shear span as follows:

$$\Delta_f = \sum \theta_i (L - y_i) \qquad \text{Equation 6.2}$$

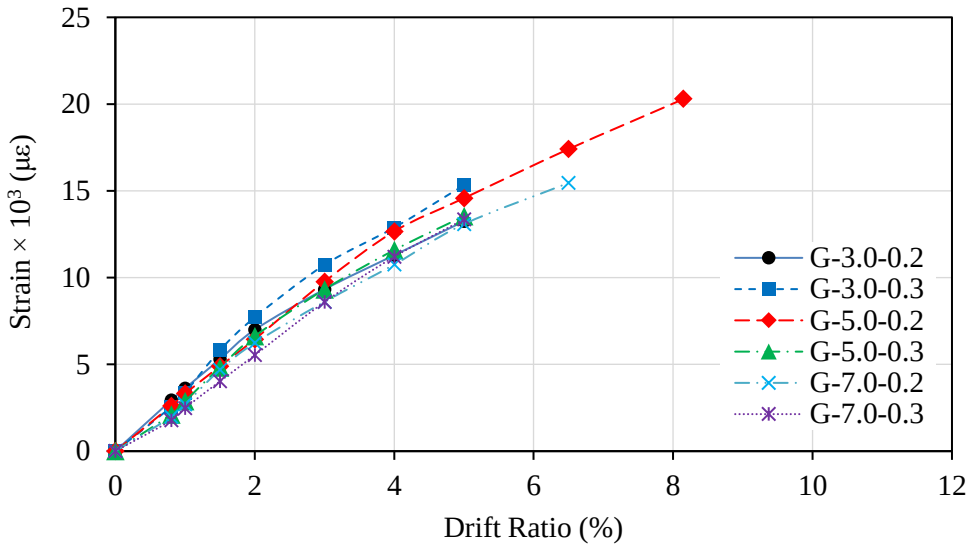

Figure 6.10: Maximum strain in outermost longitudinal bar at column hinging region versus drift ratio

where the flexural rotation of each gauge length, θ_i, could be found as the summation of the two opposite readings of the LVDTs divided by the horizontal distance in between; L is the column shear span; and y_i is the height from the center of the gauge length to the column–footing interface.

The lateral drift component associated with longitudinal bar elongation and slip, Δ_s, was based upon the difference of two rotation magnitudes measured by the two LVDT pairs immediately above the interface (Figure 6.2b). The obtained rotation, θ_s, was then multiplied by the column shear span to acquire the slip displacement component (Equation 6.3).

$$\Delta_s = \theta_s . L \qquad \text{Equation 6.3}$$

The lateral displacement due to shear, Δ_{sh}, was obtained using the readings of two pairs of LVDTs fixed diagonally over the south face of the column (Figure 6.2b). The shear distortion angle, γ, was obtained using the readings of each pair of diagonal LVDTs as follows:

$$\gamma = \frac{\delta_1 - \delta_2}{2\ell_j}(\tan\alpha + \cot\alpha) \qquad \text{Equation 6.4}$$

where δ_1 and δ_2 are deformations of the intersecting diagonal LVDTs, taken as positive in case of elongation and negative for contraction; ℓ_j and α are the initial length and angle of inclination to the horizontal for each LVDT, respectively.

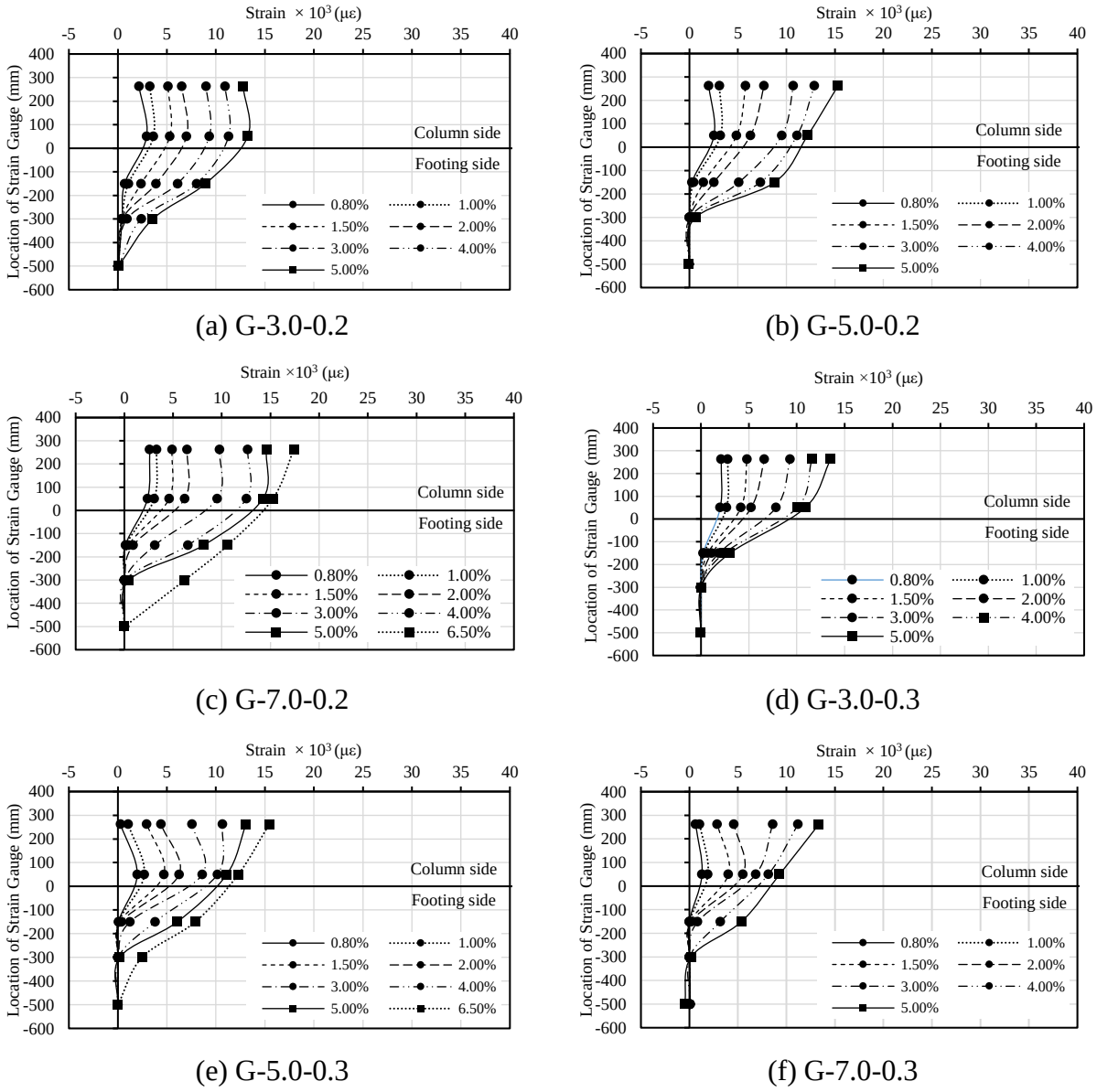

(a) G-3.0-0.2

(b) G-5.0-0.2

(c) G-7.0-0.2

(d) G-3.0-0.3

(e) G-5.0-0.3

(f) G-7.0-0.3

Figure 6.11: Strain profile in the outermost longitudinal bar

The percentages of individual drift components at each drift step for the tested specimens were depicted by Figure 6.13, with an overall error of 5% or less. Generally, the flexure drift component consistently increased from the beginning of displacement history up to failure. In addition, the variation of displacement components indicated a more stable response for specimens with aspect ratios of 5.0 and 7.0. Moreover, the contribution of the displacement associated with bar elongation and slip did not exceed 31% for the specimens with aspect ratios of 5.0 or 7.0, which was much less than similar steel-RC specimens found in the literature, where the slip drift component was

close to 45% (Lehman and Moehle 1999). For the specimens with aspect ratios 5.0 and 7.0, the response was mainly dictated by the flexure component with considerable portion attributed to bar slippage (11 to 17% except for G-5.0-0.3), while the displacement due to shear distortion did not exceed 6% at most. Conversely, G-3.0 -0.2 and G-3.0-0.3 exhibited larger contributions for the slip and shear deformations.

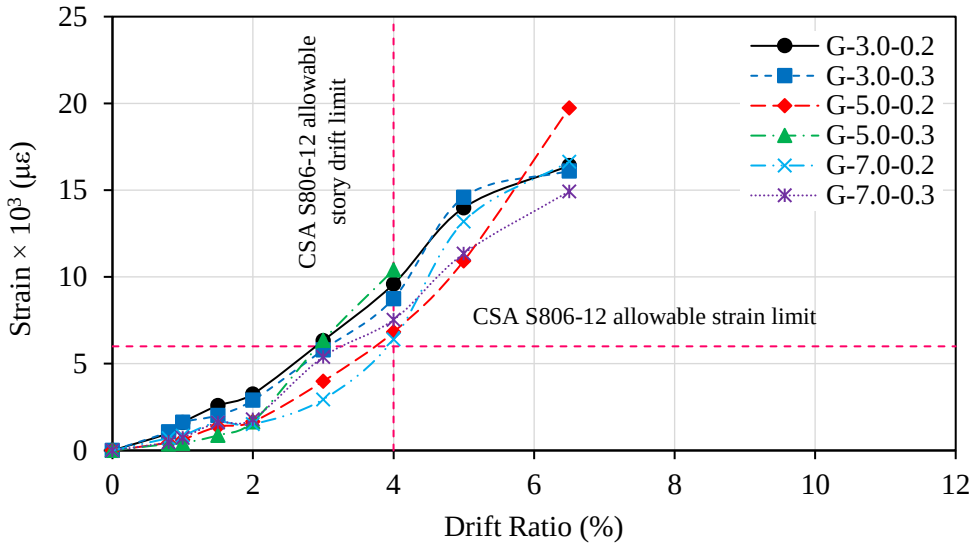

Figure 6.12: Maximum spiral strain versus drift ratio

The relative contribution of shear deformation, recorded at a drift ratio of 4.00%, was 13% for both specimens with the aspect ratio of 3.0 while the displacement component attributed to bar slip was 26 and 20% of the total lateral drift for G-3.0 -0.2 and G-3.0-0.3, respectively. This corroborated the observations reported for those specimens where more significant shear cracking occurred, yet the failure for such specimens was flexure-controlled. Furthermore, the increased slip displacement component for G-3.0 -0.2 and G-3.0-0.3 compared to their longer counterparts agreed well with the larger strains along the embedded portion of longitudinal bars observed for G-3.0 -0.2 and G-3.0-0.3. Increasing the aspect ratio from 3.0 to 5.0 resulted in a significant increase in flexure drift component along with sharp decrease in the displacement due to shear distortion and/or bar slippage, whereas the increase of aspect ratio from 5.0 to 7.0 hardly affected the shear component. Increasing the axial load level was accompanied by an increase in the shear drift component at the expense of the lateral displacement due to slip for the specimens with aspect ratio of 3.0, whereas the slip component increased with a concurrent decrease of flexure-induced

drift for the aspect ratio of 5.0. On the other hand, the effect of axial load was minimal for the specimens with 7.0 aspect ratio in terms of variation of displacement components.

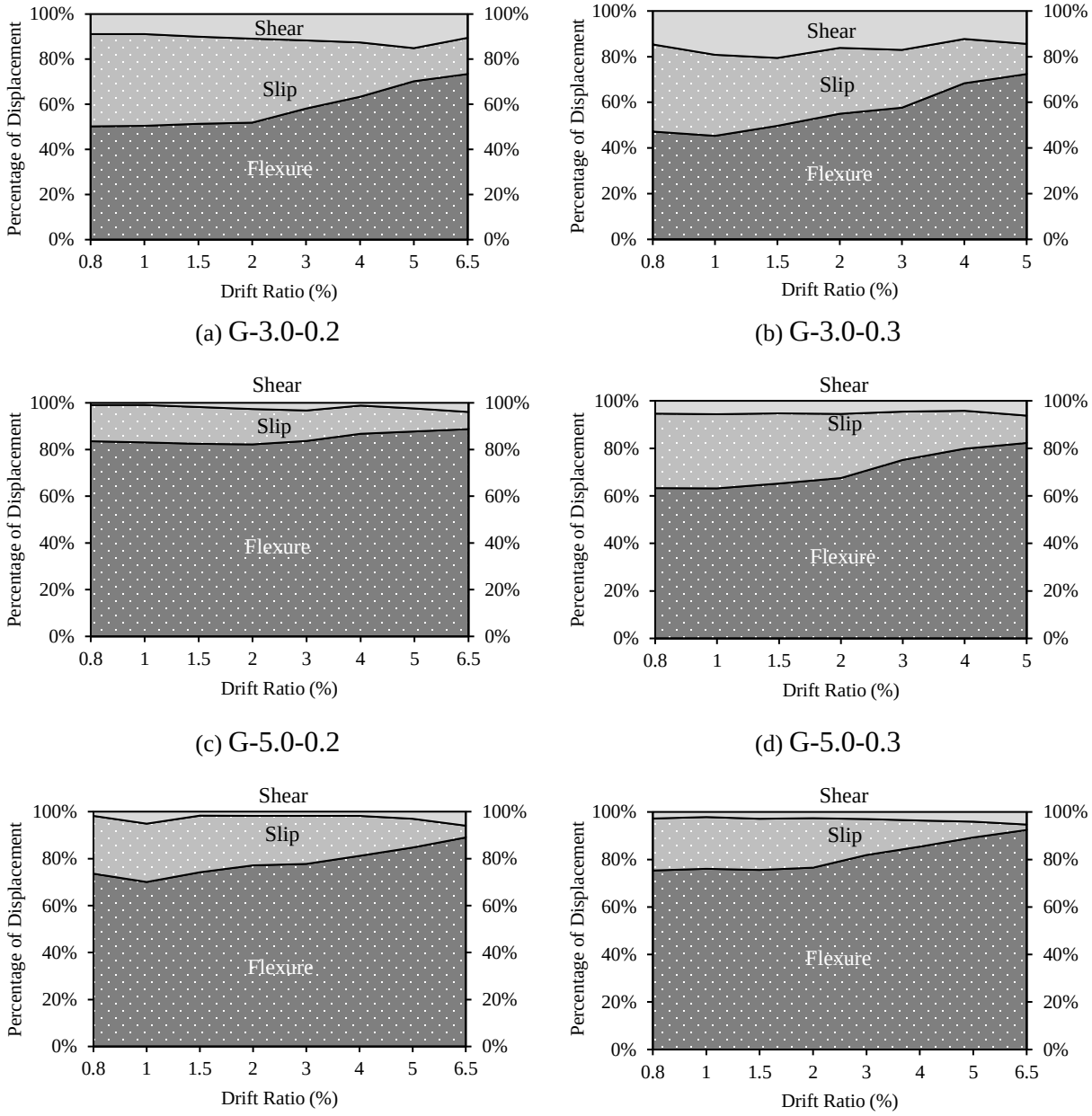

(a) G-3.0-0.2 (b) G-3.0-0.3

(c) G-5.0-0.2 (d) G-5.0-0.3

(e) G-7.0-0.2 (f) G-7.0-0.3

Figure 6.13: Contribution of displacement components to overall lateral drift

6.5. Recommendations for Confinement Reinforcement Design

As previously discussed, the requirement of Clause 12.7.3.3 of CSA S806-12 (CSA 2017) for seismic design of confinement reinforcement in FRP-RC columns is too conservative and need to be reasonably relaxed. According to the design model by Saatcioglu and Razvi (2002), from which the aforementioned design equation was derived, the model was developed based on results of an aspect ratio of 2.5. Furthermore, the drift capacity increased be 75% when the aspect ratio increased from 2.5 to 5.0 (Saatcioglu and Razvi 2002). Therefore, it was suggested to increase the design drift in Clause 12.7.3.3 of CSA S806-12 (CSA 2017) by 55%, which means decreasing the required amount of transverse reinforcement by the same amount, to allow a factor of safety. The resulted modified equation is as follows:

$$A_{sh} = 9sh_c \frac{f_c'}{f_{Fh}} \left(\frac{A_g}{A_c} - 1 \right) \frac{P}{P_o} \frac{\delta}{\sqrt{k_c}} \qquad \text{Equation 6.5}$$

where A_{sh} is the required area of transverse reinforcement; s is the transverse reinforcement spacing; h_c is the cross-sectional dimension of the column core; f_c' is the concrete compressive strength; f_{Fh} is the design stress level in FRP confinement reinforcement, taken as the least of 0.006 E_f or $\phi_f.f_{fu}$ where ϕ_f is the material resistance factor for FRP confinement reinforcement, taken as unity in this study, E_f and f_{fu} are the elastic modulus and ultimate tensile strength of FRP confinement reinforcement, respectively; A_g and A_c are the areas of the gross cross-section and column core, respectively; P/P_o is the axial load level, taken $\geq$ 0.2; δ is the design drift, taken as 0.025 and 0.04 for moderately ductile and ductile MRFs, respectively; and k_c is the confinement efficiency coefficient, taken as unity for circular hoops or spirals and $0.15\sqrt{(h_c/s)(h_c/s_\ell)}$ for rectilinear transverse reinforcement, where s_ℓ is the spacing of tie legs in rectangular columns.

Table 6.4 shows the actual experimental drifts, estimated drifts according to Clause 12.7.3.3 of CSA S806-12 (CSA 2017) and the proposed equation in addition to the ratios of the experimental drift to the estimated ones. Those values were based on the available data from the current study, previous work done by the authors and from literature, including results of circular columns (Tavassoli et al. 2015; Abdallah and El-Salakawy 2021b) and square ones (Ali and El-Salakawy 2016; Elshamandy et al. 2018; Kharal and Sheikh 2020). The utilized results were for GFRP-RC columns only whereas data from steel- or hybrid-reinforced columns were excluded. It should also

be noted that the experimental drifts of Tavassoli et al. (2015) and Kharal and Sheikh (2020) were adjusted to represent the drift ratio as defined earlier herein.

Table 6.4: Experimental and predicted drift ratios

Research	Cross-section shape	Specimen ID	δ_{exp} (%)	CSA S806-12 equation [a]		Proposed equation [b]	
				δ_{CSA} (%)	$\delta_{exp}/\delta_{CSA}$	$\delta_{Proposed}$ (%)	$\delta_{exp}/\delta_{Proposed}$
Current study	Circular	G-3.0-0.2	10.20	5.20	1.96	8.06	1.27
		G-3.0-0.3	6.50	3.11	2.09	4.82	1.35
		G-5.0-0.2	10.20	5.20	1.96	8.06	1.27
		G-5.0-0.3	6.50	3.11	2.09	4.82	1.35
		G-7.0-0.2	10.20	5.20	1.96	8.06	1.27
		G-7.0-0.3	8.15	3.11	2.62	4.82	1.69
Abdallah and El-Salakawy (2021b)	Circular	GN-0.2-50	12.76	9.21	1.39	14.28	0.89
		GH-0.2-85	4.00	2.26	1.77	3.50	1.14
		GH-0.2-50	10.21	3.71	2.75	5.75	1.78
		GH-0.1-50	12.76	7.60	1.68	11.78	1.08
Tavassoli et al. (2015)	Circular	P28-C- 12-50	12.03	7.64	1.57	11.84	1.02
		P28-C- 12-160	4.95	2.39	2.07	3.70	1.34
		P28-C- 16-160	4.29	3.47	1.24	5.38	0.80
		P28-B- 12-50	14.84	8.56	1.73	13.27	1.12
		P42-C- 12-50	7.25	4.89	1.48	7.58	0.96
		P42-C- 12-160	4.95	1.53	3.24	2.37	2.09
		P42-B- 12-160	3.13	1.71	1.83	2.65	1.18
		P42-B- 16-160	5.44	2.33	2.33	3.61	1.51
		P42-B- 16-275	3.46	1.36	2.54	2.11	1.64
Ali and El-Salakawy (2016)	Square	G-1.3-10-75	12.50	3.22	3.88	4.99	2.51
		G-1.9-10-75	8.50	3.18	2.67	4.93	1.72
		G-2.6-10-75	8.50	3.21	2.65	4.98	1.71
		G-1.3-10-100	8.50	2.19	3.88	3.39	2.51
		G-1.3-10-150	6.50	1.31	4.96	2.03	3.20
		G-1.3-15-75	8.50	3.09	2.75	4.79	1.77

		G-1.3-20-75	8.50	2.41	3.53	3.74	2.27
Elshamandy et al. (2018)	Square	G8N13-C1-100	4.20	1.70	2.47	2.64	1.59
		G8N13-C2-100	8.50	3.05	2.79	4.73	1.80
		G12N13-C3-100	3.60	1.61	2.24	2.50	1.44
		G12N13-C4-100	8.30	4.21	1.97	6.53	1.27
		G12N13-C4-100-30	6.20	3.38	1.83	5.24	1.18
		G12N13-C4-100-40	6.40	2.49	2.57	3.86	1.66
		G12N13-C4-150	4.40	2.41	1.83	3.74	1.18
		G12N13-C4-80	8.80	5.30	1.66	8.22	1.07
		G12N19-C4-100	10.10	3.67	2.75	5.69	1.78
Kharal and Sheikh (2020)	Square	TA-P42-G-15	2.93	1.28	3.74	1.98	2.42
		TA-P28-G-16	4.29	4.08	1.72	6.32	1.11

[a] Calculated according to Clause 12.7.3.3 of CSA S806-12 (CSA 2017).
[b] Calculated according to proposed equation (Equation 6.5).

The ratio of experimental-to-code estimated drift ratios ranged between 1.24 to 3.24 for circular columns and 1.66 to 4.96 for square ones, respectively. On the other hand, the range of experimental-to-estimated drift ratios using the proposed equation (Equation 6.5) was 0.96 to 2.09 for circular columns and 1.07 to 3.2 for square ones, respectively. This indicates that the current design equation of Clause 12.7.3.3 of CSA S806-12 (CSA 2017) is more conservative for square GFRP-RC columns than circular ones. It is worth mentioning that there were limited instances where the estimated drift ratios using the proposed equation (Equation 6.5) exceeded the experimental ones, particularly for specimen GN-0.2-50 from Abdallah and El-Salakawy (2021b) and P28-C-16-160 from Tavassoli et al. (2015). Nonetheless, such examples should not be considered as unsafe predictions of design drift as GN-0.2-50 represented a specimen that failed at a drift ratio of 12.76%, which is far beyond the 4.00% drift limit for ductile MRFs (CSA 2017). Furthermore, the experimental failure drift of P28-C-16-160 can be considered as an anomaly as another two specimens from the same study, namely P28-C-12-160 and P42-C-16-160, failed at higher drift ratios despite the fact that the former utilized smaller spiral size and the latter was subjected to larger axial load level than P28-C-16-160, respectively, which should have resulted in lower failure drifts than P28-C-16-160. Moreover, the variation in experimental-to-estimated drift ratios indicates that the relationship between different components, such as concrete strength,

axial load level, transverse reinforcement spacing and confinement efficiency are not linear and far more complicated. For instance, the experimental-to-estimated drift ratio was 1.27, 0.89, 1.14 and 1.78 for specimens G-5.0-0.2, GN-0.2-50, GH-0.2-85 and GH-0.2-50, respectively, where the first two specimens were normal-strength concrete columns confined at a spiral pitch of 85 and 50 mm, whereas the last two were high-strength concrete columns confined at the same spiral pitches, respectively. This implies that the design drift ratio is influenced by the synergistic effect of concrete compressive strength and spiral pitch. Further extensive parametric research is required to enhance the accuracy of the proposed equation, for which finite element modelling could significantly help.

6.6. Conclusions

The following conclusions can be reached based upon the experimental results of this study:

1. The currently available design equation in Clause 12.7.3.3 of CSA S806-12 (CSA 2017) for confinement reinforcement of GFRP-RC columns in earthquake-prone zones was found to be overly conservative. This is due to the common assumption that steel-RC columns with smaller aspect ratios would be less deformable, which seems to be inapplicable to GFRP-RC ones. Therefore, such design equations should be reasonably relaxed according to the current knowledge.
2. As expected, increasing the aspect ratio resulted in a significant decrease in the lateral load capacity, which was more pronounced when the aspect ratio increased from 3.0 to 5.0 rather than when it was further increased to 7.0. On the other hand, a larger aspect ratio hardly influenced the drift capacity, except for the specimen with the aspect ratio of 7.0 and under an axial load level of 30% whose drift capacity exceeded those associated with the shorter counterparts of the former. Similar effect was observed for the change of aspect ratio on the moment at the critical section, which was minimal in general.
3. Increasing the aspect ratio from 3.0 to 5.0 resulted in some reduction of the seismic energy dissipation up to 22%. Insignificant change was noticed, however, for the energy dissipated as the aspect ratio increased from 5.0 to 7.0. Unlike steel-RC columns, the column aspect ratio was found to be directly proportional to hinge length-to-column diameter ratio. Besides, all specimens exhibited sufficient embedment length for their longitudinal bars

into the footings. Furthermore, the variation of aspect ratio had a marginal effect on the strains in the longitudinal or transverse reinforcement.

4. While the theoretical shear analysis according to the Canadian code for FRP-RC structures indicated shear failure for the specimens with the aspect ratio of 3.0, the experimental testing for both specimens resulted in flexure-controlled type of failure. This may reflect that the available shear design provisions in the Canadian code are too strict.
5. Increasing the axial load level from 20 to 30% of the unconfined axial capacity resulted in an increased lateral load capacity accompanied with early strength degradation and lower drift capacity. Such effects were less noticeable as the column aspect ratio increased. For instance, increasing the axial load level resulted in 14 and 3% larger lateral load capacity for specimens with aspect ratios of 3.0 and 7.0, respectively; whereas the failure drift was decreased by 36 and 20% for column aspect ratios of 3.0 and 7.0, respectively. Furthermore, increasing the axial load level enhanced the moment capacity at the critical section by 11, 7 and 7% for column length-to-diameter ratio equal to 3.0, 5.0 and 7.0, respectively. On the other hand, the variation of axial load level was less impactful on the hinge length-to-column diameter ratio, energy dissipation, and longitudinal bars or spirals strains.
6. The analysis of different drift components for the tested specimens revealed higher contribution of shear deformation to the total drift for the specimens with the aspect ratio of 3.0, which concurred well with the visual observations for those specimens. On the other hand, the response of the columns with aspect ratios of 5.0 and 7.0, was mainly dominated by the contributions of flexure and bar elongation and slippage. Generally, the percentage of bar slip drift component for the aforementioned specimens was less than that reported for similar steel-RC columns found in the literature. Moreover, increasing the axial load level had different effects on the drift components for aspect ratios of 3.0 and 5.0, while for the columns with an aspect ratio of 7.0 such effect was marginal.
7. Based on the outcomes of this research, a modified version of the design equation in Clause 12.7.3.3 of CSA S806-12 (CSA 2017) was proposed. The proposed equation resulted in safe and less conservative estimates for drift ratio than the original equation. Furthermore, it was noticed that drift ratio estimates for square columns were more conservative than the predictions for circular columns.

CHAPTER 7: SEISMIC PERFORMANCE OF GFRP-RC CIRCULAR COLUMNS WITH DIFFERENT ASPECT RATIOS AND CONCRETE STRENGTHS

Authors' Affiliations and Roles:

- **Amr E. Abdallah**, PhD Candidate, Department of Civil Engineering, University of Manitoba.
  Role: Methodology, Investigation, Formal analysis, Validation, Visualization and Writing-Original Draft.

- **Ehab F. El-Salakawy**, Professor of Civil Engineering, Department of Civil Engineering, University of Manitoba.
  Role: Conceptualization, Methodology, Writing-Review & Editing, Supervision, Project administration, Resources and Funding acquisition.

Journal and Status:

Elsevier Journal of Engineering Structures, in press.

Reference:

Abdallah, A. E., and El-Salakawy, E. F. 2022. "Seismic performance of GFRP-RC circular columns with different aspect ratios and concrete strengths." *Eng. Struct.*, in press.

Note:

The manuscript had been slightly altered from the original paper by renumbering the tables and figures to include the chapter number. In addition, the reference list and the list of notations have been moved to the appropriate sections in the thesis as indicated in the table of contents.

Abstract

The available code provisions for seismic design of confinement reinforcement in fiber-reinforced polymer-reinforced concrete (FRP-RC) columns, even their most recent versions, are overly conservative. This is due to the limited available research data, particularly those related to high-strength concrete (HSC) columns and those with different aspect ratios. That is, the linear-elastic behavior of FRP could be of concern when combined with the brittle nature of HSC or implemented in shorter columns, which could be significantly influenced by shear stresses. Therefore, this study was conducted to investigate the effects of concrete compressive strength and column aspect ratio on the seismic performance of glass FRP (GFRP)-RC circular columns with variation of spiral pitch and axial load level. Nine full-scale GFRP-RC column-footing connections were cast and tested under concurrent axial loading and reversed-cyclic lateral drifts. Test results proved the conservativeness of the seismic design requirements of the Canadian standards for confinement reinforcement in GFRP-RC circular columns with regard to the effects of HSC and different aspect ratios.

Keywords: Glass fiber-reinforced polymer (GFRP), circular column, seismic loading, high-strength concrete (HSC), aspect ratio, spiral pitch, axial load level.

7.1. Introduction

Over the last two decades, the use of fiber-reinforced polymer (FRP) reinforcement in various reinforced concrete (RC) elements has been gaining more popularity owing to its favorable properties, particularly its non-corrodible nature and low electrical and magnetic conductivity. Due to the differences between the behavior of FRP reinforcement and that of steel, design provisions were developed for FRP-RC members (ACI 2015; CSA 2017; AASHTO 2018; CSA 2019). Compared to steel, FRP reinforcement has different shear and compressive strengths, lower elastic modulus and tensile strain capacity in addition to the linear-elastic behavior up to failure with absence of the yielding phenomenon. The latter, in particular, made the deployment of FRP in earthquake-resisting RC structures dubious since seismic events impose high inelastic displacement demands on the RC structures, for which yielding of steel was a primary source of seismic energy dissipation. Nonetheless, recent studies confirmed the adequacy of utilizing FRP reinforcement under seismic-simulated loading with ample amount of energy dissipation (Tavassoli et al. 2015; Ali and El-Salakawy 2016; Hasaballa and El-Salakawy 2018; Naqvi and El-Salakawy 2017; Elshamandy et al. 2018; Ghomi and El-Salakawy 2019; El-Gendy and El-Salakawy 2020; Abdallah and El-Salakawy 2021a). Most of the aforementioned studies used glass FRP (GFRP) due to its relatively low cost and satisfactory strain capacity compared to other types of FRP.

While the extensive research effort over the last two decades resulted in establishing detailed design provisions for several FRP-RC elements, such as beams and bridge deck slabs, the design of FRP-RC columns is being developed at a much slower pace. This could be evident from the manner in which FRP in compression members is dealt with. For instance, the ACI 440.1R-15 (ACI 2015) guidelines do not allow the use of FRP as main reinforcement in compression members, while less conservative philosophy is adopted by AASHTO LRFD (AASHTO 2018) design guide and the Canadian standards CSA S806-12 (CSA 2017), which allow the use of FRP but neglect its contribution in compression. On the other hand, the CSA-S6-19 standards (CSA 2019d) permits using FRP bars in columns and recognizes their load carrying capacity up to a compressive strain of 0.002. Scarcity of experimental research data could be the reason why FRP-RC column design is handled much cautiously. Furthermore, while many research studies investigated the behavior of FRP-RC columns under monotonic loading configurations (Pantelides

et al. 2013; Tobbi et al. 2014; Hadi et al. 2016; Guérin et al. 2018; Liu et al. 2019; Abdelazim et al. 2020; Barua and El-Salakawy 2020; Barua et al. 2021), the available experimental outcomes for FRP-RC columns under seismic loading are rather limited (Tavassoli et al. 2015; Ali and El-Salakawy 2016; Naqvi and El-Salakawy 2017; Elshamandy et al. 2018; Kharal and Sheikh 2020; Abdallah and El-Salakawy 2021a). Replacing conventional steel reinforcement with GFRP resulted in reduced shear and moment capacities, while the deformability and member behavior were substantially improved in addition to stable hysteretic responses. In addition, the concept of deformability in GFRP-RC members substituted for the ductility of steel-RC ones. Moreover, marginal effect was observed for the surface texture of GFRP or transverse reinforcement size on the seismic performance of GFRP-RC columns (Tavassoli et al. 2015). Furthermore, circular GFRP hoops with a minimum splice length of 60 times the hoop size provided a comparable confinement to GFRP spirals (Abdallah and El-Salakawy 2021a).

Yet, many research gaps are present within the current seismic design provisions for FRP-RC columns. The currently available seismic design equation for confinement reinforcement of FRP-RC columns in Clause 12.7.3.3 of CSA S806-12 (CSA 2017), for example, limits its applicability to a maximum concrete compressive strength of 80 MPa, while all available research data are for columns having a concrete compressive strength of 55 MPa, or less. While the use of high-strength concrete (HSC) is widespread due to its appealing strength and durability (ACI 2002), its brittle behavior may raise concerns on its adequacy, especially when combined with FRP reinforcement. Few studies were dedicated to investigate the performance of GFRP-reinforced HSC columns under monotonic loading schemes (Hadhood et al. 2017; Hadi et al. 2017; Hasan et al. 2017; Hasan et al. 2019), where GFRP-reinforced HSC columns were more influenced by the variation of transverse and longitudinal reinforcement ratio for axially- and eccentrically-loaded columns, respectively. Additionally, incorporating HSC resulted in larger load and moment magnitudes whereas the deformability of columns was significantly decreased. Moreover, the influence of decreasing the spiral pitch was more pronounced for GFRP-reinforced normal-strength concrete (NSC) columns than HSC counterparts.

Furthermore, the design equation in Clause 12.7.3.3 of CSA S806-12 (CSA 2017) was conceptually based upon the design model developed by Saatcioglu and Razvi (2002) for steel-RC columns, which assumed that longer columns should be more deformable. Such assumption was

rebutted later by Bae and Bayrak (2008), where increasing the axial load level resulted in less deformability for the steel-RC columns with larger aspect ratio. The impact of column aspect ratio is not yet addressed for GFRP-RC columns, except few studies incorporating carbon FRP (CFRP) (Sharbatdar 2003), fiber-reinforced concrete (Deng et al. 2018), or hybrid reinforcement configuration (i.e. steel for longitudinal bars and GFRP for transverse reinforcement) (Kharal et al. 2021).

This study is a part of a comprehensive research program aiming at investigating the confinement characteristics of GFRP-RC columns (Ali and El-Salakawy 2016; Naqvi and El-Salakawy 2017; Abdallah and El-Salakawy 2021a). The main goals of this paper are to study the effects of concrete strength, column aspect ratio, axial load level and spiral pitch on the performance of GFRP-RC circular columns under earthquake-simulated loading. Besides, re-evaluating the available code provisions for seismic design of FRP-RC columns is another crucial aspect of this research.

7.2. Experimental Program

7.2.1. Test specimens

Nine full-scale circular column specimens were cast and tested under simultaneous constant axial loading and reversed cyclic lateral drifts. Out of these specimens, three were tested in an earlier phase of the research program [12], as listed in Table 1. For each column, a rigid 1,400 × 900 × 600-mm footing adequately reinforced with size 15M (16-mm diameter) steel bars to ensure sufficient rotation fixity for the column and safeguard the footing against cracking during cyclic drift reversals. Each column had a 510 × 440 × 400-mm RC head at its top to facilitate applying the lateral loads (Fig. 1). This head was reinforced with 6-15M steel longitudinal bars and 4-10M steel ties to ensure safe transfer of axial and lateral loads to the column without cracking. Test specimens were modeled after the lower portion of a column between the top surface of the footing and the contra-flexure point of the column, which resembled the bottommost segment of a bridge pier column bent in double curvature or a first-story column in a multistory moment-resisting frame (MRF) construction. All columns had a diameter of 350 mm, and a clear concrete cover of 20 mm. The shear span, defined as the vertical height of the line of action for lateral loading from the column–footing interface, was either 1,750 or 2,450 mm, resulting in an aspect ratio (i.e. length-to-diameter ratio) of 5.0 and 7.0, respectively. The smaller aspect ratio represented a bridge

pier with moderate clearance height or a column in a typical MRF structure, while the larger aspect ratio simulated a highway overpass pier with adequate vertical clearance or a column in a reception hall at the entrance of a building.

Test specimens were designed according to the available codes and guidelines (CSA 2017; AASHTO 2018; CSA 2019d) in addition to the recommendations of recent studies (Tavassoli et al. 2015; Ali and El-Salakawy 2016; Abdallah and El-Salakawy 2021a), as appropriate. Consequently, each column was reinforced longitudinally by six No. 16 (15.9-mm diameter) GFRP bars, embedded through the entire thickness of the footing, whereas the confinement reinforcement was provided as No. 10 (9.5-mm diameter) GFRP spirals. However, the spiral pitch was either 85 or 50 mm, following the maximum spacing allowed in accordance with Clauses 12.7.3.4 and 8.4.3.13 of CSA S806-12 (CSA 2017), respectively. The details of reinforcement configuration are depicted by Figure 7.1. Normal-strength concrete (NSC) was utilized to construct only five specimens, while the other four specimens were cast using high-strength concrete (HSC). The casting followed the typical sequence in practice, where the footing was cast first, then, the column formwork was built and the column was cast afterwards.

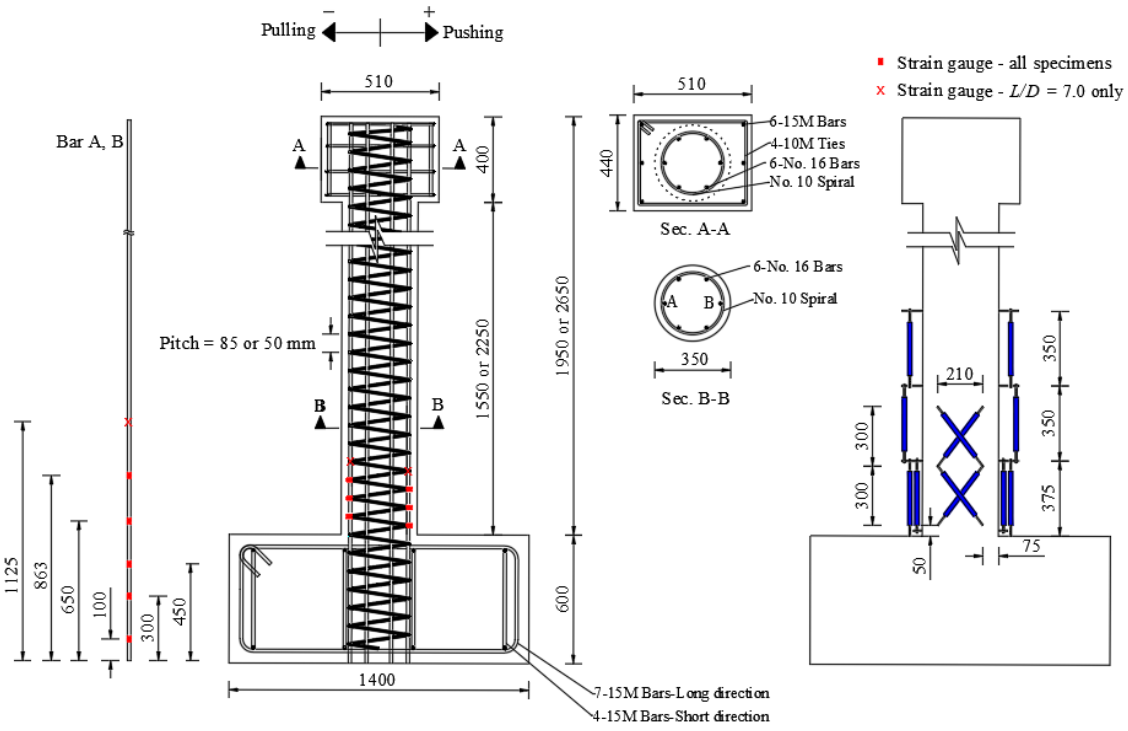

(a) Details of reinforcement and locations of strain gauges (b) Configuration of LVDTs

Figure 7.1: Details of test specimens and instrumentation (all dimensions in mm)

The designation of the test specimen was in the form of alphanumeric code; where the first letter, G, refers to the GFRP reinforcement used for all specimen; whereas the second letter is either N or H for specimens cast using NSC or HSC, respectively; the third number indicates the column aspect ratio; the fourth fraction denotes the axial load level, expressed as a ratio of the applied axial load, P, to the unconfined axial capacity of the column, P_o (0.2 or 0.3); the fifth number defines the spiral pitch. The characteristics of the test matrix are listed in Table 7.1.

Table 7.1: Properties of test specimens

Specimen ID	L/D	P/P_o	V_{cr} (kN)	f_c' (MPa)	s (mm)	L_i (mm)
GN-5.0-0.2-85[a]	5.0	0.2	25	36.9 ± 0.4	85	525
GN-5.0-0.2-50[a]	5.0	0.2	25	36.0 ± 2.0	50	500
GN-5.0-0.3-85[a]	5.0	0.3	30	41.4 ± 0.7	85	525
GH-5.0-0.2-85	5.0	0.2	62	86.4 ± 2.4	85	650
GH-5.0-0.2-50	5.0	0.2	62	89.4 ± 1.8	50	420
GN-7.0-0.2-85	7.0	0.2	28	44.7 ± 0.8	85	680
GN-7.0-0.3-85	7.0	0.3	37	43.2 ± 0.3	85	660
GH-7.0-0.2-85	7.0	0.2	50	75.5 ± 1.1	85	620
GH-7.0-0.2-50	7.0	0.2	50	81.4 ± 0.7	50	420

Note: L/D = column aspect ratio; P/P_o = axial load level; V_{cr} = applied lateral cracking load; f_c' = concrete compressive strength; s = spiral pitch; and L_i = average length of hinging region.
[a] Specimens tested by Abdallah and El-Salakawy (2021a).

7.2.2. Materials

The physical and mechanical properties of the used sand-coated GFRP bars and spirals, shown in Figure 7.2, are listed in Table 2. These properties were provided in the compliance certificate issued by the manufacturer (Pultrall Inc. 2019), which were verified by laboratory testing (CSA 2017), as appropriate; are listed in Table 7.2. It should be noted that the properties of the GFRP spirals were acquired from tests on straight bars of the same parent source material, size and manufacturing process. Besides, all specimens were cast using normal-weight, ready mixed concrete with maximum aggregated size of 20 mm, while the target 28-day compressive strength was either 35 or 80 MPa for NSC and HSC specimens, respectively. To obtain the actual

compressive strength of the columns on the day of testing (Table 7.1), standard 100 × 200-mm concrete cylinders were tested as per CSA A23.1-19/A23.2-19 (CSA 2019a). Test specimens and standard cylinders were cast in the laboratory using the same concrete batch, then they were wet-cured together for 7 days. Afterwards, specimens were left to cure in the laboratory atmosphere until the day of testing.

Table 7.2: Mechanical properties of the utilized GFRP reinforcement

Bar type	Nominal diameter (mm)	Area (mm^2)	Modulus of elasticity (GPa)	Tensile strength (MPa)	Ultimate strain (%)
No. 16	15.9	197.9 [a] (235) [b]	65.7 [c]	1,711 [d]	2.60 [d]
No. 10 (Spirals)	9.5	71 [a] (83) [b]	58.4 [c]	1,376 [d, e]	2.36 [d, e]

[a] Nominal area in accordance with CSA S807-19 (CSA 2019c).
[b] Measured area in accordance with Annex A of CSA S806-12 (CSA 2017).
[c] Measured in accordance with Annex C of CSA S806-12 (CSA 2017).
[d] Calculated using nominal area and average force according to Annex C of CSA S806-12 (CSA 2017).
[e] Obtained from tests on straight bars having the same diameter and properties according to Annex C of CSA S806-12 (CSA 2017).

(a) Longitudinal bars (b) Spirals

Figure 7.2: Samples of GFRP reinforcement

7.2.3. Test setup and instrumentation

The specimens were subjected to constant axial loading applied using a 2,000-kN capacity hydraulic jack, which transferred its reactions to the laboratory strong floor through a hinged steel frame, comprised of a stiffened steel spreader I-beam pinned to two hollow steel section (HSS) link members, pinned to two rigid RC blocks at the bottom. Additionally, a fully-dynamic

hydraulic actuator, with ±1,000-kN and ±250-mm load and stroke capacities, respectively, was utilized to apply the lateral load and drift cyclic reversals. The actuator was horizontally mounted on a strong reaction wall, where the positive and negative signs indicated pushing and pulling directions, respectively. The mid-height of the column head was aligned with the line of action of the actuator by placing the specimen above an RC leveling slab. High-strength threaded bars were utilized to anchor the footing of each specimen, RC leveling slab and blocks to the laboratory strong floor. To accommodate the different aspect ratios, the height of the actuator above the laboratory floor, the HSS link members, RC blocks and leveling slab were changed, as shown in Figure 7.3.

Each specimen had sixteen or twenty electrical strain gauges for aspect ratio of 5.0 or 7.0, respectively, attached to several locations along the outermost longitudinal bars and spiral above the column–footing interface, as illustrated by Figure 7.1a. To monitor the different components of the lateral drift; namely, the displacement component due to flexure, slip or shear, six pairs of linear variable displacement transducers (LVDTs) were fixed along a height of 1,075 mm with the configurations shown in Figure 7.1b. Three pairs of LVDTs were fixed vertically with a gauge length of 350 mm, with the bottommost pair attached with the lower ends at 25 mm above the column–footing interface, to measure the flexure displacement component. As the drift component due to longitudinal bar elongation and slippage cannot be measured independently, another vertical pair of LVDTs was attached with its bottom ends fixed at the upper surface of the footing to measure the combined component due to flexure, over the gauge length of the LVDTs, and to slippage. In addition, to measure the shear displacement component, if any, two pairs of LVDTs were fixed diagonally across the column between the vertical LVDTs with the arrangement described in Figure 7.1b.

7.2.4. Loading procedure

The test commenced by applying the specified axial load that was calculated as a ratio of the nominal unconfined axial capacity of the column, P_o (CSA 2017):

$$P_o = \alpha_1 \phi_c f_c^{'} (A_g - A_F) \qquad \text{Equation 7.1}$$

where α_1 is the ratio of average stress in the rectangular compression block to the specified concrete compressive strength (f_c'); ϕ_c is the resistance factor for concrete, which was taken equal to unity;

A_g is the gross cross-sectional area of the column; and A_F is the area of the main FRP longitudinal reinforcing bars. The lateral loading was applied thereafter; starting with a load-controlled phase followed by a 0.01-Hz displacement-controlled phase, as shown in Figure 7.4.

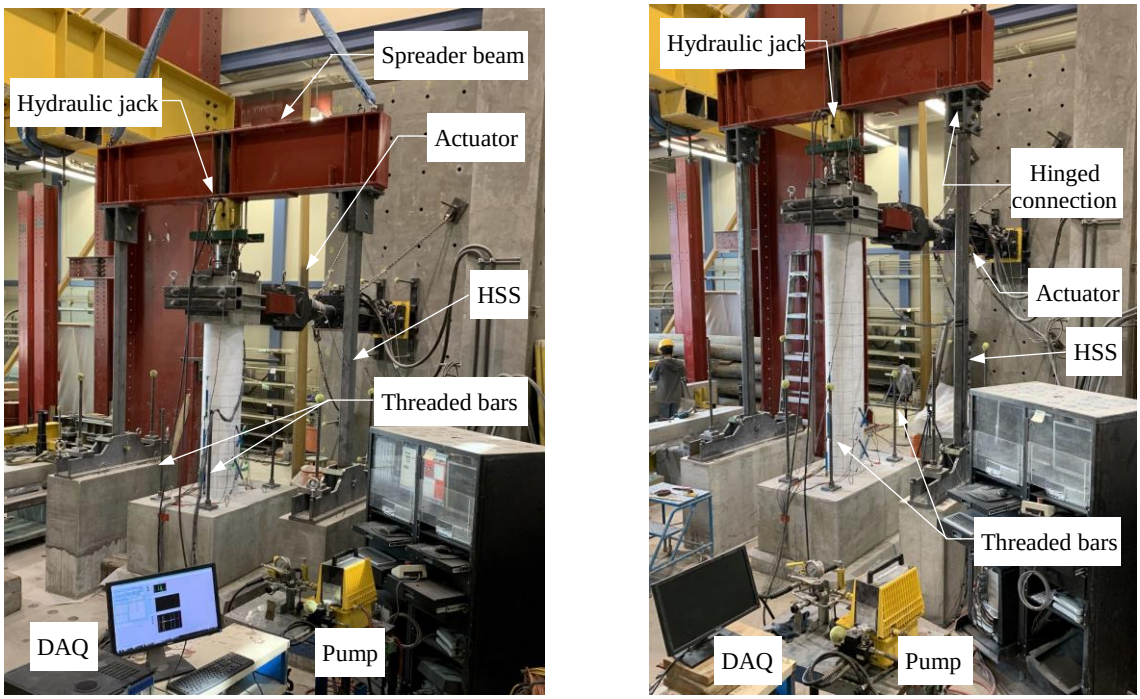

(a) Aspect ratio = 5.0 (b) Aspect ratio = 7.0

Figure 7.3: Test setup

For the load-controlled phase, two consecutive cycles were applied with a peak load corresponding to concrete first crack for one and concrete compressive strain at service stage for the other. The latter was obtained from a theoretical steel-RC specimen (CSA 2019b) equivalent in reinforcement configuration to that under consideration, reinforced with GFRP (Ali and El-Salakawy 2016; Abdallah and El-Salakawy 2021a). The displacement history was applied afterwards, in the form of quasi-static cyclic lateral drift reversal steps, to simulate seismic excitations, following the guidelines of ACI 374.1-05(19) (ACI 2019b). To guarantee a stable crack propagation, three identical cycles, in terms of drift ratio (i.e. obtained from dividing the lateral displacement at mid-height of the column head by the shear span of the column), were applied per drift step. To assess the stiffness degradation, if any, a load-controlled service cycle was applied following each drift step beyond a drift ratio of 2.00% (Ali and El-Salakawy 2016; Abdallah and El-Salakawy 2021a).

It should be noted that the peak load for such individual cycles was equal to the service load determined during the load-controlled phase.

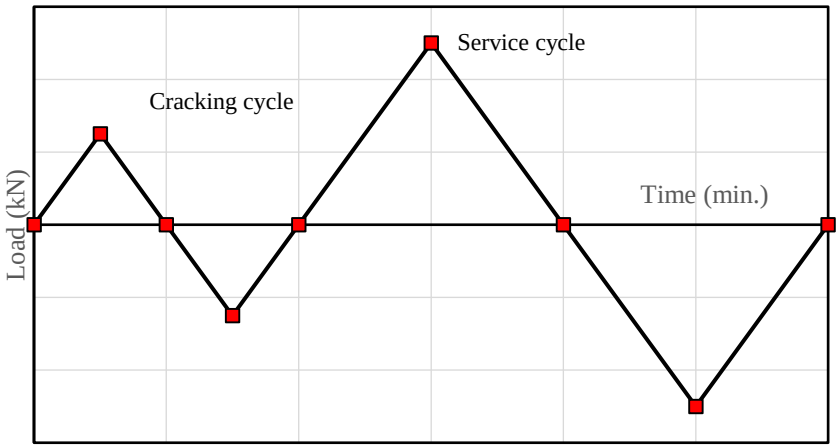

(a) Load-controlled phase

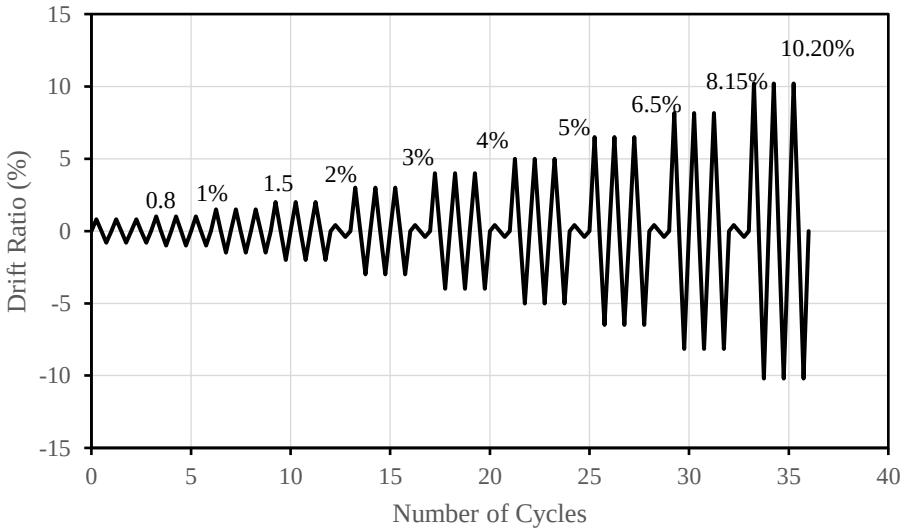

(b) Displacement-controlled phase

Figure 7.4: Lateral loading procedure

7.3. Experimental Results and Discussion

7.3.1. General observations and modes of failure

As shown in Figure 7.5, the failure was controlled by flexure for all specimens. It could also be noticed from Table 7.1 that the lateral cracking load increased as the axial load level or concrete

strength increased, or as the aspect ratio decreased. This can be attributed to the fact that increasing the axial load level imposes more compressive stresses on the column cross-section, thus requiring higher lateral load for the concrete to be cracked. Because the tensile strength of concrete is proportional to its compressive strength, increasing the concrete compressive strength would demand larger lateral load to exceed the tensile strength of concrete and cause cracking. On the other hand, as the shear span of the column increase, while the cracking moment of the column is presumably the same, the lateral cracking load is expected to decrease. In addition, concrete cover spalling was initiated at a drift ratio of 2.00% for GN-5.0-0.3-85, and GH-5.0-0.2-85; 3.00% for GN-5.0-0.2-85, GN-5.0-0.2-50, GN-7.0-0.3-85, GH-5.0-0.2-50, GH-7.0-0.2-85, and GH-7.0-0.2-50; and 4.00% for GN-7.0-0.2-85, respectively. Besides, the test parameters significantly affected the failure drift and mode of failure of the tested specimens. For NSC specimens, GN-5.0-0.2-85, GN-5.0-0.2-50 and GN-5.0-0.3-85 failed at 10.20, 12.75 and 6.50% drift ratio, respectively, experiencing a concurrent compression failure of the outermost longitudinal bar and concrete core crushing for all three specimens. Increasing the aspect ratio resulted in a failure drift of 10.20 and 8.15% for GN-7.0-0.2-85, and GN-7.0-0.3-85, respectively. The failure was characterized by concrete core crushing along with the outermost longitudinal bar failing in compression, followed by spiral rupture for GN-7.0-0.2-85, whereas the crushing of concrete core was accompanied by three-bar compression failure and spiral rupture for GN-7.0-0.3-85.

The failure of HSC specimens was, as expected, more sudden and brittle than the NSC counterparts. Specimen GH-5.0-0.2-85 failed at 4.00% drift ratio due to a sudden simultaneous failure of concrete core and spiral rupture. Contrarily, GH-5.0-0.2-50 failed at 10.20% due to a combination of concrete core devastation and compression failure of an outermost longitudinal bar, immediately followed by failure of three more longitudinal bars, including the other outermost one, and spiral rupture. For the specimens with the aspect ratio of 7.0, failure occurred at a drift ratio of 4.00 and 10.20% for GH-7.0-0.2-85 and GH-7.0-0.2-50, respectively. Although GH-7.0-0.2-85 technically failed at 4.00% drift ratio as it exhibited 28.1% strength degradation during the third cycle of that drift step, the specimen exhibited failure manifestations during 6.5% drift ratio. Combined concrete core crushing, three-bar compression failure on one side, buckling of the other three bars and spiral rupture marked the failure of GH-7.0-0.2-85. Conversely, the failure of GH-7.0-0.2-50 was identified by concrete core crushing in conjunction with failure of both outermost longitudinal bars.

(a) GN-5.0-0.2-85

(b) GN-5.0-0.2-50

(c) GN-5.0-0.3-85

(d) GH-5.0-0.2-85

(e) GH-5.0-0.2-50

(f) GN-7.0-0.2-85

(g) GN-7.0-0.3-85

(h) GH-7.0-0.2-85

(i) GH-7.0-0.2-50

Figure 7.5: Test specimens at failure

Table 7.3: Test results versus predicted values

Specimen ID	Theoretical capacity		Experimental lateral capacity		
	Lateral load (kN)	Drift[a] (%)	Maximum (kN)	At failure (kN)	Strength Degradation (%)
GN-5.0-0.2-85	54.0	5.20	+94.1 at 4.00% drift -96.0 at -10.20% drift	+58.8 at 10.20% drift	37.5
GN-5.0-0.2-50	54.0	9.21	+103.3 at 8.15% drift -115.6 at -10.20% drift	+94.0 at 12.50% drift	9.0
GN-5.0-0.3-85	58.0	3.11	+101.2 at 2.00% drift –77.5 at -2.00% drift	+73.0 at 6.50% drift	27.9
GH-5.0-0.2-85	98.0	2.26	+145.3 at 2.00% drift -117 at -2.00% drift	+115.0 at 4.00% drift	20.9
GH-5.0-0.2-50	98.0	3.71	+146.5 at 4.00% drift -121.5 at -8.15% drift	+108.0 at 8.75% drift	26.3
GN-7.0-0.2-85	38.6	5.20	+68.8 at 4.00% drift -67.7 at -10.20% drift	+56.8 at 10.20% drift	17.4
GN-7.0-0.3-85	41.4	3.11	+70.4 at 3.00% drift -69.1 at -4.00% drift	+64.0 at 8.15% drift	9.1
GH-7.0-0.2-85	70.0	2.26	+96.7 at 3.00% drift -85.3 at -2.00% drift	+69.5 at 4.00% drift	28.1
GH-7.0-0.2-50	70.0	3.71	+109.6 at 4.00% drift -98.5 at -8.15% drift	+63.75 at 7.63% drift	41.8

[a] Calculated as per Clause 12.7.3.3 of CSA S806-12 (CSA 2017).

Generally, increasing the axial load level had a marginal effect on the average length of the cover spalling region, L_i, as indicated by the values listed in Table 7.1. In addition, increasing the aspect ratio resulted in longer length of the hinging region for NSC specimen, while the influence was the opposite for the HSC specimens. This indicates a more complex impact for aspect ratio for GFRP-RC columns than that reported for steel-RC ones (Sakai and Sheikh 1989), where negligible influence on the plastic hinge length was noticed when the aspect ratio exceeded 4.0, regardless of the concrete compressive strength. Furthermore, the effect of concrete strength on the length of the spalling region was dependent upon the level of confinement; that is, increasing the concrete strength caused an increase in the hinge length for the specimens with 85-mm spiral pitch (i.e. GN-5.0-0.2-85 and GH-5.0-0.2-85), while the opposite occurred for the specimens with a spiral pitch of 50 mm (i.e. GN-5.0-0.2-50 and GH-5.0-0.2-50).

7.3.2. Effect of concrete strength

Increasing the concrete strength was accompanied by early commencement of cover spalling (i.e. at lower drift ratio) for the specimens with the 85-mm spiral pitch, which agreed with the experimental findings for steel-RC columns under simulated seismic loading (ACI 2002) and GFRP-RC ones under axial and eccentric loading (Hadi et al. 2017). Conversely, increasing the concrete strength did not affect the cover spalling initiation for the well-confined columns (i.e. columns confined with spirals at 50-mm pitch). Figure 7.6 shows the hysteretic diagrams for the tested specimens. All specimens exhibited narrow hysteretic loops with their unloading branches aiming towards the origin, which is typical for GFRP-RC columns due to the linear-elastic behavior of GFRP bars (Tavassoli et al. 2015; Ali and El-Salakawy 2016; Naqvi and El-Salakawy 2017; Elshamandy et al. 2018; Kharal and Sheikh 2020; Abdallah and El-Salakawy 2021a). As shown in Figure 7.7, which depicts the envelopes of the hysteretic diagrams, larger initial stiffness can be observed for the HSC specimens compared to NSC ones, regardless of the aspect ratio. Such observation can be attributed to the fact that increasing the concrete strength results in an increase of the concrete elastic modulus and, in turn, the stiffness of the RC member. Additionally, GH-5.0-0.2-85 and GH-5.0-0.2-50 exhibited larger lateral load capacity than their NSC counterparts, GN-5.0-0.2-85 and GN-5.0-0.2-50, by 55 and 42%, respectively. Nonetheless, such augmentations were attained to the detriment of the drift capacity (i.e. the largest full drift step reached by the specimen), which was decreased by 63 and 20% for GH-5.0-0.2-85 and GH-5.0-0.2-50, respectively. Similarly, the lateral load capacity of GH-7.0-0.2-85 increased by 29% compared to that of GN-7.0-0.2-85, accompanied by a decrease in drift capacity by 63% for the former. This can be justified by the behaviour of HSC, where the larger concrete strength results in an increase of the capacity of the concrete stress block and ultimate confined strain, which results in larger moment capacity, and, hence, lateral load capacity. However, it is well-established that increasing the concrete strength results in more brittle behaviour, which negatively affects deformability of concrete. This could be, however, overcome by increasing the confinement to the concrete core. Table 7.3 summarizes the experimental lateral load capacity along with theoretically predicted load and drift capacities (CSA 2017). Although the applied axial load was considered for the theoretical estimation of lateral load capacity, ignoring the contribution of GFRP in compression and confinement of the concrete core (CSA 2017) could be the reason for the lower theoretical load capacities with respect to the experimental ones. Generally, all specimens reached

drift capacities beyond the drift limit of 4.00% required by the Canadian standards (CSA 2017) for ductile MRFs except for GH-5.0-0.2-85 and GH-7.0-0.2-85. Nonetheless, those specimens were able to surpass their theoretically predicted failure drift (2.26%) and the drift limit of 2.50% set by the National Building Code of Canada (NRCC 2020) and the Canadian standard CSA S806-12 (CSA 2017) for moderately ductile MRFs.

It is well-established that the seismic energy could be dissipated in earthquake-resistant RC structures by means of inelastic deformations of concrete and reinforcing bars within hinging regions in addition to concrete cracking. Despite the currently adopted strong column-weak beam philosophy for design of RC structures in seismic-active regions (ACI 2019a, CSA 2017), hinging at bottom of bridge supports or first-story columns in MRFs is unavoidable as long as economic design approaches are implemented. Investigating the cumulative energy dissipated by an RC element, calculated as the area defined by the hysteresis loops, is an insightful tool to explore its damping capability. As plotted in Figure 7.8, at the 4.00% drift limit set by CSA S806-12 (CSA 2017), increasing the concrete strength caused significant increase in energy dissipation by 71, 63 and 63% for GH-5.0-0.2-85, GH-5.0-0.2-50 and GH-7.0-0.2-85, respectively, compared to their NSC counterparts. The main reason for such superior energy dissipation of HSC columns is the fact that at each drift step, the lateral load resistance endured by the HSC columns was much larger.

The maximum strains in the outermost longitudinal bars exhibited by the HSC specimens were comparable to their NSC equivalents up to 2.00% drift ratio (Figure 7.9), while higher reinforcement strains were recorded for the HSC columns thereafter. Furthermore, the distribution of the maximum strain values along the outermost longitudinal bars was plotted in Figure 7.10. For all specimens, diminishing of strains within the embedded length of the longitudinal GFRP bars confirmed the adequacy of their provided development length. At each drift step, similar strain values can be observed for each two counterpart specimens with different concrete strengths. Nonetheless, smaller strain penetration through the embedded length can be noticed for the HSC specimens compared to their NSC equivalents, which could be due to the enhanced bond strength of the former.

For the maximum spiral strains, as depicted by Figure 7.11, the maximum spiral strains in GH-5.0-0.2-85 and GH-7.0-0.2-85 significantly exceeded those recorded in GN-5.0-0.2-85 and GN-

7.0-0.2-85 beyond a drift ratio of 1.50%, increasing by 86 and 137% with respect to their NSC counterparts at 4.00% drift ratio, respectively. Such increases can be attributed to the larger magnitude of axial load applied to the HSC specimens, which results in higher lateral expansion for the concrete core and, hence, larger spiral strains.

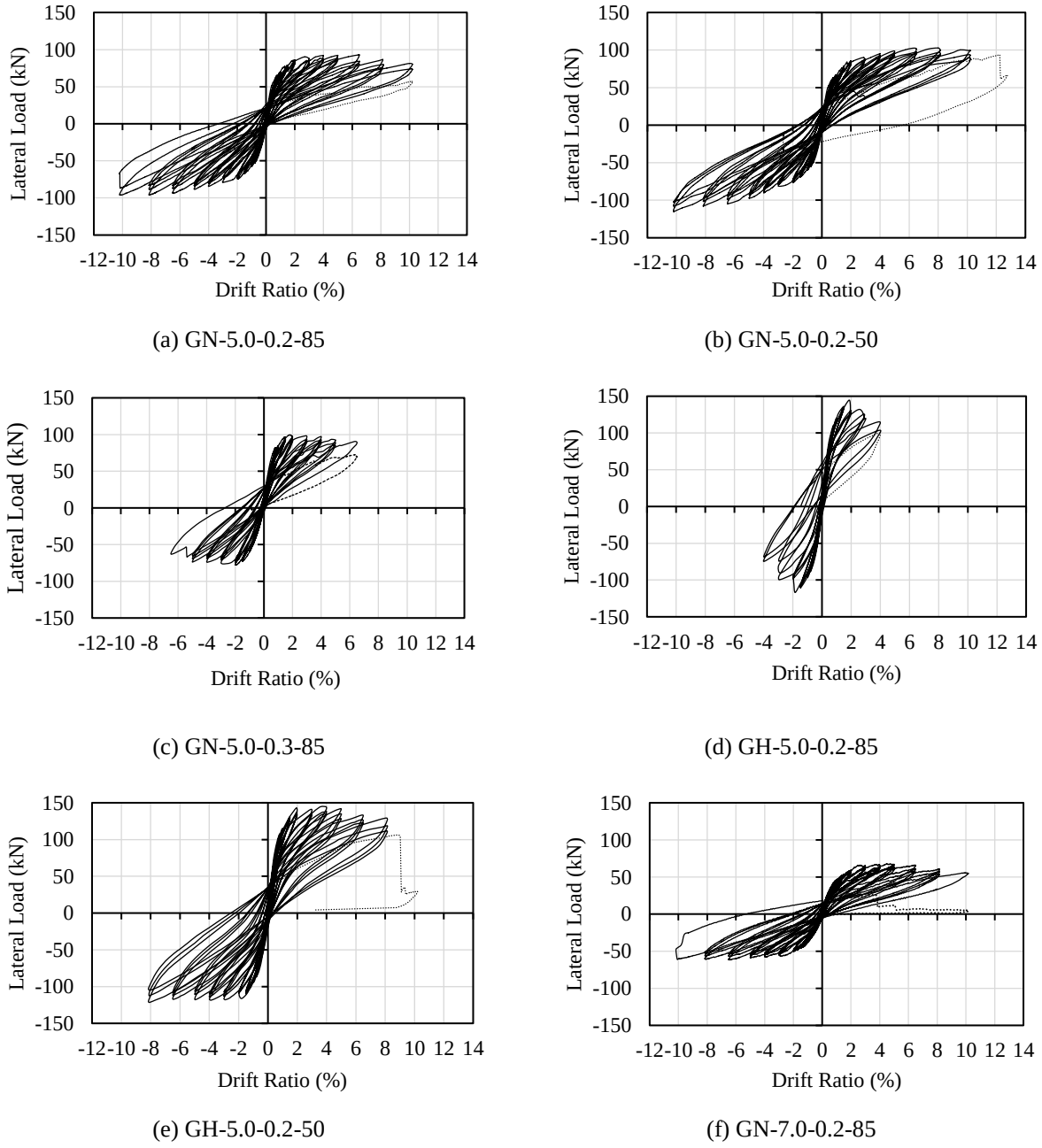

(a) GN-5.0-0.2-85

(b) GN-5.0-0.2-50

(c) GN-5.0-0.3-85

(d) GH-5.0-0.2-85

(e) GH-5.0-0.2-50

(f) GN-7.0-0.2-85

Figure 7.6: Hysteresis diagrams for test specimens

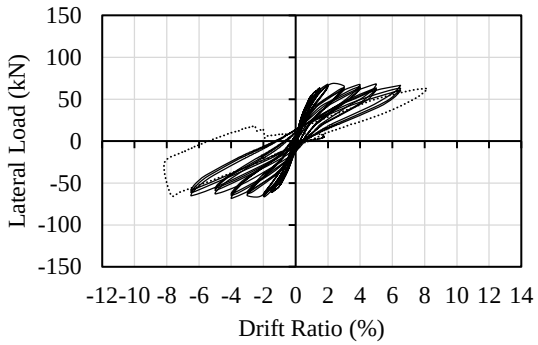

(g) GN-7.0-0.3-85

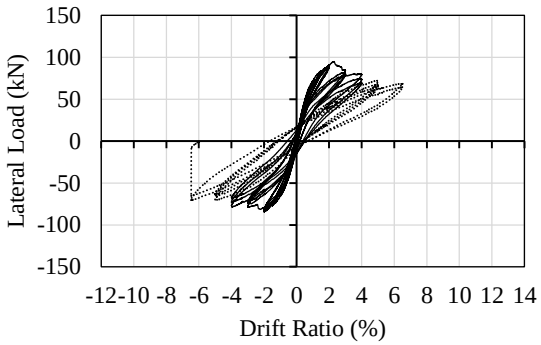

(h) GH-7.0-0.2-85

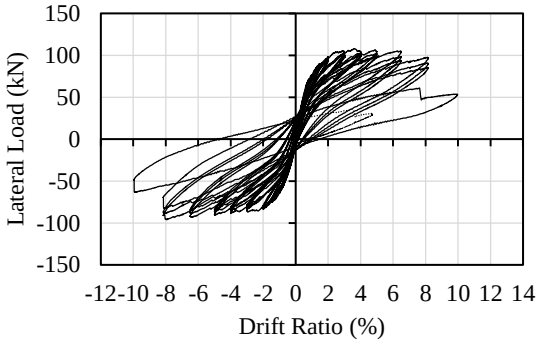

(i) GH-7.0-0.2-50

Figure 7.6: Hysteresis diagrams for test specimens – continued

In addition, the maximum spiral strains of the aforementioned HSC specimens surpassed the 6,000-με limit (CSA 2017) at 3.00% drift ratio whereas the spiral strain of GH-5.0-0.2-50 exceeded that of GN-5.0-0.2-50 and the 6,000-με limit only beyond the drift ratio of 4.00%. The experimental results showed that the 6,000-με limit (CSA 2017) would be reached by the moderately-confined HSC specimens close to failure drift, whereas for moderately confined NSC or well-confined NSC and HSC columns, such limit would be reached approximately at 4.00% drift ratio, which would usually be much less than the actual failure drift. This suggests that the 6,000-με limit set by CSA S806-12 (CSA 2017) should be re-evaluated based on the level of confinement and concrete strength.

Figure 7.12 shows the contribution of each lateral drift component based on the readings of LVDTs. To determine the flexure displacement component, Δ_f, curvature was integrated along the column shear span as in (Equation 7.2).

$$\Delta_f = \sum \theta_i (L - y_i) \qquad \text{Equation 7.2}$$

where θ_i is the flexural rotation of the i^{th} gauge length, obtained by adding the readings of the two-opposite vertical LVDTs, fixed along the aforementioned gauge length, then dividing the result by their horizontal spacing; L is the shear span of the column; and y_i is the vertical height of the midpoint of the i^{th} gauge length from the top surface of the footing.

The drift component due to bar elongation and slippage, Δ_s, was acquired using the rotation difference of the two bottommost pairs of vertical LVDTs (Figure 7.1b). The rotation difference, defined herein as slip rotation, θ_s, was multiplied by the shear span of the column to obtain the slip drift component, as denoted by Equation 7.3.

$$\Delta_s = \theta_s . L \qquad \text{Equation 7.3}$$

Using the readings of the diagonally-mounted LVDTs (Figure 7.1b), the angle of shear distortion, γ, was determined as:

$$\gamma = \frac{\delta_1 - \delta_2}{2\ell} (\tan\alpha + \cot\alpha) \qquad \text{Equation 7.4}$$

The drift component due to bar elongation and slippage, Δ_s, was acquired using the rotation difference of the two bottommost pairs of vertical LVDTs (Figure 7.1b). The rotation difference, defined herein as slip rotation, θ_s, was multiplied by the shear span of the column to obtain the slip drift component, as denoted by Equation 7.3.

$$\Delta_s = \theta_s . L \qquad \text{Equation 7.3}$$

Using the readings of the diagonally-mounted LVDTs (Figure 7.1b), the angle of shear distortion, γ, was determined as:

$$\gamma = \frac{\delta_1 - \delta_2}{2\ell} (\tan\alpha + \cot\alpha) \qquad \text{Equation 7.4}$$

where the axial deformation of each two-intersecting diagonal LVDTs, δ_1 or δ_2, had a positive sign for elongation; ℓ is the initial gauge length of the diagonal LVDTs; and α is the initial inclination of the LVDTs to the horizontal. Generally, the measurement of drift components was halted when

the identified components where no longer logical due to excessive damage to the concrete core or bending the mounting threaded rods near the end of the tests.

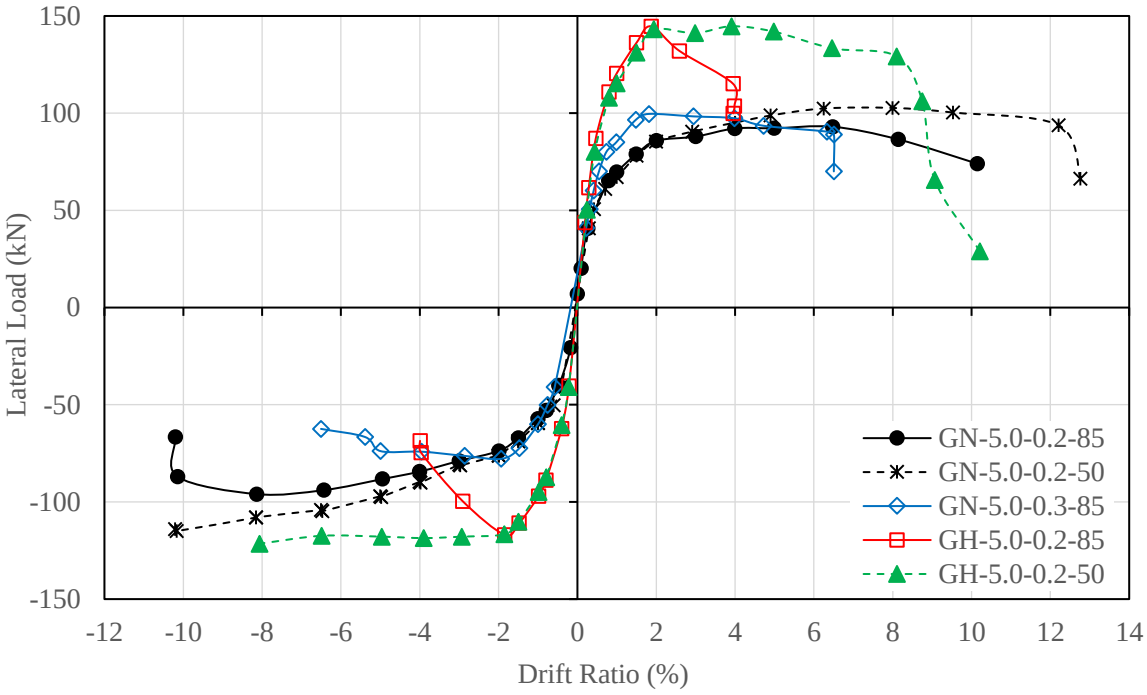

(a) columns with *L/D* = 5.0

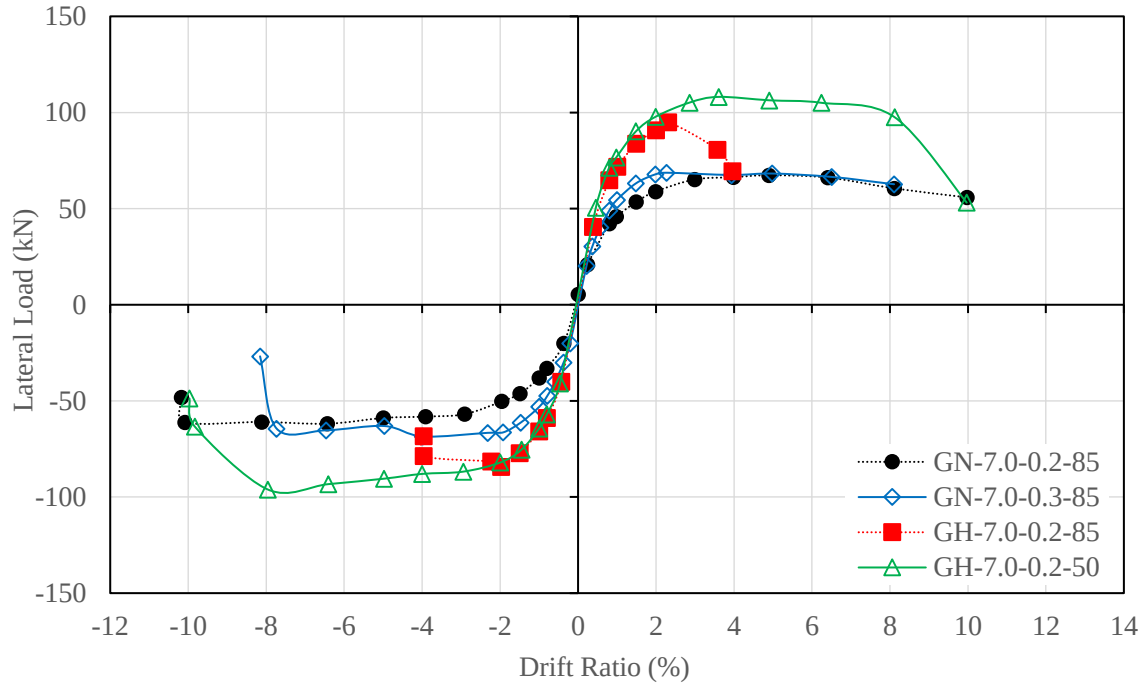

(b) columns with *L/D* = 7.0

Figure 7.7: Envelopes of hysteresis diagrams

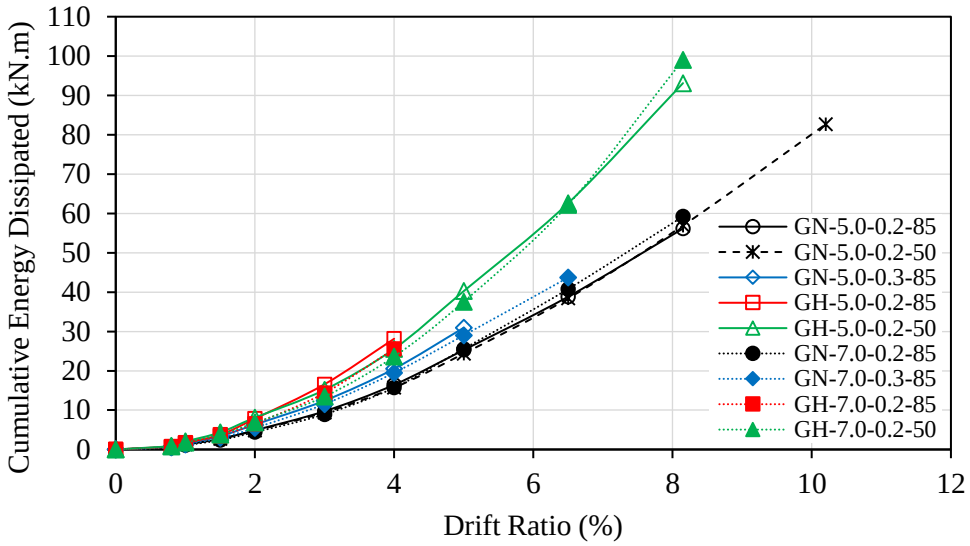

Figure 7.8: Energy dissipation

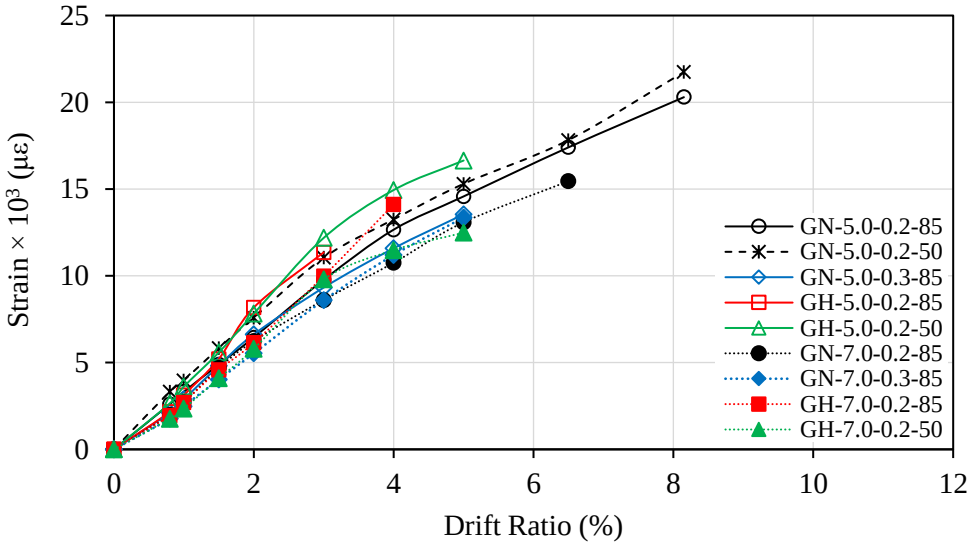

Figure 7.9: Relationships between maximum strain along outermost longitudinal bars and drift ratio

As shown in Figure 7.12, the shear displacement component represented, at the maximum, 7% of the total lateral displacement for all specimens included in this study. Additionally, the maximum percentage of the displacement component due to bar elongation and slip was approximately 32%, which is significantly less than that of similar steel-RC columns found in the literature (Lehman and Moehle 2000). The reason could be that such displacement component is much larger for steel due to yield penetration into the longitudinal steel bars, which increases with the successive lateral

drifts applied to the column. On the other hand, GFRP bars are elastic and do not exhibit any yielding. Increasing the concrete strength resulted in less stable response for specimens GH-5.0-0.2-85 and GH-5.0-0.2-50 compared to their NSC counterparts, which can be attributed to the more brittle behaviour associated with HSC. In addition, the aforementioned HSC specimens exhibited larger contribution of slip displacement, starting at 32 and 28% of the total lateral displacement at 0.8% drift ratio, which was 113 and 22% higher than such contribution for GN-5.0-0.2-85 and GN-5.0-0.2-50, respectively.

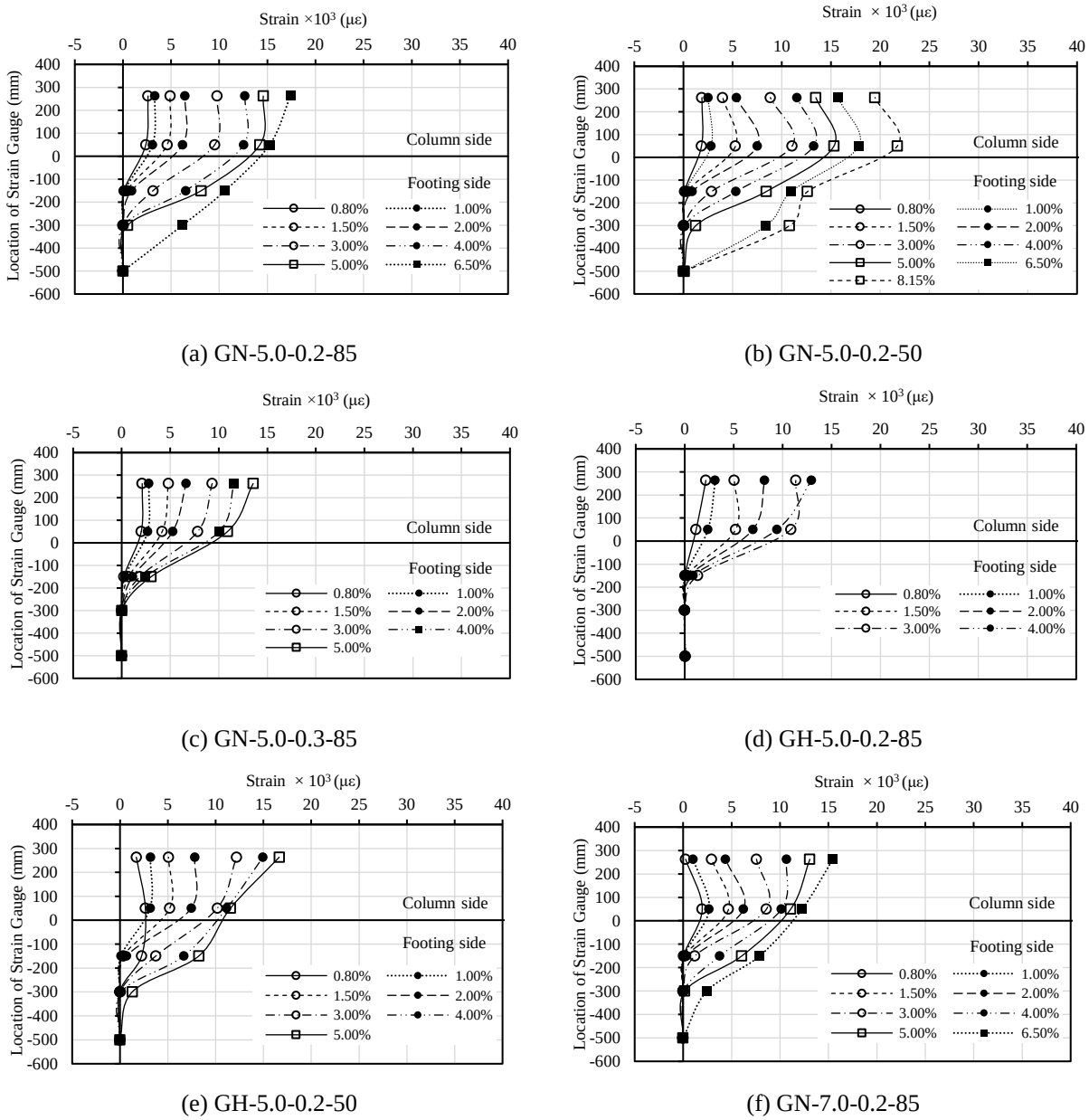

(a) GN-5.0-0.2-85

(b) GN-5.0-0.2-50

(c) GN-5.0-0.3-85

(d) GH-5.0-0.2-85

(e) GH-5.0-0.2-50

(f) GN-7.0-0.2-85

Figure 7.10: Strain profile in the outermost longitudinal bar

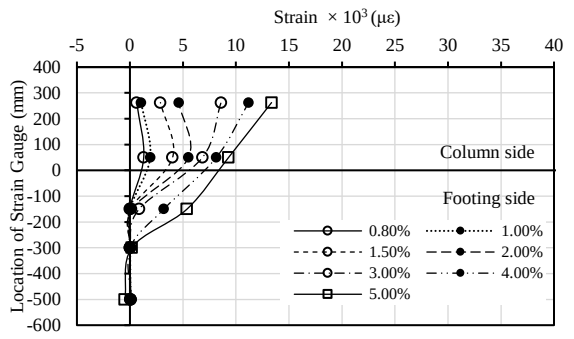

(g) GN-7.0-0.3-85

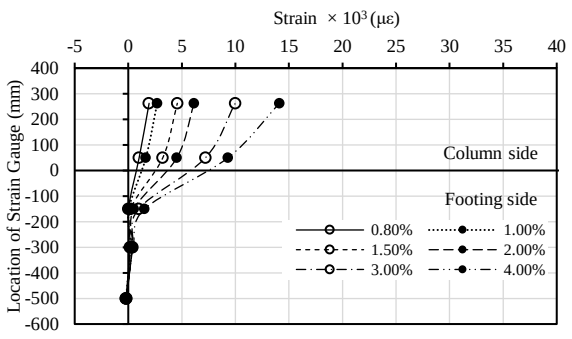

(h) GH-7.0-0.2-85

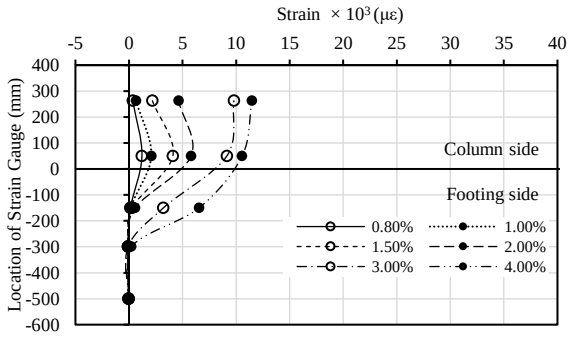

(i) GH-7.0-0.2-50

Figure 7.10: Strain profile in the outermost longitudinal bar – continued

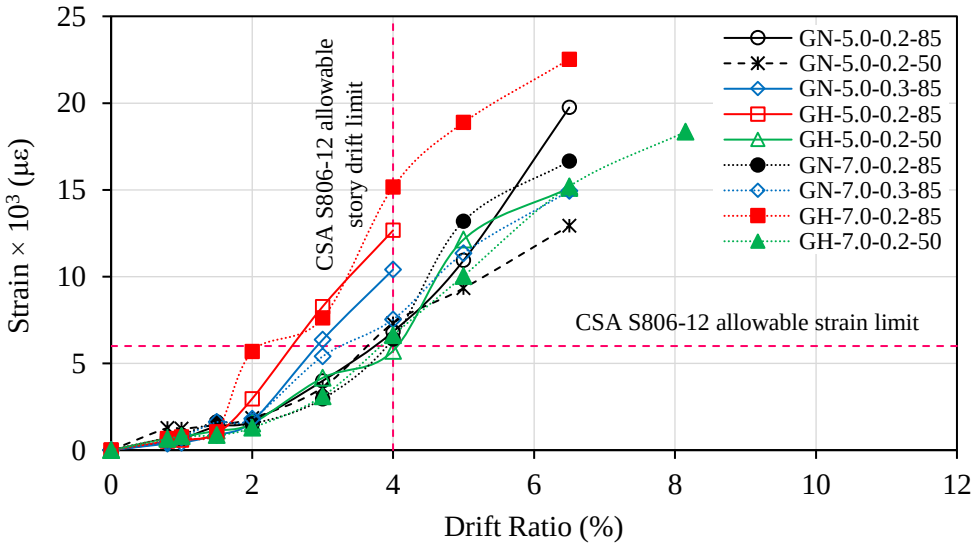

Figure 7.11: Relationships between maximum spiral strain and drift ratio

As the test progressed, the flexural displacement component became more dominant for GH-5.0-0.2-85 and GH-5.0-0.2-50, which agrees well with the intensified concrete core damage observed

for those specimens compared to their NSC counterparts. On the other hand, increasing the concrete strength did not significantly alter the contributions of the different displacement components when the aspect ratio was 7.0, except for the rapid increase of the contribution of the drift due to flexure beyond 2.00% drift ratio for GH-7.0-0.2-85.

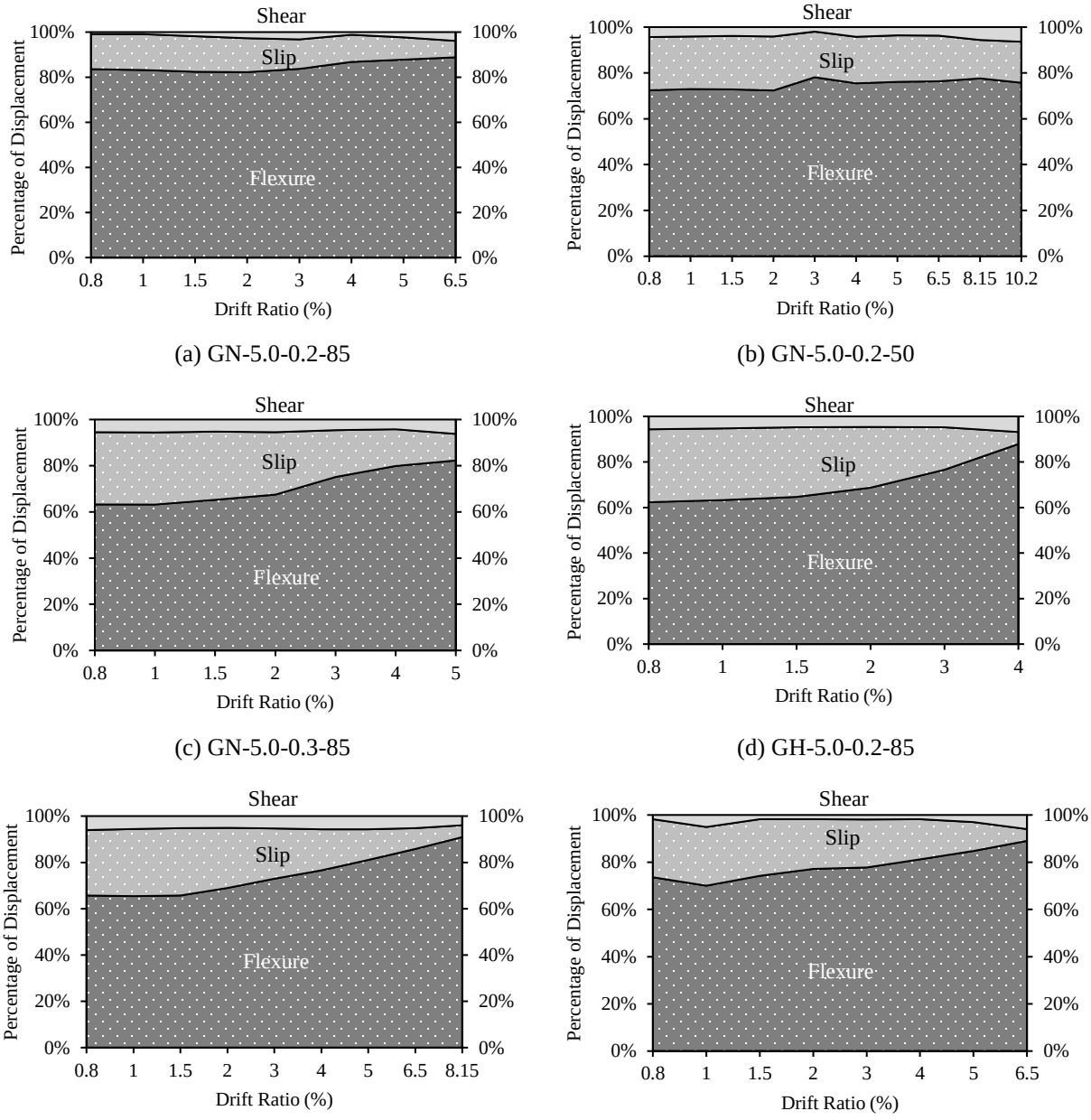

(a) GN-5.0-0.2-85

(b) GN-5.0-0.2-50

(c) GN-5.0-0.3-85

(d) GH-5.0-0.2-85

(e) GH-5.0-0.2-50

(f) GN-7.0-0.2-85

Figure 7.12: Contribution percentages of lateral drift components

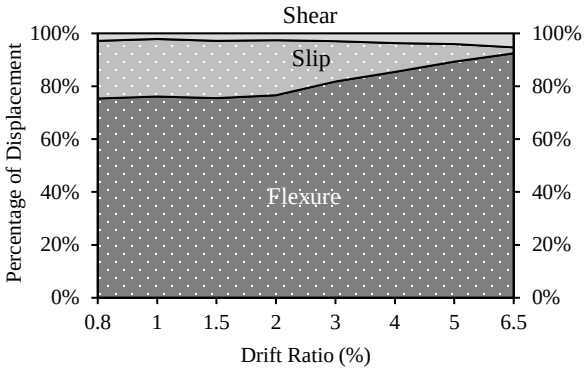

(g) GN-7.0-0.3-85

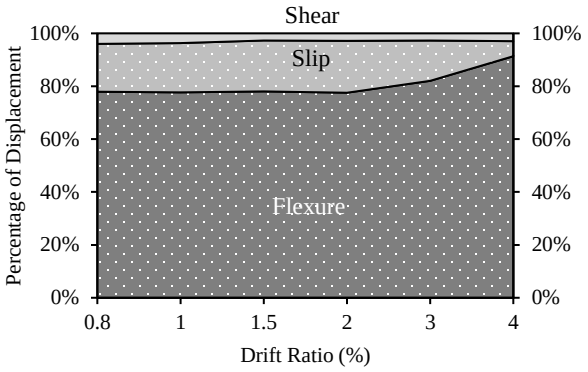

(h) GH-7.0-0.2-85

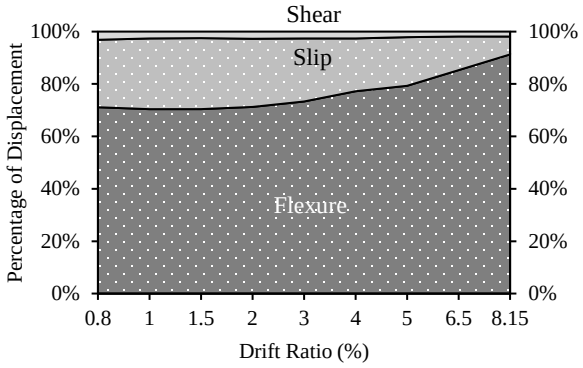

(i) GH-7.0-0.2-50

Figure 7.12: Contribution percentages of lateral drift components – continued

7.3.3. Effect of aspect ratio

As demonstrated by Figure 7.7, increasing the aspect ratio had a marginal effect on the drift capacity, which could be due to the elastic behaviour of GFRP reinforcement, except for the 30% increase noticed for GN-7.0-0.3-85 over its shorter counterpart. Although this may indicate better deformability for longer columns, incorporating the secondary moments due to *P*-Δ effect may indicate the opposite, as will be discussed later. Conversely, the increase in column aspect ratio caused a considerable decrease of the lateral load capacity, which was anticipated as the shear span increased while the moment capacity would approximately remain the same. Consequently, to better clarify the effect of aspect ratio, the hysteretic responses of the specimens were depicted in Figure 7.13 in terms of moment rather than lateral load resistance versus drift ratio. To obtain the moment resistance at the critical section, the lateral load resistance was multiplied by the lever

arm, which was considered between the mid-height of the cover spalling region (i.e. inelastic deformability hinge) and the point of lateral load application (Tavassoli et al. 2015).

For the NSC specimens, changing the aspect ratio did not alter the moment capacity of the specimens nor their hysteretic responses, apart from the stiffer response and the 29% higher moment capacity, both in the pulling direction, for specimen GN-7.0-0.3-85 with respect to its counterpart with aspect ratio of 5.0. On the other hand, increasing the aspect ratio enhanced the moment-drift relationship and the moment capacity for the HSC specimens. An increase of 14 and 17% was recorded for the moment capacity of GH-7.0-0.2-85 and GH-7.0-0.2-50 compared to their shorter counterparts, respectively. This could be attributed to the observation discussed previously, that increasing the aspect ratio resulted in longer spalling regions for NSC columns whereas the length of spalling region was hardly affected by changing the aspect ratio for HSC columns. Such results indicate that the requirements of Clause 12.7.3.3 of CSA S806-12 (CSA 2017) are overly strict due to the fact that they were based upon design models for steel-RC columns. Steel-RC columns were expected to exhibit inferior deformability as the column aspect ratio decreases, which was refuted in this study for GFRP-RC columns. Furthermore, an opposite concept, to what was assumed by Saatcioglu and Razvi (2002), can be adopted for FRP-RC columns based on the findings of this study. In other words, increasing the column aspect ratio could be detrimental to the drift capacity of the column when the secondary moment due to P-Δ effect is considered.

The hysteresis responses of the test specimens were plotted in Figure 7.14 considering the P-Δ effect. When the P-Δ effect was neglected, GN-7.0-0.3-85 exhibited higher drift capacity than its shorter counterpart (GN-5.0-0.3-85); however, GN-7.0-0.3-85 encountered higher strength degradation than GN-5.0-0.3-85 when the secondary moments due to P-Δ effect were incorporated. Notably, specimens GN-5.0-0.3-85 and GN-7.0-0.3-85 exhibited larger than 25% strength degradation at 4.00 and 3.00% drift ratios, respectively.

As shown in Figure 7.8, comparable levels of energy dissipation were observed when the aspect ratio was increased, regardless of axial load level or concrete strength. Additionally, the reported maximum longitudinal bar strain was not significantly altered for the larger aspect ratio except for the reduction in strains beyond a drift ratio of 2.00 and 1.50% for specimens GN-7.0-0.2-85 and GH-7.0-0.2-85 with respect to their shorter equivalents, respectively (Figure 7.9). Such differences

could be attributed to the localized nature of measured strain, which may result in some variation within the readings.

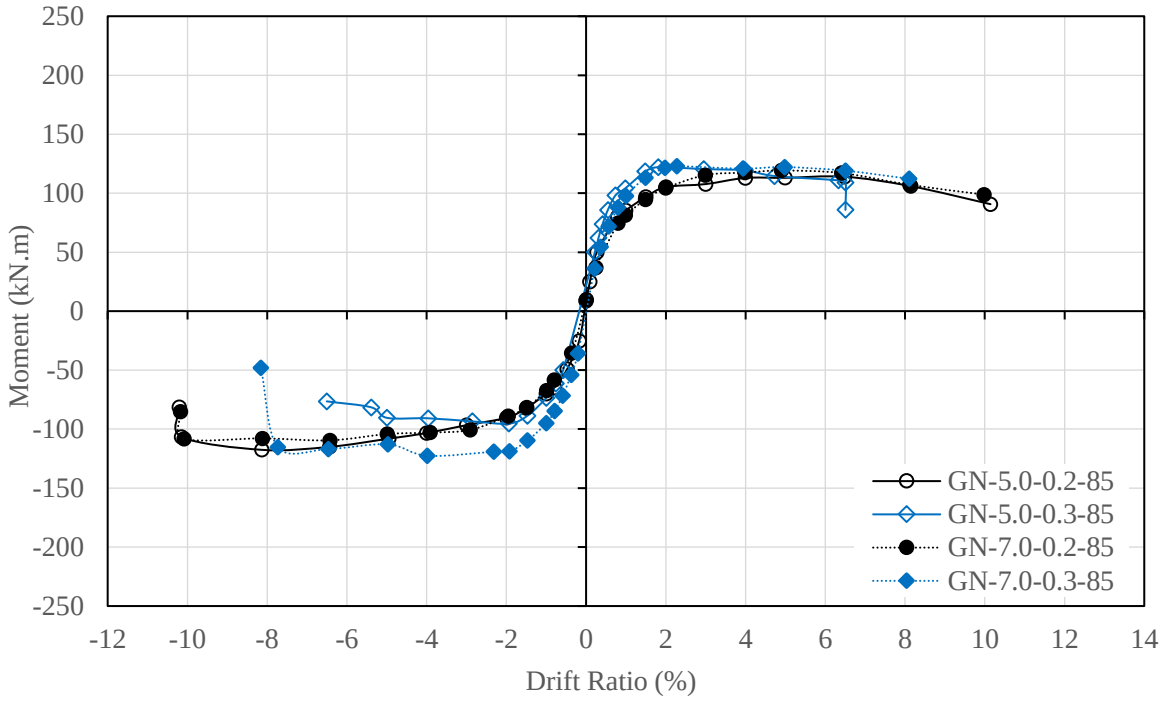

(a) NSC columns

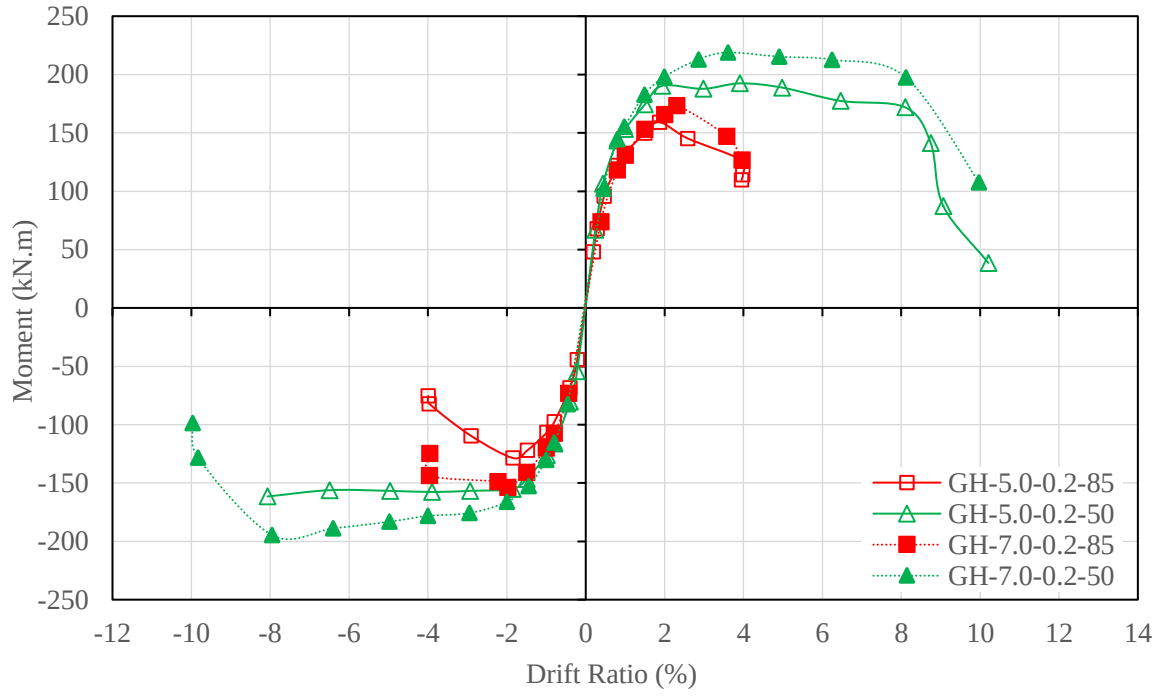

(b) HSC columns

Figure 7.13: Envelopes of hysteresis (moment-drift ratio) diagrams

Furthermore, similar strain profiles were noticed for GN-5.0-0.3-85 and GN-7.0-0.3-85 (Figure 7.10) throughout their tests, whereas such similarity was limited to 2.00 and 1.50% drift ratio for GN-7.0-0.2-85 and GH-7.0-0.2-85 versus their counterparts with aspect ratio of 5.0, respectively, followed by higher strain values for the shorter specimens, as mentioned earlier. This, in general, contradicts the observations reported for steel-RC columns [39] where consistently higher longitudinal bar strains were recorded when the aspect ratio increased.

As shown in Figure 7.11, the maximum spiral strains did not change significantly when the aspect ratio was increased for GN-5.0-0.2-85 and GH-5.0-0.2-85, whereas the spiral strains were decreased for GN-5.0-0.3-85 beyond 3.00% drift ratio when the aspect ratio increased to 7.0, reaching a 28% reduction at a drift ratio of 4.00%. This could be related to the stiffer response and improved drift capacity observed for GN-7.0-0.3-85 as discussed earlier.

It is worth mentioning that while both GH-5.0-0.2-85 and GH-7.0-0.2-85 technically failed at 4.00% drift ratio, specimen GH-7.0-0.2-85 exhibited spiral rupture only at 6.50% drift ratio, which agrees well with the maximum recorded spiral strain of 22,520 με (95% of its rupture strain), prior to strain malfunctioning. However, the maximum strain reported for GH-5.0-0.2-85 at 4.00% drift ratio was only 54% of the rupture strain of the GFRP spirals. Although such low strain contradicts the visual observations where the specimen experienced spiral rupture at 4.00% drift ratio, this can be justified by the fact that the fracture occurred outside the instrumented region for GH-5.0-0.2-85, which was the reason for incorporating more electrical strain gauges over larger length of the column for the second phase of tests, where the longer columns were prepared and tested. Increasing the aspect ratio caused less stability to the response of GN-7.0-0.2-85 and GN-7.0-0.3-85 (Figure 7.12), which concurred with the observed more severe damage occurred to those specimens with respect to their shorter counterparts. Conversely, increasing the aspect ratio from 5.0 to 7.0 had a positive effect on the response of the HSC specimens, for which the rate of change of displacement components was reduced. This agreed well with the observed modes of failure for the longer HSC specimens, which were less abrupt and brittle.

7.3.4. Effect of spiral pitch

Previous studies indicated that the less the spacing of transverse reinforcement, the better the strength and, more importantly, the deformability would be (Tavassoli et al. 2015; Ali and El-Salakawy 2016; Naqvi and El-Salakawy 2017; Abdallah and El-Salakawy 2021a). It was observed,

however, that decreasing the spiral pitch was more effective for the HSC specimens than NSC counterparts, especially in terms of drift capacity. That is, decreasing the spiral pitch from 85 to 50 mm caused an increase of 10, 2 and 14% in lateral load capacity, and 25, 219 and 219% in failure drift for specimens GN-5.0-0.2-85, GH-5.0-0.2-85 and GH-7.0-0.2-85, respectively, as shown in Figure 7.7. This can be justified by the increased brittleness of HSC columns, for which increasing the confinement reinforcement will be much more effective than NSC ones.

On the other hand, the specimen counterparts with different spiral pitches (Figure 7.8), no matter what concrete strength or aspect ratio they may have, absorbed similar amounts of energy at each drift ratio. Similarly, the maximum longitudinal bar strains were comparable when the spiral pitch changed from 85 to 50 mm, except for the decrease noticed for the strains of GH-7.0-0.2-50 with respect to those of GH-7.0-0.2-85 beyond 3.00% drift ratio, as depicted by Figure 7.9. This decrease could be attributed to the fact that beyond 3.00% drift ratio, GH-7.0-0.2-85 was about to fail; exhibiting large deformations and bar strains, whereas GH-7.0-0.2-50 was still having five more drift steps to undergo before failure. Moreover, similar strain distributions along the outermost longitudinal bars were noticed for the specimens with different spiral pitches (Figure 7.10). Furthermore, reducing the spiral pitch to 50 mm caused the spiral strains of GN-5.0-0.2-50 to decrease with respect of those of GN-5.0-0.2-85 beyond 4.00% drift ratio (Figure 7.11), while reduction of spiral strains occurred for GH-5.0-0.2-50 compared to those of GH-5.0-0.2-85 after the drift ratio of 1.50%. Similar performance to that of the latter group was observed for the HSC specimen with the aspect ratio of 7.0. Such reductions in spiral strains for the specimens confined at a 50-mm pitch compared to those having 85 mm pitch are reasonable as the reduced spiral pitch means higher volumetric reinforcement ratio and, in turn, less load share per spiral turn, given that the axial and lateral loads are the same for the specimens with either spiral pitch. As depicted by Figure 7.12, decreasing the spiral pitch resulted in lower rate of increase for the flexural displacement component, particularly for HSC concrete. On the other hand, the effect of spiral pitch on the NSC specimens was minimal. This agreed well with the visual observation for the tested specimens, as the HSC columns confined at 85-mm spiral pitch exhibited larger spalling region which indicates larger contribution of flexural displacement component.

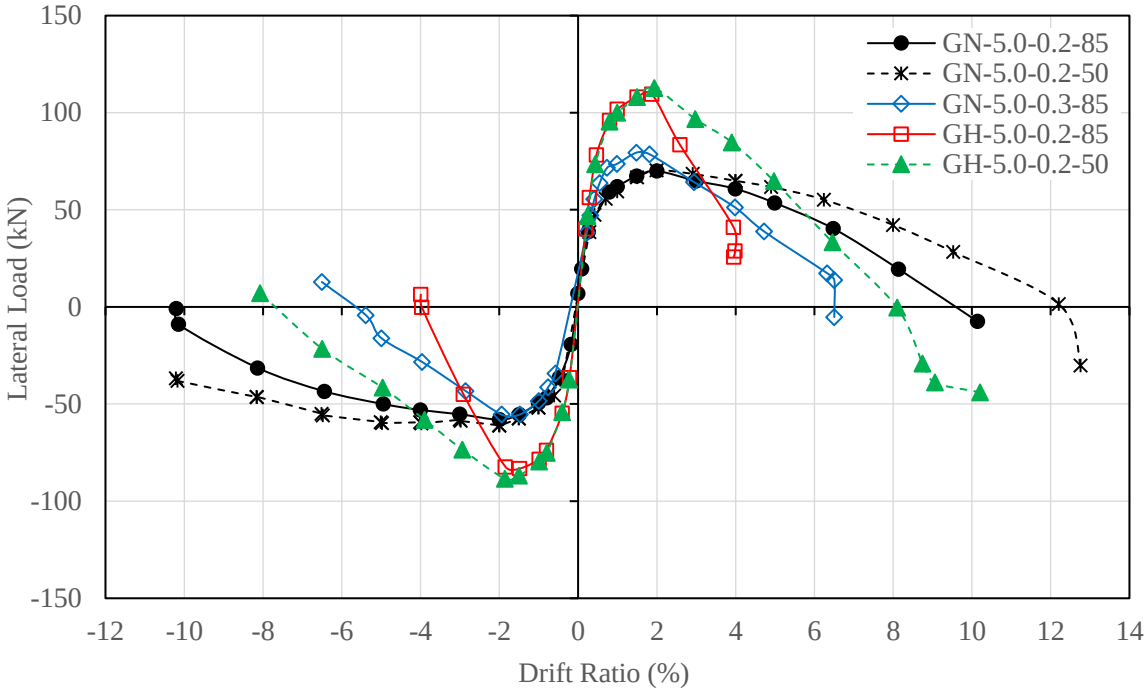

(a) columns with *L/D* = 5.0

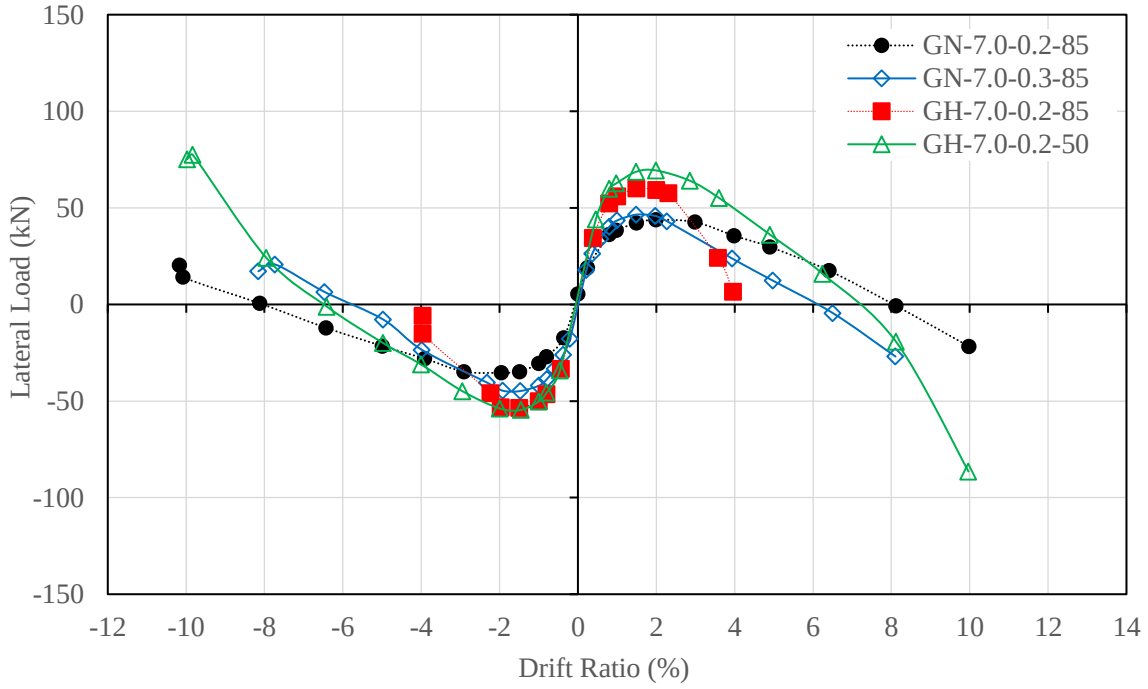

(b) columns with *L/D* = 7.0

Figure 7.14: Envelopes of hysteresis diagrams including the *P*-Δ effect

7.3.5. Effect of axial load level

As shown in Figure 7.7, increasing the axial load from 20 to 30% resulted in a 12% increase for the lateral load capacity in the pushing direction, whereas the lateral load capacity was reduced by 19% in the pulling direction when the aspect ratio was 5.0. This might be due to the less stable concrete core under higher axial load, as evident from Figure 7.12c, in addition to the higher stiffness degradation and cracking intensity associated with the larger lateral load resistance developed in the pushing direction, which resulted in much lower lateral load resistance in the pulling direction. On the other hand, the lateral load capacity increased by 7% on average when the axial load level increased for the NSC specimens with an aspect ratio of 7.0. Such difference in the effect of axial load level with variation of the aspect ratio can be attributed to the improved hysteretic response and drift capacity for GN-7.0-0.3-85 over its shorter equivalent. Generally, the improvement of lateral load capacity came at the expense of earlier strength degradation and reduced drift capacity for the specimens with higher axial load level.

It could be noticed from Figure 7.8 that increasing the axial load level caused an increase in the amount of energy dissipated by the specimens. At 4.00% drift ratio, that increase was about 25 and 24% for the specimens with aspect ratio of 5.0 and 7.0, respectively, with respect to their counterparts tested under lower axial load level. This was due to the increased lateral load resistance as a result of increasing the axial load level. On the other hand, comparable longitudinal bar strains were recorded for the NSC specimens even with different axial load levels (Figure 7.9). In a similar manner, the spiral strains, as shown in Figure 7.11, varied inconsistently for specimens GN-7.0-0.2-85 and GN-7.0-0.3-85, indicating neither an increase nor a decrease of their spiral strains with respect to each other. However, specimen GN-5.0-0.3-85 exhibited larger spiral strains over those of GN-5.0-0.2-85 beyond a drift ratio of 2.00%. Such inconsistent observations could be due to the localized nature of the measured strains, which in some cases could indicate unrealistic increases or decreases.

Furthermore, increasing the axial load level for the aspect ratio of 5.0 caused a simultaneous increase of slip drift component and a reduction in the flexural one (Figure 7.12). However, at the aspect ratio of 7.0, it was noticed that changing the axial load level did not significantly alter the contributions of the individual displacement components.

7.4. Conclusions

The key findings of this experimental investigation can be summarized as follows:

1. All tested specimens surpassed the drift ratio limit set by the Canadian standards (CSA 2017) for ductile moment resisting frames (MRFs) except for the HSC specimens confined at 85-mm spiral pitch. Nonetheless, those specimens achieved their theoretically estimated drifts and the drift limits required by the National Building Code of Canada (NRCC 2020) and the Canadian standards (CSA 2017) for moderately ductile MRFs.
2. Increasing the concrete compressive strength from 35 to 80 MPa increased the lateral load capacity by 42 and 55% but decreased the drift capacity by 20 and 63% for columns confined with GFRP spirals at 50 and 85 mm, respectively.
3. The HSC columns tested in this study dissipated larger amounts of seismic energy by up to 71% with respect to their NSC equivalents. In addition, larger longitudinal reinforcement and spiral strains were observed for the HSC columns. Moreover, for the aspect ratio of 5.0, the HSC specimens exhibited larger displacement contribution due to bar slip and less stable response in terms of the rate of change for the individual displacement components, whereas such influence was minimal for the specimen with an aspect ratio of 7.0.
4. Increasing the aspect ratio from 5.0 to 7.0 had a marginal effect on the hysteretic response in terms of moment and drift capacities, especially when the axial load level was 20%. For HSC columns, however, higher moment resistance was observed for columns with larger aspect ratio. Unlike steel-RC columns, some improvements were noticed for NSC columns in terms of drift capacity in general and moment capacity in the pulling direction only when the increase of aspect ratio was accompanied by applying a higher axial load level.
5. It is recommended for designers to carefully consider the effect of aspect ratio while designing the confinement reinforcement for GFRP-RC columns in seismic active zones. While increasing the aspect ratio for the columns tested in this study did not affect or improved their drift capacities, it resulted in higher strength degradation compared to their shorter counterparts when the secondary moments associated with P-Δ effect were incorporated.
6. While the requirement of the Canadian standards CSA S806-12 (CSA 2017) for spiral pitch to be at least one-sixth the core diameter was found to be overly conservative for NSC

circular columns (Abdallah and El-Salakawy 2021a), it would be prudent to consider such requirement for HSC columns.

7. Increasing the axial load level from 0.2 to 0.3 resulted in larger lateral load capacity for both tested aspect ratios of 5.0 and 7.0. This was accomplished, however, to the detriment of the drift capacity, which was worse for the aspect ratio of 5.0.

CHAPTER 8: CONFINEMENT CHARACTERISTICS OF GFRP-RC CIRCULAR COLUMNS UNDER SIMULATED EARTHQUAKE LOADING: A NUMERICAL STUDY

Authors' Affiliations and Roles:

- **Amr E. Abdallah**, PhD Candidate, Department of Civil Engineering, University of Manitoba.
  Role: Methodology, Investigation, Formal analysis, Validation, Visualization and Writing-Original Draft.

- **Yasser M. Selmy**, PhD Candidate, Department of Civil Engineering, University of Manitoba.
  Role: Methodology, Validation and Visualization.

- **Ehab F. El-Salakawy**, Professor of Civil Engineering, Department of Civil Engineering, University of Manitoba.
  Role: Conceptualization, Methodology, Writing-Review & Editing, Supervision, Project administration, Resources and Funding acquisition.

Journal and Status:

Journal of Composites for Construction, ASCE, in press.

Reference:

Abdallah, A. E., Selmy, Y., M., and El-Salakawy, E. F. 2022. "Confinement characteristics of GFRP-RC circular columns under simulated earthquake loading: a numerical study." *J. Compos. Constr.*, ASCE, DOI: 10.1061/(ASCE)CC.1943-5614.0001195, in press.

Note:

The manuscript had been slightly altered from the original paper by renumbering the tables and figures to include the chapter number. In addition, the reference list and the list of notations have been moved to the appropriate sections in the thesis as indicated in the table of contents.

Abstract

The seismic behavior of FRP-RC columns is far from being fully explored. Therefore, numerical and analytical studies were performed to address the effects of different parameters and evaluate the current design provisions for confinement reinforcement under seismic loading. Using a commercially available software package, a three-dimensional nonlinear finite-element model (FEM) was constructed and validated against the experimental results of full-scale GFRP-RC circular columns previously tested by the authors. The validated FEM was, then, used to conduct an extensive parametric study investigating the effect of concrete compressive strength, spiral pitch, axial load level and column aspect ratio (i.e., shear span-to-depth ratio). It was found that increasing the concrete strength caused an increase in lateral load capacity and initial stiffness, whereas the drift capacity decreased. The latter property was also significantly affected by the variation of spiral pitch and axial load level. On the other hand, the aspect ratio had a marginal effect on moment or drift capacities. Using the results of the FEMs, two new design models were proposed. The proposed models showed remarkably better predictions than the equation adopted by the Canadian standard for design of FRP-RC structures.

Keywords: Glass fiber-reinforced polymer (GFRP); finite-element analysis; circular column; seismic loading; high-strength concrete (HSC); aspect ratio; spiral pitch; axial load level; new design model.

8.1. Introduction

The use of fiber-reinforced polymers (FRPs) as a substitute for conventional steel reinforcement in reinforced concrete (RC) structures is gaining an ever-increasing popularity due to its attractive attributes, especially its non-corroding nature. However, the difference in behavior between FRP and steel reinforcement materials cast doubts on the seismic performance of FRP-RC structures. The linear-elastic behavior up to failure of FRP, with relatively lower strain capacity and modulus of elasticity, and the lack of yielding, are the most important differences. Usually, the seismic-induced energy in RC structures is dissipated through inelastic deformations exhibited by their structural components. Fortunately, such issue was addressed and rebutted by many recent research studies (Tavassoli et al. 2015; Ali and El-Salakawy 2016; Hasaballa and El-Salakawy 2018; Elshamandy et al. 2018; El-Gendy and El-Salakawy 2020).

Adequate design provisions are available for specific types of FRP-RC members including, but not limited to, beams, slabs and flat plates (ACI 2015; CSA 2017; AASHTO 2018; CSA 2019d). On the contrary, the design provisions for FRP-RC columns are being developed at a slower pace due to sparsity of experimental evidence, especially those tested under simulated seismic loading. For example, the ACI 440.1R-15 (ACI 2015) guidelines do not recommend using FRP as main reinforcement in compression members. The AASHTO LRFD (AASHTO 2018) design guide and the Canadian standards, CSA S806-12 (CSA 2017), both allow the use of FRP in RC columns but ignore its contribution to load capacity. On the other hand, the Canadian Highway Bridge Design Code, CSA S6-19 (CSA 2019d), recognizes the load carrying capacity of FRP in compression up to a strain of 2,000 με. Additionally, the only standard that includes design provisions for FRP-RC columns in seismic-resistant structures is the Canadian standards CSA S806-12 (CSA 2017). Consequently, several recent research studies were devoted to investigating the different parameters affecting the seismic behavior of FRP-RC columns (Tavassoli et al. 2015; Ali and El-Salakawy 2016; Naqvi and El-Salakawy 2017; Elshamandy et al. 2018; Kharal and Sheikh 2020; Abdallah and El-Salakawy 2021a, b). In these studies, glass FRP (GFRP) reinforcement was utilized due to its adequate strain capacity, and lower cost compared to other types of FRP. Stable hysteretic responses, with significant levels of energy dissipation, were reported for GFRP-RC columns tested under simulated-earthquake loading and different axial load levels with significant levels of energy dissipation. In addition, the conventional ductility concept for steel-RC columns

was successfully substituted by the deformability of GFRP-RC ones. Generally, replacing steel with GFRP enhanced column deformability and member-level performance. Increasing the axial load level slightly increased the lateral load capacity but caused earlier strength degradation and reduced drift capacity. Such adverse effects were alleviated by providing larger transverse reinforcement ratio (Tavassoli et al. 2015; Ali and El-Salakawy 2016; Elshamandy et al. 2018). A similar influence was observed when the concrete compressive strength increased (Abdallah and El-Salakawy 2021b). It was also concluded that the requirement of one-sixth the core diameter for spiral pitch by CSA S806-12 (CSA 2017) is overly strict (Abdallah and El-Salakawy 2021a). Moreover, increasing the spiral size was found to be less effective compared to decreasing the spiral pitch (Tavassoli et al. 2015).

Despite the amount of research dedicated to studying the seismic performance of GFRP-RC columns, the influencing parameters are far from being fully understood yet. To acquire reliable and comprehensive intuitive understanding of such behavior in a concise and effective manner, the nonlinear finite-element analysis (FEA) can be utilized. To date, there is a limited number of numerical studies on FRP-RC columns (Elchalakani et al. 2018; Alnajmi and Abed 2020; Raza et al. 2020; Tahir et al. 2021), which focused on the behavior of such columns under monotonic loading schemes. This study is based upon a three-dimensional (3D) nonlinear finite-element model (FEM) constructed using ATENA/GID software package (Červenka et al. 2020a). This software has been exploited by several researchers recently to model various FRP-RC members (Sasmal et al. 2013; Roehm et al. 2015; Hosseini et al. 2019; Attia et al. 2020; Tahir et al. 2021; El-Gendy and El-Salakawy 2021). The FEM was validated against the results of the experimental tests on GFRP-RC circular columns conducted by Abdallah and El-Salakawy (2021a, b). The validated FEM was used thereafter to perform a rigorous parametric study where the impact of some key parameters affecting the seismic behavior of RC columns were investigated. The studied parameters were the concrete strength, spiral pitch, axial load level, and column aspect ratio (i.e., shear span-to-depth ratio). Furthermore, the outcomes of the numerical study were mathematically analyzed to develop more accurate design models for the FRP confinement reinforcement in seismic-resisting columns.

8.2. Summary of the Experimental Tests on GFRP-RC Circular Columns

8.2.1. Test specimens and material properties

Eight full-scale GFRP-RC circular columns were experimentally tested by Abdallah and El-Salakawy (2021a, b) under constant axial load and unidirectional cyclic lateral drift reversals. The test specimen represented the bottommost portion of a first-story column in a moment -resisting frame (MRF) structure or a bridge support, bent in double curvature. All columns had a diameter of 350 mm and a shear span (i.e. the vertical distance between the top surface of the footing and the line of action of lateral load) of 1,750 mm. This resulted in an aspect ratio (i.e., column shear span-to-depth ratio) of 5.0. For each column, a rigid 1,400 × 900 × 600-mm footing, properly reinforced with 15M steel bars, was cast to ensure sufficient fixity to the column (Figure 8.1a). Each column was reinforced longitudinally with No. 16 (15.9-mm diameter) GFRP bars and transversally with No. 10 (9.5-mm diameter) GFRP spirals. The investigated parameters were the concrete strength (35 and 80 MPa), spiral pitch (50 and 85 mm), axial load level (10, 20 and 30%) and lap splice length for hoops (40 and 60d_s, where d_s is the nominal cross-sectional diameter of the hoop). More details about the test specimens can be found elsewhere (Abdallah and El-Salakawy 2021a, b). The physical and mechanical properties of the used GFRP materials, as obtained by laboratory testing or according to the product certificate issued by the manufacturer (Pultrall Inc. 2019), are summarized in Table 8.1. Five specimens were cast using normal-strength concrete (NSC), while high-strength concrete (HSC) was utilized to cast the other three specimens. The target 28-day compressive strength was 35 and 80 MPa for NSC and HSC, respectively.

In this study, the specimens were designated using a four-character alphanumeric code (Table 8.2); where the first character, G, denoted the GFRP reinforcement used to reinforce all specimens. The second letter, either N or H, was referring to normal- or high-strength concrete, respectively. The third number referred to the column aspect ratio, which was 5.0 for the specimen tested experimentally. The fourth fraction indicated the ratio of applied axial load, P, to the unconfined axial capacity of the column, P_o, whereas the fifth number identified the spiral pitch.

8.2.2. Test setup and loading procedure

The test setup, depicted by Figure 8.1b, consisted of three fundamental components; the full-dynamic hydraulic actuator, axial loading hinged frame and RC alignment blocks. This setup

enabled the safe application for axial loading, while allowing the whole system to move along with the lateral drift reversals applied to column head. The footing was fixed to the laboratory strong floor using high-strength threaded bars, while the actuator and the axial loading frame were connected to column head to apply the lateral and axial loads to the column, respectively. Testing commenced by applying the specified axial load. Then, the seismic-simulated loading was applied in two subsequent phases; a load-controlled phase to simulate the column at first cracking and service, followed by the displacement-controlled reversed cyclic lateral drifts, which were implemented in accordance with ACI 374.1-05 (ACI 2019). For each drift step, three identical cycles, in terms of drift ratio, were applied to ensure a stable crack propagation. Drift ratio is defined as the ratio between the lateral drift applied at mid-height of the column head and the column shear span. The sign convention for the lateral loads and drifts was positive for the pushing direction whereas the negative sign denoted pulling of the specimen. Further information on the test setup and procedure can be found in Abdallah and El-Salakawy (2021a, b).

Table 8.1: Details of experimental test matrix

Specimen ID		Axial load level (P/P_o)	Concrete strength f_c' [a, b] (MPa)	GFRP spiral Pitch (mm)
This study	Published			
GN-5.0-0.2-85	G-0.2-85s-XX [a]	0.2	36.9 ± 0.4	85
GN-5.0-0.2-50	G-0.2-50s-XX [a]	0.2	36.0 ± 2.0	50
GN-5.0-0.3-85	G-0.3-85s-XX [a]	0.3	41.4 ± 0.7	85
GH-5.0-0.2-85	GH-0.2-85[b]	0.2	86.4 ± 2.4	85
GH-5.0-0.2-50	GH-0.2-50 [b]	0.2	89.4 ± 1.8	50
GH-5.0-0.1-50	GH-0.1-50 [b]	0.1	87.3 ± 2.5	50

Note: P/P_o = axial load level; column aspect ratio for all specimens = 5.0; and f_c' = concrete compressive strength.
[a] Data from Abdallah and El-Salakawy (2021a).
[b] Data from Abdallah and El-Salakawy (2021b).

8.2.3. Summary of experimental test results

The failure of all specimens was controlled by flexure, which occurred in a more brittle manner with spiral rupture for the HSC specimens. The hysteretic response indicated higher initial stiffness for the HSC specimens compared to NSC counterparts. In addition, significantly higher lateral load capacities were observed for HSC columns, increasing by up to 55% compared to their NSC counterparts.

Nonetheless, such enhancement came at the cost of lower failure drifts for the HSC columns, which were reduced by 61 and 20% for specimens confined at a spiral pitch of 85 and 50 mm, respectively. Yet, all tested specimens surpassed the drift limits of 2.50 and 4.00% set by the National Building Code of Canada, NBCC (NRCC 2020) and the Canadian standards CSA S806-12 (CSA 2017) for ductile MRFs, respectively. The only exception was GH-0.2-85, which still achieved its predicted design drift (i.e., 2.20%), and that for moderately-ductile MRFs (CSA 2017), and NBCC (NRCC 2020); i.e., 2.50%. Furthermore, reducing the spiral pitch was found to be much more beneficial for HSC specimens as it improved the drift capacity by approximately 172%, whereas the same pitch reduction caused only a 25% increase in drift capacity for the NSC columns. Increasing the axial load slightly improved the load capacity but caused earlier strength degradation and lower drift capacity. The hysteretic envelopes of test specimens used for the validation of the FEM constructed in this study are shown in Figure 8.2.

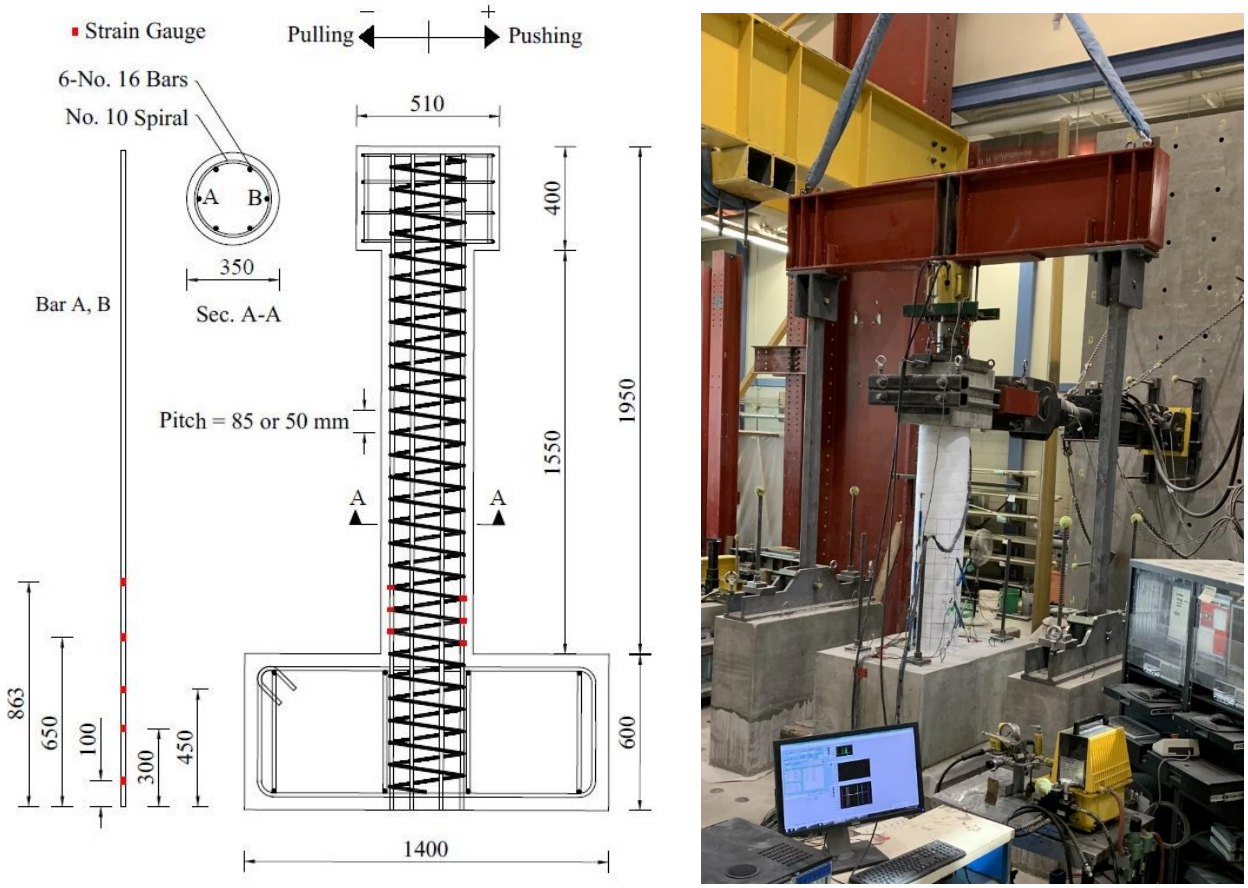

(a) (b)

Figure 8.1: Test specimens and setup (dimensions in mm)

8.3. Description of the Finite-Element Model

8.3.1. Model geometry and boundary conditions

The FEMs comprised of five main components; the column, the footing, column head, longitudinal and transverse (i.e. spirals) reinforcement of the column, and the loading and supporting steel plates, as shown in Figure 8.3. The dimensions of the FEMs were selected after the test specimens (Figure 8.1a), except for the FEMs used in the parametric study to investigate the effect of aspect ratio, as will be discussed later. Fully-rigid contact surfaces were defined in between each two adjacent components to guarantee the strain compatibility. An extensive mesh study and sensitivity analysis were conducted, where different types of elements (i.e., hexahedral and tetrahedral) were compared with varying mesh sizes (i.e., 30 to 100 mm). It was concluded that the hexahedral element can simulate the hysteretic response of the specimens more accurately. Additionally, the 50-mm mesh size was the optimum for the column, because it enabled accurate simulation of the hysteretic response with reasonable computational cost. Using larger mesh sizes resulted in inferior hysteretic responses. On the other hand, the smaller mesh sizes had marginal effect on the modelling accuracy, accompanied by significantly larger analysis duration. Besides, changing the mesh size for the column head and footing did not affect the computational accuracy. Therefore, the eight-node hexahedral (brick) elements with a maximum mesh size of 50 and 100 mm was selected to model the concrete in column and other concrete components (i.e., footing and head), respectively. For the loading and supporting steel plates, the four-node tetrahedral elements with 50-mm maximum mesh size were used.

Table 8.2: Mechanical properties of the utilized GFRP reinforcement

Bar type	Nominal diameter (mm)	Area (mm^2)	Modulus of elasticity (GPa)	Tensile strength (MPa)	Ultimate strain (%)
No. 16 [a]	15.9	197.9	65.7	1,711	2.60
No. 10 (Spirals) [a]	9.5	71	58.4	1,376	2.36

[a] Data from Abdallah and El-Salakawy (2021a, b)

Eight 200 × 200 × 25-mm steel supporting plates were used; four plates above and four plates below the footing. To simulate the effect of post-tensioning on the footing, the plates were restrained in all global directions. In addition, to avoid vertical deflection of the soffit of the footing in the FEM, a 600 × 500 × 25 steel supporting plate, restricted from vertical translation, was placed

below the footing. To avoid any stress concentration at the loading points, 25-mm thick steel plates were used at the locations of the applied loads; a circular plate with a 350-mm diameter on the top of the column and 440 × 400-mm plate on the loading side of the column head.

8.3.2. Concrete material

To model the concrete material, the fracture-plastic constitutive model available in ATENA/GID software package (Červenka et al. 2020b) was implemented. This combined model utilizes a plasticity model for concrete compressive behavior and crushing, whereas the Rankin fracture approach is adopted to model cracking (Figure 8.4). The fixed crack width model was implemented and the tension-stiffening factor, c_{ts}, was selected equal to 0.4 (Figure 8.5), as recommended by CEB-FIP Model Code 1990 (CEB 1990). The specific fracture energy was considered as a function of the concrete tensile strength, given by the following empirical formulae (Červenka et al. 2020b):

$$f_t^{'} = 0.27 f_c^{'2/3} \qquad \text{Equation 8.1}$$

$$G_F = 0.000025 f_t^{'} \quad [MN/m] \qquad \text{Equation 8.2}$$

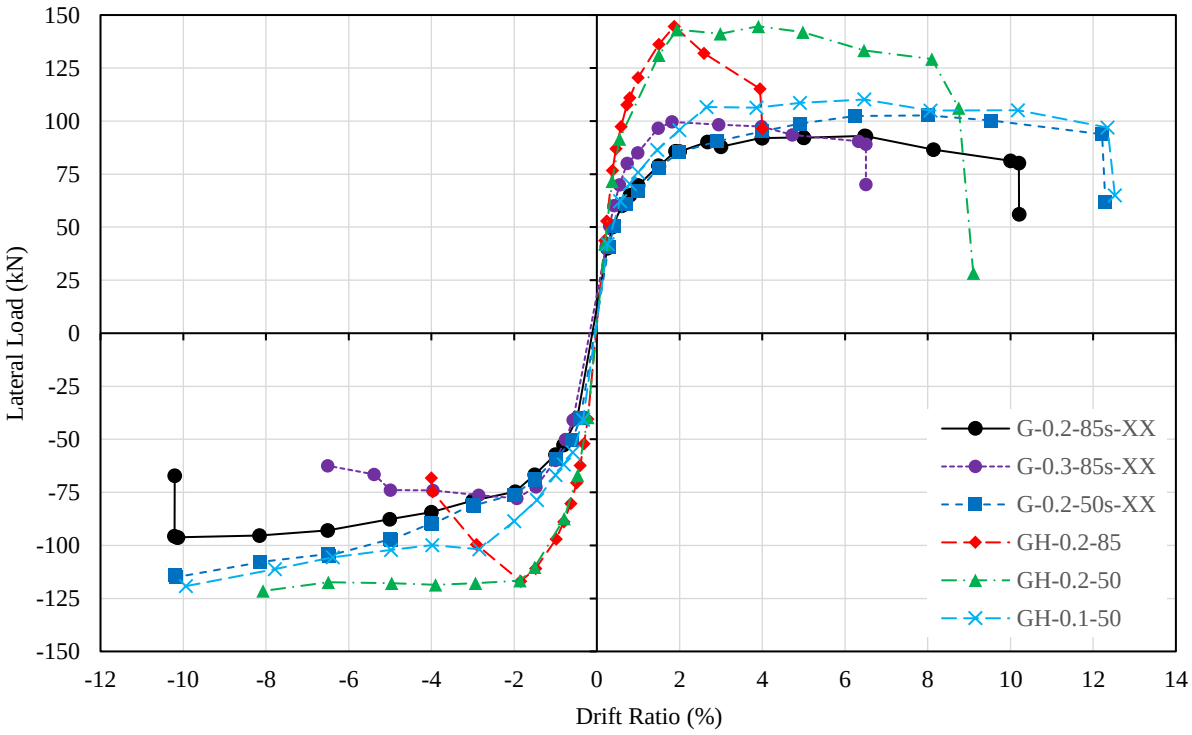

Figure 8.2: Envelopes of hysteresis diagrams for test specimens (Abdallah and El-Salakawy 2021a, b)

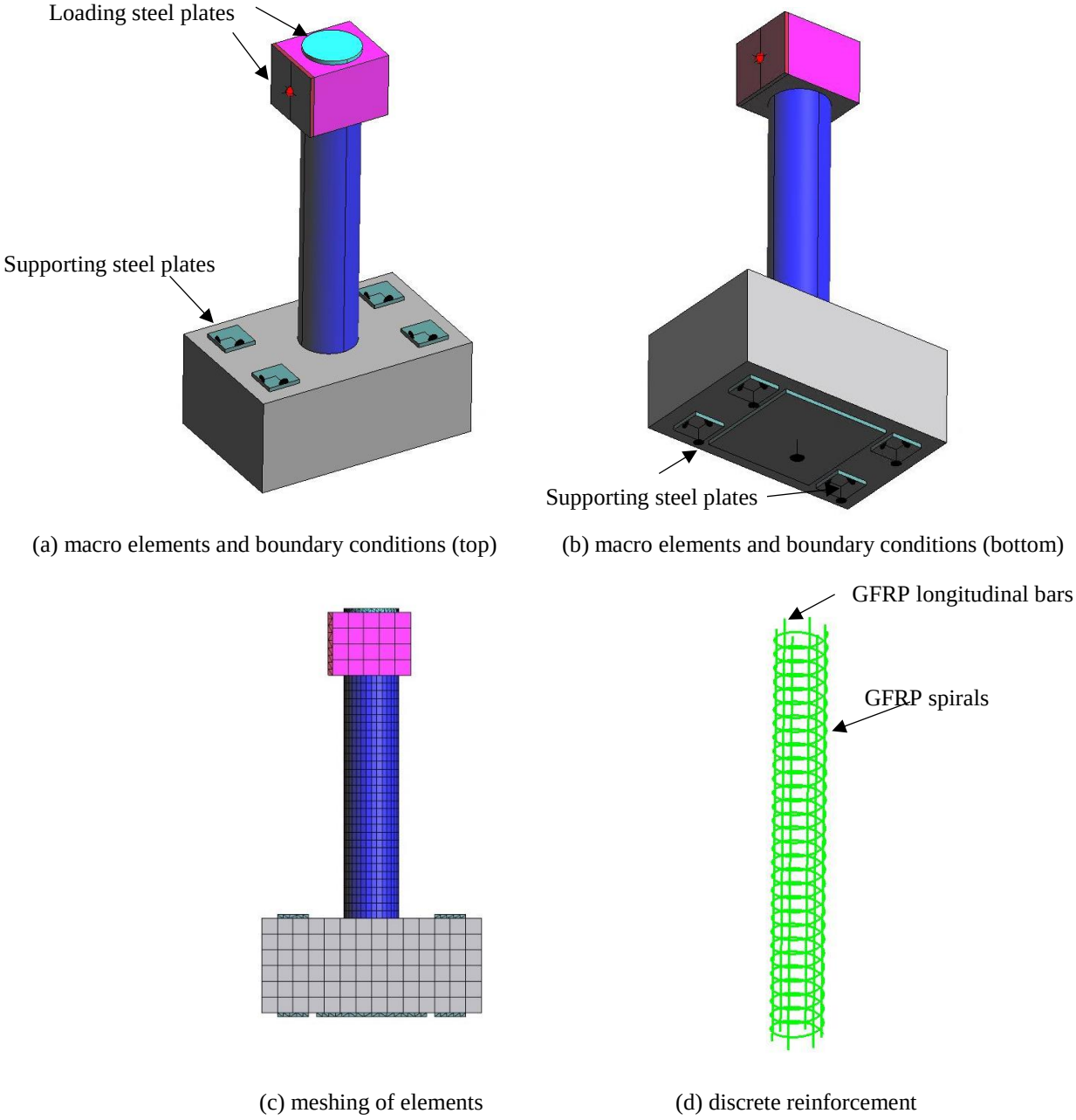

(a) macro elements and boundary conditions (top)

(b) macro elements and boundary conditions (bottom)

(c) meshing of elements

(d) discrete reinforcement

Figure 8.3: Typical details of FEM

The concrete behavior in compression and crushing was modeled following the constitutive laws of Van Mier (1986). The value of the critical compressive displacement, w_d, was taken as 5 mm, as recommended by previous studies (Sasmal et al. 2013; Hosseini et al. 2019). Additionally, to account for the reduction in concrete compressive strength after cracking (Vecchio and Collins 1986), the reduction factor, $r_c^{lim} = 0.8$, was used. The elastic modulus of concrete in compression was estimated based on the following equation (Červenka et al. 2020b):

$$E_c = \left(6{,}500 - 19.8 f_c^{'}\right)\sqrt{f_c^{'}} \qquad \text{Equation 8.3}$$

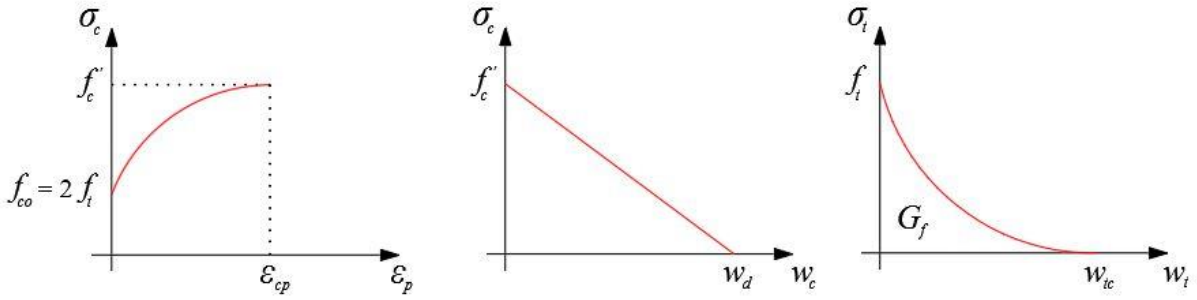

(a) Compressive hardening (b) Compressive softening (c) Tensile softening

Figure 8.4: Constitutive laws of concrete (Adapted from Červenka et al. 2020b)

The normal and tangential shear crack stiffnesses, referred to herein as K_n and K_t, respectively, are correlated through the shear factor coefficient, S_F, where the shear stiffness normal to the crack is calculated as per Equation 8.4.

$$K_n = \frac{f_{t-cr}}{w_{cr}} \qquad \text{Equation 8.4}$$

$$K_t = S_F K_n \qquad \text{Equation 8.5}$$

where $f_{t\text{-}cr}$is the tensile stress at the crack location and w_{cr} is the crack width.

Moreover, to simulate crack closure when the load is reversed, an unloading factor of zero was considered for this study (Hosseini et al. 2019; Setiawan et al. 2019; El-Gendy and El-Salakawy 2021). Table 8.3 summarizes the fundamental concrete parameters as defined for the concrete materials in the FEM.

8.3.3. Reinforcement material

Discrete truss elements were used to model the GFRP reinforcing bars and spirals. The resulting stresses are assumed to be uniformly distributed over the length of the discrete element. The stress-strain relationship of GFRP reinforcement was defined using the multi-linear constitutive law. The stress varied linearly with the strain from zero to the ultimate strength of the GFRP material, f_{Fu}, followed by a descending linear branch down to 0.1 f_{Fu}, as shown in Figure 8.6a (Nagy-György et

al. 2012). The properties of the GFRP reinforcement were taken the same as those provided in the experimental studies used for validating the FEM (Abdallah and El-Salakawy 2021a, b), as listed in Table 8.1. The bond characteristics of the GFRP longitudinal bars were modeled in the software using a user-defined bond-slip model based on the experimental results of Alves et al. (2011), as depicted by Figure 8.6b. Unlike the longitudinal GFRP bars, no signs of slippage were reported for the GFRP spirals in the experimental tests (Abdallah and El-Salakawy 2021a, b). Therefore, the perfect bond option was utilized for the spirals.

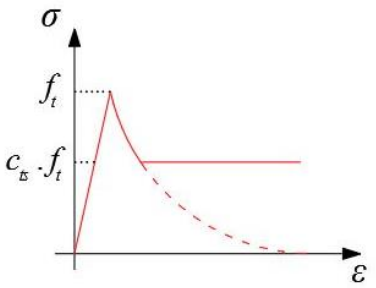

Figure 8.5: Tension stiffening of concrete (Adapted from Červenka et al. 2020b)

Table 8.3: Input parameters for the concrete constitutive model used in the validation process

Concrete property	NSC Columns	HSC Columns
Elastic modulus, E_c (MPa)	35,082	44,700
Poisson's ratio, μ	0.2	0.2
Compressive strength, $f_c^{'}$ (MPa)	37.0	90.0
Tensile strength, f_t (MPa)	3.0	4.9
Specific fracture energy, G_F ($\times 10^{-5}$ MN/m)	8.2	12.3
Fixed crack model coefficient	1.0	1.0
Tension stiffening factor, c_{ts}	0.4	0.4
Maximum aggregate size (mm)	19.0	19.0
Shear factor	20.0	20.0
Unloading factor	0.0	0.0
Critical compressive displacement, w_d (mm)	-5.0	-5.0
Plastic strain at compressive strength, ε_{cp} ($\times 10^{-3}$)	1.05	2.01
Reduction of strength due to cracks, $r_{c,\,lim}$	0.80	0.80
Failure surface eccentricity	0.52	0.52
Multiplier for the specific flow direction, β	0.50	0.50
Specific material weight, ρ (MN/m^3)	0.023	0.023

For the column head and footing, the smeared reinforcement model was implemented in the three global directions (x, y and z) with a reinforcement ratio of 1 and 3%, respectively. This approach had an advantage of reducing the analysis time and complexity without jeopardizing the accuracy and reliability of the results (Hosseini et al. 2019). This was also verified at a preliminary step of this study. For this reinforcement model, a perfect bond is assumed between the smeared reinforcement and the concrete (Červenka et al. 2020b).

8.3.4. Elastic steel material

All loading and supporting steel plates were defined in the FEMs as 3D solid elastic material with an elastic modulus and a Poisson's ratio of200 GPa and 0.3, respectively. Nonetheless, no yielding point was specified for the plates to eliminate any possibility of premature failure.

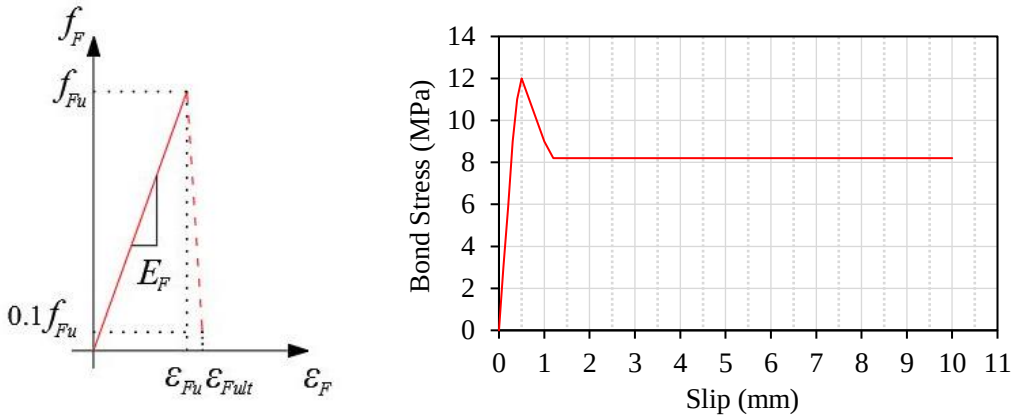

(a) Multi-linear stress-strain law (b) Bond-slip relationship

Figure 8.6: Constitutive laws for GFRP discrete reinforcement (Adapted from Alves et al. 2011)

8.3.5. Loading procedure and analysis method

First, the axial load was applied first in 20 load-controlled steps, where each loading step represented 5% of the specified axial load. Once the full axial load was applied, it was maintained for the entire analysis process. Prior to applying the cyclic drift reversals, a displacement-controlled lateral drift cycle, with 0.8% peak drift ratio, was applied to impose equivalent stresses to those imposed by the cracking and service loading cycles during the experimental testing. Afterwards, the cyclic drift reversals were applied. Each drift cycle comprised of multiple displacement-controlled steps, where each step increment was 1 mm (i.e., equivalent to about 0.06% drift ratio for a column with aspect ratio of 5.0).

To analyze the FEMs, the standard Newton-Raphson iterative method, built-in the ATENA/GID software, was utilized. The default convergence error of 1.0% was used in this study.

8.4. Model Validation

The results of the FEM were validated against the results of six specimens from the previously summarized experimental work (Abdallah and El-Salakawy 2021a, b). The steel-RC specimen and those confined using GFRP circular hoops were not included in the validation process, because they were not within the scope of this study. The validation process was performed in terms of hysteretic response, initial stiffness and energy dissipation.

8.4.1. Hysteretic response

Generally, the experimental and FEM results in terms of hysteretic response were in good agreement for the six specimens used for model validation. An example of such agreement is depicted by Figures 8.7a and b for specimen GN-5.0-0.2-85. It should be noted that only the first cycle of each drift step was plotted for better visibility. The FEMs were able to reach the failure drifts achieved by experimental testing and predicted the lateral load capacity with an error of 10% or less. Table 8.4 summarizes the predicted versus actual results. The mean ratio of predicted-to-experimental lateral load capacities was 0.97 $\pm$ 0.07 and 1.03 $\pm$ 0.41 for pushing and pulling loading directions, respectively. The coefficients of variation (COV) and determination (R^2) were 7.24% and 0.89, respectively, for the pushing direction, whereas these coefficients were 4.00% and 0.89, respectively, for the pulling loading direction.

8.4.2. Stiffness

As shown in Figure 8.7c, the FEMs were capable of simulating the stiffness degradation of the test specimens with a high degree of precision. The stiffness was calculated as the slope of the straight line joining the peak lateral loads on pushing and pulling directions during the third cycle of each drift step (El-Gendy and El-Salakawy 2021). The initial stiffness values of the columns, defined as the stiffness during the first drift step (i.e. 0.80% drift ratio), are listed in Table 8.4. The mean FEM-to-experimental initial stiffness was 1.08 $\pm$ 0.035 with COV and R^2 equal to 3.21% and 0.91, respectively.

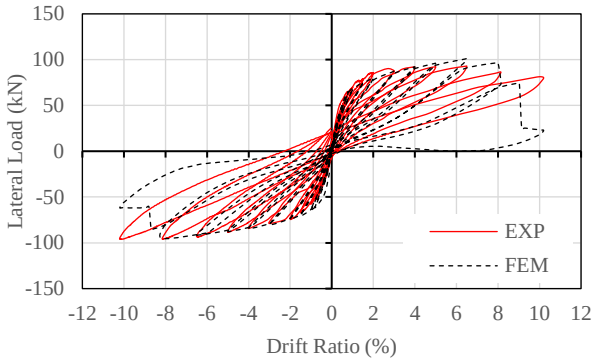

(a) Hysteretic response

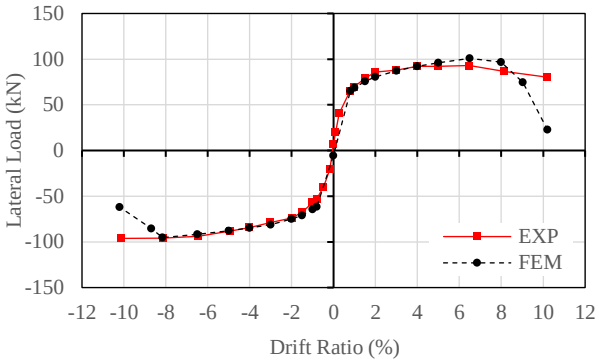

(b) Lateral load-drift envelope

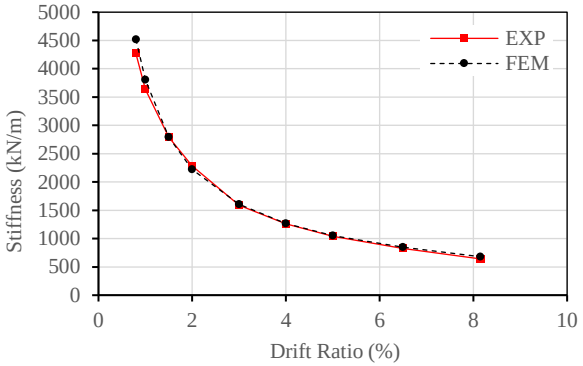

(c) Stiffness

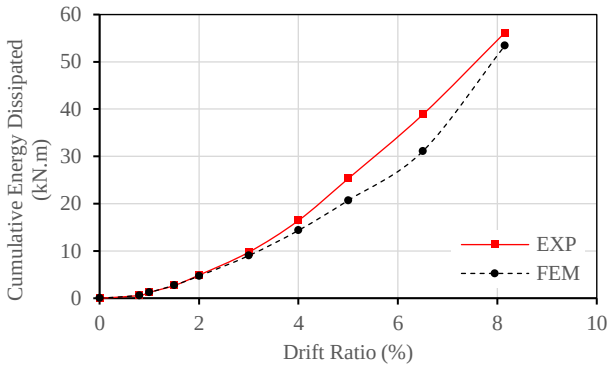

(d) Energy dissipation

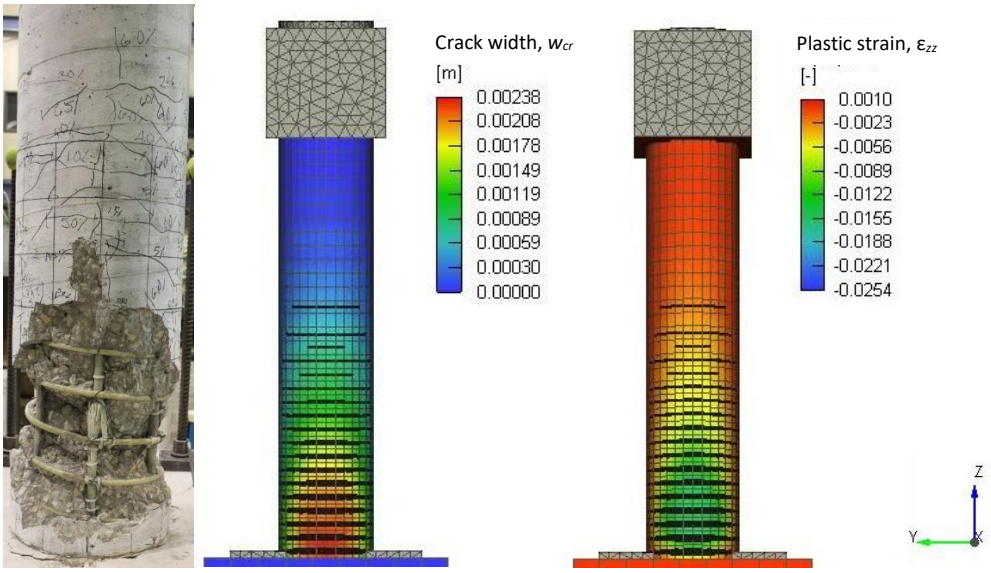

(e) Spalling region at failure

Figure 8.7: Validation of FEM – specimen GN-5.0-0.2-85

Table 8.4: Theoretical and experimental lateral load and drift capacities

Specimen	Initial stiffness (kN/m)			Ultimate drift ratio (%)			Maximum lateral load (kN)						Energy dissipation (kN-m)		
	Positive direction (pushing)						Pushing direction (+ve)			Pulling direction (-ve)					
	K_{FEM}	K_{EXP}	$\frac{K_{FEM}}{K_{EXP}}$	δ_{FEM}	δ_{EXP}	$\frac{\delta_{FEM}}{\delta_{EXP}}$	V_{FEM}	V_{EXP}	$\frac{V_{FEM}}{V_{EXP}}$	V'_{FEM}	V'_{EXP}	$\frac{V'_{FEM}}{V'_{EXP}}$	E_{FEM}	E_{EXP}	$\frac{E_{FEM}}{E_{EXP}}$
GN-5.0-0.2-85	4,519	4,266	1.06	10.20	10.20	1.00	100	94	1.07	-95	-96	0.99	53.4	56.2	0.95
GN-5.0-0.2-50	4,613	4,307	1.07	12.75	12.75	1.00	105	103	1.07	-110	-116	0.95	77.2	82.6	0.93
GN-5.0-0.3-85	4,952	4,757	1.04	6.50	6.50	1.00	92	101	0.91	-83	-78	1.06	29.5	30.9	0.95
GH-5.0-0.2-85	7,624	7,156	1.07	4.00	4.00	1.00	128	145	0.88	-123	-117	1.05	17.3	16.6	1.04
GH-5.0-0.2-50	6,969	7,629	1.09	8.60	9.00	0.96	135	147	0.92	-128	-122	1.05	89.9	93.1	0.97
GH-5.0-0.1-50	5,432	4,738	1.15	12.75	12.75	1.00	101	111	0.91	-112	-119	0.94	100.6	98.0	1.03
Mean			1.08			0.99			0.96			1.00			0.98
SD			0.035			0.015			0.079			0.049			0.042
COV (%)			3.21%			1.5%			8.2%			4.89%			4.27%
R^2			0.91			0.99			0.89			0.89			0.99

Note: K_{FEM} = initial stiffness estimated by FEM; K_{EXP} = experimental initial stiffness; δ_{FEM} = failure drift estimated by FEM; δ_{EXP} = experimental failure drift; V_{FEM} = lateral load capacity in pushing direction as estimated by FEM; V_{EXP} = experimental lateral load capacity in pushing direction; V'_{FEM} = lateral load capacity in pulling direction as estimated by FEM; V'_{EXP} = experimental lateral load capacity in pulling direction; E_{FEM} = total energy dissipation estimated by FEM; and E_{EXP} = experimental total energy dissipation.

8.4.3. Energy dissipation

The cumulative energy dissipated was estimated as the accumulative area enclosed by the hysteresis loops of the successive drift steps. The cumulative energy dissipation of the FEMs was remarkably similar to that of experimental testing, as evident from Figure 8.7d. As shown in Table 8.4, the mean FEM-to-experimental total energy absorbed was 0.99 ± 0.047 with COV and R^2 values of 4.77% and 0.99, respectively.

8.4.4. Cracking pattern

As shown in Figure 8.7e, the spalling region, as predicted by the FEM, is in good agreement with the experimental results. The length of spalling region, as indicated from the values of concrete strain, was approximately 500 mm, which is 0.95 of the experimentally measured spalling length. In addition, the cracking pattern obtained using FEM extended for about 900 mm, with more concentration of cracks, in terms of number and width, within the spalling region. This, again, agrees well with the cracking propagation observed experimentally.

8.5. Parametric Study

The calibrated FEM, as discussed previously, was used to perform a comprehensive parametric study with the main goal of studying the seismic behavior of GFRP-RC circular columns; to further propose a refined design model for the GFRP confinement reinforcement under seismic loading. All FEMs included in this parametric study had the same characteristics as the validated FEM, apart from the spiral pitch and column length, which were considered as variables. The key parameters included in this study were: (1) concrete compressive strength; (2) spiral pitch; (3) axial load level; and (4) aspect ratio (i.e., shear span-to-depth ratio). The FEMs were designated using a five-character alphanumeric code, in a similar manner to what was previously used. The only exception was the second number, which represented herein the concrete compressive strength in this parametric study, varying between 30 and 90 MPa, as discussed later.

8.5.1. Effect of concrete strength

The effect of concrete strength on the seismic response of GFRP-RC circular columns was investigated by including a wide range of concrete compressive strengths, varying between 30 and 90 MPa with an interval of 10 MPa. Moreover, to investigate the effect of concrete strength under various levels of confinement, two sets of FEMs were considered; one with 85-mm spiral pitch

and the other set had a 100-mm pitch. The properties of the different concrete grades utilized in the parametric investigation are summarized in Table 8.5, whereas the details of the FEMs are listed in Table 8.6.

Table 8.5: Properties of concrete grades used in the parametric study

Parameter	Concrete grade						
	C30	C40	C50	C60	C70	C80	C90
Compressive strength, f_c' (MPa)	30	40	50	60	70	80	90
Elastic modulus, E_c (MPa)	32,349	36,101	38,962	41,147	42,787	43,970	43,970
Tensile strength, f_t (MPa)	2.90	3.51	4.07	4.13	4.41	4.66	4.88
Specific fracture energy, G_F ($\times 10^{-5}$ MN/m)	7.3	9.0	10.3	10.5	11.3	11.8	12.3
Plastic strain at compressive strength, ε_{cp} ($\times 10^{-3}$)	0.93	1.11	1.28	1.46	1.64	1.82	2.01

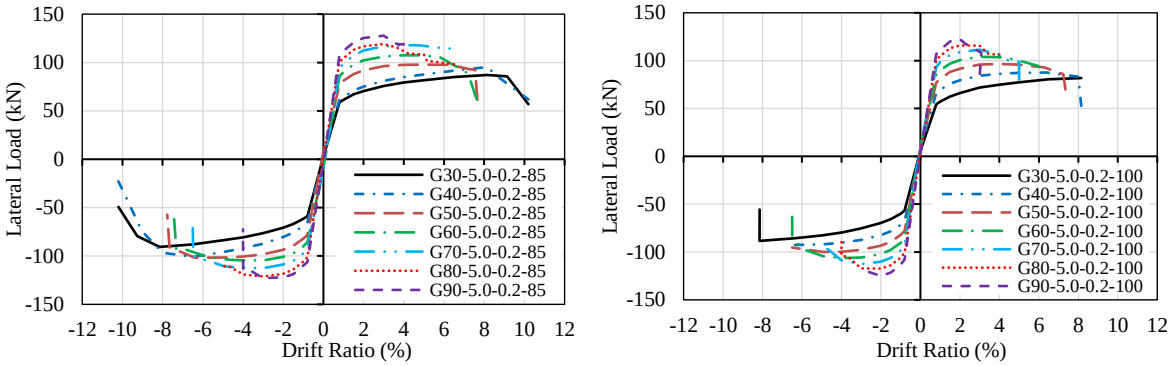

(a) spiral pitch = 85 mm (b) spiral pitch = 100 mm

Figure 8.8: Lateral load-drift envelopes of columns with different concrete strengths

As shown in Figure 8.8a, increasing the concrete strength enhanced both the lateral load resistance and stiffness, whereas the drift capacity was consistently compromised. In addition, for the spiral pitch of 85 mm, which satisfied the requirements of the Canadian standard, CSA S806-12 (CSA 2017), increasing the concrete strength by up to 20 MPa improved the lateral load resistance and stiffness of the column, without significantly reducing its drift capacity. On the other hand, for the spiral pitch of 100 mm, an increase of the concrete strength, even as small as 10 MPa, resulted in a significantly deteriorating hysteretic response and reduced deformability, as evident from Figure 8.8b. This signifies the importance of the maximum limit for spiral pitch to be one-fourth the gross diameter of the column as per the Canadian standard CSA S806-12 (CSA 2017). Generally, increasing the concrete strength from 30 up to 60 MPa resulted in a more considerable improvement in lateral load resistance than when the concrete strength increased beyond 60 MPa. Furthermore, it is evident from Figure 8.9 that the larger the concrete strength, the higher the initial

stiffness and stiffness degradation would be. This seems to be independent of spiral pitch when Figures 8.9a and b are compared.

8.5.2. Effect of spiral pitch

In this study, the effect of different spiral pitches was assessed for three concrete strengths; 30, 60, and 90 MPa. The varying levels of enhancement in the hysteretic response observed for the NSC and HSC columns by Abdallah and El-Salakawy (2021b) indicated that the effect of spiral pitch is closely related to concrete compressive strength. The values of spiral pitch implemented in this study ranged between 50 to 130 mm, with few exceptions depending on concrete compressive strength. For instance, the range from 50 to 85 mm was omitted for the FEMs having a concrete compressive strength of 30 MPa, due to the over conservative nature of such spiral pitches. On the other hand, the spiral pitches of 100 to 130 mm were excluded for the FEMs with a concrete strength equal to 90 MPa because they were deemed overly substandard. The full range (i.e., 50 to 130 mm) was applied to the concrete compressive strength of 60 MPa, as listed in Table 8.7.

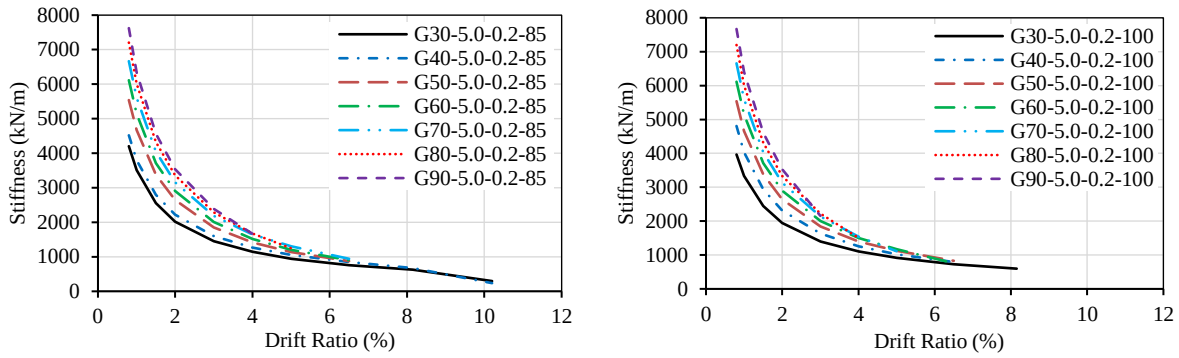

(a) spiral pitch = 85 mm (b) spiral pitch = 100 mm

Figure 8.9: Stiffness degradation for columns with different concrete strengths

For the concrete strength of 30 MPa, increasing the spiral pitch from 85 to 130 mm resulted in reducing the lateral load capacity by about 13%, while the failure drift was decreased by 36% (Figure 8.10a). On the other hand, with the same increase in spiral pitch for concrete strength of 60 MPa, the lateral load decreased by only 6% whereas a reduction of 51% was recorded for the failure drift, as depicted by Figure 8.10b. In a similar manner, increasing the spiral pitch from 50 to 100 mm reduced the failure drift by 36 and 61% for a concrete strength of 60 and 90 MPa, respectively (Figures 8.10b and c). This clearly indicates that reducing the spiral pitch could be more effective, especially in terms of deformability improvement, for columns with higher

concrete compressive strengths. Moreover, the strength degradation was comparable for the FEMs having a concrete strength of 30 MPa regardless of spiral pitch, as shown in Figure 8.11a, whereas higher strength degradation can be observed for FEMs with concrete strengths of 60 and 90 MPa beyond 2.00% drift ratio as the spiral pitch increased (Figures 8.11b and c).

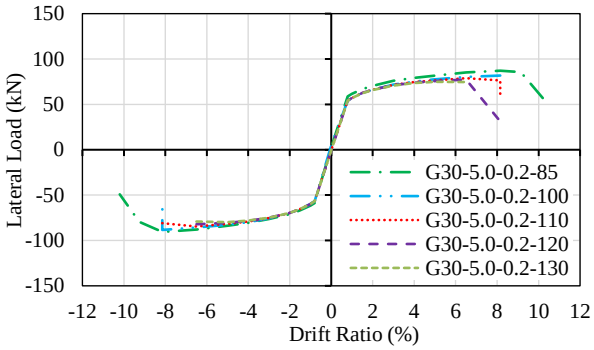

(a) Concrete strength = 30 MPa

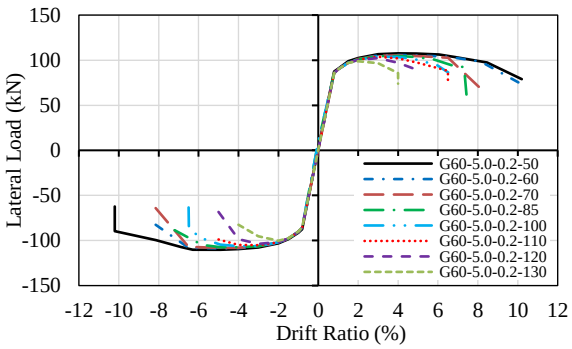

(b) Concrete strength = 60 MPa

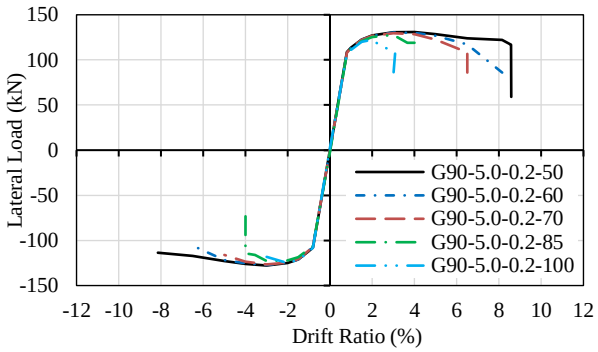

(c) Concrete strength = 90 MPa

Figure 8.10: Lateral load-drift envelopes of columns with different spiral pitches

8.5.3. Effect of axial load level

The previous experimental studies demonstrated the significant effect of axial load level on the seismic performance of GFRP-RC columns including load and drift capacities in addition to strength degradation (Tavassoli et al. 2015; Ali and El-Salakawy 2016; Elshamandy et al. 2018; Abdallah and El-Salakawy 2021a, b). The available experimental data, however, is rather limited in terms of axial load level for GFRP-RC circular columns. Therefore, the influence of axial load level was investigated through three series of FEMs, where the concrete compressive strength was 30, 60 and 90 MPa for the first, second and third series, respectively. Each series included four FEMs under axial load levels ranging from 0.2 to 0.5 with an interval of 0.1. Since developing a

design model for columns in moment-resisting frames (MRFs) under significant axial load was the main goal for this study, axial load levels less than 0.2 were not included within the scope of this study. The properties of the FEMs used in this phase are summarized in Table 8.8. The spiral pitch was taken as 85 mm for all FEMs in the three series included in this section.

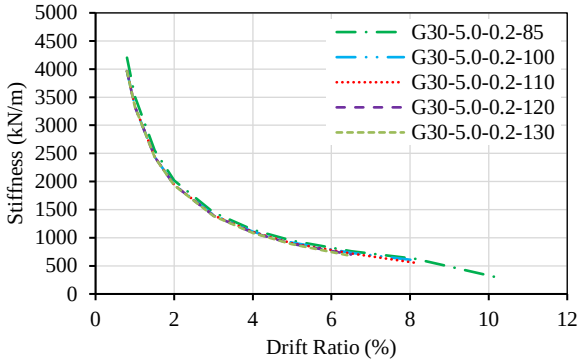

(a) Concrete strength = 30 MPa

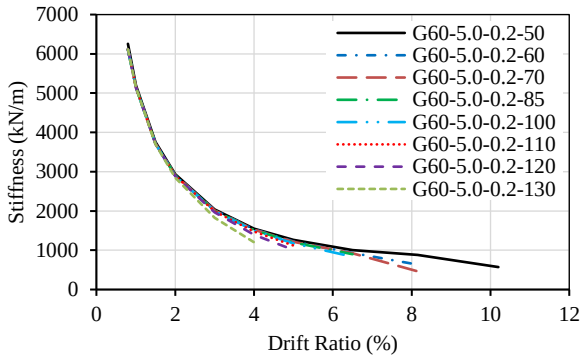

(b) Concrete strength = 60 MPa

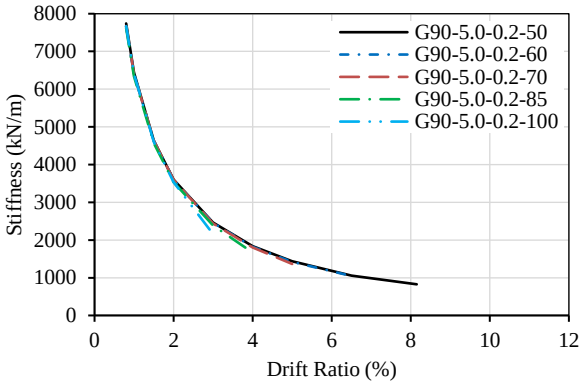

(c) Concrete strength = 90 MPa

Figure 8.11: Stiffness degradation for columns with different spiral pitches

As can be seen in Figures 8.12a, b and c, increasing the axial load level from 0.2 to 0.3 resulted in earlier strength gain (i.e., developing larger lateral load resistance than the counterpart under lower axial load level of 0.2) for the FEM accompanied by higher strength degradation and reduced failure drift regardless of the concrete compressive strength. The rate of strength degradation, however, increased proportionally with the concrete strength. As the axial load level increased further, the early strength gain was reduced, and higher strength degradation and lower failure drifts were observed. Such effect was even more severe as the concrete strength increased. A spike was observed for the lateral load resistance in the pushing direction at 0.8% drift ratio for the FEMs having a concrete compressive strength of 90 MPa when the axial load level increased beyond 0.2

(Figure 8.12c). As the axial load level increased from 0.2 to 0.5, the failure drift was reduced by 46, 61 and 75% for a concrete strength of 30, 60 and 90 MPa, respectively.

Table 8.6: Characteristics of FEMs studying the effect of concrete compressive strength

FEM	Concrete strength, f_c' (MPa)	Spiral pitch (mm)	Maximum lateral load (kN)		δ_{FEM} (%)	K_{FEM} (kN/m)
			Pushing direction (+ve)	Pulling direction (-ve)		
G30-5.0-0.2-85	30	85	87	-91	10.20	4,203
G40-5.0-0.2-85	40	85	95	-101	9.03	4,519
G50-5.0-0.2-85	50	85	98	-102	7.80	5,539
G60-5.0-0.2-85	60	85	108	-105	7.43	6,267
G70-5.0-0.2-85	70	85	118	-113	6.50	6,666
G80-5.0-0.2-85	80	85	119	-121	6.50	7,206
G90-5.0-0.2-85	90	100	128	-123	4.00	7,624
G30-5.0-0.2-100	30	100	82	-88	8.15	3,965
G40-5.0-0.2-100	40	100	88	-93	8.15	4,806
G50-5.0-0.2-100	50	100	97	-100	7.35	5,538
G60-5.0-0.2-100	60	100	106	-104	6.5	6,113
G70-5.0-0.2-100	70	100	111	-113	5.00	6,655
G80-5.0-0.2-100	80	100	116	-117	4.00	7,197
G90-5.0-0.2-100	90	100	125	-122	3.00	7,669

Note: f_c' = concrete compressive strength; δ_{FEM} = failure drift estimated by FEM; and K_{FEM} = initial stiffness estimated by FEM.

Increasing the axial load level, up to 0.4, resulted in higher initial stiffness (Figure 8.13). When the axial load level was increased further to 0.5, however, less significant increase was observed in terms of initial stiffness. Such effect was even more pronounced as the concrete strength increased. For instance, G30-5.0-0.5-85 exhibited a 23% higher initial stiffness than G30-5.0-0.2-85, whereas the initial stiffness of G60-5.0-0.5-85 increased by only 4% over that of its counterpart under an axial load level of 0.2. Nonetheless, such comparison is not applicable to the specimens with 90-MPa concrete strength due to the spike observed on the pushing side at 0.8% drift ratio for specimens G90-5.0-0.3-85, G90-5.0-0.4-85 and G90-5.0-0.5-85. The observed deterioration associated with the large axial load levels, such as 0.5, suggests conducting further experimental testing to investigate the seismic response of GFRP-RC circular columns under such high axial

load levels. Despite the fact that the reported response of GFRP-RC under high axial load level did not encounter premature material failure (Tavassoli et al. 2015; Elshamandy et al. 2018), it is crucial to investigate this significant parameter. One of the main reasons for that is the scarcity of experimental data on such axial load level, especially for columns with HSC.

Table 8.7: Characteristics of FEMs studying the effect of spiral pitch

FEM	Concrete strength, f_c' (MPa)	Spiral pitch (mm)	Maximum lateral load (kN)		δ_{FEM} (%)	K_{FEM} (kN/m)
			Pushing direction (+ve)	Pulling direction (-ve)		
G30-5.0-0.2-85	30	85	87	-91	10.20	4,203
G30-5.0-0.2-100	30	100	82	-88	8.15	3,965
G30-5.0-0.2-110	30	110	79	-85	8.15	3,964
G30-5.0-0.2-120	30	120	77	-82	7.43	3,963
G30-5.0-0.2-130	30	130	75	-80	6.50	3,962
G60-5.0-0.2-50	60	50	108	-110	10.20	6,255
G60-5.0-0.2-60	60	60	108	-109	10.20	6,116
G60-5.0-0.2-70	60	70	105	-108	8.15	6,115
G60-5.0-0.2-85	60	85	105	-108	7.43	6,115
G60-5.0-0.2-100	60	100	104	-106	6.5	6,113
G60-5.0-0.2-110	60	110	104	-105	6.5	6,112
G60-5.0-0.2-120	60	120	102	-104	5.00	6,112
G60-5.0-0.2-130	60	130	99	-100	4.00	6,114
G90-5.0-0.2-50	90	50	135	-128	8.60	7,741
G90-5.0-0.2-60	90	60	130	-127	8.15	7,673
G90-5.0-0.2-70	90	70	130	-127	6.50	7,671
G90-5.0-0.2-85	90	85	128	-123	4.00	7,624
G90-5.0-0.2-100	90	100	125	-122	3.00	7,669

Note: f_c' = concrete compressive strength; δ_{FEM} = failure drift estimated by FEM; and K_{FEM} = initial stiffness estimated by FEM.

8.5.4. Effect of aspect ratio

The variation of column aspect ratio (i.e. height-to-diameter ratio) is known to significantly affect the seismic response of steel-RC columns. Previous studies showed that reducing the column

aspect ratio resulted in larger strength degradation, higher influence of shear stresses and reduced drift capacity (Sakai and Sheik 1989; Razvi and Saatcioglu 1996; Lehman and Moehle 1999). Furthermore, it was concluded by Bae and Bayrak (2008) that increasing the column aspect ratio may adversely influence the deformability of steel-RC columns under high axial load levels. On the other hand, the effect of aspect ratio on the seismic behavior of FRP-RC columns is not yet fully explored, apart from limited experimental data. These attempts incorporated fiber-reinforced concrete, carbon FRP (CFRP), or hybrid (steel + GFRP) reinforcement (Sharbatdar 2003; Deng et al. 2018; Kharal et al. 2021). Thus, it was of interest to evaluate the impact of column aspect ratio on the seismic performance of GFRP-RC circular columns. This was sought through three groups of FEMs, where the concrete compressive strength was 30, 60, or 90 MPa. For each group, the range of column aspect ratio extended from 2.0 to 7.0. The former ratio represented what is referred to as "captive columns" in MRFs (Saatcioglu 1991), whereas the latter resembled long columns that could be utilized in areas with large floor height such as reception halls. Table 8.9 contains the characteristics of the aforementioned FEMs.

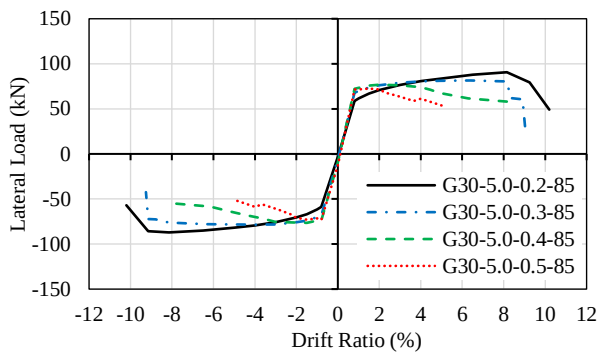

(a) Concrete strength = 30 MPa

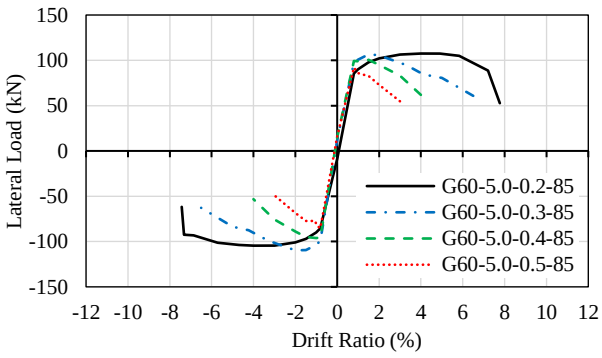

(b) Concrete strength = 60 MPa

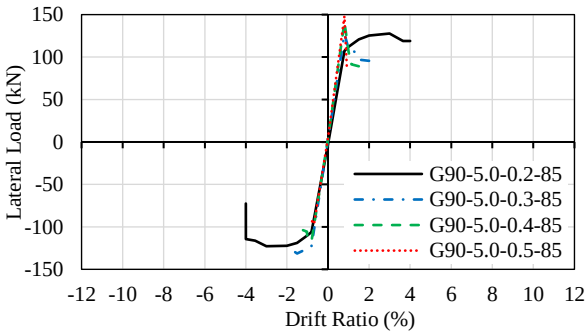

(c) Concrete strength = 90 MPa

Figure 8.12: Lateral load-drift envelopes of columns with different axial load levels

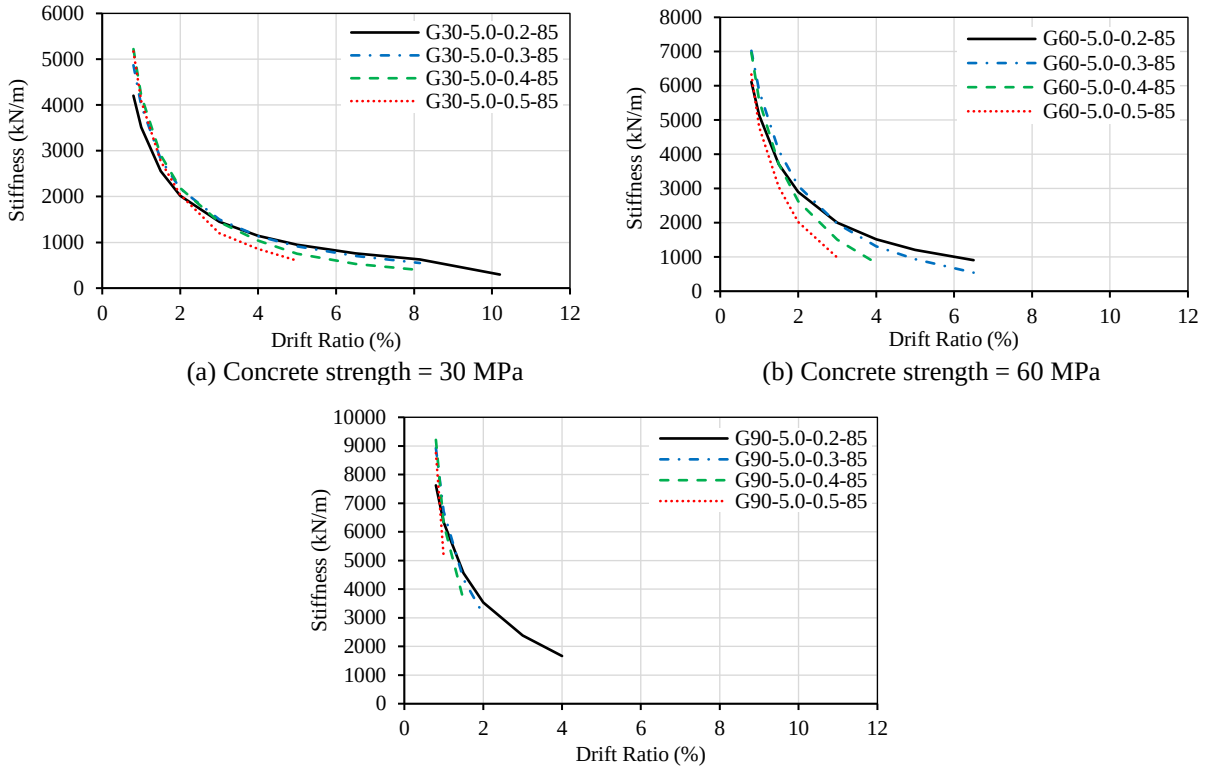

(a) Concrete strength = 30 MPa

(b) Concrete strength = 60 MPa

(c) Concrete strength = 90 MPa

Figure 8.13: Stiffness degradation for columns with different axial load levels

As expected, increasing the aspect ratio resulted in lower lateral load resistance (Figure 8.14), since the shear span increased, while the moment capacity should presumably be the same. For better comparison between the models with different aspect ratios, the moment resistance, instead of the lateral load, was plotted against drift ratio, as depicted by Figure 8.15. It can be observed that specimens with the same concrete strength exhibited similar moment capacities regardless of the aspect ratio. Nonetheless, the development of moment capacity was more gradual for the lower aspect ratios, whereas that of the larger aspect ratios was more rapid and followed by strength degradation up to failure. Similar observations were reported by Sharbatdar (2003), Deng et al. (2018), and Kharal et al. (2021). In addition, the failure drifts observed for the columns having the same concrete strength but different aspect ratios were almost identical. This contradicts the assumption of direct proportional relationship between aspect ratio and deformability, upon which the design equation in Clause 12.7.3.3 of the Canadian standard CSA S806-12 (CSA 2017), was based. In fact, the similar moment and drift capacities for the FEMs with different aspect ratios may suggest that the deformability of GFRP-RC circular columns is reduced as the aspect ratio increases. This can be due to the secondary moments attributed to the *P*-Δ effect, which would

result in higher strength degradation for columns with higher aspect ratios. Therefore, a new design model for FRP confinement reinforcement in RC columns located in seismic-active zones, is required. The only exception was G30-2.0-0.2-85, which failed at 20% lower drift ratio than its longer counterparts. On the other hand, all columns having the same concrete strength of 60 or 90 MPa exhibited similar failure drifts, regardless of their aspect ratios. This could be attributed to the fact that the specimens with a concrete strength of 60 or 90 MPa failed at moderate or low drift ratios. Conversely, the columns having the 30-MPa concrete strength achieved a much higher drift ratio than that specified by the Canadian standard CSA S806-12 (CSA 2017) for ductile MRFs (i.e., 4.00%). Such high drift ratios could be difficult to reach by shorter columns due to higher shear stresses, resulting in a more brittle failure.

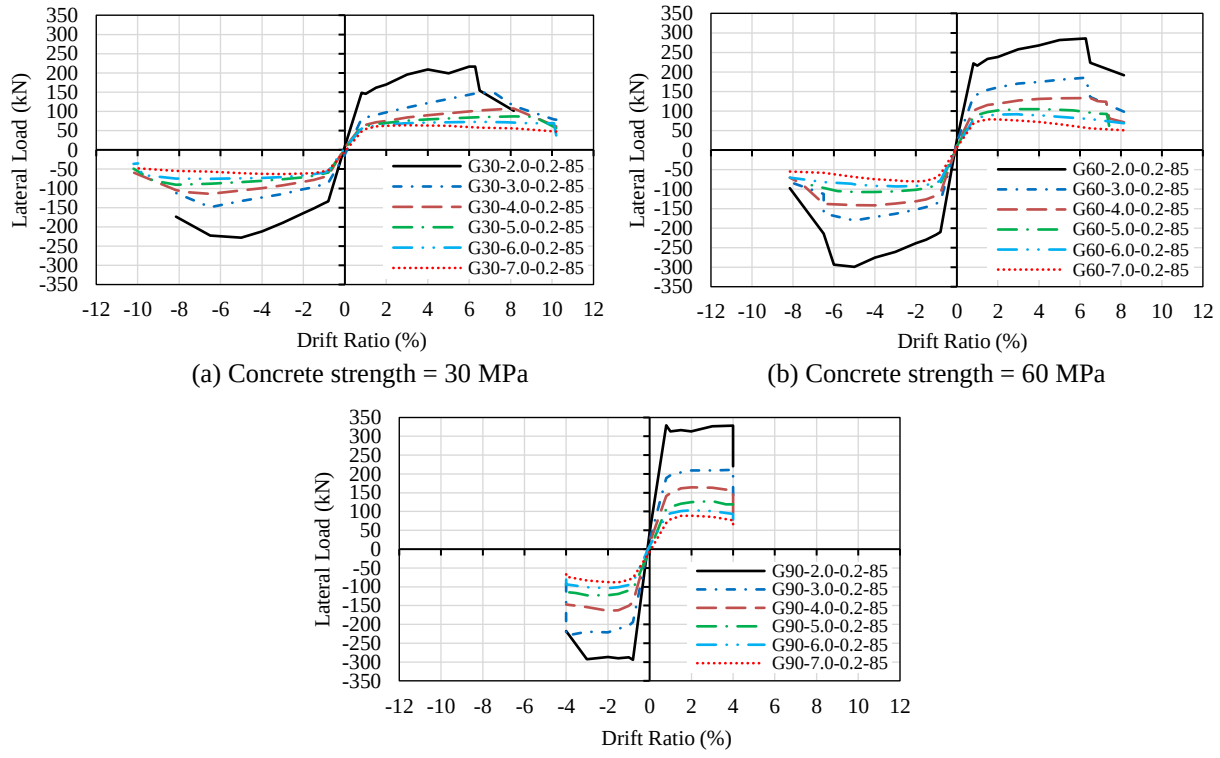

(a) Concrete strength = 30 MPa

(b) Concrete strength = 60 MPa

(c) Concrete strength = 90 MPa

Figure 8.14: Lateral load-drift envelopes of columns with different aspect ratios

For the same applied moment at the column base, a short column experiences higher intensity of shear stresses than a longer column. The interaction of such shear stresses and flexure stresses due to combined flexure and axial loading results in faster deterioration of the column section and reduces its moment capacity and deformability. Therefore, lower drift capacity can be expected

for the shorter column. Similar response was reported by Sharbatdar (2003), where shorter columns exhibited lower deformability due to higher shear stresses.

Table 8.8: Characteristics of FEMs studying the effect of axial load level

FEM	Concrete strength, f_c' (MPa)	Axial load level (P/P_o)	Maximum lateral load (kN)		δ_{FEM} (%)	K_{FEM} (kN/m)
			Pushing direction (+ve)	Pulling direction (-ve)		
G30-5.0-0.2-85	30	0.2	87	-91	10.20	4,203
G30-5.0-0.3-85	30	0.3	82	-79	9.25	4,869
G30-5.0-0.4-85	30	0.4	77	-77	8.15	5,221
G30-5.0-0.5-85	30	0.5	73	-73	5.00	5,169
G60-5.0-0.2-85	60	0.2	105	-108	7.43	6,115
G60-5.0-0.3-85	60	0.3	107	-110	6.5	7,023
G60-5.0-0.4-85	60	0.4	101	-96	4.00	6,968
G60-5.0-0.5-85	60	0.5	92	-85	3.00	6,331
G90-5.0-0.2-85	90	0.2	128	-123	4.00	7,624
G90-5.0-0.3-85	90	0.3	127	-131	2.00	8,928
G90-5.0-0.4-85	90	0.4	141	-117	1.50	9,213
G90-5.0-0.5-85	90	0.5	148	-97	1.00	8,753

Note: f_c' = concrete compressive strength; P/P_o = axial load level; δ_{FEM} = failure drift estimated by FEM; and K_{FEM} = initial stiffness estimated by FEM.

Furthermore, as could be observed from Figure 8.16 and Table 8.9, increasing the column aspect ratio caused a considerable decrease in the initial stiffness. Notably, all columns exhibited similar reduction percentages (i.e. about 40%) when the aspect ratio increased from 2.0 to 3.0, regardless of concrete compressive strength. However, for the aspect ratios larger than 3.0, more severe reduction of initial stiffness was observed as the concrete compressive strength increased.

To the best of the authors' knowledge, the literature contains no experimental or numerical data on the seismic response of GFRP-RC columns with low aspect ratios (i.e., less than 5.0), apart from few attempts for square columns that used either fiber-reinforced concrete (Deng et al. 2018) or carbon FRP reinforcement (Sharbatdar 2003). The outcomes of this study highlight the need for more research on the seismic behavior of short FRP-RC circular columns, especially those with aspect ratios less than or equal to 3.0.

Table 8.9: Characteristics of FEMs studying the effect of aspect ratio

FEM	Concrete strength, f_c' (MPa)	Aspect ratio (L/D)	Maximum lateral load (kN)		Maximum moment (kN-m)		δ_{FEM} (%)	K_{FEM} (kN/m)
			Pushing direction (+ve)	Pulling direction (-ve)	Pushing direction (+ve)	Pulling direction (-ve)		
G30-2.0-0.2-85	30	2.0	216	-228	151	-60	8.15	10,061
G30-3.0-0.2-85	30	3.0	149	-149	156	-156	10.20	5,933
G30-4.0-0.2-85	30	4.0	108	-114	151	-160	10.20	4,586
G30-5.0-0.2-85	30	5.0	87	-91	159	-152	10.20	4,203
G30-6.0-0.2-85	30	6.0	76	-75	153	-158	10.20	3,918
G30-7.0-0.2-85	30	7.0	64	-63	157	-154	10.20	3,597
G60-2.0-0.2-85	60	2.0	286	-299	200	-210	6.95	15,409
G60-3.0-0.2-85	60	3.0	185	-181	194	-190	6.70	9,573
G60-4.0-0.2-85	60	4.0	133	-142	186.	-198	7.37	7,501
G60-5.0-0.2-85	60	5.0	105	-108	183	-188	7.43	6,115
G60-6.0-0.2-85	60	6.0	92	-93	193	-196	7.85	5,568
G60-7.0-0.2-85	60	7.0	78	-80	192	-197	6.75	4,647
G90-2.0-0.2-85	90	2.0	128	-123	230	-206	4.00	22,259
G90-3.0-0.2-85	90	3.0	211	-231	221	-242	4.00	13,701
G90-4.0-0.2-85	90	4.0	164	-164	230	-229	4.00	10,086
G90-5.0-0.2-85	90	5.0	128	-123	224	-215	4.00	7,624
G90-6.0-0.2-85	90	6.0	103	-104	217	-218	4.00	6,308
G90-7.0-0.2-85	90	7.0	89	-88	218	-216	4.00	5,242

Note: f_c' = concrete compressive strength; L = column shear span; D = column diameter; δ_{FEM} = failure drift estimated by FEM; and K_{FEM} = initial stiffness estimated by FEM.

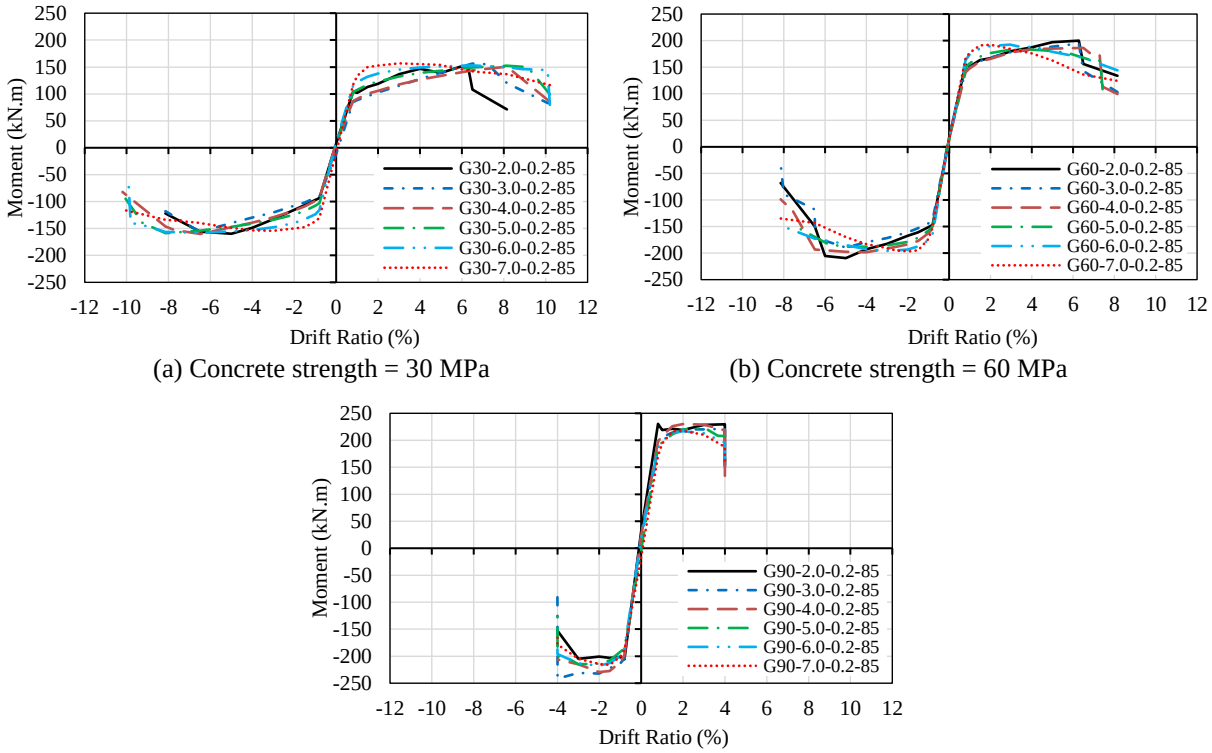

(a) Concrete strength = 30 MPa

(b) Concrete strength = 60 MPa

(c) Concrete strength = 90 MPa

Figure 8.15: Moment-drift envelopes of columns with different aspect ratios

8.6. Design Model for FRP Confinement Reinforcement

As previously discussed, it is suggested to develop a new design model for FRP confinement reinforcement of columns in seismic-active regions. This is evident from Figure 8.17a where the predicted drift ratios, according to CSA S806-12 (CSA 2017), were compared with those of the FEMs. The mean FEM-to-predicted drift ratio was 2.04 $\pm$ 0.42 with COV and R^2 of 20.63% and 0.79, respectively (Table 8.10). Therefore, the results of the FEMs were used to propose changes to the equation in Clause 12.7.3.3 of CSA S806-12 (CSA 2017). It is worth mentioning that the effect of aspect ratio was not considered in the development of the design models discussed herein. It could be observed from the previous discussion that the concrete compressive strength had a significant influence on the response of GFRP-RC columns, especially beyond 60-MPa concrete strength. Therefore, the effect of concrete strength was modeled independently as well as the combined effect of concrete strength and each of the spiral pitch and axial load level, using a variety of linear, exponential and polynomial curve fitting. Accordingly, the following design formulae (Model I) were proposed for GFRP-RC circular columns:

$$A_{sh} = 15.5 K_s h_c \frac{\left(f_c^{'}\right)^{0.85}}{f_{Fh}} \left(\frac{A_g}{A_c} - 1\right) K_P \frac{\delta}{\sqrt{k_c}} \qquad \text{Equation 8.6}$$

$$K_s = \left(57.7 - 0.5 f_c^{'}\right).e^{0.005 s.e^{0.015 f_c^{'}}} \qquad \text{Equation 8.7}$$

$$K_P = \left[4 \times 10^{-5} \left(f_c^{'}\right)^2 - 0.005 f_c^{'} + 0.24\right].e^{\frac{P}{P_o}(0.036 f_c^{'} + 1.125)} \qquad \text{Equation 8.8}$$

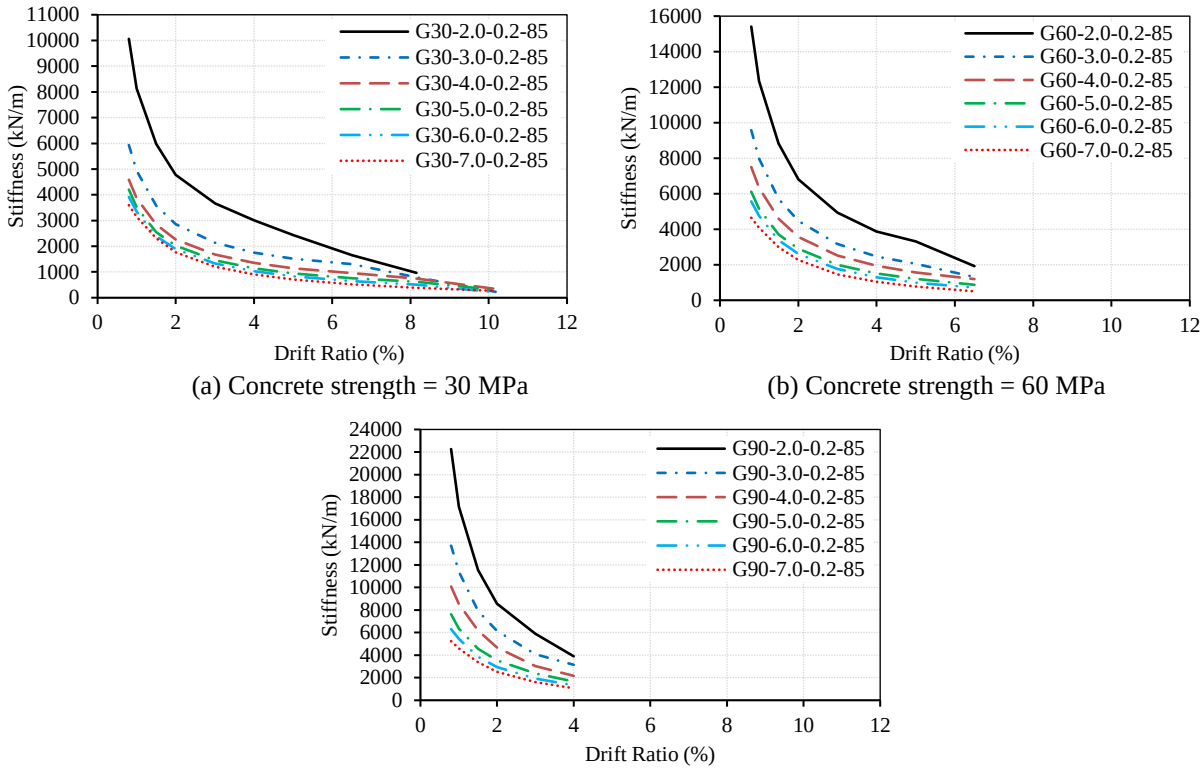

(a) Concrete strength = 30 MPa

(b) Concrete strength = 60 MPa

(c) Concrete strength = 90 MPa

Figure 8.16: Stiffness degradation for columns with different aspect ratios

where A_{sh} is the required area of confinement reinforcement; K_s is a proposed coefficient combining the effects of spiral pitch, s, and concrete compressive strength, f_c'; h_c is the cross-sectional dimension of the column core; f_{Fh} is the design stress in FRP confinement reinforcement, calculated as the least of 0.006 E_f or $\phi_f.f_{fu}$ where ϕ_f is the material resistance factor for FRP confinement reinforcement, taken as unity in this study, E_f and f_{fu} are the modulus of elasticity and ultimate tensile strength of FRP confinement reinforcement, respectively; A_g and A_c are the areas of the gross cross-section and column core, respectively; K_P is a proposed coefficient that denotes

the synergistic effect of axial load level, P/P_o (taken $\geq$ 0.2), and the concrete strength; δ is the design drift; and k_c is the confinement efficiency coefficient of the Canadian standards (CSA 2017), taken as unity for circular hoops or spirals. The mean FEM-to-predicted drift ratio using the proposed design model was substantially improved 1.01 $\pm$ 0.11 with a COV of 11.35% and R^2 of 0.91, as shown in Figure 8.17b and Table 8.10.

Yet despite the robustness of the proposed design model, its complexity could be an issue for designers in practice. To avoid such inconvenience, a simplified design model (Model II) was developed using power curve fitting for each variable independently. To estimate the required confinement reinforcement, one of the following equations can be used, depending on the concrete compressive strength of the column.

$$\text{where } f_c' \leq 60\,\text{MPa}, A_{sh} = 8.9 s^{1.02} h_c \frac{\left(f_c'\right)^{0.9}}{f_{Fh}} \left(\frac{A_g}{A_c} - 1\right) \left(\frac{P}{P_o}\right)^{0.9} \frac{\delta}{\sqrt{k_c}} \qquad \text{Equation 8.9}$$

$$\text{where } f_c' > 60\,\text{MPa}, A_{sh} = 2.2 s^{1.57} h_c \frac{\left(f_c'\right)^{0.9}}{f_{Fh}} \left(\frac{A_g}{A_c} - 1\right) \left(\frac{P}{P_o}\right)^{1.5} \frac{\delta}{\sqrt{k_c}} \qquad \text{Equation 8.10}$$

As observed from Table 8.10, Model II offers a relatively simple design approach at the expense of reduced accuracy, which is still considerably improved compared to that of the current equation of CSA S806-12 (CSA 2017). The results of the second model gave a mean FEM-to-predicted drift ratio equal to 1.14 $\pm$ 0.18 along with COV and R^2 of 15.50% and 0.86, respectively.

Table 8.10: Comparisons of the results of FEMs with code and proposed equations

FEM	Concrete strength f_c' (MPa)	Spiral pitch (mm)	Axial load level (P/P_o)	δ_{FEM} (%)	δ_{CSA} (%)	$\frac{\delta_{FEM}}{\delta_{CSA}}$	δ_{I} (%)	$\frac{\delta_{FEM}}{\delta_{I}}$	δ_{II} (%)	$\frac{\delta_{FEM}}{\delta_{II}}$
G30-5.0-0.2-85	30	85	0.2	10.20	6.50	1.60	10.24	1.00	11.45	0.89
G40-5.0-0.2-85	40	85	0.2	9.03	4.88	1.85	9.39	0.96	8.83	1.02
G50-5.0-0.2-85	50	85	0.2	7.80	3.90	2.00	8.73	0.89	7.23	1.08
G60-5.0-0.2-85	60	85	0.2	7.43	3.25	2.29	7.80	0.95	6.13	1.21
G70-5.0-0.2-85	70	85	0.2	6.50	2.79	2.33	6.49	1.00	4.68	1.39
G80-5.0-0.2-85	80	85	0.2	6.50	2.44	2.66	5.07	1.28	4.15	1.57
G90-5.0-0.2-85	90	100	0.2	4.00	2.17	1.84	3.92	1.02	3.73	1.07
G30-5.0-0.2-100	30	100	0.2	8.15	5.53	1.47	9.05	0.90	9.70	0.84
G40-5.0-0.2-100	40	100	0.2	8.15	4.15	1.96	8.13	1.00	7.49	1.09
G50-5.0-0.2-100	50	100	0.2	7.35	3.32	2.21	7.38	1.00	6.13	1.20
G60-5.0-0.2-100	60	100	0.2	6.5	2.76	2.36	6.42	1.01	5.20	1.25
G70-5.0-0.2-100	70	100	0.2	5.00	2.37	2.11	5.17	0.97	3.62	1.38
G80-5.0-0.2-100	80	100	0.2	4.00	2.07	1.93	3.89	1.03	3.21	1.24
G90-5.0-0.2-100	90	100	0.2	3.00	1.84	1.63	2.88	1.04	2.89	1.04
G30-5.0-0.2-110	30	110	0.2	8.15	5.03	1.62	8.33	0.98	8.81	0.93
G30-5.0-0.2-120	30	120	0.2	7.43	4.61	1.61	7.68	0.97	8.06	0.92
G30-5.0-0.2-130	30	130	0.2	6.50	4.25	1.53	7.07	0.92	7.43	0.87
G60-5.0-0.2-50	60	50	0.2	10.20	5.53	1.84	12.31	0.83	10.52	0.97
G60-5.0-0.2-60	60	60	0.2	10.20	4.61	2.21	10.80	0.94	8.74	1.17
G60-5.0-0.2-70	60	70	0.2	8.15	3.95	2.06	9.49	0.86	7.47	1.09

G60-5.0-0.2-110	60	110	0.2	6.5	2.51	2.59	5.63	1.15	4.72	1.38
G60-5.0-0.2-120	60	120	0.2	5.00	2.3	2.17	4.95	1.01	4.32	1.16
G60-5.0-0.2-130	60	130	0.2	4.00	2.13	1.88	4.34	0.92	3.98	1.00
G90-5.0-0.2-50	90	50	0.2	8.60	3.69	2.33	8.07	1.07	8.61	1.00
G90-5.0-0.2-60	90	60	0.2	8.15	3.07	2.65	6.57	1.24	6.46	1.26
G90-5.0-0.2-70	90	70	0.2	6.50	2.63	2.47	5.34	1.22	5.07	1.28
G30-5.0-0.3-85	30	85	0.3	9.25	4.34	2.13	8.20	1.13	7.94	1.17
G30-5.0-0.4-85	30	85	0.4	8.15	3.25	2.51	6.57	1.24	6.12	1.33
G30-5.0-0.5-85	30	85	0.5	5.00	2.6	1.92	5.26	0.95	5.00	1.00
G60-5.0-0.3-85	60	85	0.3	6.5	2.17	3.00	5.60	1.16	4.25	1.53
G60-5.0-0.4-85	60	85	0.4	4.00	1.63	2.45	4.03	0.99	3.28	1.22
G60-5.0-0.5-85	60	85	0.5	3.00	1.3	2.31	2.89	1.04	2.68	1.12
G90-5.0-0.3-85	90	85	0.3	2.00	1.45	1.38	2.53	0.79	2.03	0.99
G90-5.0-0.4-85	90	85	0.4	1.50	1.08	1.39	1.63	0.92	1.32	1.14
G90-5.0-0.5-85	90	85	0.5	1.00	0.87	1.15	1.05	0.95	0.94	1.06
Mean						2.04		1.01		1.14
SD						0.42		0.11		0.18
COV (%)						20.63		11.35		15.50
R^2						0.79		0.91		0.86

Note: f_c' = concrete compressive strength; P/P_o = axial load level; δ_{FEM} = failure drift estimated by FEM; δ_{CSA} = failure drift estimated as per CSA S806-12 (CSA 2017); δ_I = failure drift estimated using Model I (Equation 8.6); and δ_{II} = failure drift estimated using Model II (Equations 8.9 or 8.10, as appropriate).

The efficiency of the proposed models was checked by comparing the predicted drift ratios to the experimental results of Tavassoli et al. (2015), as shown in Table 8.11. It should be noted that few results were excluded from this validation process either due to their inconsistent values with the rest of specimens, or using an impractically conservative spiral pitch. As expected, Model I gave the most accurate results (Figure 8.18) with a mean FEM-to-predicted drift ratio of 0.98 $\pm$ 0.09 and COV and R^2 of 9.34% and 0.98, respectively. Model II also gave much predictions than the equation in Clause 12.7.3.3 of CSA S806-12 (CSA 2017). The mean FEM-to-predicted drift ratio, COV, and R^2 of Model II validation were 0.98 $\pm$ 0.09, 9.34%, and 0.98, respectively. Despite the considerable accuracy of the proposed design models, it is recommended to study the effects of the other parameters that affect the design of FRP confinement reinforcement and were not included in this study. Such parameters include the spiral size, column diameter, concrete cover and different FRP materials.

Table 8.11: Validation of the proposed equations against the results of Tavassoli et al. (2015)

Specimen ID	δ_{EXP} (%)	δ_{CSA} (%)	$\frac{\delta_{EXP}}{\delta_{CSA}}$	δ_{I} (%)	$\frac{\delta_{EXP}}{\delta_{I}}$	δ_{II} (%)	$\frac{\delta_{EXP}}{\delta_{II}}$
P28-C- 12-50	12.03	7.64	1.58	12.88	0.93	14.42	0.83
P28-C- 12-160	4.95	2.39	2.07	4.85	1.02	4.42	1.12
P28-B- 12-50	14.84	8.56	1.74	14.42	1.03	16.15	0.92
P42-C- 12-50	7.25	4.89	1.48	8.36	0.87	9.64	0.75
P42-B- 12-160	3.13	1.71	1.83	3.52	0.89	3.31	0.95
P42-B- 16-160	5.44	2.33	2.33	4.81	1.13	4.51	1.21
Mean			1.84		0.98		0.96
SD			0.29		0.09		0.16
COV (%)			15.80		9.34		16.23
R^2			0.97		0.98		0.96

Note: δ_{EXP} = experimental failure drift; δ_{CSA} = failure drift estimated as per CSA S806-12 (CSA 2017); δ_{I} = failure drift estimated using Model I (Equation 8.6); and δ_{II} = failure drift estimated using Model II (Equations 8.9 or 8.10, as appropriate).

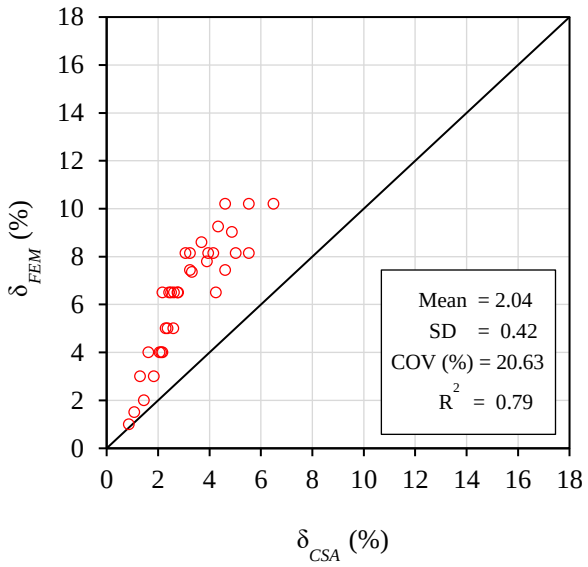

(a) CSA S806-12 (CSA 2017)

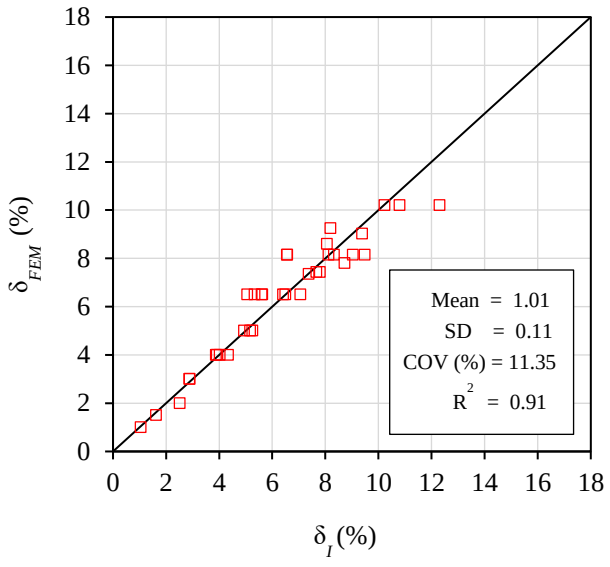

(b) Model I (Equation 8. 6)

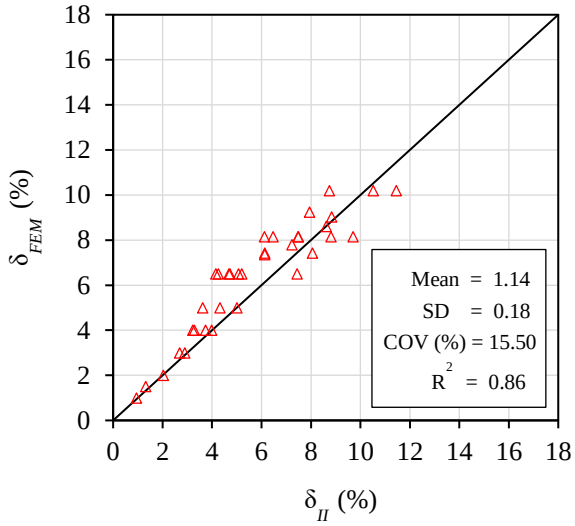

(c) Model II (Equations 8.9 or 8.10, as appropriate)

Figure 8.17: Drift ratio predictions

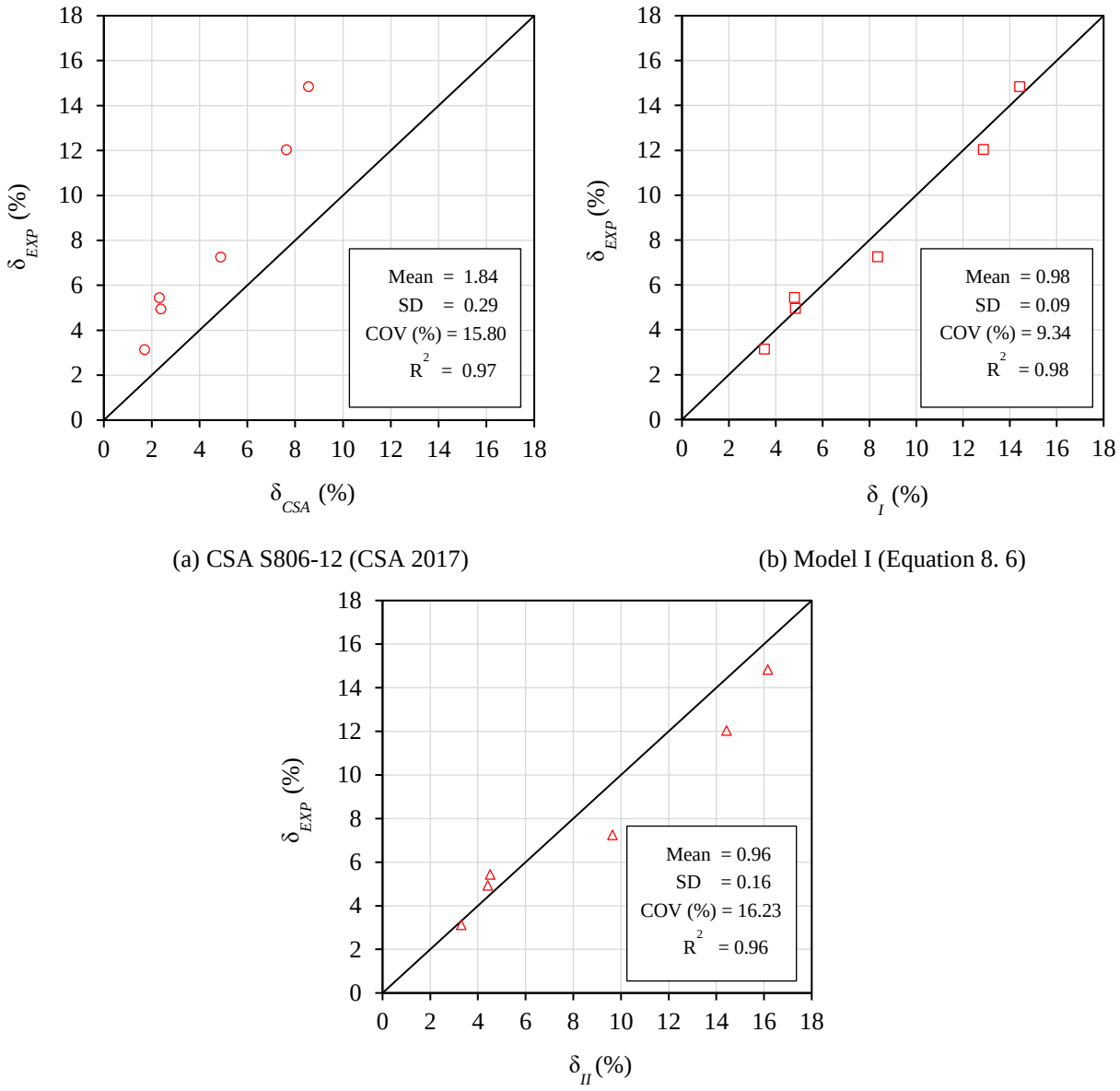

(a) CSA S806-12 (CSA 2017)

(b) Model I (Equation 8. 6)

(c) Model II (Equations 8.9 or 8.10, as appropriate)

Figure 8.18: Drift ratio predictions for specimens of Tavassoli et al. (2015)

8.7. Conclusions

The following conclusions can be reached based on the numerical and analytical studies presented in this paper:

1. Increasing the concrete compressive strength of circular GFRP-RC columns considerably enhanced the lateral load capacity, hysteretic response, and stiffness. This came, however, at

the cost of column deformability and drift capacity, which were decreased because of concrete strength increase.

2. As the spiral pitch increased, the drift capacity was reduced. This reduction was more significant as the concrete compressive strength increased. In addition, the stiffness degradation was higher as larger spiral pitch was utilized for concrete strengths of 60 and 90 MPa, whereas increasing spiral pitch hardly affected the column stiffness for a normal-strength concrete of 30 MPa.
3. Increasing the axial load level from 0.2 to 0.3 resulted in faster development of lateral load capacity along with higher stiffness degradation and lower drift capacity. The stiffness degradation and drift capacity were even worse as the axial load level increased further, accompanied by lower lateral load capacities. Such influence was even more pronounced as the concrete strength increased.
4. For the columns with aspect ratios ranging between 2.0 and 7.0, the moment and drift capacities were similar. This refutes the assumption adopted for the design equation of the Canadian standard CSA S806-12 (CSA 2017) for confinement reinforcement in FRP-RC columns subjected to seismic loading. Furthermore, taking the secondary moments due to *P*-Δ effect into account suggests the concept of lower deformability of FRP-RC columns with larger aspect ratios.
5. The proposed design Model I, considering the synergetic effects of concrete compressive strength along with each of spiral pitch and axial load level, resulted in substantial accuracy. On the other hand, Model II offered a simplified design approach, at relatively lower, yet considerable, accuracy. Both models exhibited significantly enhanced accuracy over the design equation in Clause 12.7.3.3 of CSA S806-12 (CSA 2017). The proposed design models were validated against experimental results from the literature, showing remarkable levels of accuracy.

CHAPTER 9: RECOMMENDATIONS AND FUTURE WORK

9.1. Summary

This trailblazer research study investigated the seismic behaviour of GFRP-RC circular columns through experimental and numerical phases. The experimental work involved the construction and testing of fifteen full-scale column-footing specimens to examine the influences of reinforcement type (steel versus GFRP), transverse reinforcement type (spirals versus discrete hoops), spiral pitch (85 and 50 mm), concrete compressive strength (35 and 80 MPa), axial load level (0.1, 0.2 and 0.3 of the unconfined axial capacity of the column, P_o), and aspect ratio (3.0, 5.0 and 7.0). Each specimen resembled the bottommost portion of a first-storey column isolated from a prototype office MRF structure. Test specimens are constructed as circular columns with diameter of 350 mm and varying lengths, and are cast with 1400 × 900 × 600 mm footings.

This was followed by the numerical phase where FEM was constructed and validated to replicate the seismic response of the GFRP-RC circular columns tested during the experimental phase using the commercial software package ATENA/GiD (Červenka et al. 2020b). The validated FEM was further used to perform a comprehensive parametric study to investigate the influence of some key parameters on the cyclic performance of GFRP-RC columns, including concrete compressive strength, spiral pitch, axial load level and aspect ratio. Two new seismic design models for confinement reinforcement of GFRP-RC circular columns were proposed as a result of mathematical analyses for the outcomes of the parametric study. The proposed models displayed significantly higher accuracy than the available design model by the Canadian standards (CSA 2017).

9.2. Recommendations for the Current Standards

Based on the results of the conducted experimental and numerical investigations, the main recommendations for the current design provisions of FRP-RC circular columns can be summarized as follows.

1. The requirement of the Canadian standards, CSA S806-12 (CSA 2017), for spiral pitch to be at least one-sixth the core diameter can be waived for NSC circular columns. It would be prudent, however, to consider such requirement for HSC columns (80 MPa or above).

2. The minimum lap-splice length for GFRP circular hoops of 40 times its nominal cross-sectional diameter (d_h), specified by the Canadian highway bridge design code CSA S6-19 (CSA 2019d), should be increased to 60 d_h. This recommended splice length enables comparable confinement to that provided by GFRP spirals of the same material properties.
3. An accidental increase of concrete compressive strength (i.e., within the range used in this study) does not affect the deformability of GFRP-RC circular columns. Therefore, no further action, in terms of confinement, should be taken.
4. While the theoretical shear analysis, according to the Canadian standards, CSA S806-12 (CSA 2017), for FRP-RC building structures, indicated shear failure for the specimens with the aspect ratio of 3.0, the experimental testing resulted in flexure-controlled type of failure. This may reflect that the available shear design provisions in the Canadian code are too strict.
5. The currently available design equation for confinement reinforcement of GFRP-RC columns in earthquake-prone zones (i.e., Clause 12.7.3.3 of CSA S806-12 (CSA 2017)) was found to be overly conservative. This is due to the common assumption, originally made for steel-RC columns, that shorter columns would be less deformable. This seems to be inapplicable to GFRP-RC ones and, therefore, such design equations are recommended to be reasonably relaxed.
6. For the columns with aspect ratios ranging between 2.0 and 7.0, the moment and drift capacities were similar. This refutes the assumption adopted for the design equation of the Canadian standards, CSA S806-12 (CSA 2017), for confinement reinforcement in FRP-RC columns subjected to seismic loading. Furthermore, taking the secondary moments due to *P*-Δ effect into account suggests the concept of lower deformability of FRP-RC columns with larger aspect ratios. Such changes should be reflected into new seismic design provisions for FRP confinement reinforcement.
7. Based on an extensive parametric numerical study, two design models (Model I and II) were proposed for the confinement reinforcement in FRP-RC circular columns in moment-resisting frames. Model I, considering the synergetic effects of concrete compressive strength along with each of spiral pitch and axial load level, resulted in a mean FEM-to-predicted drift ratio of 1.01 $\pm$ 0.11 and COV and R^2 of 11.35% and 0.91, respectively. On the other hand, Model II offered a simplified design approach, resulting in a mean FEM-to-predicted drift

ratio of 1.14 ± 0.18 and COV and R^2 of 15.50% and 0.86, respectively. Both models exhibited enhanced accuracy over the design equation in Clause 12.7.3.3 of CSA S806-12 (CSA 2017), which gave a mean FEM-to-predicted drift ratio of 2.04 ± 0.42 and COV equal to 20.63% and R^2 of 0.79. The proposed design models were validated against experimental results from the literature, showing remarkable levels of accuracy.

9.3. Future Work

The outcomes of this research represent a major step forward towards providing reliable seismic deign provisions for FRP-RC columns. Some aspects were not considered within the scope of this study and still need to be addressed by future research studies as discussed below:

1. All the tested columns in this study were subjected to constant axial loading along with the cyclic lateral drift reversals, whereas under actual earthquake excitations, the axial loading on the columns of an MRF building would most likely fluctuate. Moreover, exterior and corner columns may experience tensile axial loads as a result of axial loading fluctuation during such events. This suggests studying the effect of varying axial load on the seismic performance of FRP-RC structures.
2. The applied cyclic lateral drifts in this work was uniaxial, which is acceptable according to the currently available guidelines (ACI 2019b). However, for columns located in skewed or curved bridges, or those having unequal spans or column heights, significant torsional moments would likely occur during a seismic event. Therefore, the effect of different parameters on the confinement of FRP-RC columns should be verified under combined effect of simulated seismic loading and cyclic torsion.
3. This study was dedicated to the seismic behaviour of GFRP-RC circular columns only. The effects of concrete compressive strength and column aspect ratio need to be investigated for square and rectangular columns, especially when conserving their non-uniform confinement action. Additionally, the effect of cross-sectional aspect ratio (i.e. thickness-to-width ratio) of rectangular GFRP-RC columns should be studied.
4. The findings of the experimental phase of this research specified a minimum lap splice length for GFRP discrete circular hoops equal to 60 times their cross-sectional diameter. The

efficiency of this minimum lap splice length yet needs to be verified for HSC columns or under higher axial load levels.

5. The columns tested in this study incorporated continuous longitudinal GFRP bars that extended from the bottom of each footing up to the top of the column. However, columns would typically be spliced above the column–footing interface. Although this was investigated for square GFRP-reinforced NSC columns (Naqvi and El-Salakawy 2017), more research effort is required to identify the minimum lap splice length for GFRP-reinforced NSC circular columns and GFRP-reinforced HSC circular and rectangular columns.
6. The design models developed herein (Models I and II) for seismic design of FRP confinement reinforcement were based on mathematical analyses of GFRP-RC circular columns considering a limited number of parameters. To verify the reliability of such design models it is required to investigate the influence of more parameters such as column size, concrete cover, and FRP type. Furthermore, the effect of longitudinal reinforcement ratio and confinement efficiency factor (CSA 2017), k_c, on the seismic response of FRP-RC rectangular columns should be extensively studied to extend the applicability of the new design models to such members.
7. The results of the analytical work presented in Chapter 4 indicated the need for an eccentricity-based confinement model for FRP-RC columns to better simulate their performance.
8. The analytical phase of this study introduced a reliable FEM which acts as a promising tool for research purposes. However, its calculation complexity could make time-consuming for designers. A simplified hysteretic model for FRP-RC columns could be helpful in this regard, which, again, urges for an eccentricity-based confinement model.

REFERENCES

AASHTO (American Association of State Highway and Transportation Officials). 2018. *AASHTO LRFD bridge design guide specifications for GFRP–reinforced concrete*. 2nd ed, Washington DC.

Abdallah, A. E. M., and El-Salakawy, E. F. 2021a. "Confinement properties of GFRP-reinforced concrete circular columns under simulated seismic loading". *J. Compos. Constr.*, ASCE, 25(2): 04020088.

Abdallah, A. E., and El-Salakawy, E. F. 2021b. "Seismic behavior of high-strength concrete circular columns reinforced with glass fiber-reinforced polymer bars". *ACI Struct. J.*, 118(5): 221-234.

Abdelazim, W., H. M. Mohamed, and B. Benmokrane. 2020. "Inelastic second-order analysis for slender GFRP-reinforced concrete columns: Experimental investigations and theoretical study". *J. Compos. Constr.*, ASCE, 24(3): 04020016.

ACI (American Concrete Institute). 1989. *Building code requirements for reinforced concrete and commentary*. ACI 318-89, Detroit, MI.

ACI (American Concrete Institute). 2010. *Report on high-strength concrete*. ACI 363R-10, Detroit, MI.

ACI (American Concrete Institute). 2015. *Guide for the design and construction of structural concrete reinforced with fiber-reinforced polymer (FRP) bars*. ACI 440.1R-15, Detroit, MI.

ACI (American Concrete Institute). 2019a. *Building code requirements for structural concrete and commentary*. ACI 318-19. Detroit, MI.

ACI (American Concrete Institute). 2019b. *Acceptance criteria for moment frames based on structural testing and commentary*. ACI 374.1-05 (R2019). Detroit, MI.

ACI-ASCE Committee 441. 2002. "Report on high-strength concrete columns". ACI 441R-96 (R2002). *American Concrete Institute*, Detroit, MI, 13.

Afifi, M. Z., H. M. Mohamed, and Benmokrane, B. 2014. "Axial capacity of circular concrete columns reinforced with GFRP bars and spirals". *J. Compos. Constr.*, ASCE, 18(1): 04013017.

AlAjarmeh, O. S., Manalo, A. C., Benmokrane, B., Vijay, P. V., Ferdous, W., and Mendis, P. 2019. "Novel testing and characterization of GFRP bars in compression". *Construction and Building Materials*, *225*: 1112–1126.

Ali, M. A., and El-Salakawy, E. 2016. "Seismic performance of GFRP-reinforced concrete rectangular columns". *J. Compos. Constr.*, ASCE, 20(3): 04015074.

Alnajmi, L., and Abed, F. 2020. "Evaluation of FRP bars under compression and their performance in RC columns". *Materials*, 13(20): 1–19.

Alsayed, S. H., T. H. Almusallam, M. A. Amjad, and Al-Salloum, Y. A. 1999. "Concrete columns reinforced by glass fiber reinforced polymer rods". In *Proc., 4th Int. Symp. Fiber Reinforced Polymer Reinforcement for Reinforced Concrete Structures*, ACI Special Publication 188, 103–112. Detroit, MI.

Alves, J., El-Ragaby, A., and El-Salakawy, E. 2011. "Durability of GFRP bars' bond to concrete under different loading and environmental conditions". *J. Compos. Constr.*, ASCE, 15(3): 249–262.

Attia, K., El Refai, A. and Alnahhal, W. 2020. "Flexural behavior of basalt fiber-reinforced concrete slab strips with BFRP bars: Experimental testing and numerical simulation". *J. Compos. Constr.*, ASCE, 24(2): 04020007.

Azizinamini, A.; and Kuska S., 1994. "Seismic behavior of high-strength concrete columns". *5th U.S. National Conference on Earthquake Engineering*, July 1 0- 14 1994, Chicago, Illinois, 2: 599-608.

Azizinamini, A., Kuska, S., Brungardt, P., and Hatfield, E. 1994. "Seismic behavior of square high-strength concrete columns". *ACI Struct. J.*, 91(3): 336–345.

Bae, S., and Bayrak, O. 2008. "Seismic performance of full-scale reinforced concrete columns". *ACI Struct. J.*, 105(2): 123–133.

Bayrak, O., and Sheikh, S. A. 1997. "High-strength concrete columns under simulated earthquake loading". *ACI Struct. J.*, 94(6): 708–722.

Barua, S. and El-Salakawy, E. 2020. "Performance of GFRP-reinforced concrete circular short columns under concentric, eccentric, and flexural loads". *J. Compos. Constr.*, ASCE, 24(5): 04020044.

Barua, S., Mahmoud, K., and El-Salakawy, E. 2021. "Slender GFRP-RC circular columns under concentric, eccentric, and flexural loads: experimental investigation". *Journal of Bridge Engineering*, ASCE, 26(7): 04021033.

Bayrak, O., and Sheikh, S. A. 1997 "High-strength concrete columns under simulated earthquake loading". *ACI Struct. J.*, 94(6): 708-722.

CEB (Comité Euro-International du Béton). 1993. *CEB-FIB model code 90*. London: CEB.

Červenka, V., Červenka, J., Pryl, D., and Janda, Z. 2020a. *ATENA manual for ATENA-GiD interface*. Prague, Czech Republic: Červenka Consulting.

Červenka, V., Jendele, L., and Červenka, J. 2020b. *ATENA program documentation part 1: Theory*. Prague, Czech Republic: Červenka Consulting.

Choo, C. C., Harik, I. E., and Gesund, H. 2006. "Minimum reinforcement ratio for fiber-reinforced polymer reinforced concrete rectangular columns". *ACI Struct. J.*, 103(3): 460–466.

CSA (Canadian Standards Association). 2017. *Design and construction of building structures with fibre-reinforced polymer*. CSA S806-12 (R2017). Toronto, ON.

CSA (Canadian Standards Association). 2019a. *Concrete materials and methods of concrete construction/test methods and standard practices for concrete*. CSA A23.1-19/A23.2-19. Toronto, ON.

CSA (Canadian Standards Association). 2019b. *Design of concrete structures*. CSA A23.3-19. Toronto, ON.

CSA (Canadian Standards Association). 2019c. *Carbon steel bars for concrete reinforcement*. CSA G30.18-09 (R2019). Toronto, ON.

CSA (Canadian Standards Association). 2019d. *Canadian highway bridge design code*. CSA S6-19. Toronto, ON.

CSA (Canadian Standards Association). 2019e. *Specification for fibre-reinforced polymers*. CSA S807-19. Toronto, ON.

Cusson, D., and Paultre P. 1995. "Stress-strain model for confined high-strength concrete". *J. Struct. Eng.*, ASCE, 121(3): 468–77.

Davey, B.E., and Park, R. 1975. "Reinforced concrete bridge piers under seismic loading". *Research Report 75-3*. University of Canterbury, Christchurch, N.Z.

Deitz, D. H., Harik, I. E., and Gesund, H. 2003. "Physical properties of glass fiber reinforced polymer rebars in compression". *J. Compos. Constr.*, ASCE, 7(4): 363–366.

De Luca, A., Matta, F., and Nanni, A. 2010. “Behavior of full-scale glass fiber-reinforced polymer reinforced concrete columns under axial load”. *ACI Struct. J.*, 107(5): 589–596.

Deng, Z., Gao, L., and Wang, X. 2018. “Glass fiber-reinforced polymer-reinforced rectangular concrete columns under simulated seismic loads”. *Journal of the Brazilian Society of Mechanical Sciences and Engineering*, 40(2): 111.1-111.12.

Desayi, P., and Krishnan, S. 1964. “Equation for the stress–strain curve of concrete”. *J. Am. Concr. Inst.*, 61(3): 345–350.

Elchalakani, M., Karrech, A., Dong, M., Ali, M. S., and Yang, B. 2018. “Experiments and finite element analysis of GFRP reinforced geopolymer concrete rectangular columns subjected to concentric and eccentric axial loading”. *Structures*, 14: 273–289.

Elchalakani, M., Dong, M., Karrech, A., Mohamed Ali, M. S., and Huo, J. S. 2020. “Circular concrete columns and beams reinforced with GFRP bars and spirals under axial, eccentric, and flexural loading”. *J. Compos. Constr.*, ASCE, 24(3): 04020008.

Elwood, K. J., Maffei, J., Riederer, K. A., and Telleen, K. 2009a. “Improving column confinement, Part 1: Assessment of design provisions”. *ACI Concrete International*, November: 32–39.

Elwood, K. J., Maffei, J., Riederer, K. A., and Telleen, K. 2009b. “Improving Column Confinement, Part 2: Proposed new provisions for the ACI 318 building code. *ACI Concrete International*, December: 41–48.

El-Gendy, M., and El-Salakawy, E. 2019. “Effect of flexural reinforcement type and ratio on the punching behavior of RC slab-column edge connections subjected to reversed-cyclic lateral loads". *Eng. Struct.*, 200: 109703.

El-Gendy, M. G., and El-Salakawy, E. F. 2020. “GFRP shear reinforcement for slab-column edge connections subjected to reversed cyclic lateral load”. *J. Compos. Constr.*, ASCE, 24(2): 04020003.

El-Gendy, M. G., and El-Salakawy, E. F. 2021. “Finite-element analysis of FRP-reinforced concrete slab-–column edge connections subjected to reversed-cyclic lateral loads”. *J. Compos. Constr.*, ASCE, 25(1): 04020082.

Elshamandy, M. G., Farghaly, A. S., and Benmokrane, B. 2018. “Experimental behavior of glass fiber-reinforced polymer-reinforced concrete columns under lateral cyclic load”. *ACI Struct. J.*, 115 (2): 337–349.

Feng, P., Ye, L. P., and Huang, Y. L. 2005. "Deformability and new performance indices of flexural members". *Engineering Mechanics*, 22(6): 28–36.

Ghomi, S. K., and El-Salakawy, E. 2018. "Seismic behavior of exterior GFRP-RC beam-column connections: analytical study". *J. Compos. Constr.*, ASCE, 22(4): 04018022.

Ghomi, S. K., and El-Salakawy, E. 2019. "Seismic behavior of GFRP-reinforced concrete interior beam-column-slab subassemblies". *J. Compos. Constr.*, ASCE, 23(6): 04019047.

Ghomi, S. K., and E. F. El-Salakawy. 2020. "Cyclic behavior of glass fiber-reinforced polymer-reinforced concrete exterior beam-column-slab connections". *ACI Struct. J.*, 117(2): 171–183.

Guérin, M., H. M. Mohamed, B. Benmokrane, A. Nanni, and Shield, C. K. 2018. "Eccentric behavior of full-scale reinforced concrete columns with glass fiber-reinforced polymer bars and ties". *ACI Struct. J.*, 115(2): 489-499.

Hadhood, A., Mohamed, H. M., and Benmokrane, B. 2017a. "Experimental study of circular high-strength concrete columns reinforced with GFRP bars and spirals under concentric and eccentric loading". *J. Compos. Constr.*, ASCE, 21(2): 04016078.

Hadhood, A., H. M. Mohamed, and Benmokrane, B. 2017b. "Failure envelope of circular concrete columns reinforced with GFRP bars and spirals". *ACI Struct. J.*, 114(6): 1417–1428.

Hadhood, A., Mohamed, H. M., Ghrib, F., and Benmokrane, B. 2017c. "Efficiency of glass-fiber reinforced-polymer (GFRP) discrete hoops and bars in concrete columns under combined axial and flexural loads". *Composites Part B*, 114: 223–236.

Hadi, M. N. S., H. Karim, and Sheikh, M. N. 2016. "Experimental investigations on circular concrete columns reinforced with GFRP bars and helices under different loading conditions". *J. Compos. Constr.*, ASCE, 20(4): 04016009.

Hadi, M. N., Hasan, H. A., and Sheikh, M. N. 2017. "Experimental investigation of circular high-strength concrete columns reinforced with glass fiber-reinforced polymer bars and helices under different loading conditions". *J. Compos. Constr.*, ASCE, 21(4): 04017005.

Hales, T. A., C. P. Pantelides, and Reaveley, L. D. 2016. "Experimental evaluation of slender high-strength concrete columns with GFRP and hybrid reinforcement". *J. Compos. Constr.*, ASCE, 20(6): 04016050.

Hales, T. A., Pantelides, C. P., Sankholkar, P., and Reaveley, L. D. 2017. "Analysis-oriented stress-strain model for concrete confined with fiber-reinforced polymer spirals". *ACI Struct. J.*, 114(5): 1263–1272.

Hasaballa, M. H., El-Ragaby, A., and El-Salakawy, E. F. 2011. "Seismic performance of exterior beam-column joints reinforced with glass fibre reinforced polymer bars and stirrups". *Canadian Journal of Civil Engineering*, 38(10): 1092–1102.

Hasaballa, M., and El-Salakawy, E. 2016. "Shear capacity of exterior beam-column joints reinforced with GFRP bars and stirrups". *J. Compos. Constr.*, ASCE, 20(2): 04015047.

Hasaballa, M., and El-Salakawy, E. 2018. "Anchorage performance of GFRP headed and bent bars in beam-column joints subjected to seismic loading". *J. Compos. Constr.*, ASCE, 22(6): 04018060.

Hasan, H. A., Sheikh, M. N., and Hadi, M. N. S. 2017. "Performance evaluation of high strength concrete and steel fibre high strength concrete columns reinforced with GFRP bars and helices". *Construction and Building Materials*, 134: 297–310.

Hasan, H. A., Karim, H., Sheikh, M. N., and Hadi, M. N. S. 2019. "Moment-curvature behavior of glass fiber-reinforced polymer bar-reinforced normal-strength concrete and high-strength concrete columns". *ACI Struct. J.*, 116(4): 65–75.

Hosseini, F., Gencturk, B., Jain, A., and Shahzada, K. 2019. "Optimal design of bridge columns constructed with engineered cementitious composites and Cu-Al-Mn superelastic alloys". *Eng. Struct.*, 198: 109531.

Iwasaki, T., Kawashima, K., Hagiwara, R., Hasegawa, K., Koyama, T., and Yoshida, T. 1985. "Experimental investigation on hysteretic behavior of reinforced concrete bridge pier columns". *Proceedings of the Seventeenth Joint UJNR Panel Conference*, San Francisco, California, USA.

Jaeger, L. G., Tadros, G., and Mufti, A. A. 1995. "Balanced section, ductility and deformability in concrete with FRP reinforcement". *Technical Rep. No. 2-1995*, Nova Scotia CAD/CAM Centre, Technical University of Nova Scotia, Halifax, Nova Scotia, Canada.

Jawaheri Zadeh, H., and Nanni, A. 2013. "Design of RC columns using glass FRP reinforcement". *J. Compos. Constr.*, ASCE, 17(3): 294–304.

Johal, L.S.; Azizinamini, A.; Musser, D.W.; and Corley, W.G., 1987, "Seismic evaluation of columns to improve design criteria for transverse reinforcement". *Proceedings, 5th Canadian Conference on Earthquake Engineering*, Ottawa, July 1987: 799-806.

Kappos, A. J., and Konstantinidis, D. 1999. "Statistical analysis of confined high strength concrete". *Mater. Struct.*, 32 (December): 734–748.

Kawaguchi, N. 1993. "Ultimate strength and deformation characteristics of concrete members reinforced with AFRP rods under combined axial tension or compression and bending". *Fiber-Reinforced-Plastic Reinforcement for Concrete Structures, ACI Special Publication* (*SP-138),* 138: 671–685.

Kharal, Z., and Sheikh, S. A. 2018. "Seismic performance of square concrete columns confined with glass fiber-reinforced polymer ties". *J. Compos. Constr.*, ASCE, 22(6): 04018054.

Kharal, Z., and Sheikh, S. A. 2020. "Seismic behavior of square and circular concrete columns with GFRP reinforcement". *J. Compos. Constr.*, ASCE, 24(1): 04019059.

Kharal, Z., Carrette, J. K., and Sheikh, S. A. 2021. "Large concrete columns internally reinforced with GFRP spirals subjected to seismic loads". *J. Compos. Constr.*, ASCE, 25(3): 04021014.

Lehman, D. E., and Moehle, J. P. 2000. "Seismic performance of well-confined concrete bridge columns". *Pacific Earthquake Engineering Research Center*, 295.

Légeron, F., and Paultre, P. 2000. "Behavior of high-strength concrete columns under cyclic flexure and constant axial load". *ACI Struct. J.*, 97(4): 591–601.

Li, X. 1994. "Reinforced concrete columns under seismic lateral force and varying axial load". *PhD Thesis*, University of Canterbury, Christchurch, New Zealand.

Liu, J., H. Du, H. Zhou, Z. Nan, and Nie, P. 2019. "Experimental study on deformation and failure of circular concrete columns reinforced with glass fiber–reinforced polymer bars". *ACI Struct. J.*, 116(4): 45–52.

Lotfy, E. M. 2010. "Behavior of reinforced concrete short columns with fiber reinforced polymers bars". *International Journal of Civil and Structural Engineering*, 1(3): 545–557.

Mady, M., El-Ragaby, A., and El-Salakawy, E. 2011. "Seismic behavior of beam-column joints reinforced with GFRP bars and stirrups". *J. Compos. Constr.*, ASCE, 15(6): 875–886.

Mahmoud, K., and El-Salakawy, E. 2016. "Effect of transverse reinforcement ratio on the shear strength of GFRP-RC continuous beams". *J. Compos. Constr.*, ASCE, 20(1): 04015023.

Mohamed, H. M., Afifi, M. Z., and Benmokrane, B. 2014. "Performance evaluation of concrete columns reinforced longitudinally with FRP bars and confined with FRP hoops and spirals under axial load". *J. Bridge Eng.*, ASCE, 19(7): 1–12.

Mosley, C., Tureyan, A., Frosch, R. 2008. "Bond strength of nonmetallic reinforcing bars". *ACI Struct. J.*, 105(5): 634-642.

Mousa, S., H. M. Mohamed, and Benmokrane, B. 2019. "Strength and deformability aspects of circular concrete members reinforced with hybrid carbon-FRP and glass-FRP under flexure". *J. Compos. Constr.*, ASCE, 23(2): 04019005.

Mufti, A. A., Newhook, J. P., and Tadros, G. 1996. "Deformability versus ductility in concrete beams with FRP reinforcement". *2nd international conference on advanced composite materials in bridges and structures (ACMBS-II)*, Montreal, QC, Canada,189-199.

Muguruma, H., and Wanatabe, F., 1990, "Ductility improvement of high strength concrete columns with lateral confinement". *Utilization of High Strength Concrete: Second International Symposium, ACI Special Publication (SP-12)*: 47-60.

Nagy-György, T., Sas, G., Dâescu, A. C., Barros, J. A. O., and Stoian, V. 2012. "Experimental and numerical assessment of the effectiveness of FRP-based strengthening configurations for dapped-end RC beams". *Eng. Struct.*, 44: 291–303.

Naqvi, S., and El-Salakawy, E. 2017. "Lap splice in GFRP-RC rectangular columns subjected to cyclic-reversed loads". *J. Compos. Constr.*, ASCE, 21(4): 04016117.

Naqvi, S., Mahmoud, K., and El-Salakawy, E. 2017. "Effect of axial load and steel fibers on the seismic behavior of lap-spliced glass fiber reinforced polymer-reinforced concrete rectangular columns". *Eng. Struct., 134*, 376–389.

NRCC (National Research Council of Canada). 2020. *National building code of Canada (NBCC)*. Ottawa, ON, 1245.

Ozcebe, G., and Saatcioglu, M. 1987. "Confinement of concrete columns for seismic loading". *ACI Struct. J.*, 84(4): 308–315.

Pan, A., and Moehle, J. P. 1989. "Lateral displacement ductility of reinforced concrete flat plates". *ACI Struct. J.*, 86(3): 250–258.

Pantelides, C. P., M. E. Gibbons, and Reaveley, L. D. 2013. "Axial load behavior of concrete columns confined with GFRP spirals". *J. Compos. Constr.*, ASCE, 17(3): 305–313.

Park, R., Priestly, M. J. N., and Gill, W. D. 1982. "Ductility of square-confined concrete columns. *Journal of the Structural Division*, ASCE, 108(4): 929–950.

Paultre, P., Légeron, F., and Mongeau, D. 2001. "Influence of concrete strength and transverse reinforcement yield strength on behavior of high-strength concrete columns". *ACI Struct. J.*, 98(4): 490–501.

Paultre, P., Eid, R., Robles, H. I., and Bouaanani, N. 2009. "Seismic performance of circular high-strength concrete columns". *ACI Struct. J.*, 106(4): 395-404.

Pultrall Inc. 2019. "V-ROD—Technical data sheet". ADS Comp. Group. Thetford Mines, QC, Canada.

Prakash, S., Belarbi, A., and You, Y. M. 2010. "Seismic performance of circular RC columns subjected to axial force, bending, and torsion with low and moderate shear". *Eng. Struct.*, 32(1): 46–59.

Rabbat, B., Daniel, J., Weinmann, T., and Hanson, N. 1986. "Seismic behavior of lightweight and normal weight concrete columns". *ACI Struct. J.*, 83(9): 69-79.

Raza, A., Rehman, A., Masood, B., and Hussain, I. 2020. "Finite element modelling and theoretical predictions of FRP-reinforced concrete columns confined with various FRP-tubes". *Structures*, 26: 626–638.

Razvi, S. R., and Saatcioglu, M. 1996. "Design of R/C columns for confinement based on lateral drift". Ottawa Carleton Earthquake Engineering Research Center, Carleton, Ottawa.

Richart, F.E.; Brandtzaeg, A.; and Brown, R.L., 1928, "A study of the failure of concrete under combined compressive stresses". *Bulletin No. 185,* University of Illinois, Engineering Experimental Station.

Roehm, C., Sasmal, S., Novák, B., and Karusala, R. 2015. "Numerical simulation for seismic performance evaluation of fibre reinforced concrete beam-column sub-assemblages". *Eng. Struct.*, 91: 182–196.

Saatcioglu, M. 1991. "Deformability of reinforced concrete columns". *Earthquake-Resistant Structures—Inelastic Response and Design, SP-127, American Concrete Institute*, 127: 421–452.

Saatcioglu, M., and Baingo, D. 1999. "Circular high-strength concrete columns under simulated seismic loading". *J. Struct. Eng.*, ASCE, 125(3): 272–280.

Saatcioglu, M., and Ozcebe, G. 1989. "Response of reinforced concrete columns to simulated seismic loading". *ACI Struct. J.*, 86(1): 3–12.

Saatcioglu, M., and Razvi, S. R. 2002. "Displacement-based design of reinforced concrete columns for confinement". *ACI Struct. J.*, 99(1): 3-11.

Sakai, K., and Sheikh, S. A. 1989. "What do we know about confinement in reinforced concrete columns? (A critical review of previous work and code provisions)". *ACI Struct. J.*, 86(2): 192-207.

Sankholkar, P. P., Pantelides, C. P., and Hales, T. A. 2018. "Confinement model for concrete columns reinforced with GFRP spirals". *J. Compos. Constr.*, ASCE, 22(3): 04018007.

Sasmal, S., Khatri, C. P., Ramanjaneyulu, K., and Srinivas, V. 2013. "Numerical evaluation of bond-slip relations for near-surface mounted carbon fiber bars embedded in concrete". *Construction and Building Materials*, 40: 1097–1109.

Setiawan, A., Vollum, R. L., and Macorini, L. 2019. "Numerical and analytical investigation of internal slab-column connections subject to cyclic loading". *Eng. Struct.*, 184: 535–554.

Sezen, H., and Moehle, J. P. 2006. "Seismic tests of concrete columns with light transverse reinforcement". *ACI Struct. J.*, 103(6): 842–849.

Sharbatdar, M. K. 2003. "Concrete columns and beams reinforced with FRP bars and grids under monotonic and reversed cyclic loading". *Doctoral Dissertation*, University of Ottawa, Ottawa, Canada.

Sheikih, S. A., and Khoury, S. S. 1993. "Confined concrete columns with Stubs". *ACI Struct. J.*, 90(4): 414–431.

Sheikh, S. A., Shah, D. V., and Khoury, S. S. 1994. "Confinement of high-strength concrete columns," *ACI Struct. J.*, 91(1): 100-111.

Sheikh, S. A., and Toklucu, M. T. 1993. "Reinforced concrete columns confined by circular spirals and hoops". *ACI Struct. J.*, 90(5): 542–553.

Stone, W. C., and Cheok, G. S. 1989. "Inelastic behavior of full-scale bridge columns subjected to cyclic loading". *National Institute of Standards and Technology (NIST) BSS 166*, Gaithersburg, MD, USA.

Tahir, M., Wang, Z., Wei, Z., and Jameel, R. 2021. "Numerical and analytical modeling of FRP-reinforced concrete columns subjected to compression loading". *Australian Journal of Structural Engineering*, 22(2): 96-109.

Tanaka, H.; Park, R.; and McNamee, B., 1985. "Anchorage of transverse reinforcement in rectangular reinforced concrete columns in seismic design". *Bulletin of the New Zealand National Society for Earthquake Engineering*, 18(2): 165- 190.

Tavassoli, A. 2013. “Behaviour of GFRP - reinforced concrete columns under combined axial load and flexure”. *MSc Thesis*, Department of Civil Engineering, University of Toronto, Toronto, ON, Canada.

Tavassoli, A., Liu, J., and Sheikh, S. 2015. “Glass fiber-reinforced polymer-reinforced circular columns under simulated seismic loads”. *ACI Struct. J.*, 112(1): 103–114.

Tobbi, H., Farghaly, A. S., and Benmokrane, B. 2014. “Behavior of concentrically loaded fiber-reinforced polymer reinforced concrete columns with varying reinforcement types and ratios”. *ACI Struct. J.*, 111(2): 375–386.

Van Mier, J. 1986. “Multiaxial strain-softening of concrete”. *Mater. Struct.*, 19: 179–190.

Vecchio, F., and Collins, M. 1986. “Modified compression-field theory for reinforced concrete beams subjected to shear”. *ACI J. Proc.*, 83(2): 219–231.

Watson, S., and Park, R. 1994. “Simulated seismic load tests on reinforced concrete columns”. *J. Struct. Eng.*, ASCE, 120(6), 1825–1849.

Watson, S., Zahn, F.A., and Park, R. 1994. “Confining reinforcement for concrete columns”. *J. Struct. Eng.*, ASCE, 120(6): 1798-1824.

Xiao, Y., and Yun, H. W. 2002. “Experimental studies on full-scale high-strength concrete columns”. *ACI Struct. J.*, 99(2): 199–207.

Xue, W., F. Peng, and Fang, Z. 2018. “Behavior and design of slender rectangular concrete columns longitudinally reinforced with fiber-reinforced polymer bars”. *ACI Struct. J.*, 115(2): 311–322.

Zahn, F. A., Park, R., and Priestley, M. J. N. 1989. “Strength and ductility of square reinforced concrete column sections subjected to biaxial bending”. *ACI Struct. J.*, 86(2): 123–131.

Appendix A: Analysis of Six-Storey Steel-RC Frame Structure

A.1 Layout of the Reinforced Concrete Frame Building

Figures A.1 and A.2 show the plan and sectional elevation in the E-W direction for the six-storey reinforced concrete frame residential building. The structure is assumed to be located in Vancouver, BC, Canada, and is designed as a ductile moment resisting frame structure. The building has 7 bays in the N-S direction, each of 6 m width and 3 bays in the E-W direction. Two of these bays are for residential spaces of 9 m width, with a central corridor bay 6 m wide in between.

The floor system is one-way slab system, spanning in the E-W direction and supported by girders and secondary beams in the N-S direction, with 110 mm slab thickness. The cross-sections of secondary beams are 300 mm wide × 350 mm thick, while for the girders the cross-sections are 350 × 600 mm, and 350 × 550 mm for the bottom and top three storeys, respectively (Cement Association of Canada 2020). All columns are preliminarily assumed to be circular with a diameter of 350 mm.

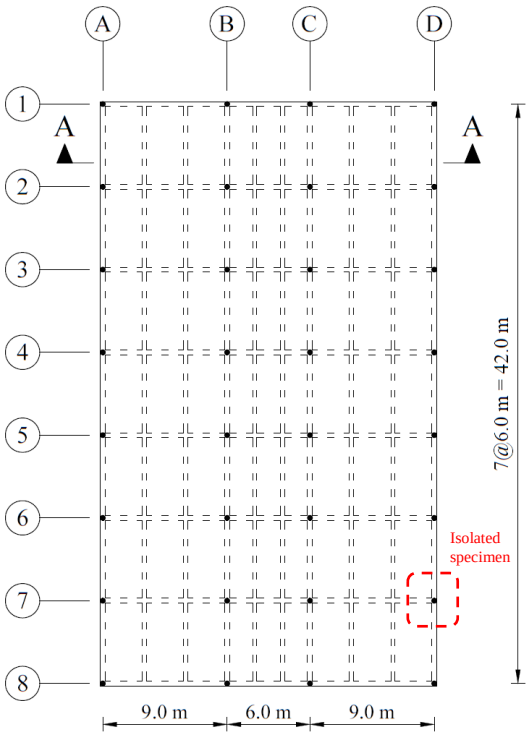

Figure A.1: Plan view for the six-story reinforced concrete frame office building

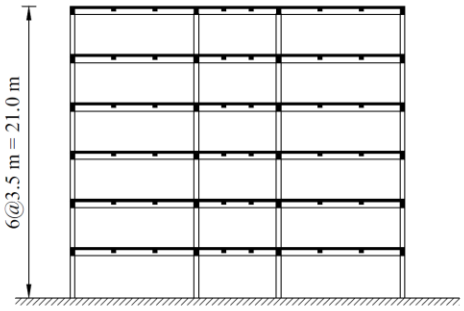

Figure A.2: Sectional Elevation for the six-storey reinforced concrete frame office building

A.4 Loads

Dead loads (Cement Association of Canada 2020; NBCC 2020)

Self-weight of reinforced concrete members calculated as 24 kN/m^3

Self-weight of one-way slab = 24 × 0.11 = 2.6 kN/m^2

Self-weight of secondary beams = 24 × 0.3 × (0.35-0.11) = 1.7 kN/m

Self-weight of top three storeys' Girders = 24 × 0.35 × (0.55-0.11) = 4.2 kN/m

Self-weight of bottom three storeys' Girders = 24 × 0.35 × (0.6-0.11) = 4.7 kN/m

1.0 kN/m^2 partition loading on all floors

0.5 kN/m^2 mechanical services loading on all floors

0.5 kN/m^2 floor covering

Floor Live loads (Cement Association of Canada 2020; NBCC 2020)

1.9 kN/m^2 on typical residential floors

Roof load (Cement Association of Canada 2020; NBCC 2020)

2.2 kN/m^2 snow load, accounting for parapets and equipment projections

1.6 kN/m^2 mechanical services loading in 6 m wide strip over corridor bay

A.5 Analysis of the Frame Structure

This structure is symmetrical and has no structural irregularities in the vertical or horizontal directions. Therefore, according to NBCC, article 4.1.8.7 (NBCC 2020), a dynamic analysis procedure is not required. A typical interior E-W frame is shown in Figure A.3, loaded with the reactions from secondary beams due to unfactored gravity dead and live loads.

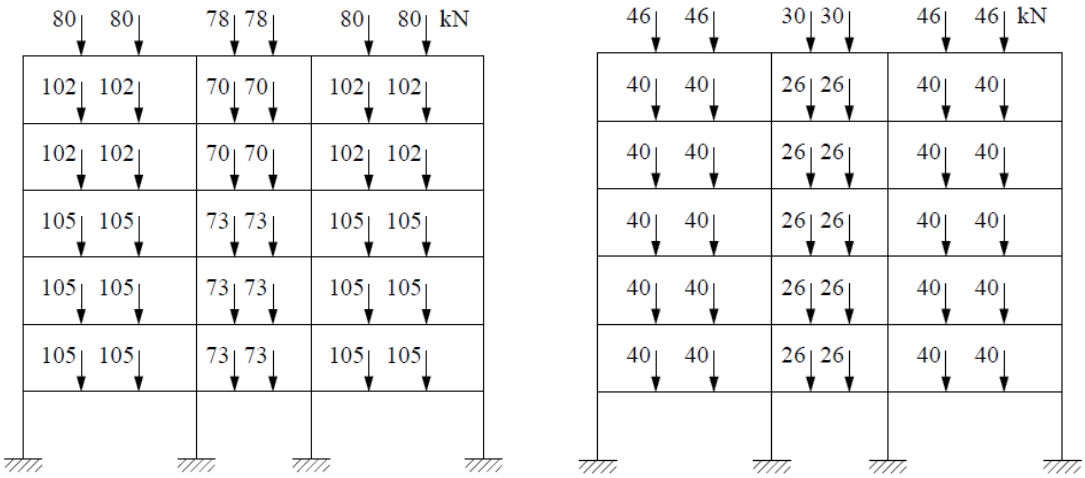

(a) Dead Loads (b) Live loads

Figure A.3: Unfactored loading cases considered in design of typical interior frame

The structure is assumed to be located in Vancouver, and founded on very dense soil and soft rock (site classification C, according to NBCC, Table 4.1.8.4.A). Based on that, the acceleration-based and velocity-based site coefficients can be determined as:

F_a = 1.0 Table 4.1.8.4.B (NBCC 2020)

F_v = 1.0 Table 4.1.8.4.C (NBCC 2020)

The 5% damped spectral response accelerations can be also determined from NBCC, Table C-2 (NBCC 2020):

$S_a(0.2)$ = 0.94

$S_a(0.5)$ = 0.64

$S_a(1.0)$ = 0.33

$S_a(2.0)$ = 0.17, $S_a(0.2)/ S_a(2.0)$ = 5.53

The design spectral response acceleration is shown in Figure A.4.

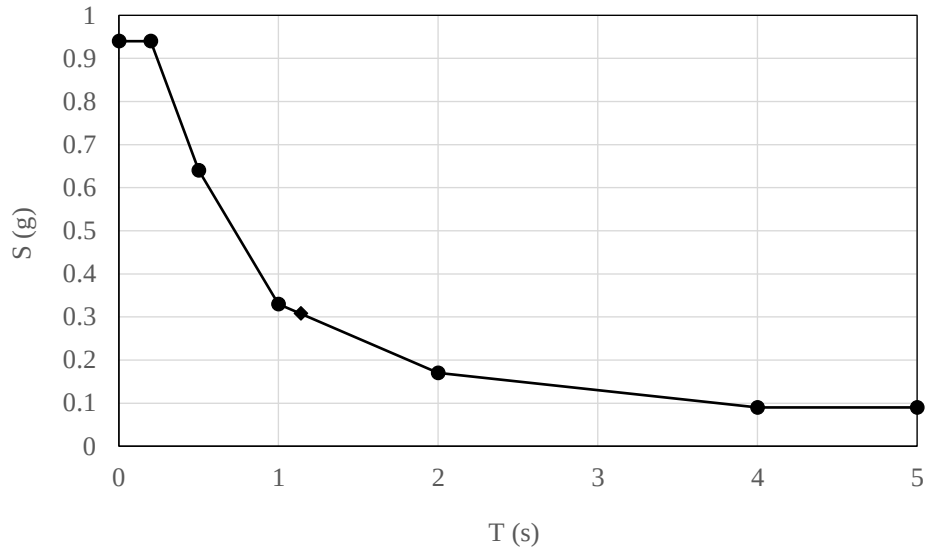

Figure A.4: Design spectral response acceleration

$T_a = 0.075\ h_n^{3/4} = 0.075(21.9)^{3/4} = 0.759$ s Article 4.1.8.11 (NBCC 2020)

However, based on a dynamic analysis by SAP2000 (Figure A.5), the period calculated by the program is 1.27 s. On the other hand, Article 4.1.8.11 of NBCC 2020 states that the fundamental lateral period should not exceed 1.5 the empirical value, for concrete moment-resisting frames. Therefore, the fundamental lateral period will be taken as:

$T_a = 1.5 \times 0.759 = 1.14$ s

From Figure A.4, $S(T_a) = 0.308$.

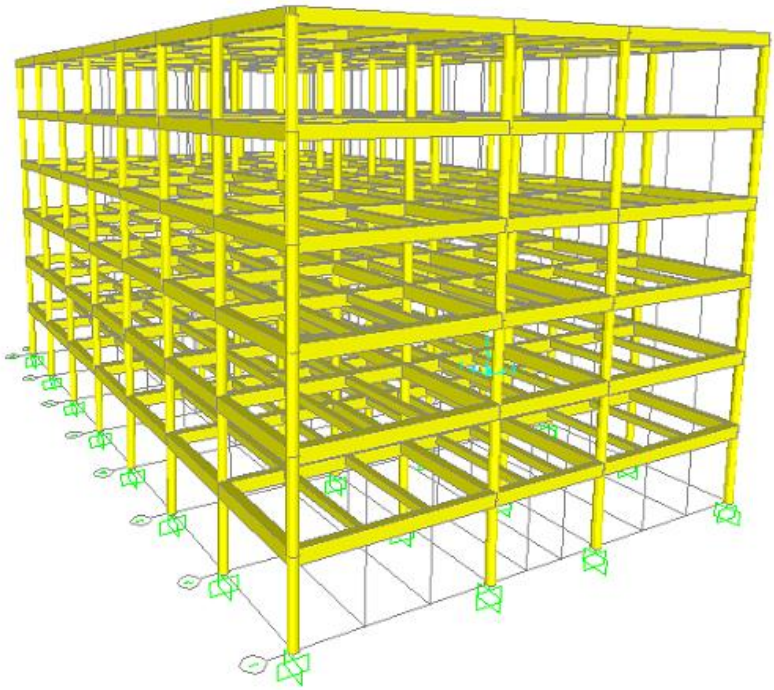

Figure A.5: 3-D Model used for dynamic analysis

I_E = 1.0 Table 4.1.8.5 (NBCC 2020)

M_v = 1.0 Table 4.1.8.11 (NBCC 2020)

J = 1.0 Table 4.1.8.11 (NBCC 2020)

R_d = 4.0 Table 4.1.8.9 (NBCC 2020)

R_o = 1.7 Table 4.1.8.9 (NBCC 2020)

$W = \sum_{i=1}^{n} W_i = 33{,}570$ kN Article 4.1.8.11 (NBCC 2020)

The lateral earthquake force, V, can be calculated according to Article 4.1.8.11 (NBCC 2020):

$$V = \frac{S_a(T_a) M_v I_E W}{R_d R_o} = \frac{0.308 \times 1 \times 1 \times W}{4 \times 1.7} = 0.045W = 1{,}510 \text{ kN}$$

$$V_{min} = \frac{S_a(2.0)M_v I_E W}{R_d R_o} = \frac{0.17 \times 1 \times 1 \times W}{4 \times 1.7} = 0.025W$$

$$V_{max} = \frac{2}{3} \times \frac{S_a(0.2)I_E W}{R_d R_o} = \frac{2}{3} \times \frac{0.94 \times 1 \times 1 \times W}{4 \times 1.7} = 0.092W$$

$$F_t = 0.07 T_a V = 0.07 \times 1.14 \times 1{,}510 = 120 \text{ kN}$$

$$\leq 0.25V = 0.25 \times 1{,}510 = 378 \text{ kN}$$

The calculations for seismic lateral forces at each floor level are summarized in Table A.1, which are computed according to Article 4.1.8.11 (NBCC 2020):

$$F_x = \frac{(V - F_t)\, W_x h_x}{\sum_{i=1}^{n} W_i h_i}$$

Table A.1: Lateral Load Calculations for Each Floor Level.

Floor	h_x (m)	W_x (kN)	$h_x W_x$ (kN.m)	F_x (kN)
6th	21.0	5,299	111,279	381+120
5th	17.5	5,579	97,633	334
4th	14.0	5,579	78,106	266
3rd	10.5	5,705	59,903	205
2nd	7.0	5,705	39,935	136
1st	3.5	5,705	19,968	68
Total	_	33,570	406,824	1,510

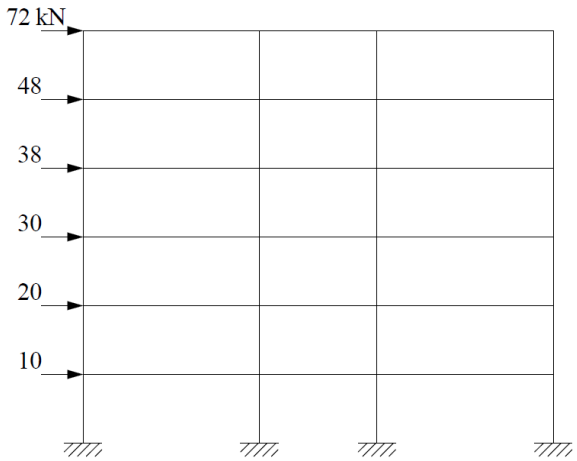

Figure A.6: Unfactored seismic lateral forces on a typical interior frame

The applied lateral forces on a typical interior frame are shown in Figure A.6. The structure is analyzed using SAP2000, to determine the member forces and moments. According to CSA A23.3-19, Clause 21.2.5.2, beam stiffness is assumed to be 0.4 of the gross moment of inertia for all beams, to make allowances for cracking. Also, an average estimated value for effective moment of inertia equals to 0.6 and 0.7 of the gross moment of inertia for columns in the top three and bottom three storeys, respectively, to account for the influence of the axial load level on the column stiffness. The axial force and bending moment diagrams for the three load configurations considered (dead, live and earthquake) are shown in Figures A.6 to A.8.The axial force, shearing force and bending moment at interior columns' bases due to each case and due to different factored load cases are summarized in Table A.2.

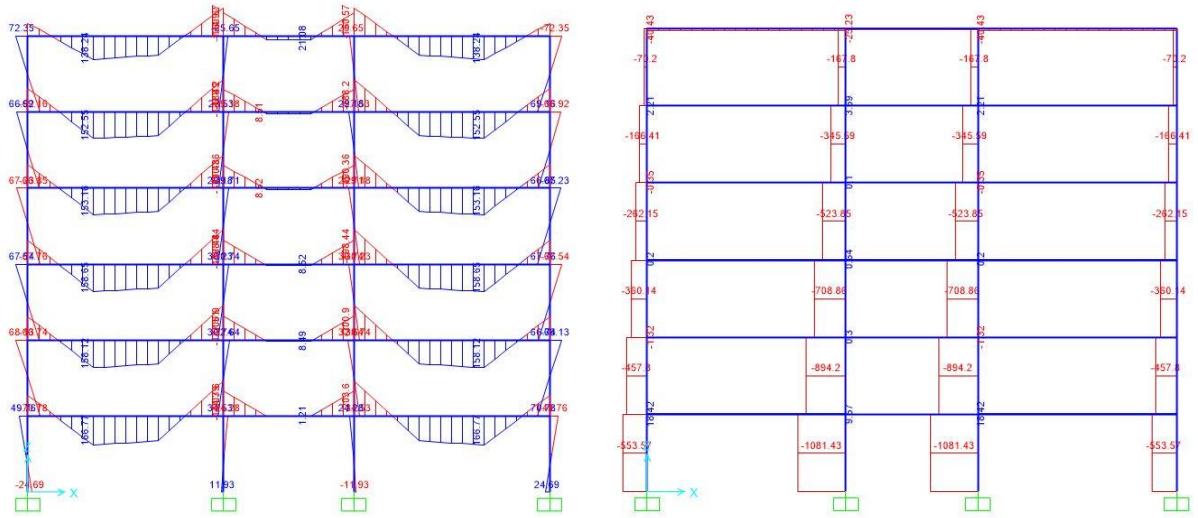

Figure A.7: Axial force and bending moment diagrams for a typical interior frame due to unfactored dead loads

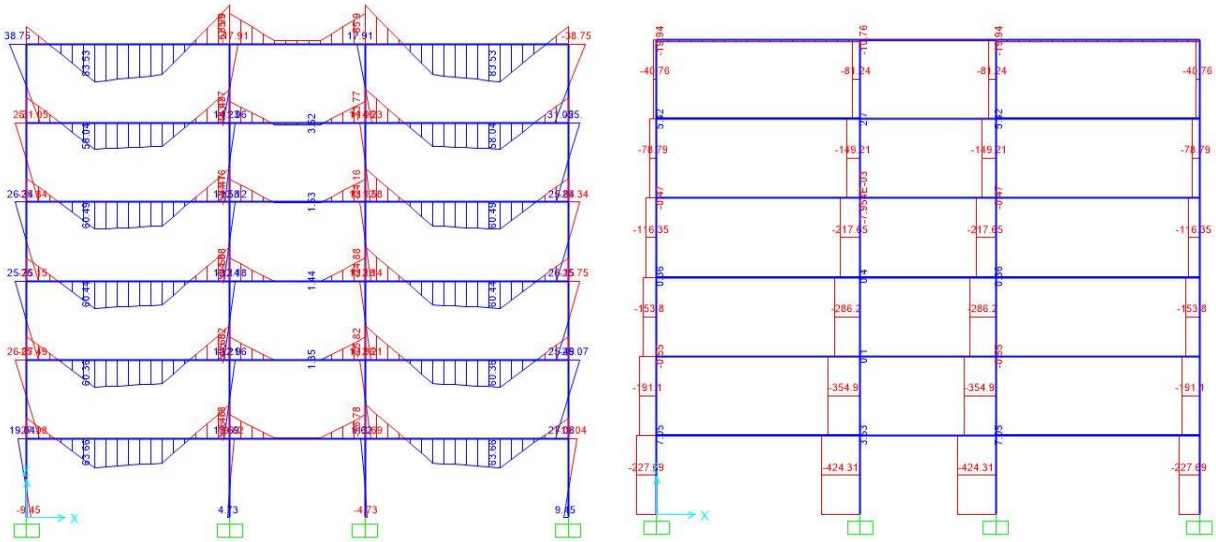

Figure A.8: Axial force and bending moment diagrams for a typical interior frame due to unfactored live loads

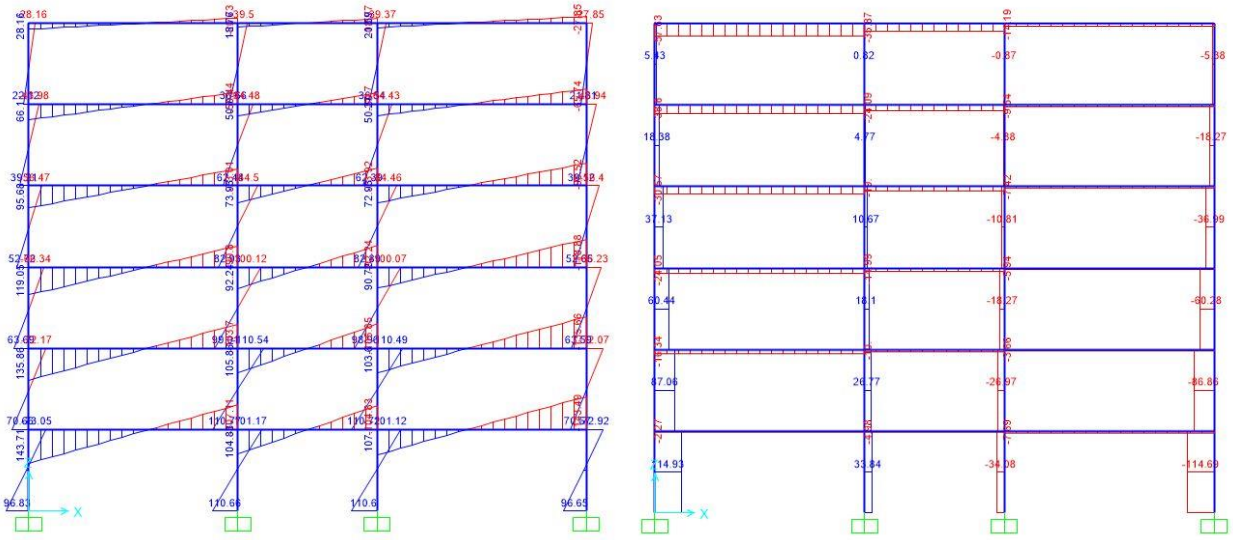

Figure A.9: Axial force and bending moment diagrams for a typical interior frame due to unfactored seismic lateral forces

Table A.2: Straining actions at the base of an exterior column.

	Dead	Live	Earthquake	Case 1 1.25D+1.5L	Case 2 1.0D+1.0E	Case 3 1.0D-1.0E	Case 4 1.0D+0.5L+1.0E	Case 5 1.0D+0.5L-1.0E
P	-554	-227	±115	-1033	-669	-439	-783	-553
V	21.3	8.1	±48.5	38.8	76.4	-33.8	80.5	-29.8
M	25	9.5	±97	45.5	122	-72	126.5	-67.3

Under seismic loading, axial load level ranges between 0.13 and 0.25 of $f'_c.A_g$, which exceeds the limit of $0.1f'_c.A_g$. Therefore, this column should be designed according to Clause 21.4.1.1 of CSA A23.3-19.

A.6 Interaction Diagram for Column Section

A.6.1 Material and sectional properties

- Concrete properties

f_c' = 35 MPa; ϕ_c = 1; $E_c = 4500\sqrt{f_c'}$ = 26,622 MPa;

α_1= 0.85 - 0.0015 f_c' = 0.797; β_1 = 0.97 - 0.0025 f_c' = 0.883; ε_{cu}= 0.0035

- Longitudinal reinforcement (steel bars)

f_y = 400 MPa; ϕ_s = 1; E_s = 200 GPa; A_b = 300 mm^2; ε_y = 0.002

- Cross section properties

A_s = 6 × 200 = 1,200 mm^2; ρ_s = 1.25%; D_g = 350 mm; R = 175 mm;

$A_g = \pi R^2$ = 3.1416 × 175^2 = 96,211 mm^2

A.6.2 Calculations required to develop interaction diagram

- Point 1: Pure axial load

$P_1 = \alpha_1 \phi_c f_c' \left(A_g - A_{st}\right) + \phi_s f_y A_{st}$ Clause 10.10.4 (CSA A23.3-19)

$P_1 = [0.797 \times 1 \times 35 \times (96211 - 1200) + 1 \times 400 \times 1200] \times 10^{-3}$ = 3,132 kN

Point 1: M_1 = 0.0 kN.m; P_1 = 3132 kN

- Balanced point

ε_{cu}= 0.0035

$\varepsilon_{s4} = \varepsilon_y = 0.002$

$f_{s4} = f_y$ = 400 MPa

$c_b = \left(\frac{\varepsilon_{cu}}{\varepsilon_{cu} + \varepsilon_{s4}}\right) d_4 = \frac{0.0035}{0.0035+0.002} \times 301.5 = 191.9$ mm

$a_b = \beta_1 c_b = 0.883 \times 191.9 = 169.3$ mm

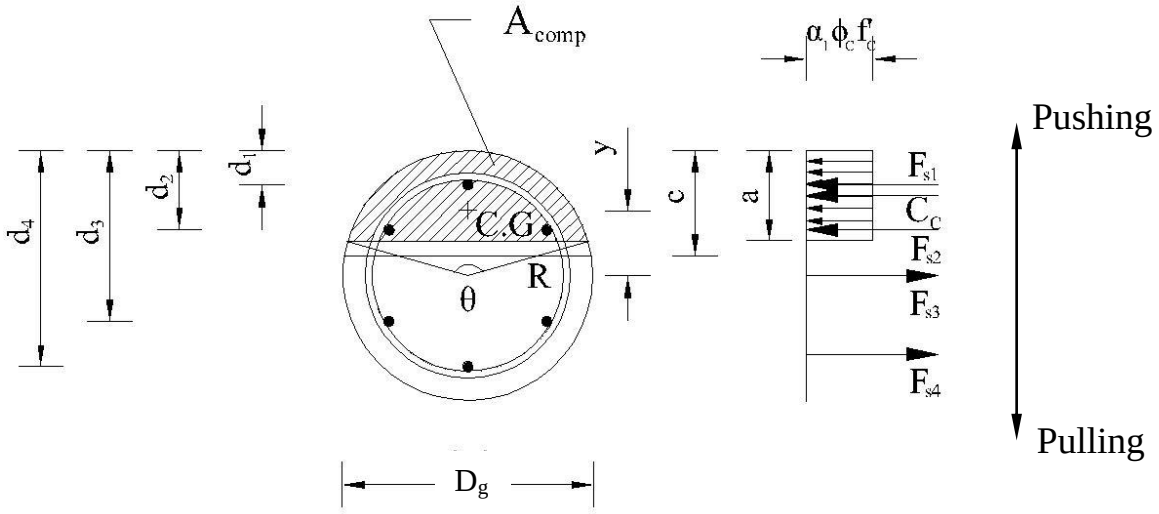

Figure A.10: Force equilibrium of the column section

Concrete area under compression,

$$A_{comp,b} = R^2\left(\cos^{-1}\left(\frac{R-a}{R}\right)\right) - (R-a)\sqrt{2Ra-a^2}$$

$$= 175^2\left(\cos^{-1}\left(\frac{175-169.3}{175}\right)\times\frac{\pi}{180}\right) - (175-169.3)\sqrt{2\times175\times169.3-169.3^2}$$

= 46,118 mm^2

Distance of the C.G. of $A_{comp,b}$ from the centroid of the column cross-section,

$$y = \frac{4Rsin^3\frac{\theta}{2}}{3(\theta-\sin\theta)}$$

Where,

$$\theta = 2\cos^{-1}\left(1-\frac{a}{R}\right) = 2\cos^{-1}\left(1-\frac{169.3}{175}\right) = 176.3°\times\frac{\pi}{180} = 3.08 \text{ rad}$$

$$y_b = \frac{4\times175\times sin^3\frac{176.3}{2}}{3(3.08-\sin 176.3)} = 77.4 \text{ mm}$$

$$C_{cb} = \alpha_1\phi_c f'_c A_{comp,b} = 0.797\times1\times35\times46{,}118\times10^{-3} = 1{,}287 \text{ kN}$$

$$\varepsilon_{s1} = \varepsilon_{cu}\left(1-\frac{d_1}{c_b}\right) = 0.0035\times\left(1-\frac{48.5}{246.9}\right) = 0.0026 > \varepsilon_y = 0.002$$

$f_{s1} = f_y = 400$ MPa

$F_{s1} = A_{s1}(\phi_s f_{s1} - \alpha_1 \phi_c f_c') = 200 \times (1 \times 400 - (0.797 \times 1 \times 35)) \times 10^{-3} = 74.4$ kN

$\varepsilon_{s2} = \varepsilon_{cu}\left(1 - \frac{d_2}{c_b}\right) = 0.0035 \times \left(1 - \frac{111.75}{246.9}\right) = 0.0015 < \varepsilon_y = 0.002$

$f_{s2} = E_s \varepsilon_{s2} = 200{,}000 \times 0.0015 = 292.3$ MPa

$F_{s2} = A_{s2}(\phi_s f_{s2} - \alpha_1 \phi_c f_c') = 400 \times (1 \times 292.3 - (0.797 \times 1 \times 35)) \times 10^{-3} = 105.8$ kN

$\varepsilon_{s3} = \varepsilon_{cu}\left(1 - \frac{d_3}{c_b}\right) = 0.0035 \times \left(1 - \frac{238.25}{246.9}\right) = -0.00085 < \varepsilon_y = 0.002$

$f_{s3} = E_s \varepsilon_{s3} = 200{,}000 \times (-0.00085) = -169.2$ MPa

$F_{s3} = \phi_s A_{s3} f_{s3} = 1 \times 400 \times (-170.36) \times 10^{-3} = -67.7$ kN (Tension)

$\varepsilon_{s4} = \varepsilon_{cu}\left(1 - \frac{d_4}{c_b}\right) = 0.0035 \times \left(1 - \frac{301.5}{246.9}\right) = -0.002 \geq \varepsilon_y = 0.002$

$f_{s4} = f_y = -400$ MPa

$F_{s4} = \phi_s A_{s4} f_{s4} = 1 \times 200 \times (-400) \times 10^{-3} = -80.0$ kN (Tension)

$P_b = C_{cb} + F_{s1} + F_{s2} + F_{s3} + F_{s4} = 1{,}287 + 74.4 + 105.8 - 67.7 - 80 = 1{,}320$ kN

$M_b = C_{cb} \times y_b + F_{s1}(R - d_1) + F_{s2}(R - d_2) + F_{s3}(R - d_3) + F_{s4}(R - d_4)$

$= 1{,}287 \times 77.4 + 74.4\,(175 - 48.5) + 105.8\,(175 - 111.75) + (-67.7)\,(175 - 238.25) + (-80)$

$(175 - 301.5) = 130$ kN.m

Balanced point: $M_b = 130$ kN.m; $P_b = 1{,}320$ kN

- <u>Point 2: $c_2 = 315$ mm</u>

$a_2 = \beta_1 c_2 = 0.883 \times 315 = 278$ mm

$A_{comp,2} = R^2\left(\cos^{-1}\left(\frac{R-a}{R}\right)\right) - (R-a)\sqrt{2Ra - a^2}$

$= 175^2\left(\cos^{-1}\left(\frac{175-278}{175}\right)\right) - (175 - 278)\sqrt{2 \times 175 \times 278 - 278^2}$

$= 81{,}947$ mm^2

Distance of the C.G. of A_{comp2} from the center of cross section of the column,

$$y = \frac{4R sin^3 \frac{\theta}{2}}{3(\theta - \sin\theta)}$$

Where,

$\theta = 2\cos^{-1}\left(1 - \frac{a}{R}\right) = 2\cos^{-1}\left(1 - \frac{278}{175}\right)$ = 252.1° = 4.4 rad

$y_2 = \frac{4\times175\times sin^3\frac{252.1}{2}}{3(4.4-\sin 252.1)}$ = 23 mm

$C_{c2} = \alpha_1 \phi_c f'_c A_{comp,2}$ = 0.797 × 1 × 35 × 81,947 = 2,287 kN

$\varepsilon_{s1} = \varepsilon_{cu}\left(1 - \frac{d_1}{c_2}\right) = 0.0035\times\left(1 - \frac{48.5}{315}\right) = 0.003 > \varepsilon_y = 0.002$

$f_{s1} = f_y$ = 400 MPa

$F_{s1} = \phi_s A_{s1}(f_{s1} - \alpha_1 \phi_c f'_c)$ = 1 × 200 × (400 – (0.797 × 1 × 35)) = 74.4 kN

$\varepsilon_{s2} = \varepsilon_{cu}\left(1 - \frac{d_2}{c_2}\right) = 0.0035\times\left(1 - \frac{111.75}{315}\right) = 0.0023 > \varepsilon_y = 0.002$

$f_{s2} = f_y$ = 400 MPa

$F_{s2} = \phi_s A_{s2}(f_{s2} - \alpha_1 \phi_c f'_c)$ = 1 × 400 × (400 – (0.797 × 1 × 35)) = 148.8 kN

$\varepsilon_{s3} = \varepsilon_{cu}\left(1 - \frac{d_3}{c_2}\right) = 0.0035\times\left(1 - \frac{238.25}{315}\right) = 0.00085 < \varepsilon_y = 0.002$

$f_{s3} = E_s \varepsilon_{s3}$ = 200,000 × 0.00085 = 170.6 MPa

$F_{s3} = \phi_s A_{s3}(f_{s3} - \alpha_1 \phi_c f'_c)$ = 1 × 400 × (170.6 – (0.797 × 1 × 35)) = 57 kN

$\varepsilon_{s4} = \varepsilon_{cu}\left(1 - \frac{d_4}{c_2}\right) = 0.0035\times\left(1 - \frac{301.5}{315}\right) = 0.00015 < \varepsilon_y = 0.002$

$f_{s4} = E_s \varepsilon_{s4}$ = 200,000 × 0.00015 = 30 MPa

$F_{s4} = \phi_s A_{s4}(f_{s4} - \alpha_1 \phi_c f'_c)$ = 1 × 200 × (30 – (0.797 × 1 × 35)) = 0.4 kN

$P_2 = C_{c2} + F_{s1} + F_{s2} + F_{s3} + F_{s4}$ = 2,287 + 74.4+ 148.8 + 57 + 0.4= 2,568 kN

$M_2 = C_{c2} \times y_2 + F_{s1}(R - d_1) + F_{s2}(R - d_2) + F_{s3}(R - d_3) + F_{s4}(R - d_4)$

= 2,287 × 23 + 74.4 (175 – 48.5) + 148.8 (175 − 97.5) + 57 (175 – 238.25) + 0.4 (175 – 301.5)

= 67.9 kN.m

Point 2: $M_2 = 67.9$ kN.m; $P_2 = 2{,}568$ kN

- Point 3: $c_3 = 245$ mm

$a_3 = \beta_1 c_3 = 0.883 \times 245 = 216.2$ mm

$$A_{comp3} = R^2\left(\cos^{-1}\left(\frac{R-a}{R}\right)\right) - (R-a)\sqrt{2Ra-a^2}$$

$$= 175^2\left(\cos^{-1}\left(\frac{175-216.2}{175}\right)\right) - (175-216.2)\sqrt{2\times 175\times 216.2 - 216.2^2}$$

= 62,396 mm^2

Distance of the C.G. of A_{comp3} from the center of cross section of the column,

$$y = \frac{4R\sin^3\frac{\theta}{2}}{3(\theta - \sin\theta)}$$

Where,

$\theta = 2\cos^{-1}\left(1-\frac{a}{R}\right) = 2\cos^{-1}\left(1-\frac{216.2}{175}\right) = 207.2° = 3.62$ rad

$y_3 = \frac{4\times 175\times \sin^3\frac{207.2}{2}}{3(3.99-\sin 207.2)} = 52.6$ mm

$C_{c3} = \alpha_1\phi_c f_c' A_{comp3} = 0.797 \times 1 \times 35 \times 62{,}396 \times 10^{-3} = 1{,}742$ kN

$\varepsilon_{s1} = \varepsilon_{cu}\left(1-\frac{d_1}{c_3}\right) = 0.0035\times\left(1-\frac{48.5}{245}\right) = 0.0028 > \varepsilon_y = 0.002$

$f_{s1} = f_y = 400$ MPa

$F_{s1} = \phi_s A_{s1}(f_{s1} - \alpha_1\phi_c f_c') = 1 \times 200 \times (400 - (0.797 \times 1 \times 35)) \times 10^{-3} = 74.4$ kN

$\varepsilon_{s2} = \varepsilon_{cu}\left(1-\frac{d_2}{c_3}\right) = 0.0035\times\left(1-\frac{111.75}{245}\right) = 0.0019 \geq \varepsilon_y = 0.002$

$f_{s2} = 200{,}000 \times 0.0019 = 380.7$ MPa

$F_{s2} = \phi_s A_{s2}(f_{s2} - \alpha_1\phi_c f_c') = 1 \times 400 \times (380.7 - (0.797 \times 1 \times 35)) \times 10^{-3} = 141$ kN

$\varepsilon_{s3} = \varepsilon_{cu}\left(1 - \frac{d_3}{c_3}\right) = 0.0035 \times \left(1 - \frac{238.25}{245}\right) = 0.000096 < \varepsilon_y = 0.002$

$f_{s3} = E_s\varepsilon_{s3} = 200{,}000 \times 0.000096 = 19.3$ MPa

$F_{s3} = \phi_s A_{s3}(f_{s3} - \alpha_1\phi_c f_c') = 1 \times 400 \times (19.3 - (0.797 \times 1 \times 35)) \times 10^{-3} = -3.5$ kN (Tension)

$\varepsilon_{s4} = \varepsilon_{cu}\left(1 - \frac{d_4}{c_3}\right) = 0.0035 \times \left(1 - \frac{301.5}{245}\right) = -0.0008 < \varepsilon_y = 0.002$

$f_{s4} = E_s\varepsilon_{s4} = 200{,}000 \times (-0.0008) = -161.4$ MPa

$F_{s4} = \phi_s A_{s4} f_{s4} = 1 \times 200 \times (-161.4) \times 10^{-3} = -32.3$ kN (Tension)

$P_3 = C_{c3} + F_{s1} + F_{s2} + F_{s3} + F_{s4} = 1{,}742 + 74.4 + 141 - 3.5 - 32.3 = 1{,}921$ kN

$M_3 = C_{c3} \times y_3 + F_{s1}(R - d_1) + F_{s2}(R - d_2) + F_{s3}(R - d_3) + F_{s4}(R - d_4)$

$= 1{,}742 \times 52.6 + 74.4\,(175 - 48.5) + 141\,(175 - 111.75) - 3.5\,(175 - 238.25) - 32.3\,(175 - 301.5) = 114.2$ kN.m

Point 3: $M_3 = 114.2$ kN.m; $P_3 = 1{,}921$ kN

- Point 4: $c_4 = 140$ mm

$a_4 = \beta_1 c_4 = 0.883 \times 140 = 123.6$ mm

$A_{comp4} = R^2\left(\cos^{-1}\left(\frac{R-a}{R}\right)\right) - (R-a)\sqrt{2Ra - a^2}$

$= 175^2\left(\cos^{-1}\left(\frac{175-123.6}{175}\right)\right) - (175 - 123.6)\sqrt{2 \times 175 \times 123.6 - 123.6^2}$

$= 30{,}361$ mm^2

Distance of the C.G. of A_{comp4} from the center of cross section of the column,

$$y = \frac{4R\sin^3\frac{\theta}{2}}{3(\theta - \sin\theta)}$$

Where,

$\theta = 2\cos^{-1}\left(1 - \frac{a}{R}\right) = 2\cos^{-1}\left(1 - \frac{123.6}{175}\right) = 145.8° = 2.54$ rad

$y_4 = \frac{4\times175\times sin^3\frac{145.8}{2}}{3(3.62-\sin 145.8)}$ = 102.8 mm

$C_{c4} = \alpha_1\phi_c f_c' A_{comp4} = 0.797 \times 1 \times 35 \times 30{,}361 \times 10^{-3}$ = 847.5 kN

$\varepsilon_{s1} = \varepsilon_{cu}\left(1-\frac{d_1}{c_4}\right) = 0.0035\times\left(1-\frac{48.5}{140}\right) = 0.0023 > \varepsilon_y = 0.002$

$f_{s1} = f_y = 400$ MPa

$F_{s1} = \phi_s A_{s1}(f_{s1} - \alpha_1\phi_c f_c') = 1 \times 200 \times (400 - (0.797 \times 1 \times 35)) \times 10^{-3}$ = 74.4 kN

$\varepsilon_{s2} = \varepsilon_{cu}\left(1-\frac{d_2}{c_4}\right) = 0.0035\times\left(1-\frac{111.75}{140}\right) = 0.0007 < \varepsilon_y = 0.002$

$f_{s2} = E_s\varepsilon_{s2} = 200{,}000 \times 0.0007$ = 141.3 MPa

$F_{s2} = \phi_s A_{s2}(f_{s2} - \alpha_1\phi_c f_c') = 1 \times 400 \times (141.3 - (0.797 \times 1 \times 35)) \times 10^{-3}$ = 45.3 kN

$\varepsilon_{s3} = \varepsilon_{cu}\left(1-\frac{d_3}{c_4}\right) = 0.0035\times\left(1-\frac{238.25}{140}\right) = -0.0025 > \varepsilon_y = 0.002$

$f_{s3} = f_y = -400$ MPa

$F_{s3} = \phi_s A_{s3} f_{s3} = 1 \times 400 \times (-400) \times 10^{-3}$ = – 160 kN (Tension)

$\varepsilon_{s4} = \varepsilon_{cu}\left(1-\frac{d_4}{c_4}\right) = 0.0035\times\left(1-\frac{301.5}{140}\right) = -0.004 > \varepsilon_y = 0.002$

$f_{s4} = f_y = -400$ MPa

$F_{s4} = \phi_s A_{s4} f_{s4} = 1 \times 200 \times (-400) \times 10^{-3}$ = – 80 kN (Tension)

$P_4 = C_{c4} + F_{s1} + F_{s2} + F_{s3} + F_{s4}$ = 847.5 + 74.4 + 45.3 – 6.1 – 48.7= 727.2 kN

$M_4 = C_{c4} \times y_4 + F_{s1}(R-d_1) + F_{s2}(R-d_2) + F_{s3}(R-d_3) + F_{s4}(R-d_4)$

= 847.5 × 102.8 + 74.4 (175 – 48.5) + 45.3 (175 − 111.75) + (– 160) (175 – 238.25) + (– 80) (175 – 301.5) = 119.6 kN.m

Point 4: $M_4 = 119.6$ kN.m; $P_4 = 727.2$ kN

- Point 5: c_5 = 105 mm

$a_5 = \beta_1 c_5 = 0.883 \times 105$ = 92.7 mm

$A_{comp5} = R^2\left(\cos^{-1}\left(\frac{R-a}{R}\right)\right) - (R-a)\sqrt{2Ra-a^2}$

$= 175^2\left(\cos^{-1}\left(\frac{175-92.7}{175}\right)\right) - (175-92.7)\sqrt{2\times175\times92.7 - 92.7^2}$

$= 20{,}389\ \text{mm}^2$

Distance of the C.G. of A_{comp5} from the center of cross section of the column,

$$y = \frac{4Rsin^3\frac{\theta}{2}}{3(\theta - \sin\theta)}$$

Where,

$\theta = 2\cos^{-1}\left(1-\frac{a}{R}\right) = 2\cos^{-1}\left(1-\frac{92.7}{175}\right) = 123.9° = 2.16$ rad

$y_5 = \frac{4\times175\times sin^3\frac{123.9}{2}}{3(2.16-\sin 123.9)} = 120.4$ mm

$C_{c5} = \alpha_1\phi_c f_c' A_{comp5} = 0.797\times1\times35\times20{,}389\times10^{-3} = 569$ kN

$\varepsilon_{s1} = \varepsilon_{cu}\left(1-\frac{d_1}{c_5}\right) = 0.0035\times\left(1-\frac{48.5}{105}\right) = 0.0019 < \varepsilon_y = 0.002$

$f_{s1} = E_s\varepsilon_{s1} = 200{,}000\times0.0019 = 376.7$ MPa

$F_{s1} = \phi_s A_{s1}(f_{s1} - \alpha_1\phi_c f_c') = 1\times200\times(376.7 - (0.797\times1\times35))\times10^{-3} = 69.8$ kN

$\varepsilon_{s2} = \varepsilon_{cu}\left(1-\frac{d_2}{c_5}\right) = 0.0035\times\left(1-\frac{111.75}{105}\right) = -0.00023 < \varepsilon_y = 0.002$

$f_{s2} = E_s\varepsilon_{s2} = 200{,}000\times(-0.00023) = -45$ MPa

$F_{s2} = \phi_s A_{s2} f_{s2} = 1\times400\times(-45)\times10^{-3} = -18$ kN (Tension)

$\varepsilon_{s3} = \varepsilon_{cu}\left(1-\frac{d_3}{c_5}\right) = 0.0035\times\left(1-\frac{238.25}{105}\right) = -0.0044 > \varepsilon_y = 0.002$

$f_{s3} = f_y = -400$ MPa

$F_{s3} = \phi_s A_{s3} f_{s3} = 1\times400\times(-400)\times10^{-3} = -160$ kN (Tension)

$\varepsilon_{s4} = \varepsilon_{cu}\left(1-\frac{d_4}{c_5}\right) = 0.0035\times\left(1-\frac{301.5}{105}\right) = -0.0066 > \varepsilon_y = 0.002$

$f_{s4} = f_y = -$ 400 MPa

$F_{s4} = \phi_s A_{s4} f_{s4} = 1 \times 200 \times (-400) \times 10^{-3}$ = – 80.0 kN (Tension)

$P_5 = C_{c5} + F_{s1} + F_{s2} + F_{s3} + F_{s4}$ = 569 + 69.8 – 18 – 160 – 80 = 381 kN

$M_5 = C_{c5} \times y_5 + F_{s1}(R - d_1) + F_{s2}(R - d_2) + F_{s3}(R - d_3) + F_{s4}(R - d_4)$

= 569 × 120.4 + 69.8 (175 – 48.5) – 18 (175 − 111.75) + (– 160) (175 – 238.25) + (– 80) (175 – 301.5) = 96.4 kN.m

$e_5 = \frac{M_5}{P_5} = \frac{92.4}{933.0} = 99.0$ mm

Point 5: $M_5 = 96.4$ kN.m; $P_5 = 381$ kN

- Point 6: $c_6 = 74$ mm

$a_6 = \beta_1 c_6 = 0.883 \times 74 = 64.9$ mm

$A_{comp6} = R^2 \left(\cos^{-1}\left(\frac{R-a}{R}\right)\right) - (R-a)\sqrt{2Ra - a^2}$

$= 175^2 \left(\cos^{-1}\left(\frac{175-64.9}{175}\right)\right) - (175 - 64.9)\sqrt{2 \times 175 \times 64.9 - 64.9^2}$

= 12,280 mm^2

Distance of the C.G. of A_{comp8} from the center of cross section of the column,

$$y = \frac{4R sin^3 \frac{\theta}{2}}{3(\theta - \sin\theta)}$$

Where,

$\theta = 2\cos^{-1}\left(1 - \frac{a}{R}\right) = 2\cos^{-1}\left(1 - \frac{64.9}{175}\right) = 102° = 1.78$ rad

$y_6 = \frac{4 \times 175 \times sin^3 \frac{102}{2}}{3(1.78 - \sin 102)} = 136.5$ mm

$C_{c6} = \alpha_1 \phi_c f_c' A_{comp6} = 0.797 \times 1 \times 35 \times 12{,}280 \times 10^{-3} = 342.8$ kN

$\varepsilon_{s1} = \varepsilon_{cu}\left(1 - \frac{d_1}{c_8}\right) = 0.0035 \times \left(1 - \frac{48.5}{74}\right) = 0.0012 < \varepsilon_y = 0.002$

$f_{s1} = E_s\varepsilon_{s1} = 200{,}000 \times 0.0012 = 238.1$ MPa

$F_{s1} = \phi_s A_{s1}(f_{s1} - \alpha_1\phi_c f_c') = 1 \times 200 \times (238.1 - (0.797 \times 1 \times 35)) \times 10^{-3} = 42.0$ kN

$\varepsilon_{s2} = \varepsilon_{cu}\left(1 - \frac{d_2}{c_8}\right) = 0.0035 \times \left(1 - \frac{111.75}{74}\right) = -0.0018 < \varepsilon_y = 0.002$

$f_{s2} = E_s\varepsilon_{s2} = 200{,}000 \times (-0.0018) = -364.3$ MPa

$F_{s2} = \phi_s A_{s2} f_{s2} = 1 \times 400 \times (-364.3) \times 10^{-3} = -145.7$ kN (Tension)

$\varepsilon_{s3} = \varepsilon_{cu}\left(1 - \frac{d_3}{c_8}\right) = 0.0035 \times \left(1 - \frac{238.25}{74}\right) = -0.0079 < \varepsilon_y = 0.002$

$f_{s3} = f_y = -400$ MPa

$F_{s3} = \phi_s A_{s3} f_{s3} = 1 \times 400 \times (-400) \times 10^{-3} = -160$ kN (Tension)

$\varepsilon_{s4} = \varepsilon_{cu}\left(1 - \frac{d_4}{c_8}\right) = 0.0035 \times \left(1 - \frac{301.5}{74}\right) = -0.011 < \varepsilon_y = 0.002$

$f_{s4} = f_y = -400$ MPa

$F_{s4} = \phi_s A_{s4} f_{s4} = 1 \times 200 \times (-400) \times 10^{-3} = -80.0$ kN (Tension)

$P_6 = C_{c8} + F_{s1} + F_{s2} + F_{s3} + F_{s4} = 342.8 + 42 - 145.7 - 160 - 80 \approx 0.0$ kN

For interaction diagram, $P_8 = 0.0$ kN

$M_6 = C_{c8} \times y_8 + F_{s1}(R - d_1) + F_{s2}(R - d_2) + F_{s3}(R - d_3) + F_{s4}(R - d_4)$

$= 342.8 \times 136.5 + 42\,(175 - 48.5) + (-145.7)\,(175 - 111.75) + (-160)\,(175 - 238.25) + (-80)$

$(175 - 301.5) = 63.1$ kN.m

Point 6: $M_6 = 63.1$ kN.m; $P_6 = 0.0$ kN

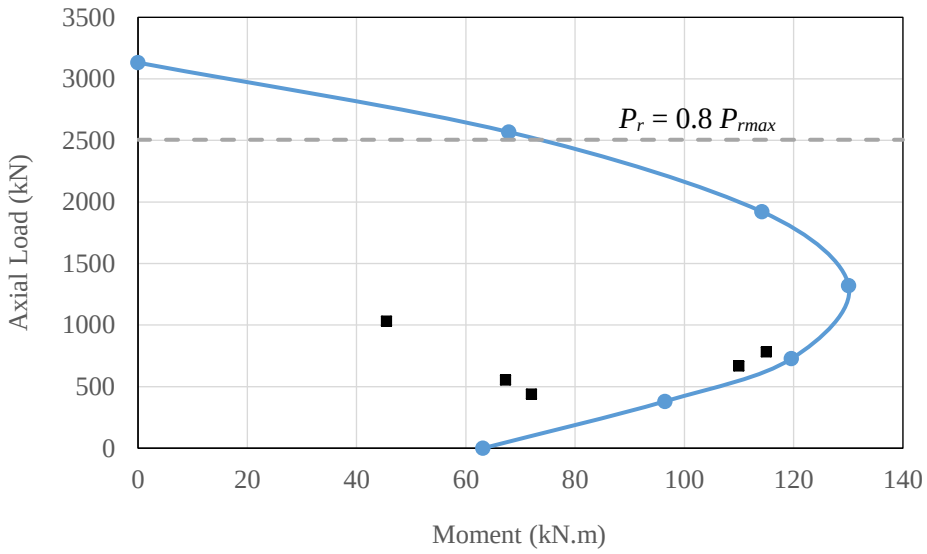

Figure A.11: Column interaction diagram and checking load combinations.

As previously discussed, the average axial load is 0.2 $f'_c.A_g$. However, the axial load level was expressed in terms of P_o, as per Clause 12.7.3.3 of CSA S806-12 (CSA 2017), since this study is dedicated to study the behaviour of GFRP-RC columns. Therefore, the applied axial load was expressed as:

$$P = 0.2P_o = 0.2\alpha_1\phi_c f_c^{'}(A_g - A_F) = 0.2\times 0.797\times 1\times 35\times(96,211 - 6\times 198) = 537\ \text{kN}$$

Assume c = 121 mm

$a = \beta_1 c = 0.883 \times 121 = 106.8$ mm

$$A_{comp} = R^2\left(\cos^{-1}\left(\frac{R-a}{R}\right)\right) - (R-a)\sqrt{2Ra - a^2}$$

$$= 175^2\left(\cos^{-1}\left(\frac{175-106.8}{175}\right)\right) - (175 - 106.8)\sqrt{2\times 175\times 106.8 - 106.8^2}$$

$= 24848.8\ \text{mm}^2$

Distance of the C.G. of A_{comp} from the center of cross section of the column,

$$y = \frac{4Rsin^3\frac{\theta}{2}}{3(\theta - \sin\theta)}$$

Where,

$\theta = 2\cos^{-1}\left(1 - \frac{a}{R}\right) = 2\cos^{-1}\left(1 - \frac{106.78}{175}\right) = 134.1° = 2.34$ rad

$y = \frac{4 \times 175 \times sin^3\frac{134.1}{2}}{3(2.34 - \sin 134.1)} = 112.29$ mm

$C_c = \alpha_1 \phi_c f_c' A_{comp} = 0.797 \times 1 \times 35 \times 24848.8 = 693.6$ kN

$\varepsilon_{s1} = \varepsilon_{cu}\left(1 - \frac{d_1}{c}\right) = 0.0035 \times \left(1 - \frac{48.5}{121}\right) = 0.0021 > \varepsilon_y = 0.002$

$f_{s1} = f_y = 400$ MPa

$F_{s1} = \phi_s A_{s1}(f_{s1} - \alpha_1 \phi_c f_c') = 1 \times 200 \times (400 - (0.797 \times 1 \times 35)) = 74.4$ kN

$\varepsilon_{s2} = \varepsilon_{cu}\left(1 - \frac{d_2}{c}\right) = 0.0035 \times \left(1 - \frac{111.75}{119.5}\right) = 0.00027 < \varepsilon_y = 0.002$

$f_{s2} = E_s \varepsilon_{s2} = 200{,}000 \times (0.00027) = 53.5$ MPa

$F_{s2} = \phi_s A_{s2}(f_{s2} - \alpha_1 \phi_c f_c') = 1 \times 400 \times (53.5 - (0.797 \times 1 \times 35)) = 10.2$ kN

$\varepsilon_{s3} = \varepsilon_{cu}\left(1 - \frac{d_3}{c}\right) = 0.0035 \times \left(1 - \frac{238.25}{119.5}\right) = -0.0034 > \varepsilon_y = 0.002$

$f_{s3} = f_y = -400$ MPa

$F_{s3} = \phi_s A_{s3} f_{s3} = 1 \times 400 \times (-400) = -160.0$ kN (tension)

$\varepsilon_{s4} = \varepsilon_{cu}\left(1 - \frac{d_4}{c}\right) = 0.0035 \times \left(1 - \frac{301.5}{119.5}\right) = -0.005 > \varepsilon_y = 0.002$

$f_{s4} = f_y = -400$ MPa

$F_{s4} = \phi_s A_{s4} f_{s4} = 1 \times 200 \times (-400) = -80.0$ kN (tension)

Check force equilibrium:

$P = C_{c8} + F_{s1} + F_{s2} + F_{s3} + F_{s4}$

$537 = 693.6 + 74.4 + 10.2 - 160.0 - 80.0$

$537 \approx 538.2$ kN

$M = C_c \times y + F_{s1}(R - d_1) + F_{s2}(R - d_2) + F_{s3}(R - d_3) + F_{s4}(R - d_4)$

M = 693.6 × 90.79 + 74.4 (175 – 48.5) + 10.2 (175 − 111.75) + (– 160) (175 – 238.25) +

(– 80) (175 – 301.5)

= 108.2 kN.m

Lateral load capacity, $V = M/1.75$ = 108.2/1.75 = 61.8 kN

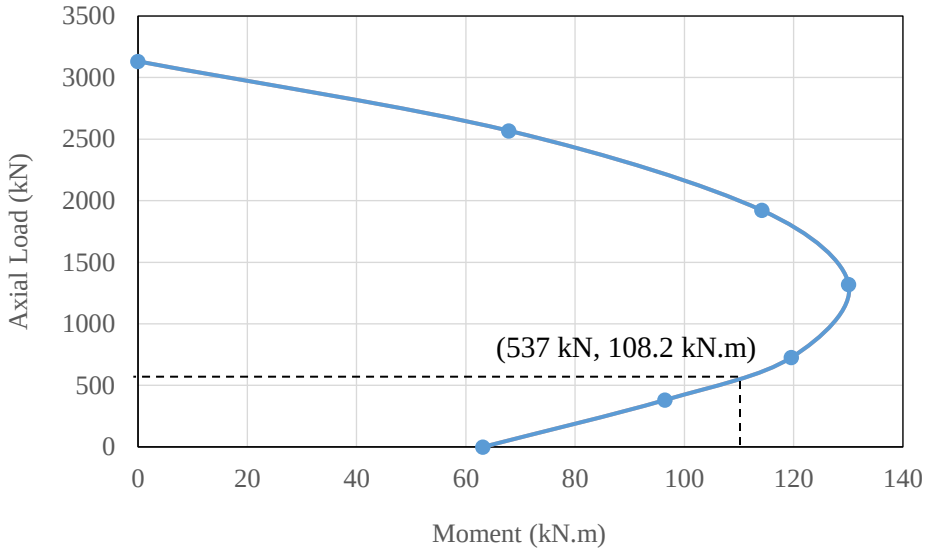

Figure A.12: Column interaction diagram for specimen S1

A.1 DESIGN FOR SHEAR

A.2.1 Material and sectional properties

- Shear reinforcement and characteristics:

f_y = 400 MPa; ϕ_s = 1; E_s = 200 GPa; A_v = 200 mm^2; ε_y = 0.002;

Applied lateral shear force, V_f = 61.8 kN

From CSA A23.3-19, Clauses 11.3.3 and 11.3.4

$V_r = V_c + V_s$

$V_c = \varphi_c \lambda \beta \sqrt{f_c'} b_w d_v$

b_w= 350 mm (Clause 11.2.10.3)

$d = 259$ mm $< 0.8h = 0.8 \times 350 = 280$ mm

$d_v \geq 0.9d = 0.9 \times 280 = 252$ mm

$\geq 0.72h = 0.72 \times 350 = 252$ mm

From CSA A23.3-19, Clause 21.3.2.7.2.

$\beta \leq 0.1$ and $\theta \geq 45°$

From CSA A23.3-19, Clause 11.3.6.4.

$$\varepsilon_x = \frac{\left(\frac{M_f}{d_v} + V_f + 0.5N_f\right)}{2E_S A_S}$$

$$\varepsilon_x = \frac{\left(\frac{108.2\times10^6}{252} + 61.8\times10^3 - 0.5\times537\times10^3\right)}{2\times200{,}000\times200} = 2.783\times 10^{-3} < 0.003$$

$$\beta = \frac{0.4}{(1 + 1500\varepsilon_x)} \times \frac{1300}{(1000 + S_{Ze})}$$

Since, $A_v > A_{v,min}$

S_{Ze} = 300 mm (as the section contains at least minimum transverse reinforcement)

$$\beta = \frac{0.4}{(1+1500\times2.783\times10^{-3})} \times \frac{1300}{(1000+300)} = 0.077 < 0.1$$ OK

$\theta = 29 + 7000\varepsilon_x = 29 + 7000 \times 2.783\times 10^{-3} = 48.5° > 45°$ OK

$V_c = 1 \times 1 \times 0.077 \times \sqrt{35} \times 350 \times 252 \times 10^{-3} = 40.2$ kN

$V_s = V_r - V_c = 61.8 - 40.2 = 21.6$ kN

From CSA A23.3-19, Clause 11.3.5.1

$$s = \frac{\varphi_s A_v f_y d_v \cot\theta}{V_s} = \frac{1\times200\times400\times252\times\cot 48.5}{21{,}600} = 825.7 \text{ mm}$$

From CSA A23.3-19 Clause 11.2.8.2

$$A_{v,min} = 0.06\sqrt{f_c'}\frac{b_w s}{f_y}$$

$200 = 0.06\sqrt{35}\frac{350\times s}{400}$

s = 643.9 mm

When s = 85 mm

$V_s = \frac{1\times200\times400\times252\times\cot 48.5}{85}$ = 209.8 kN

$V_r = V_s + V_c = 209.8 + 40.2 = 250$ kN $> V_f = 61.8$ kN OK

$V_{rmax} = 0.25\varphi_c f_c' b_w d_v = 0.25 \times 1 \times 35 \times 350 \times 252 \times 10^{-3} = 771.75$ kN $> V_r$ OK

From CSA A23.3-19, Clause 21.4.4.3

Confinement reinforcement in accordance with Clause 21.2.8.2 shall be provided at both ends of the columns over a length equal to the largest of one-sixth of the clear height, the maximum cross-sectional dimension, or 450 mm, with the spacing not exceeding the smallest of:

- Eight longitudinal bar diameters = 8 × 15.9 = 128 mm
- 24 tie diameters = 24 × 11 = 264 mm
- One-half of the minimum column dimension = 350/2 = 175 mm

From CSA A23.3-19, Clause 21.2.8.1

Buckling prevention ties shall comply with Clause 7.6.5.5 or 7.6.5.6 and shall be detailed as hoops, seismic crossties or spirals. The tie spacing shall not exceed the smallest of:

- Six longitudinal bar diameters = 6 × 15.9 = 96 mm
- 24 tie diameters = 24 × 11 = 265 mm
- One-half of the minimum column dimension = 350/2 = 175 mm

From CSA A23.3-19, Clause 21.3.1.4.2

The first hoop shall be located not more than 50 mm from the face of a supporting member. The maximum spacing of the hoops shall not exceed:

- d / 4 = 350/4 = 87.5 mm (governs)

- eight times the diameter of the smallest longitudinal bars = 8 × 15.9 = 128 mm
- 24 times the diameter of the hoop bars = 24 × 11 = 264 mm
- 300 mm

Select 10M spiral at pitch = 85 mm

Check for confinement reinforcement from CSA A23.3-19, Clause 21.2.8.2

$$\rho_s = C_c K_p \frac{f'_c}{f_{yh}} = 0.4 \times 0.2 \times \frac{35}{400} = 0.007$$

$$\rho_s = \frac{A_b \times l}{A_c \times s}$$

$s = 204$ mm OK

Check for minimum spiral reinforcement from Clause 10.9.4

The ratio of spiral reinforcement shall be not less than the value given by

$$\rho_s = 0.5 \left(\frac{A_g}{A_c} - 1\right)^{1.4} \frac{f'_c}{f_y} = 0.5 \times \left(\frac{96211.3}{61575.2} - 1\right)^{1.4} \times \frac{35}{400} = 0.0146$$

$$\rho_s = \frac{A_b \times l}{A_c \times s}$$

$s = 97.8$ mm OK

Appendix B: Design of GFRP-RC Specimen G1

B.1 Characteristics of the GFRP-RC Specimen G1

The specimen G1 is a column-footing specimen that consists of a circular GFRP-RC column and a steel-RC footing. Due to the scarcity of data on modelling GFRP-RC structures, the GFRP-RC specimens were modeled after the isolated steel-RC specimen S1. The GFRP-RC column was checked for flexure, shear and confinement in accordance with CSA S806-12 (CSA 2017) and CSA S6-19 (CSA 2019d), as discussed in detail in this appendix. The specimen is assumed to be hypothetically loaded under gravity loads and uniaxial lateral drift reversals, simulating the seismic action in one direction only.

The column has a diameter of 350 mm and a shear span of 1,750 mm. The column is reinforced longitudinally with 6-No. 16 (15.9-mm diameter) GFRP bars and transversally with a No. 10 (9.5-mm diameter) GFRP spiral. The target concrete compressive strength of the column is 35 MPa whereas the properties of the used GFRP longitudinal and transverse reinforcement are listed in Table 3.1. The specified axial load applied to the column is 0.2 the nominal unconfined axial capacity of the column, calculated as per CSA S806-12 (CSA 2017) [Equation 3.1].

B.2 Interaction Diagram for Column Section

B.2.1 Material and sectional properties

- Concrete properties

f_c' = 35 MPa; ϕ_c = 1; E_c = 4500$\sqrt{f_c'}$ = 26,622 MPa;

α_1= 0.85 - 0.0015 f_c' = 0.797; β_1 = 0.97 - 0.0025 f_c' = 0.883; ε_{cu}= 0.0035

- Longitudinal reinforcement (GFRP bars)

f_{Fu} = 1,711 MPa; ϕ_f = 1; E_f = 65.7 GPa; A_b = 197.9 mm^2; ε_{Fu} = 0.026

- Cross section properties

A_f = 6 × 197.9 = 1,188 mm^2; ρ_f = 1.23%; D_g = 350 mm; R = 175 mm;

$A_g = \pi R^2$ = 3.1416 × 175^2 = 96,211 mm^2

B.2.2 Calculations required to develop interaction diagram

- Point 1: Pure axial load

$P_1 = \alpha_1 \phi_c f_c' \left(A_g - A_F\right)$

P_1 = (0.797 × 1 × 35 × (96,211 − 1,188) × 10^{-3} = 2,686 kN

Point 1: M_1 = 0.0 kN.m; P_1 = 2,686 kN

- Point 2: c_2 = 315 mm

$a_2 = \beta_1 c_2$ = 0.883 × 315 = 278 mm

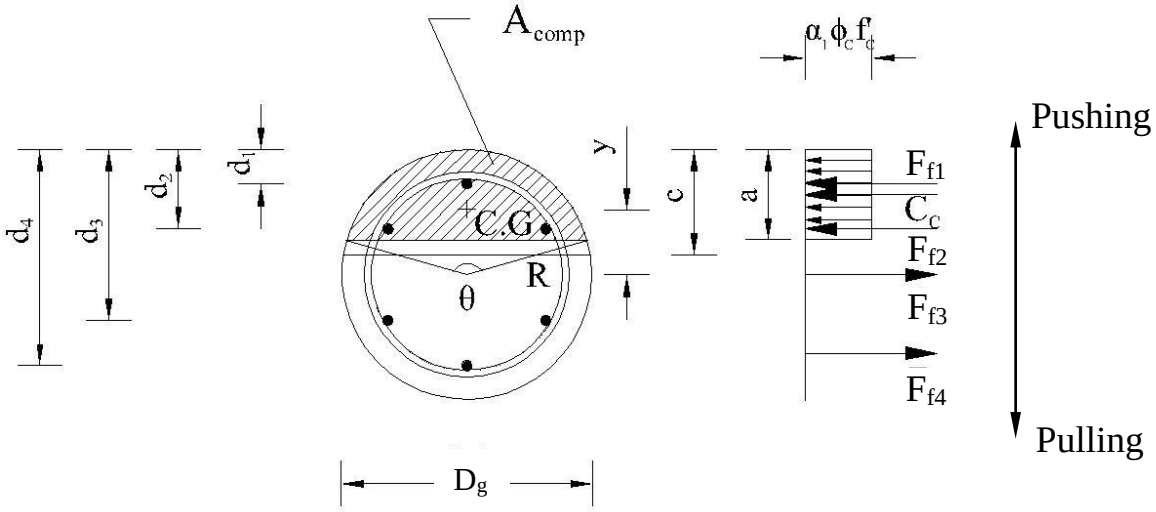

Figure B.1: Force equilibrium of the column section

$F_{f1} = F_{f2} = F_{f3} = F_{f4} = 0$ (neglect GFRP bars in compression)

Concrete area under compression,

$$A_{comp,b} = R^2\left(\cos^{-1}\left(\frac{R-a}{R}\right)\right) - (R-a)\sqrt{2Ra-a^2}$$

$$= 175^2\left(\cos^{-1}\left(\frac{175-278}{175}\right)\right) - (175-278)\sqrt{2\times 175\times 278 - 278^2}$$

= 81,947 mm^2

Distance of the C.G. of A_{comp2} from the center of cross section of the column,

$$y = \frac{4Rsin^3\frac{\theta}{2}}{3(\theta - \sin\theta)}$$

Where,

$\theta = 2\cos^{-1}\left(1 - \frac{a}{R}\right) = 2\cos^{-1}\left(1 - \frac{278}{175}\right)$ = 252.1° = 4.4 rad

$y_2 = \frac{4\times175\times sin^3\frac{252.1}{2}}{3(4.4-\sin 252.1)}$ = 23 mm

$C_{c2} = \alpha_1\phi_c f_c' A_{comp,2} = 0.797 \times 1 \times 35 \times 81{,}947$ = 2,287 kN

$P_b = C_{c2} + F_{f1} + F_{f2} + F_{f3} + F_{f4}$ = 2,287 + 0 + 0 + 0 + 0 = 2,287 kN

$M_2 = C_{c2} \times y_2 + F_{f1}(R - d_1) + F_{f2}(R - d_2) + F_{f3}(R - d_3) + F_{f4}(R - d_4)$

= 2,287 × 23 = 52.7 kN.m

Point 2: M_2 = 52.7 kN.m; P_2 = 2,287 kN

- <u>Point 3: c_3 = 245 mm</u>

$F_{f1} = F_{f2} = F_{f3} = 0$ (neglect GFRP bars in compression)

$a_3 = \beta_1 c_3 = 0.883 \times 245$ = 216.2 mm

$$A_{comp3} = R^2\left(\cos^{-1}\left(\frac{R-a}{R}\right)\right) - (R-a)\sqrt{2Ra - a^2}$$

$$= 175^2\left(\cos^{-1}\left(\frac{175-216.2}{175}\right)\right) - (175 - 216.2\ \ )\sqrt{2\times175\times216.2\ \ - 216.2\ \ ^2}$$

= 62,396 mm^2

Distance of the C.G. of A_{comp3} from the center of cross section of the column,

$$y = \frac{4Rsin^3\frac{\theta}{2}}{3(\theta - \sin\theta)}$$

Where,

$\theta = 2\cos^{-1}\left(1 - \frac{a}{R}\right) = 2\cos^{-1}\left(1 - \frac{216.2}{175}\right) = 207.2° = 3.62$ rad

$y_3 = \frac{4\times175\times sin^3\frac{207.2}{2}}{3(3.99-\sin 207.2)} = 52.6$ mm

$C_{c3} = \alpha_1\phi_c f_c' A_{comp3} = 0.797 \times 1 \times 35 \times 62{,}396 \times 10^{-3} = 1{,}742$ kN

$\varepsilon_{f4} = \varepsilon_{cu}\left(1 - \frac{d_4}{c_3}\right) = 0.0035 \times \left(1 - \frac{312.05}{245}\right) = -0.00096$

$f_{f4} = E_f\varepsilon_{f4} = 65{,}700 \times (-0.00096) = -62.9$ MPa

$F_{f4} = \phi_f A_{f4} f_{f4} = 1 \times 197.9 \times (-62.9) \times 10^{-3} = -12.5$ kN

$P_3 = C_{c3} + F_{f1} + F_{f2} + F_{f3} + F_{f4} = 1{,}742 + 0 + 0 + 0 - 12.5 = 1{,}729$ kN

$M_3 = C_{c3} \times y_3 + F_{f1}(R - d_1) + F_{f2}(R - d_2) + F_{f3}(R - d_3) + F_{f4}(R - d_4)$

$= 1{,}742 \times 52.6 + 0 + 0 + 0 + (-12.5)(175 - 312.05) = 93.3$ kN.m

Point 3: $M_3 = 93.3$ kN.m; $P_3 = 1{,}729$ kN

- Point 4: $c_4 = 175$ mm

$F_{f1} = F_{f2} = 0$ (neglect GFRP bars in compression)

$a_4 = \beta_1 c_4 = 0.883 \times 175 = 154.4$ mm

$A_{comp4} = R^2\left(\cos^{-1}\left(\frac{R-a}{R}\right)\right) - (R-a)\sqrt{2Ra - a^2}$

$= 175^2\left(\cos^{-1}\left(\frac{175-154.4}{175}\right)\right) - (175 - 154.4)\sqrt{2\times175\times154.4 - 154.4^2}$

$= 40{,}925$ mm^2

Distance of the C.G. of A_{comp4} from the center of cross section of the column,

$y = \frac{4R sin^3\frac{\theta}{2}}{3(\theta - \sin\theta)}$

Where,

$\theta = 2\cos^{-1}\left(1 - \frac{a}{R}\right) = 2\cos^{-1}\left(1 - \frac{154.4}{175}\right) = 166.5° = 2.91$ rad

$y_4 = \frac{4\times175\times sin^3\frac{166.5}{2}}{3(2.91-\sin 166.5)}$ = 85.5 mm

$C_{c4} = \alpha_1\phi_c f_c' A_{comp4}$ = 0.797 × 1 × 35 × 40,925 × 10^{-3} = 1,142.3 kN

$\varepsilon_{f3} = \varepsilon_{cu}\left(1-\frac{d_3}{c_4}\right) = 0.0035\times\left(1-\frac{243.53}{175}\right) = -0.0014$

$f_{f3} = E_f\varepsilon_{f3}$ = 65,700 × (– 0.0014) = – 90 MPa

$F_{f3} = \phi_f A_{f3} f_{f3}$ = 1 × 395.8 × (– 90) × 10^{-3} = – 35.7 kN

$\varepsilon_{f4} = \varepsilon_{cu}\left(1-\frac{d_4}{c_3}\right) = 0.0035\times\left(1-\frac{312.05}{140}\right) = -0.0027$

$f_{f4} = E_f\varepsilon_{f4}$ = 65,700 × (– 0.0027) = – 180.1 MPa

$F_{f4} = \phi_f A_{f4} f_{f4}$ = 1 × 197.9 × (– 180.1) × 10^{-3} = – 35.7 kN

$P_4 = C_{c4} + F_{f1} + F_{f2} + F_{f3} + F_{f4}$ = 1,142.3 + 0 + 0 – 35.7 – 35.7 = 1,071 kN

$M_4 = C_{c4}\times y_4 + F_{f1}(R-d_1) + F_{f2}(R-d_2) + F_{f3}(R-d_3) + F_{f4}(R-d_4)$

= 1,142.3 × 85.5 + 0 + 0 + (– 35.7) (175 – 243.53) + (– 35.7) (175 – 312.05) = 105 kN.m

Point 4: M_4 = 105 kN.m; P_4 = 1,071 kN

- Point 5: c_5 = 140 mm

$F_{f1} = F_{f2} = 0$ (neglect GFRP bars in compression)

$a_5 = \beta_1 c_5$ = 0.883 × 140 = 123.6 mm

$A_{comp5} = R^2\left(\cos^{-1}\left(\frac{R-a}{R}\right)\right) - (R-a)\sqrt{2Ra-a^2}$

$= 175^2\left(\cos^{-1}\left(\frac{175-123.6}{175}\right)\right) - (175-123.6)\sqrt{2\times175\times123.6-123.6^2}$

= 30,361 mm^2

Distance of the C.G. of A_{comp5} from the center of cross section of the column,

$$y = \frac{4R sin^3 \frac{\theta}{2}}{3(\theta - \sin\theta)}$$

Where,

$\theta = 2\cos^{-1}\left(1 - \frac{a}{R}\right) = 2\cos^{-1}\left(1 - \frac{123.6}{175}\right)$ = 145.8° = 2.54 rad

$y_5 = \frac{4\times175\times sin^3\frac{145.8}{2}}{3(2.54-\sin 145.8)}$ = 102.8 mm

$C_{c5} = \alpha_1 \phi_c f_c' A_{comp5} = 0.797 \times 1 \times 35 \times 30{,}361 \times 10^{-3}$ = 847.5 kN

$\varepsilon_{f3} = \varepsilon_{cu}\left(1 - \frac{d_3}{c_5}\right) = 0.0035 \times \left(1 - \frac{243.53}{140}\right) = -0.0026$

$f_{f3} = E_f \varepsilon_{f3} = 65{,}700 \times (-0.0026) = -170.04$ MPa

$F_{f3} = \phi_f A_{f3} f_{f3} = 1 \times 395.8 \times (-170.04) \times 10^{-3} = -67.3$ kN

$\varepsilon_{f4} = \varepsilon_{cu}\left(1 - \frac{d_4}{c_5}\right) = 0.0035 \times \left(1 - \frac{312.05}{140}\right) = -0.0043$

$f_{f4} = E_f \varepsilon_{f4} = 65{,}700 \times (-0.0043) = -282.6$ MPa

$F_{f4} = \phi_f A_{f4} f_{f4} = 1 \times 197.9 \times (-282.6) \times 10^{-3} = -56$ kN

$P_5 = C_{c5} + F_{f1} + F_{f2} + F_{f3} + F_{f4}$ = 847.5 + 0 + 0 – 67.3 – 56 = 724.2 kN

$M_5 = C_{c5} \times y_5 + F_{f1}(R - d_1) + F_{f2}(R - d_2) + F_{f3}(R - d_3) + F_{f4}(R - d_4)$

= 847.5 × 102.8+ 0 + 0 + (– 67.3) (175 – 243.53) + (– 56) (175 – 312.05) = 99.4 kN.m

Point 5: M_5 = 99.4 kN.m; P_5 = 724.2 kN

- Point 6: c_6 = 105 mm

$F_{f1} = 0$ (neglect GFRP bars in compression)

$a_6 = \beta_1 c_6 = 0.883 \times 105 = 92.7$ mm

$A_{comp6} = R^2\left(\cos^{-1}\left(\frac{R-a}{R}\right)\right) - (R-a)\sqrt{2Ra - a^2}$

$= 175^2 \left(\cos^{-1}\left(\frac{175-92.7}{175}\right)\right) - (175 - 92.7)\sqrt{2 \times 175 \times 92.7 - 92.7^2}$

$= 20{,}389 \text{ mm}^2$

Distance of the C.G. of A_{comp6} from the center of cross section of the column,

$$y = \frac{4R\sin^3\frac{\theta}{2}}{3(\theta - \sin\theta)}$$

Where,

$\theta = 2\cos^{-1}\left(1 - \frac{a}{R}\right) = 2\cos^{-1}\left(1 - \frac{92.7}{175}\right) = 123.9° = 2.16$ rad

$y_6 = \frac{4\times175\times\sin^3\frac{123.9}{2}}{3(2.16-\sin 123.9)} = 120.4$ mm

$C_{c6} = \alpha_1\phi_c f'_c A_{comp6} = 0.797 \times 1 \times 35 \times 20{,}389 \times 10^{-3} = 569$ kN

$\varepsilon_{s2} = \varepsilon_{cu}\left(1 - \frac{d_2}{c_6}\right) = 0.0035 \times \left(1 - \frac{106.48}{105}\right) = -0.00005$

$f_{f2} = E_f\varepsilon_{f2} = 65{,}700 \times (-0.00005) = -3.2$ MPa

$F_{f2} = \phi_f A_{f2} f_{f2} = 1 \times 395.8 \times (-3.2) \times 10^{-3} = -1.3$ kN

$\varepsilon_{f3} = \varepsilon_{cu}\left(1 - \frac{d_3}{c_6}\right) = 0.0035 \times \left(1 - \frac{243.53}{105}\right) = -0.0046$

$f_{f3} = E_f\varepsilon_{f3} = 65{,}700 \times (-0.0046) = -303.4$ MPa

$F_{f3} = \phi_f A_{f3} f_{f3} = 1 \times 395.8 \times (-303.4) \times 10^{-3} = -120.1$ kN

$\varepsilon_{f4} = \varepsilon_{cu}\left(1 - \frac{d_4}{c_6}\right) = 0.0035 \times \left(1 - \frac{312.05}{105}\right) = -0.0069$

$f_{f4} = E_f\varepsilon_{f4} = 65{,}700 \times (-0.0069) = -453.4$ MPa

$F_{f4} = \phi_f A_{f4} f_{f4} = 1 \times 197.9 \times (-453.4) \times 10^{-3} = -89.8$ kN

$P_6 = C_{c6} + F_{f1} + F_{f2} + F_{f3} + F_{f4} = 569 + 0 - 1.3 - 120.1 - 89.8 = 357.9$ kN

$M_6 = C_{c6} \times y_6 + F_{f1}(R - d_1) + F_{f2}(R - d_2) + F_{f3}(R - d_3) + F_{f4}(R - d_4)$

$= 569 \times 120.4 + 0 + (-1.3)(175 - 106.48) + (-120.1)(175 - 243.53) + (-89.8)(175 - 312.05) = 89$ kN.m

Point 6: $M_6 = 89$ kN.m; $P_6 = 357.9$ kN

- Point 7: $c_7 = 77$ mm

$F_{f1} = 0$ (neglect GFRP bars in compression)

$a_7 = \beta_1 c_7 = 0.883 \times 77 = 67.9$ mm

$$A_{comp7} = R^2\left(\cos^{-1}\left(\frac{R-a}{R}\right)\right) - (R-a)\sqrt{2Ra-a^2}$$

$$= 175^2\left(\cos^{-1}\left(\frac{175-67.9}{175}\right)\right) - (175-67.9)\sqrt{2\times175\times67.9-67.9^2}$$

$= 13{,}128$ mm^2

Distance of the C.G. of A_{comp7} from the center of cross section of the column,

$$y = \frac{4R\sin^3\frac{\theta}{2}}{3(\theta-\sin\theta)}$$

Where,

$\theta = 2\cos^{-1}\left(1-\frac{a}{R}\right) = 2\cos^{-1}\left(1-\frac{67.9}{175}\right) = 104° = 1.83$ rad

$y_7 = \frac{4\times175\times\sin^3\frac{104}{2}}{3(1.83-\sin 104)} = 134.7$ mm

$C_{c7} = \alpha_1\phi_c f'_c A_{comp7} = 0.797 \times 1 \times 35 \times 13{,}128 \times 10^{-3} = 366.4$ kN

$$\varepsilon_{s2} = \varepsilon_{cu}\left(1-\frac{d_2}{c_7}\right) = 0.0035 \times \left(1-\frac{106.48}{77}\right) = -0.0013$$

$f_{f2} = E_f\varepsilon_{f2} = 65{,}700 \times (-0.0013) = -88$ MPa

$F_{f2} = \phi_f A_{f2} f_{f2} = 1 \times 395.8 \times (-88) \times 10^{-3} = -34.9$ kN

$$\varepsilon_{f3} = \varepsilon_{cu}\left(1-\frac{d_3}{c_7}\right) = 0.0035 \times \left(1-\frac{243.53}{77}\right) = -0.0076$$

$f_{f3} = E_f \varepsilon_{f3} = 65{,}700 \times (-0.0076) = -497.3$ MPa

$F_{f3} = \phi_f A_{f3} f_{f3} = 1 \times 395.8 \times (-497.3) \times 10^{-3} = -196.9$ kN

$\varepsilon_{f4} = \varepsilon_{cu}\left(1 - \frac{d_4}{c_7}\right) = 0.0035 \times \left(1 - \frac{312.05}{77}\right) = -0.0107$

$f_{f4} = E_f \varepsilon_{f4} = 65{,}700 \times (-0.0107) = -701.9$ MPa

$F_{f4} = \phi_f A_{f4} f_{f4} = 1 \times 197.9 \times (-701.9) \times 10^{-3} = -139$ kN

$P_7 = C_{c7} + F_{f1} + F_{f2} + F_{f3} + F_{f4} = 366.4 + 0 - 34.9 - 196.9 - 139 \simeq 0$ kN

$M_7 = C_{c7} \times y_7 + F_{f1}(R - d_1) + F_{f2}(R - d_2) + F_{f3}(R - d_3) + F_{f4}(R - d_4)$

$= 366.4 \times 134.7 + 0 + (-34.9)(175 - 106.48) + (-196.9)(175 - 243.53) + (-139)(175 - 312.05) = 79.5$ kN.m

Point 7: $M_7 = 79.5$ kN.m; $P_7 = 0.0$ kN

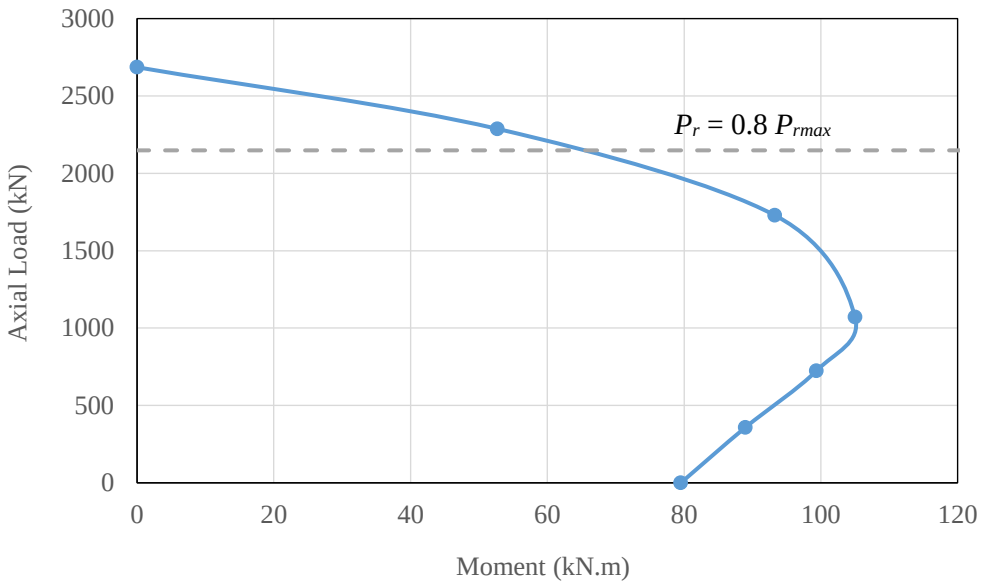

Figure B.2: Column interaction diagram for specimen G1.

As previously discussed, the average axial load is 0.2 $f'_c A_g$. However, the axial load level was expressed in terms of P_o, as per Clause 12.7.3.3 of CSA S806-12 (CSA 2017), since this study is

dedicated to study the behaviour of GFRP-RC columns. Therefore, the applied axial load was expressed as:

$$P = 0.2P_o = 0.2\alpha_1\phi_c f_c^{'}(A_g - A_F) = 0.2\times 0.797\times 1\times 35\times\left(96,211-6\times 198\right) = 537 \text{ kN}$$

Assume c = 121.8 mm

$a = \beta_1 \text{c} = 0.883 \times 121.8 = 107.5$ mm

$F_{f1} = F_{f2} = 0$ (neglect GFRP bars in compression)

$$A_{comp} = R^2\left(\cos^{-1}\left(\frac{R-a}{R}\right)\right) - (R-a)\sqrt{2Ra-a^2}$$

$$= 175^2\left(\cos^{-1}\left(\frac{175-107.5}{175}\right)\right) - (175-107.5)\sqrt{2\times 175\times 107.5 - 107.5^2}$$

= 25,077 mm^2

Distance of the C.G. of A_{comp} from the center of cross section of the column,

$$y = \frac{4Rsin^3\frac{\theta}{2}}{3(\theta - \sin\theta)}$$

Where,

$\theta = 2\cos^{-1}\left(1-\frac{a}{R}\right) = 2\cos^{-1}\left(1-\frac{107.5}{175}\right) = 134.6° = 2.35$ rad

$\text{y} = \frac{4\times 175\times sin^3\frac{134.6}{2}}{3(2.35-\sin 134.6)} = 111.9$ mm

$\text{C}_c = \alpha_1\phi_c f_c' A_{comp} = 0.797\times 1\times 35\times 25{,}077 = 699.9$ kN

$$\varepsilon_{f3} = \varepsilon_{cu}\left(1-\frac{d_3}{c}\right) = 0.0035\times\left(1-\frac{243.53}{121.8}\right) = -\ 0.0035$$

$f_{f3} = E_f\varepsilon_{f3} = 65{,}700\times(-0.0035) = -229.8$ MPa

$F_{f3} = \phi_f A_{f3} f_{f3} = 1\times 395.8\times(-229.8)\times\ 10^{-3} = -91.0$ kN

$$\varepsilon_{f4} = \varepsilon_{cu}\left(1-\frac{d_4}{c}\right) = 0.0035\times\left(1-\frac{312.05}{121.8}\right) = -\ 0.0055$$

$f_{f4} = E_f \varepsilon_{f4} = 65{,}700 \times (-0.0055) = -359.2$ MPa

$F_{f4} = \phi_f A_{f4} f_{f4} = 1 \times 197.9 \times (-359.2) \times 10^{-3} = -71.1$ kN

Check force equilibrium:

$P = C_c + F_{s1} + F_{s2} + F_{s3} + F_{s4}$

Or, 537 = 699.9 + 0 + 0 – 91 – 71.1

Or, 537 kN ≈ 537.8 kN

$M = C_c \times y + F_{s1}(R - d_1) + F_{s2}(R - d_2) + F_{s3}(R - d_3) + F_{s4}(R - d_4)$

= 699.9 × 111.9 + 0 + 0 + (– 91) (175 – 243.53) + (– 71.1) (175 – 312.05) = 94.3 kN.m

Lateral load capacity, V = M/1.75 = 94.3/1. 75 = 53.9 kN

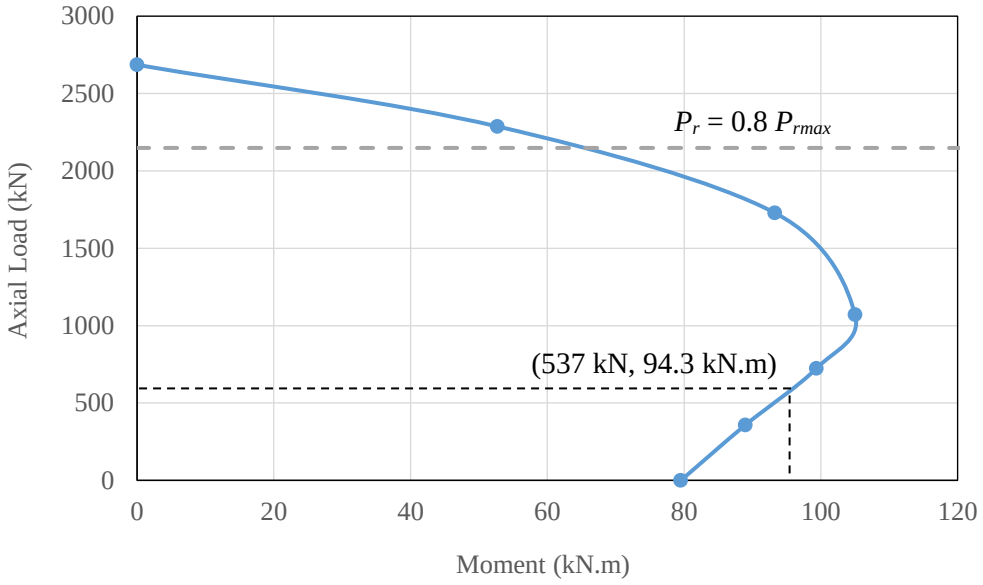

Figure B.3: Column interaction diagram for specimen G1.

B.3 DESIGN FOR SHEAR

B.3.1 Material and sectional properties

- Shear reinforcement characteristics:

f_{Fu} = 1,376 MPa; ϕ_f = 1; E_{fv} = 58.4 GPa; A_v = 2 × 71.0 = 142 mm^2; ε_{Fu} = 0.0236.

Applied lateral shear force, V_f = 53.9 kN

$V_r = V_c + V_s$

$V_c = 0.05\lambda\phi_c k_m k_r (f_c')^{1/3} k_s k_a b_w d_v \left(1 - \frac{N_f}{14A_g}\right)$

b_w= 350 mm

$d = 266$ mm $< 0.8h = 0.8 \times 350 = 280$ mm

$d_v \geq 0.9d = 0.9 \times 280 = 252$ mm

$\geq 0.72h = 0.72 \times 350 = 252$ mm

$k_m = \sqrt{\frac{V_f d}{M_f}} = \sqrt{\frac{0.280}{1.75}} = 0.4 < 1.0$

$k_r = 1 + \left(E_{frp} \,.\, \rho_{fw}\right)^{1/3} = 1 + (65700 \times 0.0123)^{1/3} = 10.31$

$k_s = 1$ ($d = 280$ mm < 300 mm)

$k_a = \frac{2.5}{\frac{M_f}{V_f d}} = \frac{2.5}{\frac{1.75}{0.280}} = 0.4 < 1.0$ (Take $k_a = 1.0$)

$V_c = 0.05\lambda\phi_c k_m k_r (f_c')^{1/3} k_s k_a b_w d_v \left(1 - \frac{N_f}{14A_g}\right)$

$V_c = 0.05 \times 1 \times 1 \times 0.4 \times 10.31 \times (35)^{1/3} \times 1 \times 1 \times 74{,}159 \times \left(1 - \frac{(-537 \times 10^3)}{14 \times 96{,}211}\right) \times 10^{-3}$

V_c = 87.6 kN

$V_c > 0.11\lambda\phi_c\sqrt{f_c'} b_w d = 0.11 \times 1 \times 1 \times \sqrt{35} \times 82{,}513 \times 10^{-3} = 53.7$ kN OK

$V_c < 0.22\lambda\phi_c\sqrt{f_c'} b_w d = 0.22 \times 1 \times 1 \times \sqrt{35} \times 82{,}513 \times 10^{-3} = 107.4$ kN OK

From CSA S806-12 Clause 8.4.5.2

$A_{vF,min} = 0.07\sqrt{f_c'}\frac{b_w s}{0.4 f_{Fu}}$

f_{Fu} < 1,200 MPa

f_{Fu} Or $0.005 \times E_{fv} = 0.005 \times 58{,}400 = 292$ MPa

$142 = 0.07\sqrt{35}\frac{350\times s}{0.4\times 292}$

$s = 114$ mm

When $s = 85$ mm

$$\varepsilon_l = \frac{\frac{M_f}{d_v} + (V_f - V_P) + 0.5N_f - A_P f_{Po}}{2(E_F A_F + E_P A_P)}$$

$\varepsilon_l = \frac{\left(\frac{94.3\times 10^6}{252} + 53.9\times 10^3 - 0.5\times 537\times 10^3\right)}{2\times 65{,}700\times 6\times 197.9} = 1.02\times 10^{-3}$

$\theta = 30° + 7000\varepsilon_l = 30 + (7000 \times 1.02 \times 10^{-3}) = 37.1° > 30°$ OK

$V_{sF} = \frac{0.4\phi_F A_{Fv} f_{Fu} d_v \cot\theta}{s}$

$V_{sF} = \frac{0.4\times 1\times 142\times 292\times 252\times \cot 37.1}{85} \times 10^{-3} = 65$ kN

$V_r = V_c + V_{sF} = 87.6 + 65 = 152.6$ kN $> V_f = 53.9$ kN OK

From CSA S806-12, Clause 8.4.3.13

The FRP spirals in compression members shall satisfy the following requirements:

- Spiral reinforcement shall have a minimum diameter of 6 mm;
- Spiral pitch shall not exceed 1/6 of the core diameter;
- Clear spacing between successive turns of the spiral shall not exceed 75 mm nor be less than 25 mm; and
- Volumetric ratio of spiral reinforcement shall be not less than the value given by:

  $$\rho_{Fs} = \frac{f_c'}{f_{Fh}}\left(\frac{A_g}{A_c} - 1\right)\frac{P}{P_o}$$

  $f_{Fh} = 0.006\ E_F = 0.006 \times 58{,}400 = 350.3$ MPa (governs)

  f_{Fu} Or $\phi_F f_{Fu} = 1 \times 1{,}376 = 1{,}376$ MPa

$$\rho_{Fs} = \frac{35}{350.3}\left(\frac{96{,}211}{70{,}921} - 1\right) \times 0.2 \;=\; 0.007$$

The provided volumetric ratio of spiral reinforcement can be calculated as

$$\rho_{Fs,,pro} = \frac{A_{vF} \times l}{A_c \times s} = \frac{71 \times \pi \times 300.5}{70{,}921 \times 85} = 0.011 > 0.007 \qquad \text{OK}$$

All requirements are met except for the second one (i.e., for the spiral pitch to be less than or equal to 1/6 of the core diameter) as it was deemed too conservative. One of the objectives of this study is to evaluate the conservativeness of such limit for spiral pitch (i.e., 1/6 of the core diameter).

From CSA S806-12, Clause 12.7.3.3

Confinement reinforcement in accordance with Clause 12.7.3.3 shall be provided in the form of circular spirals, circular hoops, rectilinear hoops, overlapping hoops, grids, and cross ties, with the required amount calculated as:

$$A_{sh} = 14 s h_c \frac{f_c^{'}}{f_{Fh}}\left(\frac{A_g}{A_c} - 1\right)\frac{P}{P_o}\frac{\delta}{\sqrt{k_c}}$$

$f_{Fh} = 0.006\, E_F = 0.006 \times 58{,}400 = 350.3$ MPa (governs)

f_{Fu} Or $\phi_F f_{Fu} = 1 \times 1{,}376 = 1{,}376$ MPa

$h_c = 300.5$ mm; $A_c = 70{,}921$ mm^2

$$142 = 14 \times 85 \times 300.5 \times \frac{35}{350.3}\left(\frac{96{,}211}{70{,}921} - 1\right) \times 0.2 \times \frac{\delta}{\sqrt{1}}$$

$\delta = 0.056 = 5.6\%$

From CSA S806-12, Clause 12.7.3.3

The spacing of the transverse reinforcement shall not exceed the least of:

- One-quarter of the minimum column dimension = 350/4 = 87.5 mm;
- 150 mm; or
- Six times the smallest longitudinal bar diameter = 6 × 15.9 = 96 mm

Select No. 10 spiral at pitch = 85 mm